Optical near-field characterization of Slow-Bloch Mode based photonic crystal devices

Thanh Phong Vo

N° d'ordre: 2011-24 Année 2011

ECOLE CENTRALE DE LYON

THESE

Présenté par

VO Thanh Phong

Pour obtenir le titre de Docteur de l'Ecole Centrale de Lyon

Spécialité: Nanophotonique

OPTICAL NEAR-FIELD CHARACTERIZATION OF SLOW-BLOCH MODE BASED PHOTONIC CRYSTAL DEVICES

Composition du Jury :

Directrice de Thèse	Ségolène CALLARD	Professeur des Universités
Rapporteurs :	Yannick DE WILDE	Directeur de Recherche CNRS
	Olivier GAUTHIER-LAFAYE	Chargé de Recherche CNRS
Examinateurs :	Thierry GROSJEAN	Chargé de Recherche CNRS
	Isabelle LEDOUX-RAK	Professeur des Universités
	Christian SEASSAL	Directeur de recherche C.N.R.S

Institut des Nanotechnologies de Lyon (INL) - CNRS UMR 5270

Acknowledgment

Looking back, I am surprised and at the same time very grateful for all I have received throughout five years in France. It has certainly shaped me as a person and has led me where I am now. All these years of studies are full of such gifts.

I would first to give my deepest gratitude to my advisor Ségolène CALLARD for the opportunity of doing doctoral research under her supervision. She has always encouraged me in the difficult time, unconditionally supported me even when I was thinking about giving up. Though nearly three years of working with her, she has helped me to see life and science in their full depth, and taught me how to appreciate the good scientific work that helps other researchers to build on it. She has enlightened me through her wide knowledge of nano-photonics and pointed me out the best direction where my work should go and what is necessary to obtain it. Frankly, she is the best advisor that I have ever seen.

I would like to thank Dr. Yannick DE WILDE and Dr. Olivier GAUTHIER-LAFAYE as accepted to be my reviewers and for insightful comments and discussions. My dissertation greatly improved thanks to their comments. I am grateful to my thesis committee. Especially to Prof. Isabelle LEDOUX-RAK for kind helps during my master study at ENS Cachan and Dr. Thierry GROSJEAN for fruitful discussions and collaboration in NANOEC program.

I would like to thank Dr. Christian SEASSAL for training me of using EBL and RIE, his supports and fruitful discussions concerning my experimental results, and to be the member of my thesis committee. I am grateful to Dr. Adel RAHMANI and Dr. Ali BELAROUCI for their FDTD simulations and helpful discussions during my work.

Thank you all my colleagues who work at 4th floor of F7: Alain, Aziz, Bertrand, Benoit, Brice, Christelle, Emmanuel, José, Ségolène, Thérèse et Yves. Especially Thérèse and Yves for their kind help. Similar acknowledge to Brice and Aziz for their supports in building the experimental set-up.

I would like to thank Nanophotonics group’s members for their scientific discussions and kind helps. I also acknowledge Philippe Regreny for growing the epitaxial structures and thank the people from CEA-LETI and NANO-LYON platform for their kind helps.

Last but not the least, I would like to thank my family: my wife Kim-Thu and little angel Lionel who give me the big motivation to live in a beautiful life and will stand beside me forever. The last similar thank you is devoted to my both parents, my sisters and my brothers for spiritually supporting me through my life.

ÉCOLE CENTRALE LYON **Direction de la recherche**

Liste des personnes Habilitées à Diriger des Recherches en poste à l'Ecole Centrale de Lyon

Nom-Prénom	*Corps grade*	Laboratoire ou à défaut département ECL	Etablissement
AURIOL Philippe	*professeur*	AMPERE	ECL
BEROUAL Abderrahmane	*professeur*	AMPERE	ECL
BURET François	*professeur*	AMPERE	ECL
JAFFREZIC-RENAULT Nicole	*directeur de recherche*	AMPERE	CNRS/ECL
KRÄHENBÜHL Laurent	*directeur de recherche*	AMPERE	CNRS/ECL
MARTELET Claude	*professeur*	AMPERE	ECL
NICOLAS Alain	*professeur*	AMPERE	ECL
NICOLAS Laurent	*directeur de recherche*	AMPERE	CNRS/ECL
SCORLETTI Gérard	*professeur*	AMPERE	ECL
SIMONET Pascal	*chargé de recherche*	AMPERE	CNRS/ECL
THOMAS Gérard	*professeur*	AMPERE	ECL
VOLLAIRE Christian	*professeur*	AMPERE	ECL

Nbre Ampère 12

HELLOUIN Yves	*maître de conférences*	DER EEA	ECL
LE HELLEY Michel	*professeur*	DER EEA	ECL

Nbre DER EEA 2

GUIRALDENQ Pierre	*professeur émérite*	DER STMS	ECL
VINCENT Léo	*professeur*	DER STMS	ECL

Nbre DER STMS 2

LOHEAC Jean-Pierre	*maître de conférences*	ICJ	ECL
MAITRE Jean-François	*professeur émérite*	ICJ	ECL
MARION Martine	*professeur*	ICJ	ECL
MIRONESCU Elisabeth	*professeur*	ICJ	ECL
MOUSSAOUI Mohand	*professeur*	ICJ	ECL
MUSY François	*maître de conférences*	ICJ	ECL
ZINE Abdel-Malek	*maître de conférences*	ICJ	ECL

Nbre ICJ 7

DAVID Bertrand	*professeur*	ICTT	ECL

Nbre ICTT 1

CALLARD Anne-Ségolène	*professeur*	INL	ECL
CLOAREC Jean-Pierre	*maître de conférences*	INL	ECL
GAFFIOT Frédéric	*professeur*	INL	ECL
GAGNAIRE Alain	*maître de conférences*	INL	ECL
GARRIGUES Michel	*directeur de recherche*	INL	CNRS/ECL
GENDRY Michel	*directeur de recherche*	INL	CNRS/ECL
GRENET Geneviève	*directeur de recherche*	INL	CNRS/ECL
HOLLINGER Guy	*directeur de recherche*	INL	CNRS/ECL

JOSEPH Jacques	*professeur*	INL	ECL
KRAWCZYK Stanislas	*directeur de recherche*	INL	CNRS/ECL
LETARTRE Xavier	*chargé de recherche*	INL	CNRS/ECL
MARTIN Jean-René	*professeur émérite*	INL	ECL
O'CONNOR Ian	*professeur*	INL	ECL
PHANER-GOUTORBE Magali	*professeur*	INL	ECL
ROBACH Yves	*professeur*	INL	ECL
SAINT-GIRONS Guillaume	*chargé de recherche*	INL	CNRS/ECL
SEASSAL Christian	*chargé de recherche*	INL	CNRS/ECL
SOUTEYRAND Eliane	*directeur de recherche*	INL	CNRS/ECL
TARDY Jacques	*directeur de recherche*	INL	CNRS/ECL
VIKTOROVITCH Pierre	*directeur de recherche*	INL	CNRS/ECL

Nbre INL 20

CHEN Liming	*professeur*	LIRIS	ECL

Nbre LIRIS 1

BAILLY Christophe	*professeur*	LMFA	ECL
BERTOGLIO Jean-Pierre	*directeur de recherche*	LMFA	CNRS/ECL
BLANC-BENON Philippe	*directeur de recherche*	LMFA	CNRS/ECL
BOGEY Christophe	*chargé de recherche*	LMFA	CNRS/ECL
CAMBON Claude	*directeur de recherche*	LMFA	CNRS/ECL
CARRIERE Philippe	*chargé de recherche*	LMFA	CNRS/ECL
CHAMPOUSSIN J-Claude	*professeur émérite*	LMFA	ECL
COMTE-BELLOT geneviève	*professeur émérite*	LMFA	ECL
FERRAND Pascal	*directeur de recherche*	LMFA	CNRS/ECL
GALLAND Marie-Annick	*professeur*	LMFA	ECL
GODEFERD Fabien	*chargé de recherche*	LMFA	CNRS/ECL
GOROKHOVSKI Mikhail	*professeur*	LMFA	ECL
HENRY Daniel	*directeur de recherche*	LMFA	CNRS/ECL
JEANDEL Denis	*professeur*	LMFA	ECL
JUVE Daniel	*professeur*	LMFA	ECL
LE RIBAULT Catherine	*chargée de recherche*	LMFA	CNRS/ECL
LEBOEUF Francis	*professeur*	LMFA	ECL
PERKINS Richard	*professeur*	LMFA	ECL
ROGER Michel	*professeur*	LMFA	ECL
SCOTT Julian	*professeur*	LMFA	ECL
SHAO Liang	*chargé de recherche*	LMFA	CNRS/ECL
SIMOENS Serge	*chargé de recherche*	LMFA	CNRS/ECL
TREBINJAC Isabelle	*maître de conférences*	LMFA	ECL

Nbre LMFA 23

BENAYOUN Stéphane	*professeur*	LTDS	ECL
CAMBOU Bernard	*professeur*	LTDS	ECL
COQUILLET Bernard	*maître de conférences*	LTDS	ECL
DANESCU Alexandre	*maître de conférences*	LTDS	ECL
FOUVRY Siegfrid	*chargé de recherche*	LTDS	CNRS/ECL
GEORGES Jean-Marie	*professeur émérite*	LTDS	ECL
GUERRET Chrystelle	*chargé de recherche*	LTDS	CNRS/ECL
HERTZ Dominique	*past*	LTDS	ECL
ICHCHOU Mohamed	*professeur*	LTDS	ECL
JEZEQUEL Louis	*professeur*	LTDS	ECL
JUVE Denyse	*ingénieur de recherche*	LTDS	ECL
KAPSA Philippe	*directeur de recherche*	LTDS	CNRS/ECL
LE BOT Alain	*chargé de recherche*	LTDS	CNRS/ECL

LOUBET Jean-Luc	*directeur de recherche*	LTDS	CNRS/ECL
MARTIN Jean-Michel	*professeur*	LTDS	ECL
MATHIA Thomas	*directeur de recherche*	LTDS	CNRS/ECL
MAZUYER Denis	*professeur*	LTDS	ECL
PERRET-LIAUDET Joël	*maître de conférences*	LTDS	ECL
SALVIA Michelle	*maître de conférences*	LTDS	ECL
SIDOROFF François	*professeur*	LTDS	ECL
SINOU Jean-Jacques	*maître de conférences*	LTDS	ECL
STREMSDOERFER Guy	*professeur*	LTDS	ECL
THOUVEREZ Fabrice	*professeur*	LTDS	ECL
TREHEUX Daniel	*professeur*	LTDS	ECL
VANNES André-Bernard	*professeur émérite*	LTDS	ECL
VINCENS Eric	*maître de conférences*	LTDS	ECL
		Nbre LTDS 26	
	Total HdR ECL	91	

dernière page de la thèse

AUTORISATION DE SOUTENANCE

Vu les dispositions de l'arrêté du 7 août 2006,

Vu la demande de la Directrice de Thèse

Madame S. CALLARD

et les rapports de

Monsieur Y. DE WILDE
Directeur de Recherche CNRS - Laboratoire de Spectroscopie en lumière polarisée - Institut Langevin
ESPCI Paris Tech - 10, rue Vauquelin - 75005 PARIS

Et de

Monsieur O. GAUTHIER-LAFAYE
Chargé de Recherche CNRS - Laboratoire d'Analyse et d'Architecture des Systèmes (LAAS)
7, avenue du Colonel Roche - 31077 TOULOUSE cedex 4

Monsieur VO Thanh-Phong

est autorisé à soutenir une thèse pour l'obtention du grade de **DOCTEUR**

Ecole doctorale MATERIAUX

Fait à Ecully, le 26 août 2011

P/Le Directeur de l'E.C.L.
La Directrice des Etudes

ECOLE CENTRALE DE LYON
SCOLARITE
3ème Cycle

M-A. GALLAND

Table of contents

General introduction

Photonic crystals (PC) are periodic dielectric structures on the scale of the wavelength of photons (a few hundred nanometers). Like the electrons or phonons in a crystalline material, the dispersion relation of photons in a photonic crystal has a special form, which is represented as a band diagram[1]. Their most famous properties are the presence of an energy band in which the propagation of photons is forbidden: the photonic band-gap (PBG). An effective band gap in three dimensions requires a three-dimensional crystal. However, such crystals are technologically difficult to fabricate. In contrast, two-dimensional crystals, made in the membranes of high index dielectric are objects whose manufacture is now well controlled by many research groups. In addition, they have the advantage of being well adapted to the development of components devoted to planar photonic integrated circuits. The propagation of photons is controlled horizontally by the 2D-PC and vertically by total internal reflection in the membrane. During the past decade, 2D-photonic crystal (PC) slabs have proven to be a real "play-ground" for implementing solid-states concepts to nanophotonics: photonic band gap, defect modes, Bloch modes and more recently randomness. This has enabled the realization of a wide variety of nanophotonic components. Typically, a 2D-PC consists of a lattice of air holes in a semiconductor membrane. By inserting defects, a hole vacancy for instance, it is possible to create various basic components, such as a microcavity. Photonic crystals enable the production of very small components of the order of the half wavelength. Their advantage is also to be able to integrate in one unique PC and in a one-step technology, a compact optical circuit. In such circuit, the guides or the filters are passive components in which light is injected and distributed along the optical functionalities of the device. Other components can have active properties. To make the PC active, light emitters are introduced into the crystal. The optical response of the system will then depend on the coupling between the emitters and 2D-PC modes. By inserting these emitters in a cavity, it is possible for instance to make micro-light sources such as micro-lasers with low threshold. In the field of quantum electrodynamics, we note that the realization of small-sized cavities, with a low modal volume (V) but a high quality factor (Q) provides a Q/V ratio authorizing a change in the spontaneous emission rate[2]. The strong coupling regime has been observed at very low temperatures in cavities between the photonic crystal cavity mode and a quantum dot placed in the cavity[3,4]. These achievements offer very interesting

perspectives for quantum information processing, as the realization of single photon sources[5]. Apart from defects, a different way to exploit the band diagram is to use allowed energy bands, *i.e* modes whose propagation are allowed in the crystal (named Bloch modes) but controlled, in terms of wave vector and group velocity by the dispersion relation. In particular, slow Bloch modes for which the group velocity vanishes opened the way to new types of components such as micro-lasers without cavity. Among them, surface addressable PC exploiting slow Bloch modes (SBMs) emitting in the vertical direction, *i.e.* located at the Γ-point of the Brillouin zone have attracted much attention[5,6,7,8]. Near this point, low curvature flat bands give rise to delocalized and stationary optical modes. They are currently recognized to yield very versatile photonic structures whose operation are not restricted to the in plane wave-guiding regime. Slow Bloch modes operating at the Γ-point have already shown to be suitable for directly achieving laser vertical emission with peculiar polarizations, as azimuthal or radial polarisations[9,10,11,12]. Many applications based on the novel properties of slow light can be addressed from non-linear optics, optical switching, quantum optics to optical storage[13,14]... It demonstrates that the full use of the dispersion relation of photonic crystals offers several ways to control the light in time and space on the scale of the wavelength. Lastly, it has also been proposed to introduce randomness into 2D-PC to realize light Anderson's localization[15,16,17]. The theory of Anderson localization was developed in 1958[18] and predicts the complete localization of waves in random media by multiple scattering. Successful realization of Anderson's localization in active 2D PC could be useful to better understand localization mechanisms of wave in other random media. Moreover, extremely high quality factor of Anderson' localized mode could be used to fabricate optical devices such as micro lasers or single photon sources in future.

Manufacture of high dimensional PCs still remains quite complex. At INL, the choice was to develop 2DPC based on III-V materials, especially InP. The advantage of these materials is that they may be transparent in the range of telecommunications wavelengths (1.3µm-1.6µm). Micro and nano-patterning these materials benefits from the expertise of the laboratory in terms of epitaxy and clean-room technology. The fabrication of active structures implies the epitaxial growth of the InP membrane and InAsP compounds, in the form of quantum wells or quantum dots.

In general, with the miniaturization of photonic components, it is necessary to develop characterization tools to observe the electromagnetic field in such small-scale structures. Direct access and local distribution of the electromagnetic field in terms of intensity, phase and polarization are required to validate the designs. The objective is also to improve understanding of the physical phenomena that occur at these scales, such as the phenomena of coupling between the emitter and a photonic structure. In the case of slow Bloch modes, one of the important features is the global lateral expansion of the modes and the field distribution inside the PC. Theoretically, the expansion, *i.e.* the mode surface (S) is proportional to the band curvature (which is intrinsic to the 2D-PC design) and to the lifetime of the mode in the structure[19,20]. In the case of an active structure, like a micro-laser, the mode expansion can also be governed by other mechanisms involving carrier-induced refractive-index change[5]. In brief, the real expansion of these slow modes in 2D PC structures is one of the elements to understand the complicated mechanisms of optical losses. In turn, the lifetime of photon in PC structures is directly linked to optical losses and is the essential parameter to improve the light-matter interaction[3,4,5]. In addition, a local inspection can help to explain the unexpected behavior of some components. In the particular case of photonic crystals, the structuration of space implies a structuration of the optical modes at scale well below the wavelength. Observation of modes is impossible by conventional optical techniques because they are limited laterally by the diffraction. While far-field optical techniques allow to obtain the global information on the overall structure, by transmission, reflection, or photoluminescence, they fail to reveal details of the optical modes present in a cavity smaller than the wavelength. Conversely, near-field scanning optical microscopy (NSOM) is able to overcome this limit. It opened a clear path for the characterization of micro and nano-device optics. Direct visualization of the field pattern in photonic crystal based structures was made possible by the development of a NSOM setup dedicated to these structures.

Our principle objective is to study Slow-Bloch mode based on active structures. In order to fulfill this goal, a NSOM set-up adapted to characterize slow light mode was developed. More specifically, we want to obtain the field distribution of the slow mode into the structure, investigate its expansion and polarization properties. Indeed, NSOM enables a direct access to evanescent fields confined at PC surface and thus yields local information about the field distribution of nanostructured materials. Among various configurations, we focus to develop the NSOM setup in transmission due to its

advantages. In comparison with NSOM configuration working in reflection mode, this configuration allows us to gain a better control of the illumination spot including its size, its shape, its position as well as effective pumping power on the surface of sample. Moreover, although dielectric fiber probes were demonstrated adapted to characterize the near-field optical properties of cavity modes (under light-line) in 2D-PC[21,22], it might be a challenge to work with strong vertical laser emission of slow light operating above light-line. The alternative metal-coating tip with circular aperture can be qualified for this issue. However, these aperture-probes suffer from the low transmission coefficient (10^{-4}-10^{-5} for 100nm-aperture size[3]) that reduces optical coupling of near-field mode to free-space. Since larger aperture increases the transmission but reduces the spatial resolution, trade-off between the coupling light and resolution of image needs to be considered.

In order to overcome these root issues associated with the conventional near-field probes, Femto-ST, INL, GEMaC and Lovalite SAS collaborate in the frame of ANR "Nano ANtennas for the Optical Electromagnetic nanoCollection (NANOEC)" project. This project is aimed to elaborate the novel efficient nanoantennas (NAs) as innovative tools for probing the nanoscale electromagnetic field surrounding the nanostructures (photonic crystals, plasmonic devices, etc…). Although many types of optical nano-antennas have been developed, such as monopole[23,24], dipole[25], bowtie[26] or Yugi-Uda antennas[27],[28]… they share the same operating principle that established for the radio-frequency regime[29]. Generally, the optical nano-antennas can act as nano-transmitters or nano-receivers to transform reciprocally the electromagnetic field between nano-objects in surface and free-space radiation[30]. These NAs-based techniques have been expected to reveal optical information still inaccessible with conventional measurements responding to the present and future needs of the growing nano-optics community. The novel optical properties of NAs, such as electromagnetic field redirection or polarization sensitivity, especially the field enhancement and confinement have illustrated the essential contributions of such structures to the strong improvement of the spatial resolution and coupling enhancement in optical imaging. These attributes have also opened up the new brilliant perspectives of NAs application in single molecule detection[31], non-linear optics[32],[33] or recently quantum optics[34].

Among the large varieties of designing NAs to obtain the optimal properties for nano-imaging purposes as above-stated, the free-standing bowtie aperture antenna (BNA)

mounted on near-field probe have been surged as a promising candidate[26,35,36,37]. Indeed, the optical abilities of specially-designed BNAs such as the high optical throughput, polarization sensitivity, field enhancement and confinement inside the gap zone are expected to increase the signal-to-noise ratio, thus enhance coupling efficiency of near-field to BNA tip as well as improve the spatial resolution in optical patterns. Moreover BNA-probe is also expected to have no perturbation to the real electromagnetic field distributed on surface which is a strict requirement in slow light characterization.

In this dissertation, the content is arranged into five chapters. Chapter 1 briefly reviews the principle theories concerning photonic crystals, near-field scanning optical microscope and nano-antenna concepts. In chapter 2 we present the details of our NSOM setup working in transmission mode and the optical alignment system which have been built in our laboratory. In addition, nano-fabrication processes such as Epitaxy, Electron Beam Lithography (EBL), Reactive Ion Etching (RIE) and chemical etching which were employed to fabricate from PC structures to near-field probes are described. We also include in this chapter the FDTD simulation principle using for theoretical study of photonic crystals and the description of micro-photoluminescence set-up used for our far-field characterization. Chapter 3 is dedicated to present the simulation, fabrication and far-field characterization results of photonic crystals. Chapter 4 is dedicated to indicate and discuss about experimental results based on NSOM measurement. In the first section of chapter 4, we present the surface mode characterization with conventional probes (apertureless dielectric and Al-coating circular aperture probe) to demonstrate the impacts of probe nature to near-field optical pattern. The second section of chapter 4 is dedicated to the surface mode characterization with BNA-tip. We show that BNA-tip can provide the spatial resolution of $\lambda/13$ in mapping the near-field patterns with coupling enhancement of two orders of magnitude. The third section of chapter 4 is to present and discuss about the surface mode expansion over photonic crystal structure. In chapter 5 we briefly introduce the disordered photonic crystal concepts and present two separated disorder methods (fluctuation of hole position and modification of hole size) as well as their simulation results. The experimental results performed by our NSOM set-up to track Anderson's localization in these two cases of disordered photonic crystal are also presented and discussed.

References

[1] *Joannopoulos J, Johnson S G, Meade R and Winn J 2007 Photonic Crystals, Molding the Flow of Light 2nd Edn (Princeton, NJ: Princeton University Press)*

[2] *N. Chauvin, P. Nedel, C. Seassal, B. Ben Bakir, X. Letartre, M. Gendry, A. Fiore, and P. Viktorovitch," Control of the spontaneous emission from a single quantum dash using a slow-light mode in a two-dimensional photonic crystal on a Bragg reflector" Phys. Rev. B 80, 045315 (2009).*

[3] *R.A. Taylor et al, "Cavity Enhancement of Single Quantum Dot Emission in the Blue", Nanoscale Res Lett (2010) 5:608–612*

[4] *J. Vu·ckovic and Y. Yamamoto,"Photonic crystal microcavities for cavity quantum electrodynamics with a single quantum dot," Applied Physics Letters 82, pp. 2374{2376, Apr. 2003.*

[5] *M. Notomi, "Manipulating light with strongly modulated photonic crystals," Rep. Prog. Phys. 73 (2010) 096501 (57pp)*

[6] *P. Viktorovitch, B. Ben Bakir, S.Boutami, J.L. Leclercq, X. Letartre, P. Rojo-Romeo, C. Seassal, M.Zussy, L. Di Cioccio, J.M. Fedeli, "3-D harnessing of light with 2.5 D photonic Crystals," Laser and Photonics Eviews, Vol 4, pp. 401-413 (2010)*

[7] *F. Raineri, C. Cojocaru, R. Raj, P. Monnier, A. Levenson, C. Seassal, X. Letartre, and P. Viktorovitch, "Tuning a two-dimensional photonic crystal resonance via optical carrier injection," Opt. Lett. 30, 64-66 (2005)*

[8] *Ben B. Bakir, Ch, X. Letartre, P. Viktorovitch, M. Zussy, L. Di Cioccio, J. M. Fedeli, "Surface-emitting microlaser combining two-dimensional photonic crystal membrane and vertical Bragg mirror", Applied Physics Letters, Vol. 88, No. 8. (2006)*

[9] *Sakai, K., Miyai, E., Sakaguchi, T., Ohnishi, D., Okano, T., and Noda, "Lasing band-edge identification for a surface-emitting photonic crystal laser," IEEE J. Sel. Areas Commun., 23, pp. 1335–1340 (2005)*

[10] *K. Sakai, and S. Noda, "Optical trapping of metal particles in doughnut-shaped beam emitted by photonic-crystal laser," Electron. Lett. 43 (2), 107 (2007).*

[11] *Eiji Miyai, Kyosuke Sakai, Takayuki Okano, Wataru Kunishi, Dai Ohnishi, and Susumu Noda, "Lasers producing tailored beams", Nature 441, 946 (22 June 2006)*

[12] *S-H Kwon, Y-H Lee, "High Index-Contrast 2D Photonic Band-Edge Laser", IEICE Tran. Elect., 87, 308 (2004)*

[13] *Krauss T F 2008 Why do we need slow light? Nature Photon. 2 448–50*

[14] *Baba T 2008 Slow light in photonic crystals Nature Photon. 2 465–73*

[15] *John, S. Strong localization of photons in certain disordered dielectric super lattices. Phys. Rev. Lett. 58, 2486-2489 (1987)*

[16] *Topolancik, J., Ilic, B., & Vollmer, F. Experimental observation of strong photon localization in disordered photonic crystal waveguides. Phys. Rev. Lett. 99, 253901-1-4 (2007)*

[17] *Topolancik, J., & Vollmer, F. Random high-Q cavities in disordered photonic crystal waveguides. Appl. Phys. Lett. 91, 201102-1-3 (2007)*

[18] *Anderson, P. W. Absence of diffusion in certain random lattices. Phys. Rev. 109, 1492-1505 (1958)*

[19] *J. M. Gerard and B. Gayral, "Strong Purcell effect for InAs quantum boxes in three-dimensional solid-state microcavities," J. Lightwave Technol., vol. 17, pp. 2089–2095, 1999.*

[20] *X. Letartre, J. Mouette, J. L. Leclercq, P. Rojo Romeo, C. Seassal, and P. Viktorovitch, "Switching Devices With Spatial and Spectral Resolution Combining Photonic Crystal and MOEMS Structures," J. Lightwave Technol. 21, 1691- (2003)*

[21] *Nicolas Louvion, Adel Rahmani, Christian Seassal, Ségolène Callard, Davy Gérard, and Frédérique de Fornel, "Near-field observation of subwavelength confinement of photoluminescence by a photonic crystal microcavity," Opt. Lett. 31, 2160-2162 (2006)*

[22] *G. Le Gac, A. Rahmani, C. Seassal, E. Picard, E. Hadji, and S. Callard, "Tuning of an active photonic crystal cavity by an hybrid silica/silicon near-field probe," Opt. Express 17(24), 21672–21679 (2009).*

[23] *H.G. Frey, S. Witt, K. Felderer, and R. Guckenberger, "High-Resolution Imaging of Single Fluorescent Molecules with the Optical Near-Field of a Metal Tip," Phys. Rev. Lett. 93, 200801 (2004).*

[24] *T. Taminiau, R. Moerland, F. Segerink, L. Kuipers, and N. V. Hulst, "λ /4 resonance of an optical monopole antenna probes by single molecule fluorescence," Nano Lett. 7, 28 (2007).*

[25] *P. Mühlschlegel, H.-J. Eisler, O. Martin, B. Hecht, and D. Pohl, "Resonnant optical antenna," Science 308, 1607–1609 (2005)*

[26] *P. J. Schuck, D. P. Fromm, A. Sundaramurthy, G. S. Kino, and W. E. Moerner, "Improving the mismatch between light and nanoscale objects with gold bowtie nanoantennas," Phys. Rev. Lett. 94, 017402 (2005)*

[27] *Kosako, T.; Kadoya, Y.; Hofmann, H. F. "Directional control of light by a nano-optical Yagi-Uda antenna". Nat Photon 4, 312–315*

[28] *Curto, A.; Volpe, G.; Taminiau, T.; Kreuzer, M.; van Hulst, "Unidirectional emission of a quantum dot coupled to a nanoantenna", Science 329, 930-933 (2010)*

[29] *Novotny, L.; Hecht, B. Principle of nano-optics; Cambridge University Press, 2006*

[30] *Novotny, L.; van Hulst, N."Antennas for light", Nature Photonics, 2011, 5, 83*

[31] *E. Cubukcu et al, "Split ring resonator sensors for infrared detection of single molecular monolayers", Appl. Phys. Lett. 95, 043113 (2009)*

[32] *T. Hanke, G. Krauss, D. Träutlein, B. Wild, R. Bratschitsch, and A. Leitenstorfer, "Efficient Nonlinear Light Emission of Single Gold Optical Antennas Driven by Few-Cycle Near-Infrared Pulses," Phys. Rev. Lett. 103(25), 257404 (2009).*

[33] *Danckwerts M, Novotny L. Optical frequency mixing at coupled gold nanoparticles. Phys Rev Lett, 2007, 98: 026104*

[34] *Greffet J.-J.; Laroche M.; Marquier, F. « Impedance of a nanoantenna and a single quantum emitter », Phys Rev Lett. 2010 Sep 10;105(11):117701*

[35] *J. Farahani, D. Pohl, H.-J. Eisler, and B. Hecht, "Single quantum dot coupled to a scanning optical antenna : A tunable superemitter," Phys. Rev. Lett. 95(1), 017402.1–4 (2005).*

[36] *R. Grober, R. Schoelkopf, and D. Prober, "Optical antenna: Towards a unity efficiency near-field optical probe," Appl. Phys. Lett. 70(11), 1354–6 (1997)*

[37] *L. Wang, S. Uppuluri, E. Jin, and X. Xu, "Nanolithography using high transmission nanoscale bowtie apertures," Nano Lett. 6, 361 (2006)*

Chapter 1: Theory

This chapter will present context of this work and the principle elements of theory concerning photonic crystal, near-field scanning optical microscope and optical nano-antenna.

1.1. Photonic crystal

1.1.1. Introduction

Quantum mechanics theory demonstrates that the solid crystals, where the atoms or molecules are repeated in space, present a periodic potential for electrons propagating through it and make electrons behave very differently from those in homogeneous conducting media[1,2]. For instance, electron waves might be forbidden to propagate in certain directions at various ranges of energy. This analogy could also be applied to the light wave, an electromagnetic wave, in photonic crystal media where atoms and molecules are replaced by differing dielectric components while periodic potential is substituted by periodic dielectric function. The photonic crystal concepts have been surged and discussed a long time, and defined as a function of their periodic structures of dielectrics arranged either in one, two or three dimensions of space[2,3]. Photons propagating in these media experience periodic perturbations and strong dispersion. These effects could provide photonic band gaps or low band curvatures in diagram exactly as electron behaviors in solid crystal media.

Photonic crystals are also a wonderful platform used to transfer solid state concepts to photonics. Recently they also have been proposed to realize Anderson localization (AL) experiments with photon, thanks the concepts of disordered photonic crystals. The Anderson localization was named after his prediction in 1958 that disorder in periodic/homogeneous systems may lead to localized states of waves[4], and a strong localization regime can be achieved. In 1987 it was predicted that the AL regime may be easier to reach in randomized photonic crystals with wide band gap, where the localization phenomenon is assisted by random scattering of Bloch waves. Lately it has been demonstrated experimentally in quasi one-dimensional photonic crystal waveguides[5,6].

Generally photonic crystals (PC) are sorted by their periodic arrangements of dielectric materials. By this definition, we have 1D-PC, 2D-PC or 3D-PC depending on the periodicity of dielectrics in one, two or three dimensions respectively as shown in Figure 1.1

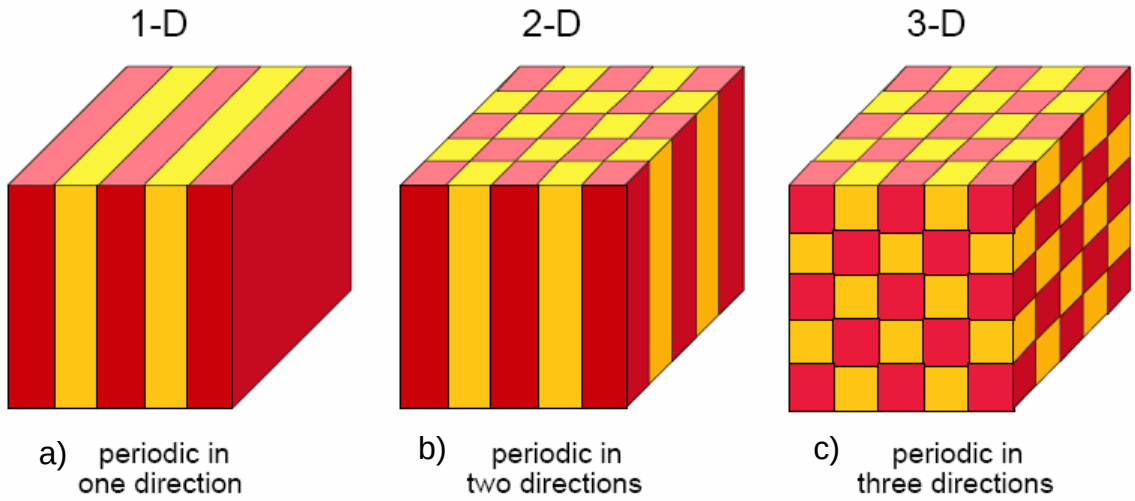

Figure 1.1: The models of photonic crystals in which dielectric structures are periodic in a) 1D, b) 2D or c) 3D. The different colors in blocks represent the differences in dielectric materials[7].

Among these structures, 2D photonic crystal slabs (Figure 1-b) have important advantages. They can be patterned using state-of-the-art semiconductor micro-fabrication techniques, such as the electron beam lithography process. This guarantees a strong index modulation with a high structural resolution. Furthermore, it is very simple to introduce functional defects and components (simply by designing the soft mask for lithography). The feature size is easily measured with a scanning electron microscope. In fact, our research works mainly deal with this 2D active photonic crystal slab bond on transparent glass substrate.

We here will briefly introduce theory of electromagnetism that governs the field in photonic crystal and investigate their essential optical properties as well their perspectives in optoelectronics.

1.1.2. Electromagnetism in dielectric media

Generally all the macroscopic electromagnetic fields are governed by a set of four Maxwell equations[8]. We assume that the dielectric media considered contains no free charges and electric currents, in MKS unit, the Maxwell's equations are expressed as:

$$\nabla \cdot D(r,t) = 0,$$
$$\nabla \cdot B(r,t) = 0,$$
$$\nabla \times E(r,t) = -\frac{\partial}{\partial t} B(r,t),$$
$$\nabla \times H(r,t) = \frac{\partial}{\partial t} D(r,t). \quad \textbf{(1)}$$

Where (respectively) ***E*** and ***H*** stand for the macroscopic electric field and magnetic field; ***D*** and ***B*** are used for displacement and magnetic induction. The relation between ***B*** and ***H*** is formulated as:

$$B(r,t) = \mu_0 H(r,t) \quad \textbf{(2)}$$

where $\boldsymbol{\mu_0}$ donates to magnetic permeability in vacuum, $\mu_0 = 4\pi \times 10^{-7}$ Henry/m.

The displacement field ***D*** are linked to a power series of electric field ***E*** components through permittivity ε (ε_0 = 8.854 x 10^{-12} Farad/m) and $\chi^{(n)}$ n-th order components of electric susceptibility of medium[9]. In order to simplify this relation, we assume that (1) our field strengths are small enough to be considered as a linear system, so that $\chi^{(n)}$ can be neglected; (2) we choose to work in the frequency range so that value of dielectric constants is independent on frequency (no material dispersion); (3) only transparent materials where ε (r) is real and positive are considered; (4) our materials are macroscopic and isotropic. With these assumptions we can express ***D*** and ***E*** as following:

$$D(r,t) = \varepsilon_0 \varepsilon(r) E(r,t). \quad \textbf{(3)}$$

Substitute all above relations into Maxwell's equations, finally we obtain:

$$\nabla \cdot \{\varepsilon(r) E(r,t)\} = 0, \quad \textbf{(4)}$$
$$\nabla \cdot H(r,t) = 0,$$
$$\nabla \times E(r,t) = -\mu_0 \frac{\partial}{\partial t} H(r,t),$$
$$\nabla \times H(r,t) = \varepsilon_0 \varepsilon(r) \frac{\partial}{\partial t} E(r,t) \quad \textbf{(5)}$$

These linear equations depict the complicated relations among electromagnetic fields ***E*** and ***H*** in time (t) and space (r) dependence. Consider our field as harmonic modes and separate into two terms of time and space as follows:

$$\begin{aligned} \boldsymbol{E}(r,t) &= \boldsymbol{E}(r)\mathrm{e}^{-\mathrm{i}\omega t}, \\ \boldsymbol{H}(r,t) &= \boldsymbol{H}(r)\mathrm{e}^{-\mathrm{i}\omega t} \end{aligned} \quad \textbf{(6)}$$

where ω is the eigen-angular frequency and *E(r)* and *H(r)* are now eigen-functions of wave functions. Insert into Eq. (3) we obtains:

$$\begin{aligned} &\nabla \cdot H(r) = 0 \\ &\nabla \cdot [\varepsilon(r)E(r)] = 0 \end{aligned} \qquad (7)$$

$$\begin{aligned} &\nabla \times E(r) - i\omega\mu_0 H(r) = 0 \\ &\nabla \times H(r) + i\omega\varepsilon(r)\varepsilon_0 E(r) = 0 \end{aligned} \qquad (8)$$

Eq. (7) points out that no point sources or sinks of electric and magnetic fields in the medium and the field configurations are transverse. Rearrange Eq. (8) and replace $c=(\varepsilon_0\mu_0)^{-1/2}$, one obtains the master equation in H(r):

$$\boxed{\nabla \times \left(\frac{1}{\varepsilon(r)} \nabla \times H(r) \right) = \left(\frac{\omega}{c} \right)^2 H(r)} \qquad (9)$$

The master equation (9) contains the solutions of magnetic field modes in space of a given photonic structure ε(r) corresponding to frequencies ω. The fields must satisfy the transversality conditions stated in Eq. (7). The allowable electromagnetic modes as solutions of master equation are used to construct the photonic band diagram as indicated in Figure 2.

In order to recover ***E(r)*** from ***H(r)***, from Eq. (8) we have:

$$E(r) = \frac{i}{\omega\varepsilon_0\varepsilon(r)} \nabla \times H(r) \qquad (10)$$

1.1.3. Optical properties of photonic crystal

The band diagram of photonic crystals could provide most of the information needed to predict their optical properties. The band structures depend on the specific geometry and composition of the photonic crystal such as the lattice size, the diameter of the lattice elements, and the contrast in refractive index[2]. The band diagram describes the dispersion between normalized frequency and in-plane wave-vector $k_{//}$ in the first Brillouin zones of the reciprocal space. Due to symmetry properties, the rest of Brillouin zones could be built by symmetric translation of this irreducible zone to cover whole area of structure[2]. The Brillouin zone is a two-dimensional region of wavevectors, where the bands $\omega_n(k_{//})$ are actually surfaces. In practice the band extreme almost occurs along the boundaries of the irreducible zone. So, it is conventional to plot the bands only along these zone boundaries as depicted in Figure 1.2-right.

For a given photonic crystal with a periodic dielectric function $\varepsilon(r)$, resolving the master Eq.9 enables to obtain the band structure functions $\omega_n(k)$, n being the band number, and the allowable modes[10,11]. The various novel properties of strongly modulated photonic crystals can be deduced from two important features indicated in band diagram: (1) the appearance of multi-dimensional photonic band gaps and (2) the strong modification of dispersion. Exploiting these properties lead to many device applications from microlaser to biosensor.

We begin to present the band diagram of 1D photonic crystal or multilayer film structure. Though the simplest system, 1D PC suffices to show the fundamental optical properties which are useful to explain the other phenomenon occurring in high-dimensional system of interest. Figure 1.2-left illustrates a typical 1D PC with given dielectric function $\varepsilon(r)=\varepsilon(r+a)$, where a is the periodicity.

The photonic diagram of Figure 1.2-right shows a band gap which contains no allowable mode. Band gaps are formed owing to the opposite splitting of two accidental degenerate modes propagating in PC structure with presence of the oscillating potential provided by $\varepsilon(x)=\varepsilon(x+a)$: the field $e(x)=\cos(\pi x/a)$ is more concentrated in higher dielectric material than the field $o(x)=\sin(\pi x/a)$, so it that *e* remains in the low frequencies region. The area below PBGs is named dielectric band (or valence band) since it contains the modes which conserve their energy in dielectric materials (higher dielectric constant). Similarly the band concerning the higher frequency is named the air band (or conduction

band) since it contains the modes which conserve their energy in air (lower dielectric constant)[11,12]. This is analogous to the valence band and conduction band in semiconductor band structure.

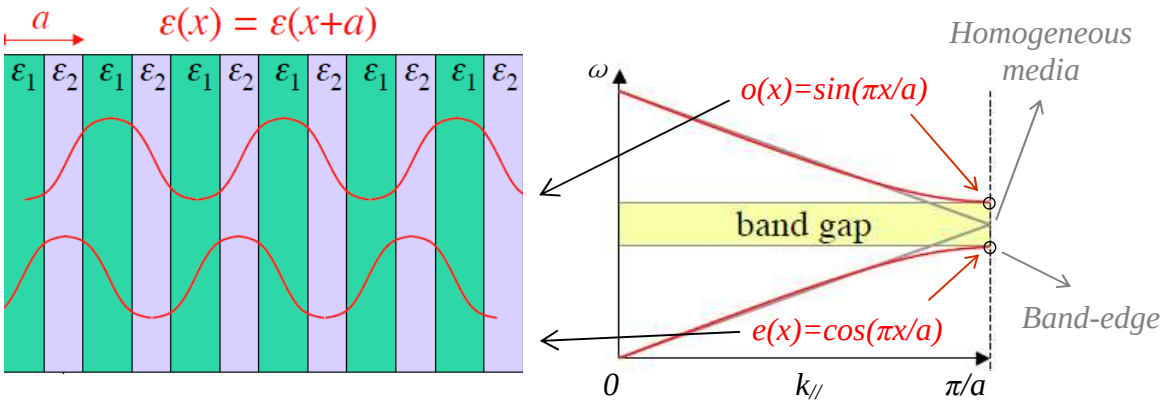

Figure 1.2: Illustration of electromagnetic field distribution in periodic dielectrics of 1D-PC (multilayer thin film structure). The higher dielectric material ε_2 is favorable for the low-frequency modes e(x) and vice versus, thus generating the band gaps between two degeneracy modes.

Another way to exploit the optical property of 1DPC through the band diagram is to consider the modes near band edge (at $k_{//} = \pi/a$ in Figure 1.2-right). At these band edges the photons are undergoing multiple reflections and therefore only propagate slowly through the photonic structure with a mean velocity, v_g. Near the band edges, the group velocity, envelope of light propagates within the material, defined as $v_g = \partial\omega/\partial k$ approaches zero and slow light (stationary wave) is generated.

The following section will focus on the optical properties of higher dimensional PCs based on photonic band-gap and band edge.

a. Localized modes or defect modes of 2D PC slab

As definition, 2D PC is periodic in two directions and homogeneous in the third. The band-gaps, the range of frequencies in which contains no guided modes, may appear in the plane of periodicity. As a result, incident light entering into this gap will be reflected. Unlike 1D PC, 2D PC can prevent light from propagating in any direction within the plane. Moreover, 2D PC provides the 3D confinements of light thanks to specific design.

Let consider the photonic band diagram of a triangular 2D-PC as shown in Figure 1.3-a. We are interested in the triangular lattice PC since it is able to provide the large photonic band gap. Since no allowable mode exists, density of states (DOS) in this gap is zero. Thus, a photonic crystal with PBG is able to operate effectively as a perfect reflector of light with very low losses[1, 12]. This triangular PC configuration (air holes in Si slab), PBG appears solely in TE-polarization mode (in plane electric fields) between normalized frequency of 0.208÷0.275.

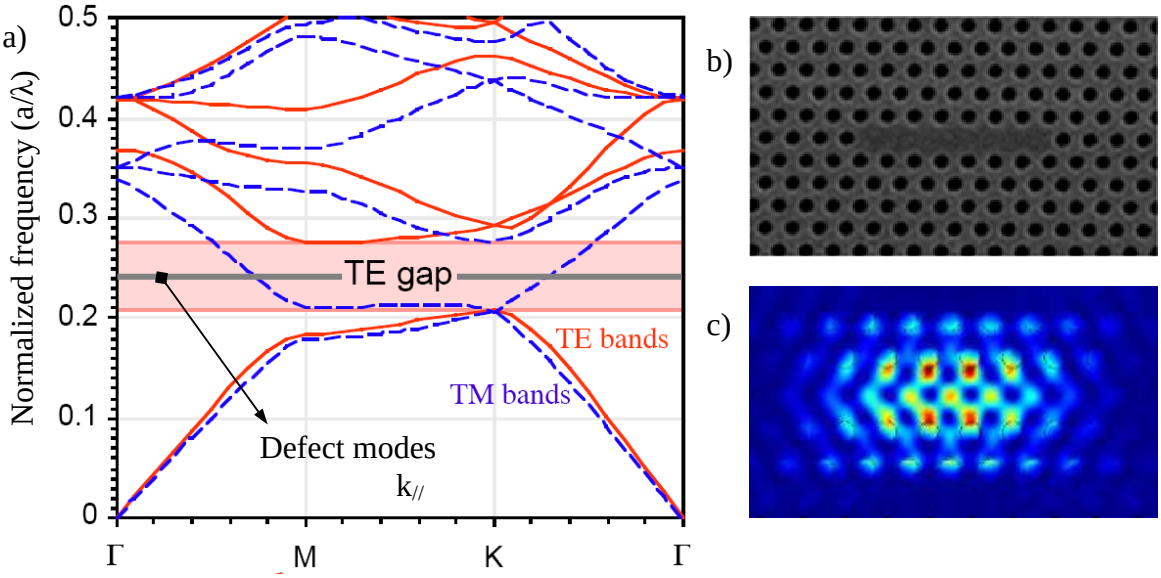

Figure 1.3: a) Sketch of triangular 2D-PC structured by an array of air holes (r=0.3a, a=440nm being the center-to-center periodicity, and typical ε_{air}=1) in high dielectric material (Si slab, ε=12). Band diagram of this PC presents a large band gaps for TE mode. The normalized frequencies are plotted around the boundary of the first Brillouin zones where Γ, M, K are high symmetric points[2]. b) SEM image of a seven-hole missing linear cavity (CL-7). c) Optical image of electric field intensity distributes inside the CL-7 structure by FDTD simulation.

It is possible to create allowed bands within the photonic bandgaps by introducing point defects or line defects in the lattice of photonic crystals. Light thus will be strongly confined within the defects for frequencies regardless of k-vector in the bandgap of the surrounding photonic crystals since the DOS is altered significantly (Figure 1.4). Therefore these modes are named localized modes or defect modes. Figure.3-b shows the SEM image of a seven-hole missing linear cavity (CL-7) in the InP slab. Figure.3-c indicates the corresponding electric field intensity of a fundamental defect mode distributed in the cavity by FDTD simulation[13]. This confinement of light within cavity is

also demonstrated with near-field measurement technique providing a high-Q lasing modes.

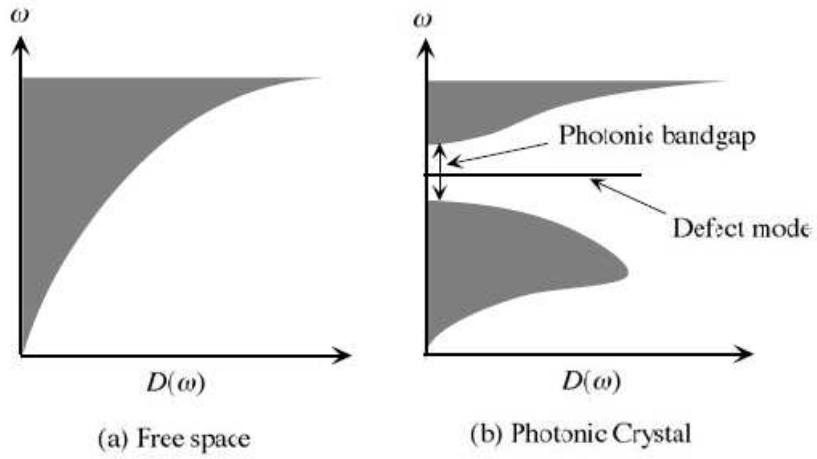

Figure 1.4: Diagram of the density of states (DOS) of radiation field. a) in free space. b) in photonic crystal media. The DOS in this media is strongly modified indeed, especially for defect modes in photonic band-gap which indicates the sharp peak[1].

PBG studies are motivated by their novel potential applications in optoelectronics devices. First, the enhanced efficiency of light-matter interaction in high Q-nanocavity of PC is used to improve the performance of various optical devices, such as lasers, optical switches, modulators, memories and single photon emitters[14,15]. Second, a strong light confinement with low losses makes PC suitable for high density of photonic integration[16]. Third, PC containing high Q-nanocavities can modify the dwell time and transit time which enables slow light and adiabatic tuning of light provides unprecedented functionalities in photonics[17,18].

b. Slow light modes (SBM)

In order to investigate this kind of modes, let us consider the photonic band diagram of honeycomb[19] 2D-PC as shown in Figure 1.5. The lower inset is a SEM image of honeycomb structure where A is lattice parameter. There is no band-gap occurring in the region of the first modes. At the Γ-point, there are three slow modes, labeled monopolar M, hexapolar H and dipolar D occurring at normalized frequencies of 0.45, 0.47 and 0.50 respectively with a low band curvature (α) and null of group velocity v_g. The upper insets show three intensity mode patterns corresponding to these modes obtained by 2D- FDTD simulation.

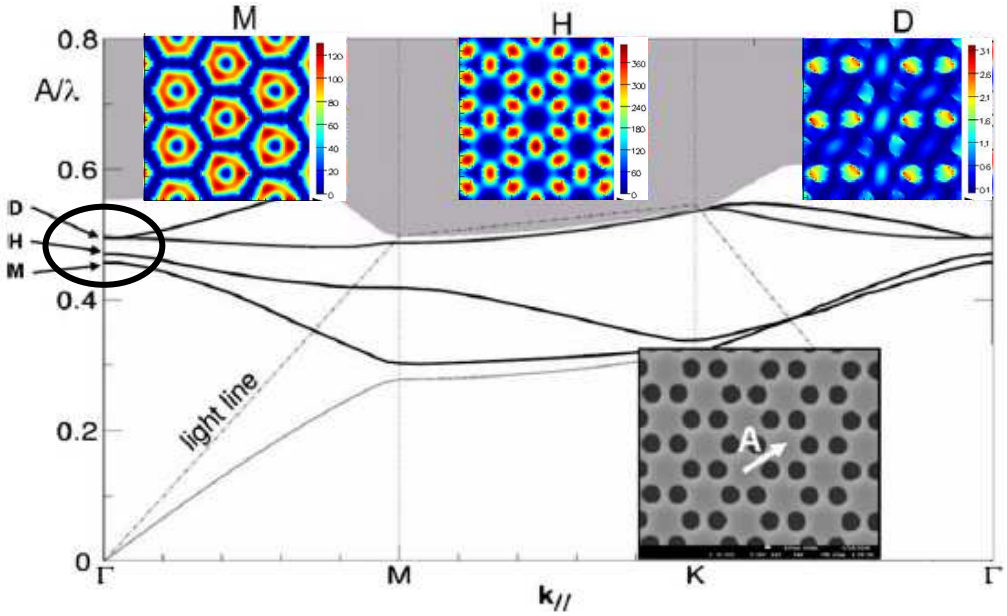

Figure 1.5: Band diagram of honeycomb 2D PC with lattice parameter A of 775 nm and air filling factor of 20%. The lower inset shows the SEM image of given PC. M, H, D stand for three slow modes: monopolar, hexapolar and dipolar respectively at Γ-point. Upper insets indicate the electromagnetic field (H_z component) corresponding to three slow modes M-H-D.

In theory the frequency dispersion could be described as the second order of k-vector function using parabolic approximation:

$$\omega = \omega_0 + v_G(k - k_0) + \frac{\alpha}{2}(k - k_0)^2 \qquad (1)$$

$$v_G = \left(\frac{d\omega}{dk}\right)_{k0}, \quad \alpha = \frac{\partial^2 \omega}{\partial^2 k}$$

For extreme dispersion, *e.g* at Γ-point of this diagram where $v_g=0$ at $k=k_0$, the guided modes become the stationary modes that propagate in the plane of PC. Thus the Eq.1 can be reduced into:

$$\omega = \omega_0 + \frac{\alpha}{2}(k - k_0)^2 \qquad (2)$$

$$DOS = \left(\frac{dN}{d\omega}\right)_{membrane} = \frac{1}{2\pi h}\frac{1}{\alpha} \quad (3)$$

$$Purcell\ factor = \left(\frac{DOS_{membrane}}{DOS_{vacuum}}\right) \approx \frac{1}{\alpha} \quad (4)$$

$$S_M = \alpha\tau_M \quad (5)$$

The typical value of α is in the order of 10^{-5}($m^2.s^{-1}$). This parameter strongly impacts on the optical properties of given PC. Indeed, as shown in Eq.3 and Eq.4, the density of state and Purcell factor are inversely proportional to the value of α. The Purcell factor is defined as the ratio of DOS of the membrane and the DOS of the vacuum: it measures the enhancement of spontaneous emission rates of emitters placed in this medium. The flatter the extreme, the smaller the band curvature and therefore the stronger optical confinement is provided by the 2D PC, resulting in an increased Purcell factor. The honeycomb structure is known to present a flat band curvature. Moreover, as shown in Eq.5, the surface mode S_M which is defined by the area over which mode can extend and keep coherency during its lifetime τ_M is linearly proportional to the α-value. The lifetime is linked to the coupling time τ_c between the SBM and radiating modes and τ_{loss}, which is related to other losses of unavoidable imperfection of structure fabrication. In the case of an active structure, like a micro-laser, the mode expansion can also be governed by other mechanisms involving carrier-induced refractive-index change[20]. Thus estimation of surface mode could reveal information above the mode confinement with slow light[15,16].

The research works on slow light are motivated by the fact that it is expected to enhance the various light–matter interactions. These enhancements might relate to (1) the interaction time, which will become longer as the group velocity v_g becomes smaller and (2) the spatial length of an optical pulse will be compressed in proportion to v_g leading to enhancement of the field intensity per unit input power[13, 21]. Generally, light–matter interaction is very weak, which is a fundamental obstacle for photonics applications, particularly as regards photonic information processing. Thus, slow light has the potential to solve this efficiency problem. Furthermore, slow light can be used to realize an all-optical buffer memory, a very important component for construction of various all-optical processing devices such as photonic routers[22]. Slow light is another candidate for all-optical memories, in which information packets with bit streams are delayed to hold the information. If we can reduce the speed of light, the same amount of delay can be

achieved with much smaller devices that could be integrated in a single chip. Another advantage of slow light, as stated above is related to its compactness[23]. The size of photonic circuits and components can be significantly reduced if slow light media are employed, which is advantageous for photonic integration.

However, slow light structures also leave researchers several major limitations that need further studies, such as dispersion and loss. The dispersion limit the available bandwidth, that is, the information content can be slowed down or stored, whereas loss limits the storage time and interaction efficiency.

Although many challenges remain, especially in optical storage, the slow-light enhancement of linear and nonlinear functions appears to be maturing rapidly and should bear fruit in the short term.

1.2. NSOM

1.2.1. Introduction

Basically, the electromagnetic field present at the surface of an object can be described in two terms: propagating light and evanescent light. The former concerns the components that can propagate away from surface at a minimum distance comparable to the light wavelength, in a zone labeled far-field. The latter are confined to the surface within a distance that can be well under the wavelength, in a zone labeled near-field[24]. Propagating light can be detected in the far-field by using conventional far-field microscopes; it gives precious information about the spectral properties of the object, about its radiation pattern or the distribution of light at the object surface as far as low spatial frequencies are concerned. In fact, as illustrated in Figure 1.6, due to diffraction, the simple propagation phenomenon acts as a low-filter for the spatial frequency of the considered object. This is a wave-phenomenon which is not restricted to optical wave. When an optical system is used to image the object, the cut-off frequency of the filter can be formulated by the Abbe-Rayleigh's criterion [25] which stipulates that the optical resolution of a far-field microscope cannot exceed $\Delta x=0.6\lambda/NA$ where λ is the light wavelength and NA the numerical aperture. The information about the high-spatial frequencies (*i.e* the finest modulations of the electromagnetic field) are contains in the non-propagating field and remains in the close vicinity of the object.

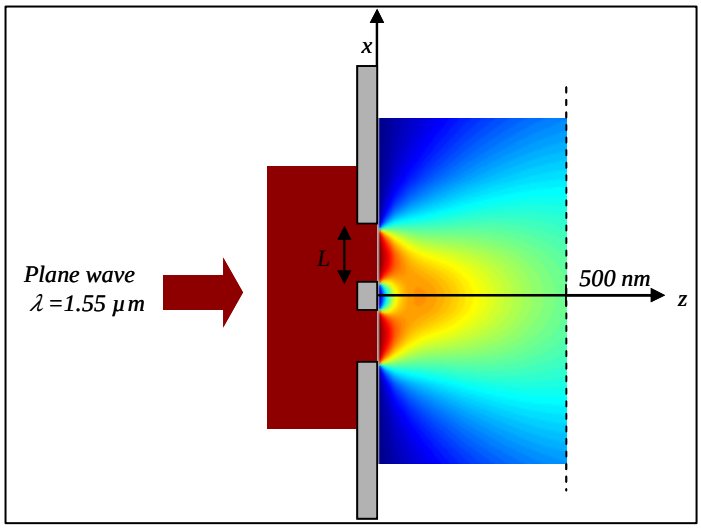

Figure 1.6: The illustrations of diffracted field through sub-wavelength apertures. Incident plane wave passed though sub-wavelength slits generated evanescent field bounded to the surface of thin film and exponentially decayed as a function of distance z from surface.

To illustrate this phenomenon, the evolution of the field intensity as a function of the distance has been computed in Figure 1.7 for a typical nanophotonic device: a photonic cystal based micro-laser. The microlaser consists of a linear microcavity created in a 2D-triangular photonic crystal. In this cavity, the fundamental mode presents a lasing effect and has been extensively studied. Basically, this mode is confined into the cavity and the field at the cavity surface is merely evanescent. Theoretically, the intensity can be computed at the surface (z=0 nm) of the cavity and at different altitudes (z>0) from the surface. Away from surface, the intensity decreases exponentially; simultaneously the mode modulation in *xy*-planes parallel to the surface becomes larger. Around $z=\lambda/2$, almost all the near-field details present at the surface are lost since only the far-field optical signal is collected. In order to overcome these limitations and access into the nanoscale world, specific devices that allow unveiling the information in near-field have been developed. Near-field Scanning Optical Microscopy (NSOM) has been developed for this demand. Since its development, NSOM related technologies have been utilized in many research areas and has become an important part in nano-optics research.

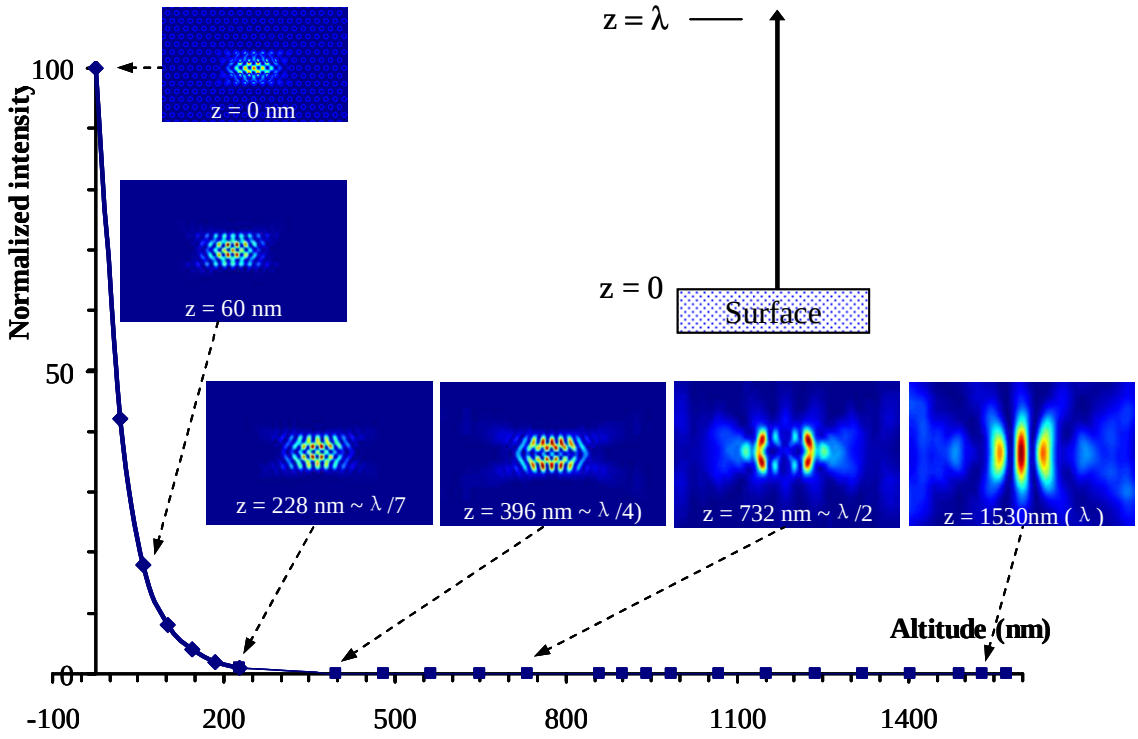

Figure 1.7: Evolution of optical intensity and patterns of cavity mode on photonic crystal at λ=1530nm as a function of distance z from surface to the NSOM probe. Further moving away from the surface leads to significant reduction of the spatial resolution and exponential decay of the near-field intensity.

1.2.2. NSOM principle

NSOM operating principle relies on a fundamental idea proposed in 1928 by Synge, an Irish scientist. In order to extend the optical resolution into the nanometer regime, he proposed to use a very small light source emerging from a 100 nm diameter pinhole in a thin, opaque metal film with a strong excitation light[26]. He proposed to uses this tiny spot of light to illuminate subwavelength-separated particles and made the hypothesis that a nanoscale resolution could be reached if the spot is placed in the near-field of the sample (no more than the aperture diameter, or 100nm).

The first experiment was successfully conducted by Ash *et al.* in 1972 in the microwave regime where they demonstrated a resolution of λ/60 with a scanning near-field microwave microscope[27]. In 1984, two research groups achieved independently measurement by near-field scanning optical microscopy in visible light regime[28,29]. NSOM concepts development continued and finally different image acquisition/light detection techniques were developed such as illumination mode[30,31,32,33], collection mode[34] and scattering mode for apertureless NSOM[35,36,37] as shown in Figure 1.8.

In typical NSOM systems, optical signal is recorded point by point by the very sharp probe that scatters evanescent light which can turn into propagating light detectable by a sensitive photo detector. The NSOM images are constructed by a computer during the scan. Meanwhile, in order to maintain sub-diffraction spatial resolution, the distance between the tapered NSOM tip and surface must be kept as low as few tenth of wavelength and regulate using force microscopy, as shear-force or atomic force microscopy[38]. Shear force is particularly used in NSOM because it is a short range damping force exerted on a laterally vibrating tapered NSOM tip[39]. The vibration amplitude of the tip is damped due to the shear force interaction between tip and the sample surface. This damping depends of the distance from the tip to surface, which is regulated by a closed feedback loop to remain constant around 10nm. Various techniques such as optical detection schemes[40,41] and the piezoelectric tuning fork schemes[42,43] have been proposed for shear-force detection. However, mechanical detection, based on tuning fork quartz, is often preferred over optical detection scheme, since it presents several advantages: it does not need additional optical system, it is easy to implement, cheap and sensitive.

There are six common NSOM configurations (in Figure 1.8) that dominate most of the experimental set-up. In collection mode NSOM (Figure 1.8-a/d), the sample is illuminated by a far-field device and the NSOM probe is used to collect light, whether in transmission (Figure 1.8-a) or in reflection (Figure 1.8-d). In illumination mode NSOM (Figure 1.8-b), the sample is illuminated with the tip and the light is collected from the sample in the far-field in transmission (Figure 1.8-b) or reflection (Figure 1.8-e). In illumination/collection mode (Figure 1.8-c) the sample is illuminated with light through the tip and light from the sample is collected though the same tip. In dark-field mode, or photon channeling mode (PSTM) (Figure 1.8-f), incident light is totally internally reflected from the substrate surface. In this way, the evanescent optical signal present in the near-field region of the sample is collected through the tip aperture.

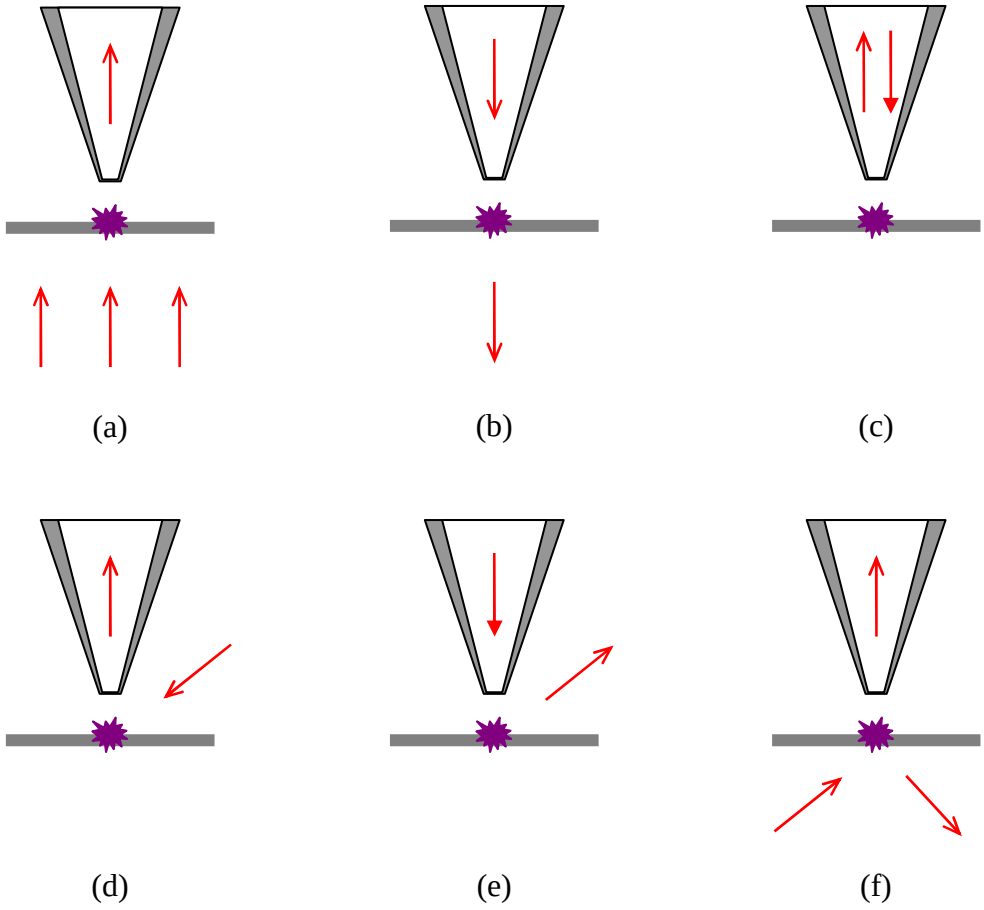

Figure 1.8: Six common NSOM configurations[44]: a) collection; b) illumination; c) illumination/collection ; d) oblique collection ; e) oblique illumination ; f) dark-field

NSOM configurations are also sorted in term of the probe characteristics into aperture-NSOM and apertureless-NSOM. In aperture-NSOM, a sub-wavelength aperture

opened at the apex of a metallized probe is used to illuminate or collect light in the near-field of the sample. Conversely, apertureless-NSOM uses generally a non-transparent tip, as an AFM cantilever or STM tip which scatters the near-field signal in the far-field. However, scattered light directing to the photodetector includes scattering from probe apex, surface roughness and surface features. In order to suppress the contribution of probe apex, surface roughness scattering the lock-in technique could be utilized. Note that the use of a transparent probe, as a dielectric tapered optical fiber tip can be considered as an apertureless probe: no aperture is defined and the tip scatters the near-field signal in the far-field with the practical interest that the signal is partly guided by the fiber to the detector.

A NSOM configuration can be modified to be adapted to a specific experiment purpose. In our case, we use a NSOM configuration designed to work in transmission and collection mode with transparent samples. This NSOM set-up is able operate either with apertureless tapered fiber probe or nano-aperture probe milled at the apex of metallized polymer probe. The NSOM in transmission/collection mode is advantageous in experiments that need to control precisely the position and the size of pumping excitation spot with respect to the structures on sample. Furthermore, this apertureless NSOM has demonstrated to be efficient to characterize Bloch modes emitting under the light cone, and for which the field at the sample surface is essentially evanescent[45]. Inversely, NSOM with circular aperture or bowtie nano-aperture is designed to investigate the slow Bloch modes above line cone (*e.g.* Γ-point) which have a strong vertical emission. The details of this NSOM set-up are described in chapter 2.

1.2.3. Apertureless NSOM

In apertureless NSOM, the probe acts as a scatterer of evanescent field and converts it into propagating field. This kind of NSOM probe can be very sharp (as small as AFM tip), and provides a better spatial resolution than aperture one, reportedly up to 10nm [46]. Apertureless probes can be made either of dielectric or metallic material depending on their applications. For surface plasmon resonance-supported nanostructures, a metallic probe is preferred since its strong coupling with surface plasmon enhances the scattered light[47]. However, dielectric probe are more efficient in certain cases as it presents some advantages[48]:

(1) Low fluorescence quenching,

(2) Low nonlinear coefficient for second-harmonic imaging,

(3) Higher wear resistance,

(4) Strong field enhancement by phonon polariton resonance in polar dielectrics,

(5) No corrosive decomposition,

(6) Simple and reproducible fabrication.

The spatial resolution of apertureless NSOM is determined by the tip radius, which scatters the near-field of high spatial frequency at the tip apex[49]. However, the optical signal collected by apertureless NSOM sharp tip includes both the signal scattered from the background surface and that of the tip apex. The elimination of the background signal dominating over the signal from the sample–probe system becomes more challenging with a sharper tip. Normally lock-in amplifier could efficiently eliminate the background signal although the stray signals still exist after lock-in technique.

In case of strong vertical radiation from surfaces, for instance slow band-edge modes above light line at high symmetric points in photonic crystal, the light that couples into the optical fiber comes partly from the evanescent field but also from the propagating light through the flank of the bare tapered probe. If the light coming from the radiated light is dominant and unavoidable, the collected optical signal to photodetector will contain a large part of radiated field with respect to the evanescent field. This significantly reduces the spatial resolution in NSOM optical image. The dielectric probe is more adapted when the field at the sample surface is purely evanescent.

1.2.4. Aperture NSOM

Aperture NSOM can transmit information about the near-field signal through the evanescent coupling between the light presents in the near-field of the sample and the evanescent tail of the guided mode of the tapered fiber. Generally, the higher spatial resolution is obtained with the smallest aperture thanks to the stronger localized evanescent field at the nano-aperture. However, according to diffraction theory[50,51], light passes through small hole punched on perfectly conducting sheet with transmission efficiency proportional to the forth power of hole diameter a, or $(a/\lambda)^4$. Thus, the

improvement of spatial resolution by reducing the aperture size has to be trade-off with low optical intensity in NSOM images.

In our NSOM setup, the aperture probe is specially designed not only to efficiently filter out low spatial frequency of radiation field (circular nano-aperture), but also to enhance the coupling efficiency of the evanescent field (bow-tie nano-aperture antenna or BNA probe). Theoretically, bowtie nano-aperture probes can act as novel nano-collectors and nano-polarizers to near-field mode due to their properties of field enhancement and polarization sensitivity[52,53,54]. The enhanced and confined field in the gap zone of BNA-probe as indicated in Figure 1.9 plays a key factor to improving the spatial resolution of resulting NSOM image.

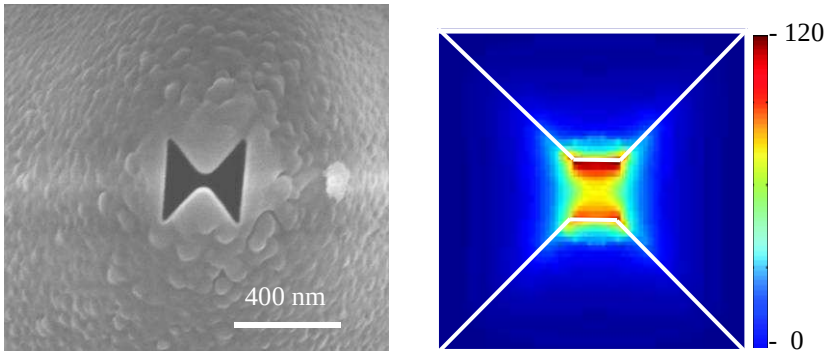

Figure 1.9: The near field confinement and enhancement in gap zone of bowtie aperture antennas. (a) SEM image of a BNA on NSOM probe. (b) Electric field confinement in aperture at resonance wavelength in simulation[53,].

Moreover, in comparison to the other shapes of aperture, such as square or rectangular one, bowtie nano-aperture provides the much higher transmission[55,56] as shown in Figure 1.10. This novel property is very important to overcome the low throughput associated with conventional apertures.

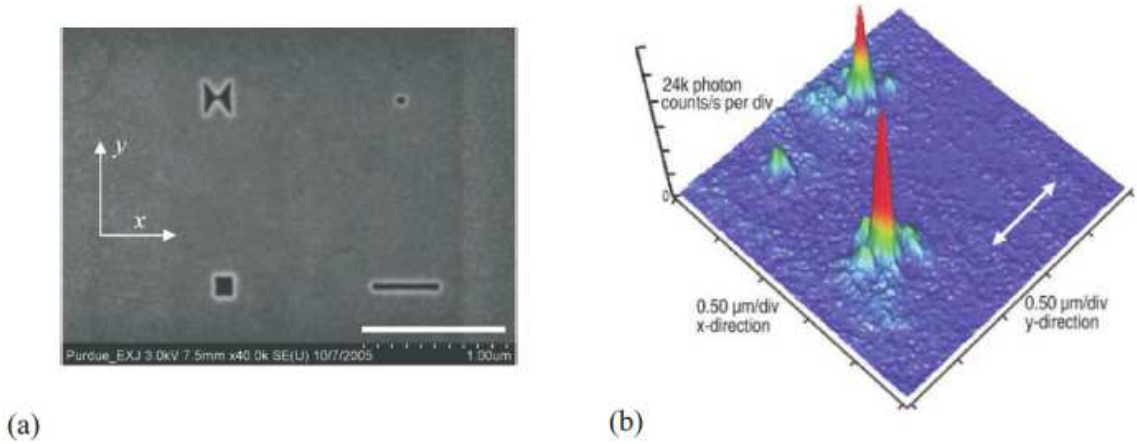

(a) (b)

Figure 1.10: (a) SEM pictures of the individual bowtie slot antenna and comparable square and rectangular aperture antennas in a 160 nm thick gold film. (b) NSOM image of the antenna array in (a), which was 45° clockwise rotated with respect to the SEM image. The incident light was polarized along y-axis as shown by the arrow.

1.3. Optical nano-antenna

1.3.1. Introduction

The conventional antenna plays a key role in today's technologies to transmit or receive the electromagnetic wave in radio and micro frequencies from distance. However, their optical analog is basically nonexistent in human life. Recent researches in nano-optics and plasmonics has generated considerable interest in the optical antenna concept, and several studies are currently focused on how to translate established radiowave and microwave antenna theories into the optical frequency regime.

The absence of optical antennas in technological applications is primarily associated with diffraction limit in nanoscale and their small dimension. Antennas have characteristic dimensions of the order of a wavelength of light, demanding fabrication accuracies better than 10 nm. The advent of nanoscience and nanotechnology provides access to this length scale with the use of novel top-down nanofabrication tools (e.g. focused ion beam milling and electron-beam lithography) and bottom-up self-assembly schemes. The fabrication of optical antenna structures is an emerging opportunity for novel optoelectronic devices.

While radio antennas were developed as solutions to a communication problem, the invention of optical antennas was motivated by microscopy. In analogy to its radiowave and microwave counterparts, we define the optical antenna as a device designed to efficiently convert free-propagating optical radiation to localized energy, and vice versa. In the context of microscopy, an optical antenna effectively replaces a conventional focusing lens or objective, concentrating external laser radiation to dimensions smaller than the diffraction limit.

The introduction of the antenna concept into the optical frequency regime will provide access to new technological applications. Optical antennas will likely be employed to enhance absorption cross sections and quantum yields in photovoltaic, to release energy efficiently from nanoscale light-emitting devices, to boost the efficiency of photochemical or photophysical detectors, and to increase spatial resolution in optical microscopy.

1.3.2. Fundamentals of antennas

Optical antennas are strongly analogous to their RF and microwave counterparts, but there are crucial differences in their physical properties and scaling behavior. Most of these differences arise because metals are not perfect conductors at optical frequencies, but are instead strongly correlated plasmas described as a free electron gas. Optical antennas are also not typically driven with galvanic transmission lines - localized oscillators are instead brought close to the feed point of the antennas, and electronic oscillations are driven capacitively[57]. Moreover, optical antennas can take various unusual forms (tips, nanoparticles, etc.) and their properties may be strongly shape and material dependent owing to surface plasmon resonances.

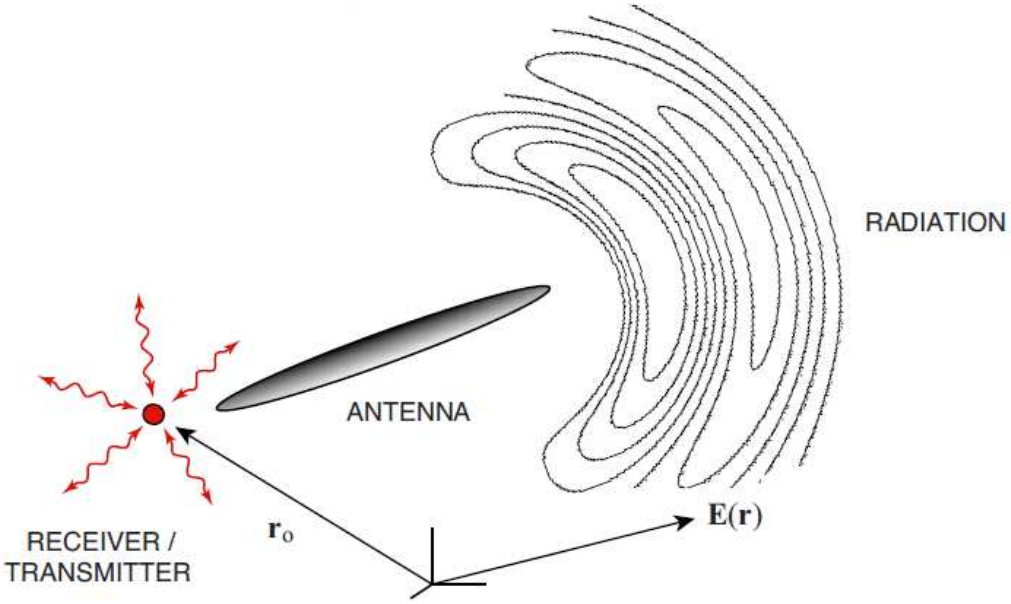

Figure 1.11: Problem statement of optical antenna theory. A receiver or transmitter (atom, ion, molecule...) interacts with free optical radiation via an optical antenna[58]

The general problem statement of optical antenna theory is illustrated in Figure 1.11. A receiver or transmitter interacts with free optical radiation via an optical antenna. The receiver or transmitter is ideally an elemental quantum absorber or emitter, such as an atom, ion, molecule, quantum dot, or defect center in a solid. The antenna enhances the interaction between the emitter or absorber and the radiation field. It therefore provides the prospect of controlling the light–matter interaction on the level of a single quantum system. The presence of the antenna might modify the properties of the

receiver/transmitter, such as its transition rates and, in the case of a strong interaction, even the energy-level structure. Likewise, the antenna properties depend on those of the receiver–transmitter, and it becomes evident that the two must be regarded as a coupled system.

The antennas performance is normally characterized by the following parameters[59]: radiation pattern, directivity, gain, polarization and impedance. Below is briefly described the above parameters in theory. For more details, referred to the Hongcang Guo's PhD dissertation[60]

a. Angular pattern (P)

Radiation pattern of antenna describes the angular dependence of radiation field as antenna acts as transmitter. Consider a model of an ideal dipole in which the current amplitude I of an ideal dipole is uniform along the element length Δz as shown in Figure 1.12-a. Figure 1.12-b/c present the normalized field radiation pattern from such dipole in *xy*-plane. In general, the total field power generated by antenna could be separated into two quantities: a near-field power and radiated power upon the observation distance *r* (distance from antenna to the detector). The general field expressions and inferred quantities could be estimated by solving the Maxwell equations.

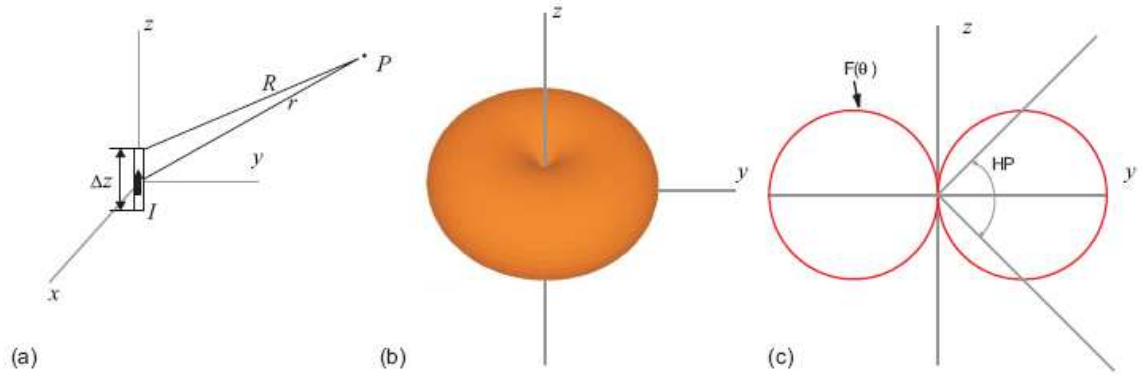

Figure 1.12: (a) An ideal dipole with uniform current I in length Δz ($\Delta z << \lambda$ and R ~ r). (b) The radiation pattern of an ideal dipole. (c) E-plane radiation pattern polar plot of E_θ

Radiated power: in case of the large distance *($r >> \lambda$)*, the power could transmit to the far distance, since it is named radiated power. More specifically, the electric and magnetic field components of radiation are described by the Eq.(6):

$$E = \frac{I\Delta z}{4\pi} i\omega\mu \frac{e^{-i\beta r}}{r} \sin\theta\hat{\theta}$$
$$H = \frac{I\Delta z}{4\pi} i\beta \frac{e^{-i\beta r}}{r} \sin\theta\hat{\phi}. \quad (6)$$

where $\beta=\omega\sqrt{(\mu\varepsilon)}=2\pi/\lambda$. Using the Poynting vector definition, the power flux density S surrounding ideal dipole at sphere radius of r is:

$$S = \frac{1}{2} E \times H^*$$
$$= \frac{1}{2}\left(\frac{I\Delta z}{4\pi}\right)^2 \omega\mu\beta \frac{sin^2\theta}{r^2}\hat{r} \quad (7)$$

This vector has a real magnitude and radical direction which obtains maximum value at $\theta=\pm 90^0$ and is proportional to r^{-2}. Thus the total power radiated from this ideal dipole is:

$$P_f = \int\int S \cdot ds =$$
$$= \frac{\omega\mu\beta}{12\pi}(I\Delta z)^2. \quad (8)$$

Since this quantity is real, it might travel way from the source to far-field and indicates the dissipated power. Correspondingly, the electric and magnetic components of Eq.(6) are also named the radiated field.

Near-field power *($r<<\lambda$):* the corresponding near fields now become:

$$H' = \frac{I\Delta z e^{-i\beta r}}{4\pi r^2} \sin\theta\hat{\phi},$$
$$E' = -i\eta \frac{I\Delta z}{4\pi\beta} \frac{e^{-i\beta r}}{r^3} \sin\theta\hat{\theta} + i\eta \frac{I\Delta z}{2\pi\beta} \frac{e^{-i\beta r}}{r^3} \cos\theta\hat{r} \quad (9)$$

where $\eta=\sqrt{(\mu/\varepsilon)}$ is the intrinsic impedance. In Eq. (9), magnetic H' is a function of r^{-2} and equivalent to the induction field of slowly oscillating current. Electric field E' is a function of r^{-3} and equivalent to the field of an electrostatic or quasi-static dipole with opposite charges of $+q$ and $-q$ separated in distance of Δz.

The Poynting vector is calculated as:

$$\begin{aligned} S' &= \frac{1}{2}[E'_\theta H'^{*}_\phi \hat{r} - E'_r H'^{*}_\phi] \\ &= -\frac{i\eta}{2\beta}\left(\frac{I\Delta z}{4\pi}\right)^2 \frac{1}{r^5}(\sin\theta^2 \hat{r} - \sin\theta\hat{\theta}) \end{aligned} \quad (10)$$

Unlike the radiated power density, this near-field quantity has an imaginary magnitude which is corresponding to the standing wave located very near the dipole and decay as a function of r^5. Similar to the radiated power, this near-field power density gets maximum value at the $\theta=\pm 90^0$. The interface to distinguish between near- and far-field distance is determined at $r_0=\lambda/2\pi$ in which their power densities are equal. In the region inside sphere of radius r_0 the reactive field dominates over the radiative fields. Inversely, outside this sphere the radiative field dominates.

b. Directivity (D)

Directivity D is a measure of an antenna's ability to concentrate radiated power into a certain direction. It corresponds to the angular power density relative to a hypothetical isotropic radiator. Normally it is defined as:

$$D(\theta,\phi) = \frac{P(\theta,\phi)}{P_{av}} \quad (11)$$

where $P(\theta, \phi)$ is the angular radiated power per unit solid angle, and P_{av} is an equivalent power that would be obtained with an isotropic source. By directing the radiated power in a specific direction, the radiation intensity of antenna in that direction can be increased with the factor of D in comparison with the power in case of isotropic radiator.

c. Gain (G)

The gain G of an antenna measures the efficiency of transforming a potential power at the input terminals to the radiated power in the selective direction. It follows a definition similar to that of the directivity, but instead of normalizing with the average radiated power, the gain is defined relative to the total power P_{total} (including the radiated power P_f and power dissipated into heat and other channels P_{loss}):

$$G = D\varepsilon_r, \quad \varepsilon_r = \frac{P_f}{P_f + P_{loss}} \quad (12)$$

where ε_r being the antenna radiation efficiency that indicates the losses of the input power of antenna. Both D and G are usually measured in decibels.

d. Impedance

The impedance of antenna presents the power dissipations. As definition, it is composed of real and imaginary parts:

$$Z=R+iX$$

while the real part R, input resistance, indicates the radiation losses R_r and ohmic losses R_{Ohmic}, the imaginary part X, input reactance, presents the power stored in near-field. At the resonance, the reactance X can be neglected. Based on the energy conservation law, it could be inferred:

$$R=R_r+R_{Ohmic}$$

R_r being the radiation resistance of an antenna referred to the input terminals as: $Rr=2P_f/I^2$, I being the current.

R_{ohmic} is determined as:

$$R_{oh\min} \approx \frac{L}{2\pi a} R_S, \qquad R_S = \sqrt{\frac{\omega\mu}{2\sigma}} \qquad (13)$$

R_S being the surface resistance.

1.3.3. Optical properties of bowtie nano-aperture antenna (BNA).

The most interesting properties of optical antenna are their ability of field confinement and enhancement. In contrast to simple wire types of antennas, BNA has the advantage of robustness, greater control of the radiation pattern[61]. Bowtie slot antennas are promising designs to obtain a particularly strong field enhancement due to their sharp edge design[62]. Recently, it was demonstrated that the coupling of BNA to the tapered optical fiber with specific design can cancel the background effect while keeping the high nanoantenna addressing efficiency[53,63]. It has been proved that the BNA shows the strong confinement of field as compared to the other aperture-shaped antennas[64].

The following parts are dedicated to the description of the BNA and their optical properties. These summarize the essential results found in Hongcang's PhD dissertation[60] and by Dr. Thierry Grosjean at FEMTO.[53,54]

a. BNA description

Resonant spectrum of a single BNA is known as the complex function of substrate material and geometries[61] (aperture perimeter, flare angle, film thickness and gap size...). The general model of BNA opened at the apex of NSOM probe and its geometries are illustrated in Figure 1.13. Its geometries are defined by *l* (length), *w* (width), *θ* (flare angle), *g* (gap size) and *h* (metal thickness). Impacts of metal material on the optical properties of BNA must also be taken into account.

In our case, BNA was designed to support the resonant wavelength around 1.55µm[54]. For that purpose, BNA was opened at the apex of a metallized polymer tip which was coated by 100nm thickness of aluminum. Aluminum material was used owning to the high conductivity at the infra-red region leading to high antenna effect and the smallest skin depth in visible region to prevent optical losses through the tapered region of fiber. The refractive index of 1.52 and opening angle 15° of such tip is considered. The 500 nm-radius of rounded curvature of tip assures the propagation of all guided modes reaching to the tip end where BNA is located. Geometries of BNA[54] are defined by a 310 nm-lateral size with 45 nm-square gap width and 45°-flare angles in Figure 1.13.

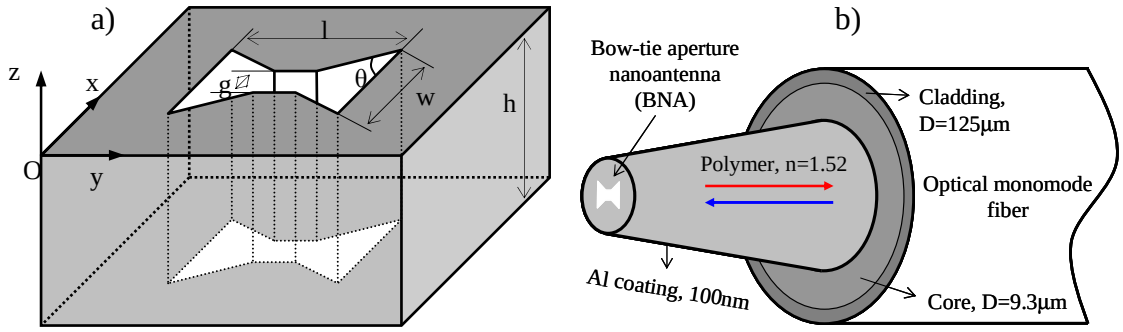

Figure 1.13: (a) Bow-tie aperture nanoantenna (BNA) model in the aluminum thin film. Its geometries are defined by l (length), w (width), θ (flare angle), g (gap size) and h (metal thickness). The incident vector kz is directed upwards whose electric filed E is linearly polarized along the x-axis. The axis of BNA is selected parallel to x-axis. (b) Diagram of an example BNA located on the apex of polymer tip.

b. Resonance depends on geometries

As above-mentioned, the geometries of BNA are defined by a set of parameters, such as perimeter *p*, gap size *g*, flare angle *θ*... Generally, physical properties of single optical antenna are strongly impacted by all their geometries since they relate to the oscillation nature of conduction electrons. Below are summarized some essential results[60] about the geometric parameters that strongly impact on spectrum of bowtie antenna.

b1. Resonance *v.s* Perimeter

In ref [60], the optical resonance of BNA as a function of perimeter (*p*) is investigated numerically using the similar model as sketched in Figure 1.13 but BNA is designed on gold film instead of aluminum film. Value of p is determined as relation:

$$p=2[l+\sqrt{2}w-(\sqrt{2}-1)g] \quad (14)$$

The impact of p on resonant spectrum of BNA is investigated by varying the outline dimensions *l or w (l=w)*. The other geometries, like gap (g=40nm), flare angle (θ=45°) and film thickness (h=30nm) are fixed. Figure 1.14 presents the calculated transmission curves of BNAs with respect to p-values varied from 0.93µm to 2.38µm in step of 0.48µm. Note that the transmission curves are obtained for an array of BNAs in which period varies from 350nm to 650nm in steps of 100nm. Figure 1.14-a indicates that resonant wavelengths of BNAs shift to the longer wavelength as increase of perimeters. The linear dependence between aperture perimeter and resonant wavelength is clearly confirmed in Figure 1.14-b.

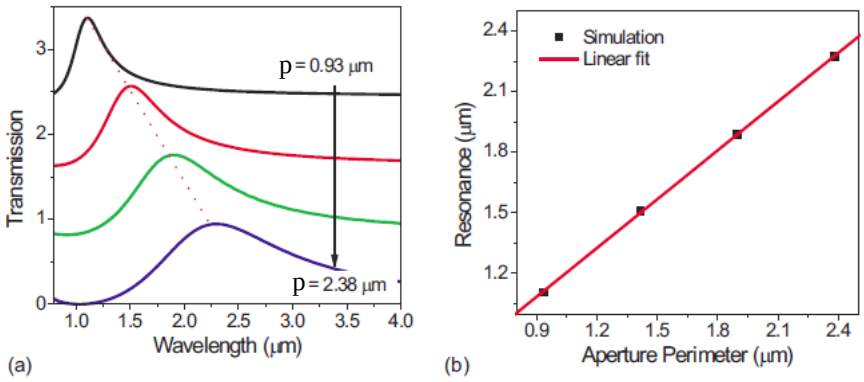

Figure 1.14: Simulated transmission of BNA spectrum in gold film[61].

For BNA, the resonances are emerged from oscillation of charges accumulating inside the gap edge induced by presence of external electric field as shown in Figure 1.15-

a. As a result, this charge oscillation ignites the current flowing along perimeter of the bowtie aperture as depicted in Figure 1.15-b. In fact, the oscillation path length of conduction electron that impacts the strength of flowing current is governed by the dimension of antenna or in case of BNA, the perimeter of aperture (p). This effect is analogous to the resonant spectrum of a loop antenna in optical frequency[61] in which its resonant wavelength is proportional to square root of surface loop ($S^{-1/2}$). This surface is corresponding to the area around bowtie aperture where the charges oscillate.

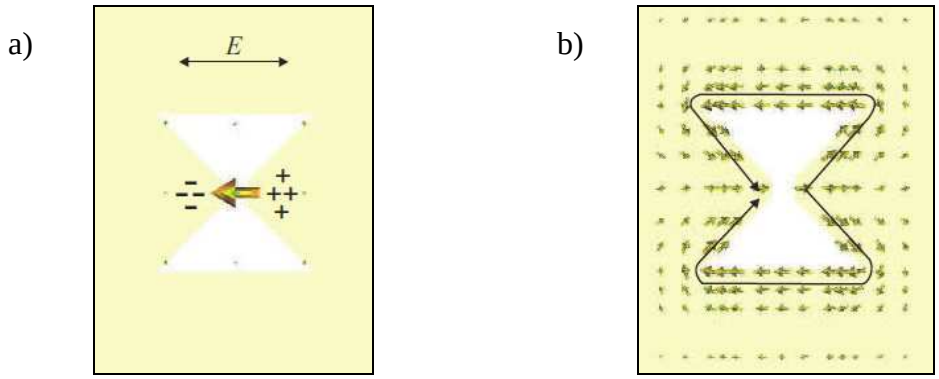

Figure 1.15: a) *Electric field polarized along the antenna gap results in the accumulation of charges in the gap edge at resonance. (b) Current density distribution shows the current flows around the perimeter of aperture. The detail could be found in ref [60].*

b2. Resonance ***v.s*** **gap size**

The gap size is one of the most important parameters as it is attributed to the confinement and enhancement effects of BNA and in turn, these effects lead to determine the spatial resolution of near-field detection and the optical power throughput[65]. In principle, the polarized charges accumulated around the gap zone are driven by Coulomb force between two opposite charges distributed at the edge of gap zone and restoring force along the oscillation path length[60]. Increasing the gap size leads to reduction of Coulomb force but improvement of restoring one, thus results in the blue-shift of the resonance wavelength of the antenna. Note that this effect could also be explained based on the relation between perimeter and resonant spectrum as stated in section b.1. As depicted in Eq. (14), the increase of gap size (g) while keeping the other geometric parameters of BNA unchanged results in the alternation of perimeter (smaller), and also exhibits the blue-shift of resonant wavelength.

Figure 1.16 shows the transmission spectra of BNAs with various gap sizes. The outline dimension of the antenna are fixed at $l=w=$ 300nm along with the period of antenna array, gold film thickness and flare angle are 450nm, 30nm and 90° respectively. By changing the gap size from 30nm to 60nm in steps of 10nm, the spectrum exhibits the blue-shift of wavelength. This result is consistent with the previous predictions.

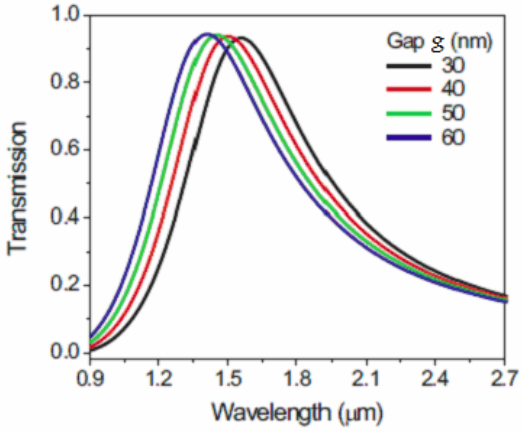

Figure 1.16: Simulated transmission spectra of antenna as a function of gap size on gold film reported in ref [60]. The increase of gap size results in the blue-shift of resonant wavelength attributed to improvement of the restoring forces.

The other geometries, such as thickness, flare angle, material... which also have important influences on the resonances of antenna were investigated more details in references [52,53,60].

c. Field confinement and enhancement of BNA

Field enhancement and confinement are the natural phenomenon in antenna. Bowtie antennas have abilities to concentrate electromagnetic energy into a tight space of gap zone thereby generating a zone of high energy density. Theoretically, the enhanced and confined field of BNA is attributed to the oscillating electric dipole as charges accumulate[53,54,60,66,67] . In specifically designed BNA, for instance, single BNA opened on Al-coating probe as present in Figure 1.13, it is demonstrated in simulation that vertical guided mode inside the structure rather than a localized plasmon resonance, is responsible for the light confinement ability[53]. In fact, Fabry–Perot phase-matching condition governs the transmission of light through aperture, analogously to the case of the enhanced optical transmission obtained through annular aperture arrays[68]. While the confined field is responsible for the spatial resolution of NSOM optical images, the enhanced field results

in the coupling enhancement of near-to-free space radiation. As indicated in Eq. (9-10), the optical fields and power density of radio antenna in near-field are proportional to the length Δz and a larger inverse power of distance r from the radiation zone respectively.

Figure 1.17 presents the enhancement factors of the electric field intensity in the gap zone normalized to the incident power calculated for a BNA on gold film as a function of gap size (Figure 1.17-a) or distance from the antenna surface (Figure 1.17-b). The small increase of either gap size (g) or distance (r) away from resonant zone might result in a large drop of field intensity.

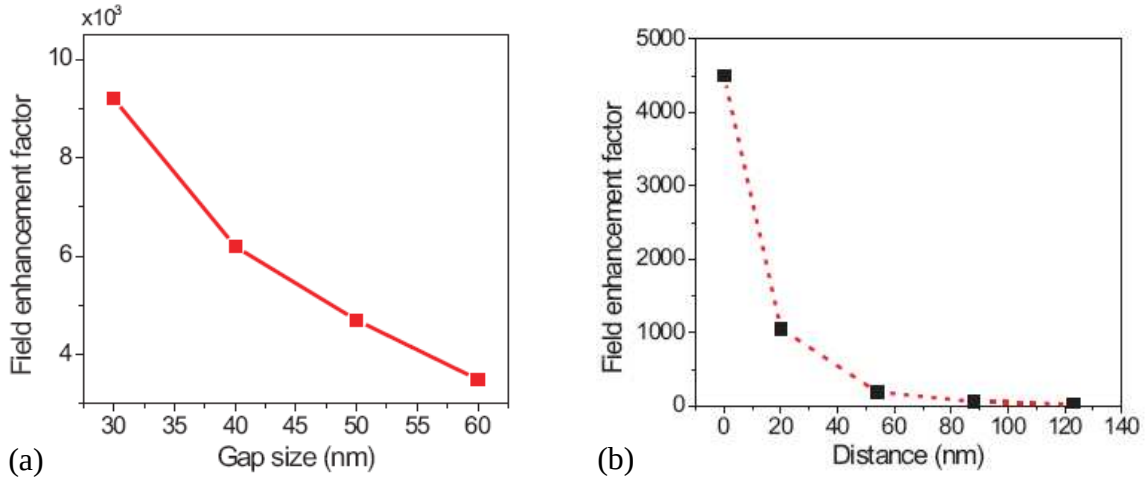

Figure 1.17: Near-field enhancement factor of electric field $E^2_{NA}/E^2_{Incident}$ by FDTD in ref [60] versus: a) gap size varying from 30nm to 60nm. b) distance from antenna surface.

The confined field as the function of distance r is determined at FWHM of the field pattern, which depends mainly on the current density distribution induced by the external field as depicted in Figure 1.18.

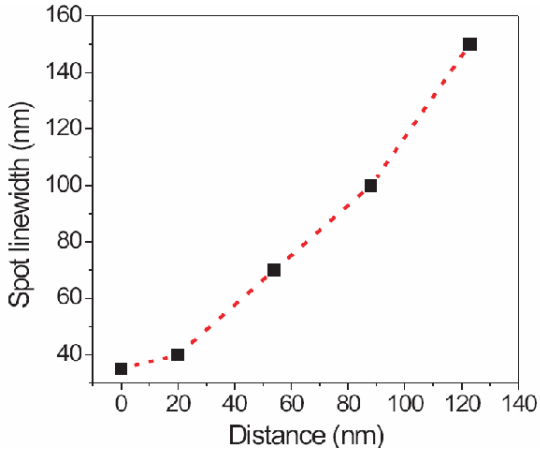

Figure 1.18: Field confinement of antenna (spot line-width) is measured at resonance as a function of distance from the antenna surface[60].

In case of BNA-probe designed on the aluminum thin film as sketched in Figure 1.13, the optical properties of BNA-tip are simulated by Dr. Thierry Grosjean (FEMTO group). A Gaussian excitation beam of TE mode at resonant wavelength 1.55µm is injected into the fiber. Figure 1.19 indicates the electric field intensity of BNA in emission mode with various incident polarization directions as shown in ref [54]. In Figure 1.19-a, the electric field distribution in *xy*-plane is mapped along last 2.0µm from tip apex. The incident field polarizes in x-direction to excite the fundamental guided mode in BNA. Due to the large curvature at the rounded end, the tip shows no cut-off diameter at working wavelength. This property helps driving efficiently the optical energy to the tip end with less loss. The cartography was constructed with color scale of power of 2/5 in order to increase the contrast. It explicitly indicated that the electric field dramatically enhances and confines with factor of 350 (~ 3.22^5) inside the BNA gap.

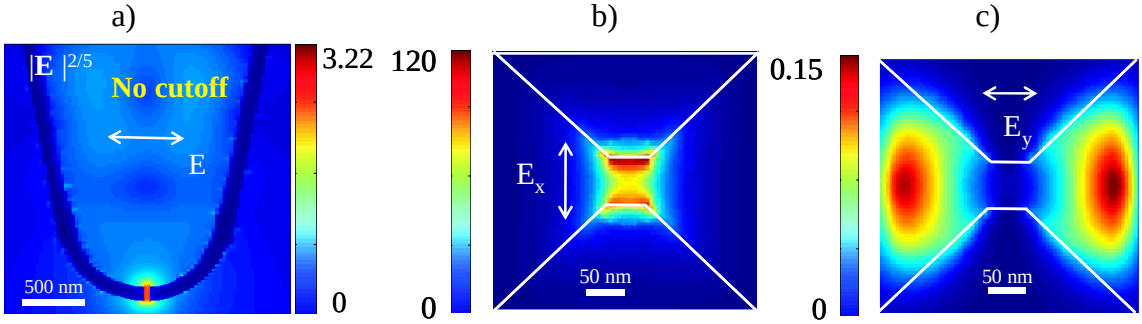

Figure 1.19: (a). Global electric field distribution inside the tip body in the xz-plane and polarized along x-axis of BNA. The field intensity is normalized to the maximum input power. At the position of BNA, field enhancement can be estimated to the value of 350 and confined mainly into the gap. (b). The electric field intensity in the xy-plane placed 10 nm away from BNA and excited along x-axis (E_x) indicates explicitly the enhancement at BNA gap. (c). The electric field intensity excited along y-axis (E_y) shows no intensity enhancement at BNA gap[54].

In order to obtain the radiation patterns of BNA-tip versus each polarization component of excitation beam (E_x and E_y), a detector is placed at 10nm away BNA-tip surface. This distance is corresponding to the working distance of NSOM-based BNA in shear-force mode. Figure 1.19-b/c shows the detail of enhanced and confined field patterns in the transverse (*x*-*y*) plane. With the electric field polarized in *x*-direction (Figure 1.19-b), the enhancement factor of field intensity (normalized to the incident one) in the gap

zone could reach 120 times. On contrary, if BNA is excited by the electric field polarized in y-direction (Figure 1.19-c), very low enhancement factor is observed in the gap zone.

d. Polarization

High asymmetric shape of BNA results in the charge accumulation in the gap zone with presence of external field and responsible for the high polarization sensitivity of BNA. M.Mivelle *et al.* studied the normalized coupling power (P/P_0) of dipoles (Figure 1.20) measured in the fiber at distance of 4.6μm away from antenna[54]. With this approach, BNA is excited by single pulsed dipoles placed 10nm outside the fiber (collection mode) and polarized in three directions *Ox*, *Oy* and *Oz* respectively. With electric field excitation, the enhancement factor through BNA in case of Ox-polarization reaches 76 times in comparison with power obtained in vacuum. We define the polarization ratio as ratio of coupling powers through BNA between Ox and Oy excitation direction at resonant wavelength. As calculated from Figure 1.20-a, this ratio reaches 170 times. Note that the curve of *Oy*-polarization in Figure 1.20-a is multiplied by factor of 10^3 for comparison. The enhanced power is neglected for Oz-polarization. In case of using a non-local excitation by plane wave to excite BNA in collection mode, the polarization ratio results in the theoretical value of 37. The sensitivity of BNA to the polarization of electric field is also confirmed as shown in Figure 1.20-b. Under magnetic field excitation, with the same condition as Figure 1.20-a, however, maximum enhanced power only reaches value of unity and is negligible in comparison with the electric field excitation.

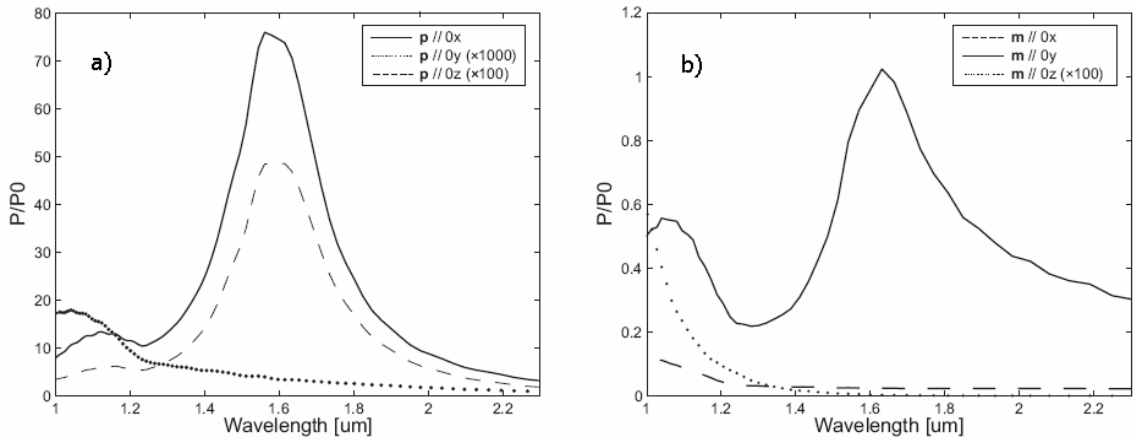

Figure 1.20: Collection spectra of BNA at the rounded apex of Al-coating probe versus normalized coupling power (P/P_0) reported by M. Mivelle et al.[54] indicates resonant wavelength of 1.55μm. a) using electric dipole excitation. b) using magnetic dipole excitation[54].

Further investigations of polarization ration versus BNA gap size provide the facts that both polarization sensitivity and resolution of BNA are strongly improved up to the value of $3x10^4$ times by the gap size of 5nm with dipole excitation. Therefore, BNA-probe might be used as an electric nanopolarizer to probing the near-field sources with high spatial resolution.

Conclusion

In chapter 1 we have stated briefly the related theories of photonic crystal structures, near-field scanning optical microscope and optical frequency nano-antenna. In section 1.1, the general optical properties and potential applications of 2D-PC laid on cavity mode and slow light mode are discussed. In section 1.2 we reviewed NSOM developments as a novel tool for nanophotonics researches and discussed about NSOM configurations. Section 1.3 is reserved for the optical antenna and their properties. We especially discussed about bowtie nano-antenna embedded on fiber probes as a nano-collector and nano-polarizer for near-field investigation.

References

[1] K. Sakoda, "Optical Properties of Photonic Crystals," Springer- Verlag, Berlin, Heidelberg (2001).

[2] Joannopoulos J, Johnson S G, Meade R and Winn J 2007 Photonic Crystals, Molding the Flow of Light 2nd Edn (Princeton, NJ: Princeton University Press)

[3] Ohtaka K 1979 Energy band of photons and low-energy photon diffraction Phys. Rev. B 19 5057

[4] Anderson, P. W. Absence of diffusion in certain random lattices. Phys. Rev. 109, 1492-1505 (1958)

[5] Topolancik, J., & Vollmer, F. Random high-Q cavities in disordered photonic crystal waveguides. Appl. Phys. Lett. 91, 201102-1-3 (2007)

[6] Topolancik, J., Ilic, B., & Vollmer, F. Experimental observation of strong photon localization in disordered photonic crystal waveguides. Phys. Rev. Lett. 99, 253901-1-4 (2007)

[7] Introduction to photonic crystals, Steven G. Jonhson and J.D.Joannopoulos, MIT, 2003

[8] James Clerk Maxwell, "A Dynamical Theory of the Electromagnetic Field", Philosophical Transactions of the Royal Society of London **155**, 459-512 (1865)

[9] Bloembergen, N.1965 Non-linear optics. New York: W.A.Benjamin

[10] Meade R D, Rappe A M, Brommer K D, Joannopoulos J D and Alerhand O L 1993 Accurate theoretical analysis of photonic band-gap materials Phys. Rev. B **48** 8434–7

[11] Johnson S G and Joannopoulos J D 2001 Block-iterative frequency-domain methods for Maxwell's equations in a planewave basis Opt. Express 8 173–90].

[12] Settle M, Salib M, Michaeli A and Krauss T F 2006 Low loss silicon on insulator photonic crystal waveguides made by 193 nm optical lithography Opt. Express 14 2440–5

[13] Gaëlle LE GAC, "Etude de l'impact d'une pointe SNOM sur les propriétés des modes optiques d'une cavité à base de cristaux photoniques", doctoral dissertation, INL, CNRS UMR 5270 (2009)

[14] Notomi M, Shinya A, Mitsugi S, Kuramochi E and Ryu H Y 2004 Waveguides, resonators and their coupled elements in photonic crystal slabs Opt. Express 12 1551–61

[15] Smith S.D et al., "Optical bistability, photonic logic, and optical computation", Appl. Opt. 25 1550–64 (1986)

[16] Kuramochi E, Tanabe T and Notomi M 2009 Very-large-scale photonic crystal coupled cavity waveguides with large delay per pulse width ratio Conf. on Lasers and Electro-Optics (CLEO09) (Baltimore, MD) CThU1

[17] Notomi M 2007 Adiabatic tuning of optical Microsystems IEEE LEOS Newslett 21 16–21

[18] Notomi M, Tanabe T, Shinya A, Kuramochi E, Taniyama H, Mitsugi S and Morita M 2007 Nonlinear and adiabatic control of high-Q photonic crystal nanocavities Opt. Express 15 17458–81

[19] N. Chauvin, P. Nedel, C. Seassal, B. Ben Bakir, X. Letartre, M. Gendry, A. Fiore, and P. Viktorovitch," Control of the spontaneous emission from a single quantum dash using a slow-light mode in a two-dimensional photonic crystal on a Bragg reflector" Phys. Rev. B 80, 045315 (2009).

[20] F. Raineri, C. Cojocaru, R. Raj, P. Monnier, A. Levenson, C. Seassal, X. Letartre, and P. Viktorovitch, "Tuning a two-dimensional photonic crystal resonance via optical carrier injection," Opt. Lett. 30, 64-66 (2005)

[21] T. F. Krauss, "Slow light in photonic crystal waveguides," J. Phys. D 40, 2666-2670 (2007)

[22] E. Parra and J. R. Lowell, "Toward applications of slow-light technology," Opt. Photon. News 18, 41-45 (2007)

[23] William M. J. Green, Michael J. Rooks, Lidija Sekaric, and Yurii A. Vlasov, "Optical modulation using anti-crossing between paired amplitude and phase resonators," Opt. Express 15, 17264-17272 (2007)

[24] Near-Field Nano/Atom Optics and Technology, Ohtsu, M., (ed.) Springer, Tokyo, Japan, 302 pages (1998).

[25] M. Abbé, Archiv. Mikroscop. Anat. Entwicklungsmech. 9, 413 (1873).

[26] E. Synge, Philos. Mag. 6, 356 (1928)/E. Synge, Philos. Mag. 11, 65 (1931)

[27] Ash, E.A., Nicholls, G.,"Super-resolution aperture scanning microscope". Nature 237, 510–512 (1972)

[28] Pohl, D.W., Denk, W., Lanz, M.,"Optical stethoscopy: image recording with resolution λ/20", Appl. Phys. Lett. 44, 651–653, (1984)

[29] Lewis, A., Isaacsson, M., Harootunian, A., Murray, A., "Development of a 500 Å spatial resolution light microscope. Light is efficiently transmitted through l/16 diameter apertures", Ultramicroscopy 13, 227–231, (1984)

[30] Pohl, D.W., Denk, W., Lanz, M.,"Optical stethoscopy: image recording with resolution λ/20", Appl. Phys. Lett. 44, 651–653, (1984)

[31] Dürig, U., Pohl, D.W., Rohner, F., 1986. Near-field optical-scanning microscopy.J. Appl. Phys. 59, 3318–3327 /// Harootunian, A., Betzig, E., Isaacson, M., Lewis, A.,"Super-resolution fluorescence near-field scanning optical microscopy". Appl. Phys. Lett. 49, 674–676 (1986)

[32] Harootunian, A., Betzig, E., Isaacson, M., Lewis, A.,"Super-resolution fluorescence near-field scanning optical microscopy". Appl. Phys. Lett. 49, 674–676 (1986)

[33] Lewis, A., Isaacsson, M., Harootunian, A., Murray, A., "Development of a 500 A° spatial resolution light microscope. Light is efficiently transmitted through λ/16 diameter apertures", Ultramicroscopy 13, 227–231, (1984)

[34] Betzig, E., Isaacson, M., Lewis, A.,"Collection mode near-field scanning optical microscopy." Appl. Phys. Lett. 51, 2088–2090 (1987)

[35] Fischer, U.C., Pohl, D., 1989. Observation of single-particle plasmons by nearfield optical microscopy. Phys. Rev. Lett. 62, 458–461

[36] Fischer, U.C., Koglin, J., Fuchs, H., 1994. The tetrahedral tip as a probe for scanning near-field optical microscopy at 30 nm resolution. J. Microsc. 176, 231–237

[37] Inouye, Y., Kawata, S., 1994. Near-field scanning optical microscope with a metallic probe tip. Opt. Lett. 19, 159–161.

[38] Toledo-Crow, T., Yang, P.C., Chen, Y., Vaez-Iravani, M., 1992. Near-field differential scanning optical microscope with atomic force regulation. Appl. Phys. Lett. 60, 2957–2959

[39] Froehlich, F.F., Milster, T.D., 1997. Mechanical resonance behavior of nearfield optical microscope probes. Appl. Phys. Lett. 70, 1500–1502

[40] Toledo-Crow, T., Yang, P.C., Chen, Y., Vaez-Iravani, M., 1992. Near-field differential scanning optical microscope with atomic force regulation. Appl. Phys. Lett. 60, 2957–2959

[41] Betzig, E., Finn, P.L., Weiner, J.S., 1992. Combined shear force and near-field scanning optical microscopy. Appl. Phys. Lett. 60, 2484–2486

[42] Karrai, K., Grober, R.D., 1995. Piezoelectric tip–sample distance control for near field optical microscopes. Appl. Phys. Lett. 66, 1842–1844

[43] Ruiter, A.G.T., Veerman, J.P., van der Werf, K.O., van Hulst, N.F., 1997. Dynamic behavior of tuning fork shear-force feedback. Appl. Phys. Lett. 71, 28–30

[44] M. A. Paesler and P. J. Moyer, Near field Optics, John Wiley & Sons, New York (1 996)

[45] G. Le Gac, A. Rahmani, C. Seassal, E. Picard, E. Hadji, and S. Callard, "Tuning of an active photonic crystal cavity by an hybrid silica/silicon near-field probe," Opt. Express 17, 21672-21679 (2009)

[46] Inouye and Kawata, 1994; Kawata and Inouye, 1995; Gleyzes et al., 1995; Zenhausern et al., 1994)

[47] Kneipp, K.,Wang, Y., Kneipp, H., Perelman, L.T., Itzkan, I., Dasari, R.R., Feld, M.S., 1997. Single molecule detection using surface-enhanced Raman scattering (SERS). Phys. Rev. Lett. 78, 1667–1670.

[48] Haefliger, D., Plitzko, J.M., Hillenbrand, R., 2004. Contrast and scattering efficiency of scattering-type near-field optical probes. Appl. Phys. Lett. 85, 4466–4468.

[49] Kim, J., & Song, K.-B. (2007). Recent progress of nano-technology with NSOM. Micron Oxford England 1993, 38(4), 409-426

[50] Bethe, H.A., 1944. Theory of diffraction by small holes. Phys. Rev. 66, 163–182

[51] Bouwkamp, C., 1954. Diffraction theory. Rep. Prog. Phys. 17, 35–100

[52] Hongcang Guo, Todd P. Meyrath, Thomas Zentgraf, Na Liu, Liwei Fu, Heinz Schweizer, and Harald Giessen, "Optical resonances of bowtie slot antennas and their geometry and material dependence," Opt. Express 16, 7756-7766 (2008)

[53] I. A. Ibrahim, M. Mivelle, T. Grosjean, J.-T. Allegre, G. W. Burr, and F. I. Baida, "Bowtie-shaped nanoaperture: a modal study," Opt. Lett. **35**, 2448-2450 (2010)

[54] M. Mivelle, I. A. Ibrahim, F. Baida, G. W. Burr, D. Nedeljkovic, D. Charraut, J-Y. Rauch, R. Salut, and T. Grosjean, "Bowtie nano-aperture as interface between near-fields and a single-mode fiber," Opt. Express **18**, 15964-15974 (2010)

[55] H. F. Ghaemi, T. Thio, D. E. Grupp, T. W. Ebbesen, and H. J. Lezec, Surface plasmons enhance optical transmission through subwavelength holes, Phys. Rev. B 58 6779 (1998)

[56] E. X. Jin and X. Xu, Plasmonic effects in near-filed optical transmission enhancement through a single bowtie-shaped aperture, Appl. Phys. B. 84, 3 (2006)

[57] D. W. Pohl, “Near-field optics seen as an antenna problem,” in Near-field Optics, Principles and Application

[58] Palash Bharadwaj, Bradley Deutsch, and Lukas Novotny, “Optical antennas”, Advances in Optics and Photonics 1, 438–483 (2009).

[59] W. L. Stutzman, A. A. Thiele, Antenna theory and design (John Wiley & Sons, New York, 1996).

[60] Hongcang Guo, “Fabrication and Optical Characterization of Metamaterials and Nano-Antennas”, PhD dissertation (2008)

[61] *W. L. Stutzman, A. A. Thiele, Antenna theory and design (John Wiley & Sons, New York, 1996).*

[62] *P. J. Schuck, D. P. Fromm, A. Sundaramurthy, G. S. Kino, and W. E. Moerner, Improving the mismatch between light and nanoscale objects with gold bowtie nanoantennas, Phys. Rev. Lett. 94, 017402 (2005)*

[63] *Grosjean T, Mivelle M, Baida FI, Burr GW, Fischer UC, Diabolo nanoantenna for enhancing and confining the magnetic optical field. Nano Lett, 2011, 11(3):1009-13*

[64] *E. X. Jin and X. Xu, Plasmonic effects in near-filed optical transmission enhancement through a single bowtie-shaped aperture, Appl. Phys. B. 84, 3 (2006)*

[65] *L. Wang and X. Xu, High transmission nanoscale bowtie-shaped aperture probe for near-field optical imaging, Appl. Phys. Lett. 90, 261105 (2007)*

[66] *R. Grober, R. Schoelkopf, and D. Prober, "Optical antenna: Towards a unity efficiency near-field optical probe," Appl. Phys. Lett. 70(11), 1354–6 (1997)*

[67] *A. Alù and N. Engheta, "Hertzian plasmonic nanodimer as an efficient optical nanoantenna," Phys. Rev. B 78(19), 195111 (2008)*

[68] *F. I. Baida, D. V. Labeke, G. Granet, A. Moreau and A. Belkhir, Appl. Phys. B 79, 1 (2004).*

Chapter 2: Experimental set-up description

This chapter is devoted to describe the main experimental setups that are employed to perform our experiments from NSOM, near-field probe, far-field measurements to micro-fabrication facilities. The FDTD simulation principle is also included.

2.1. NSOM set-up

Conventional optical far-field techniques, such as micro-photoluminescence give valuable information on the radiating part of the optical field but do not provide the spatial resolution, required to compare for instance computed map to the measured light distribution. Moreover, in the far field, confined or guided light can be detected only indirectly through out-of-plane losses. Near-field optical microscopy, on the other hand, allows one to probe the evanescent tail of guided modes with spatial resolution below the diffraction limit ($\lambda/2$). In order to characterize optical properties of photonic nano-structures operating at 1.55µm, near-field scanning optical microscopy (NSOM) has proved to be an invaluable tool.

In the context of these work, which deals essentially with the characterization of 2D active photonic crystal based devices, a NSOM set up in collection mode has been developed. Among its specifications, it had to work in transmission, enable the direct access to sample surface and permit a perfect control of the excitation spot size and position with respect to the structure. Our NSOM configuration is built to meet he above-mentioned criteria in the scope of the NanoEC program.

2.1.1. Description

A NSOM in transmission was selected since it enables to resolve some drawbacks of a former set-up[1,2] which was working in reflection mode (see Figure 2.1-b). As a matter of fact, in the reflection configuration, the sample is illuminated in oblique incidence. First, this produces elliptic excitation spot and second, it can be partially shadowed by the tip during the scan. Furthermore, the exact location of the spot on the structure was difficult to estimate. In transmission configuration, all these problems are solved as the excitation is focused on the sample in normal incidence, producing a symmetric and circular spot. The control of the size and the location of the excitation spot is easily performed thanks to the spot visualization through the inverted microscope. However, NSOM in transmission mode is restricted to transparent samples (*e.g.* sample based on silica substrate) due to backside illumination condition.

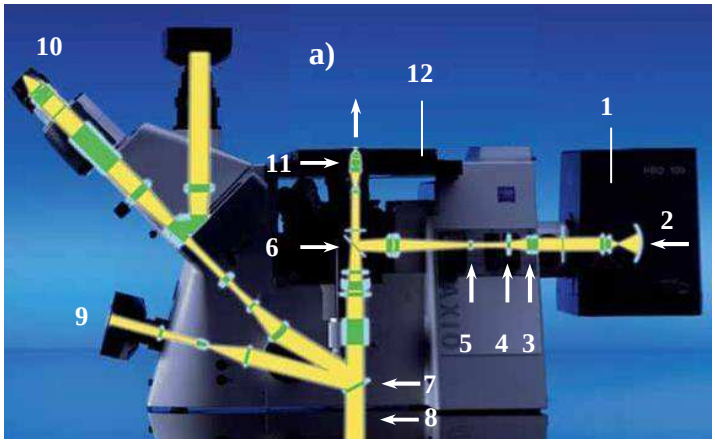

Figure 2.1-a: NSOM set-up relied on Axio Observer inverted microscope (D1). Main components consists of HAL lamp (1), laser alignment system (2), filter slider (3), aperture stop (4), field diagram (5), reflector cube (6), switching beam path between base port/front port/vis observation (7), base port (8), light outputs: front port (9), eye piece (10), objectives 10x-40x–63x (11), CCD camera for sample observation at side port (not showed here) and sample holder with translational stage (12). For future development, in addition to visible and infra-red camera, the outputs could be connected to spectrum analyzer or monochromator to analyze in real time the emission light from sample.

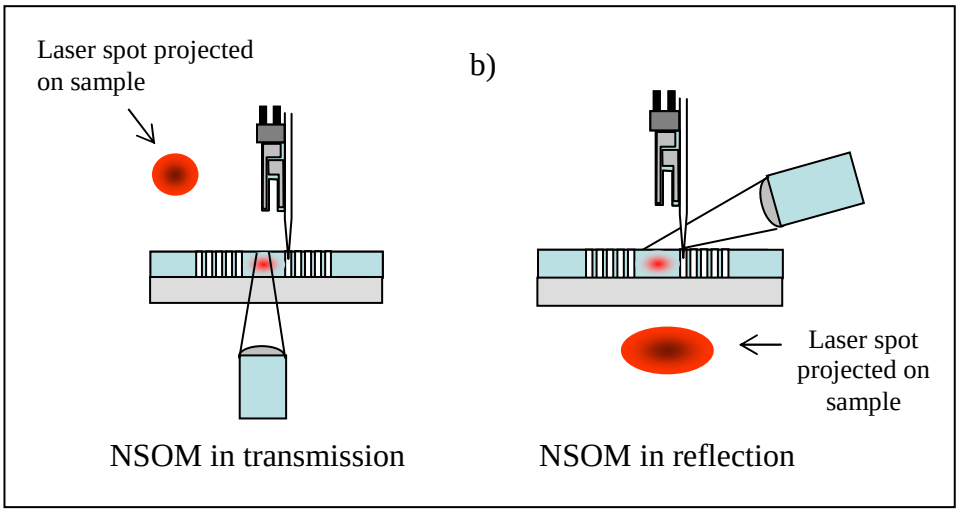

Figure 2.1-b: Illustration of two configurations: (left) New NSOM set-up in transmission mode and (right) previous NSOM set-up in reflection mode.

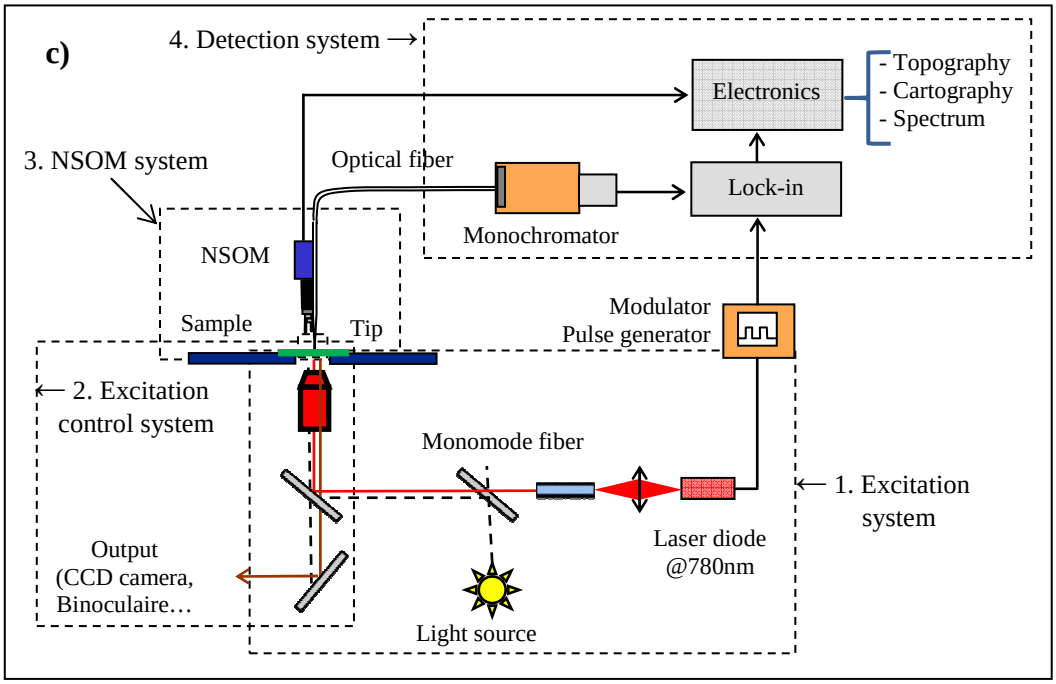

Figure 2.1-c: Principle of NSOM set-up consists of four sub-systems: 1. excitation (modulator, pulse generator, laser diode, light source and single mode fiber), 2. excitation control (microscopy stand including optical components, sample and CCD camera), 3. NSOM (NSOM head and tip) and 4. detection system (monochromator, lock-in amplifier and other electronics devices).

NSOM set-up is built based on a commercial Axio Observer.D1 inverted microscope stand as indicated in Figure 2.1-a. Observation of the sample and the excitation spot is provided by a CCD working in the visible range and mounted on one of the output side port. Figure 2.1-c shows the experimental set-up. It can be decomposed of four main sub-systems: 1. Illumination, which consists in the white light source to observe the sample and a pump laser diode to excite the structure; 2. Alignment system allows to control precisely the excitation laser spot (size and position) onto structure; 3. NSOM head allows to control the tip-sample interaction; 4. A detection chain allows to filter, detect and amplify the near-field optical signal.

a. Illumination

Our samples consist in active 2D-photonic structures. They contain emitters, InAsP quantum wells, embedded in the center of a 250 nm InP slab. Their photoluminescence

occurs in the range of 1250-1650 nm. At this wavelength region, InP material is transparent.

- Excitation source

The pumping is performed with a 50 mW laser diode with a centre wavelength of 780 nm (Figure 2). To avoid overheating the structure, which can prevent lasing effect and lead to destruction of the structure, the diode is pulsed (10% of duty cycle). To ameliorate the signal to noise ratio, the laser diode is also modulated at low frequency (2kHz) to allow a lock-in detection of the signal. The signal of the laser diode is coupled into a monomode fiber (9µm core diameter) through Thorlab's coupler (objective 20X). The laser beam is then collimated and is directed into the optical system of the microscope after passing a dichroic mirror. The white light emitted by an halogen bulb (HAL100) is sent as well into the microscope.

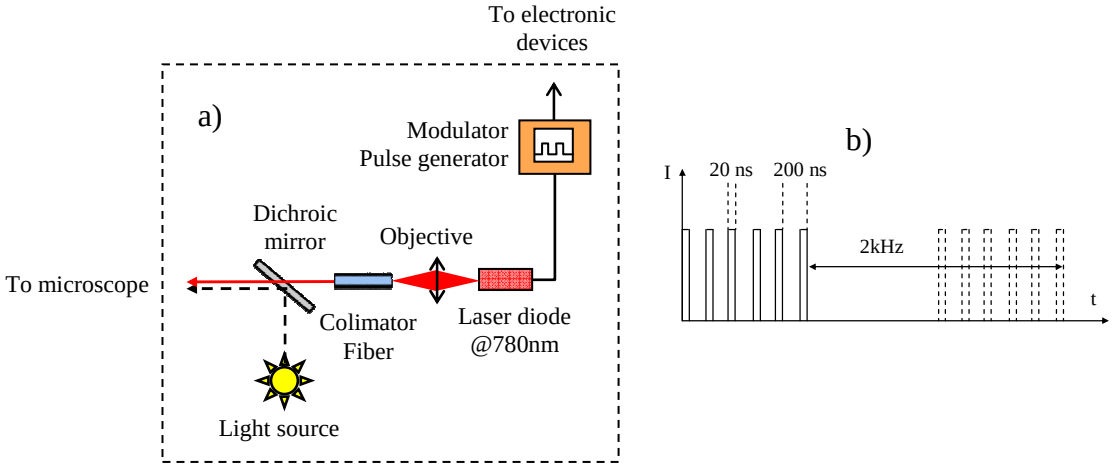

Figure 2.2: Details of excitation system. a) Sketch contains main components. b) Laser diode is modulated with 2kHz and pulsed with duration of 20ns and duty cycle of 10%.

The incident power on the structure has to remain high enough to excite properly the structure. In particular, for microlaser study, it has to exceed the pumping lasing threshold. In our case, the pumping power has to be at least of the order of the milliwatt. Consequently, the optimization of the pumping power along the optical path of the excitation is crucial.

At the backside surface of the sample, the pumping power $I_{pumping}$ can be estimated by the following relation:

$$I_{pumping} = I_{laser} \times \theta_{fiber\ coupling} \times \theta_{microscope\ coupling}$$

where: - $I_{pumping}$ is the laser power estimated at the interface of sample.

- I_{laser} is the power measured at the output of the laser diode, mW

- $\theta_{fiber\ coupling}$ is the coupling efficiency of laser to the optical fiber (in fact it is the ratio between output and input power of fiber)

- $\theta_{microsope\ coupling}$ is the coupling coefficient of laser inside the microscope (it is the ratio between the output and input laser power of the microscope).

$\theta_{fiber\ coupling}$ can be optimized through optical alignment system and has been estimated to be 0.47. $\theta_{microscope\ coupling}$ reflects the intrinsic optical losses of optical system in microscope, and is estimated to be 0.53. Thus for a 5.2mW of initial pumping power, $I_{pumping}$ obtains 5.2(mW) x 0.47 x 0.53 ~1.3 mW measured on sample surface, corresponding to 75% of losses.

- Alignment

Inside the microscope, the optical path is presented in Figure 2.3. The collimated laser beam as well as the white light emitted by the halogen lamp is directed into the microscope and pass through a filter slider (blank in our case), a reflected light aperture stop and a field diagram (reflected light luminous-field stop). In the microscope, the laser beam is deflected vertically by a Bragg reflector and focused by microscope objective on the structure

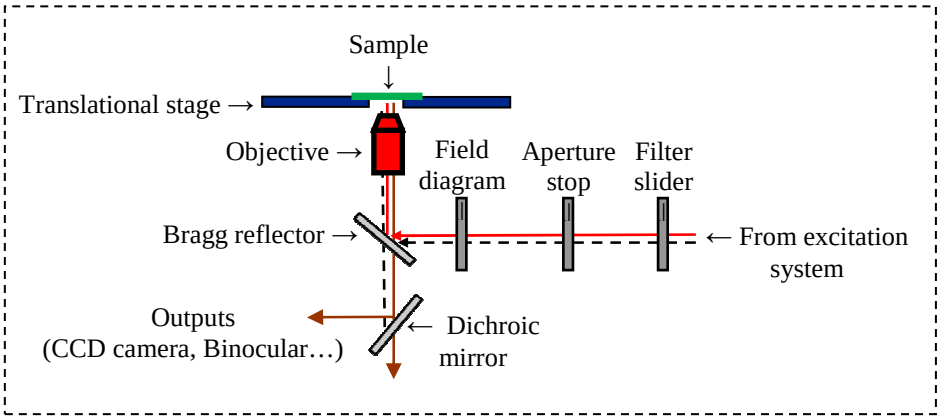

Figure 2.3: Deployment principle of excitation control system. This system includes microscopy stand with all optical components (filter slider, aperture stop, field diagram, Bragg reflector, mirror and objective), translational stage, sample and output devices (CCD camera, binocular...)

We found that the Bragg reflector significantly influences $\theta_{\text{microscope coupling}}$. Selecting carefully the reflector can improve a lot the pumping power on sample. What we expect from this reflector is to have high reflectivity in the visible range and a good transmission in infra-red range. The optical properties of the commercial Bragg reflector was characterized as shown in Figure 2.4-a: the reflectivity is 25% at our working wavelength (λ~780nm), about 15-30% around 1.55µm and reached nearly 100% at 1600 nm. This is actually more suited for excitation wavelength around 810 nm. To meet our criteria, we design a homemade Bragg reflector. It consists of a stack of 9 thin layers of titanium dioxide (n≈2.5, 115nm thickness) alternate with silica (n≈1.5, 148nm thickness). It is deposited on a glass substrate by microwave PECVD (Plasma-enhanced chemical vapor deposition). Figure 2.4-b indicates the reflectivity. It shows that the reflectivity reaches nearly 75% in the visible region and 11% in the infra-red. This mirror improves 3-fold the reflectivity with respect to the commercial reflector. Moreover, conversely to the commercial mirror, the homemade mirror is free from polarizing effects, which is of utmost importance for our experiments. That is the reason why we decided to use it throughout our experiment instead of the commercial one.

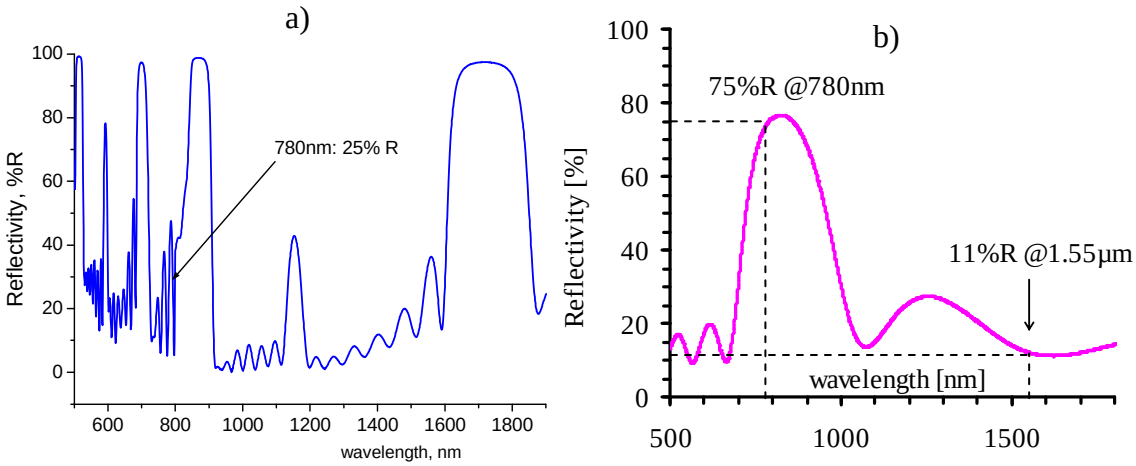

Figure 2.4: Reflection properties of Bragg reflectors measuring at incident angle of 45°. a): Reflectivity of a commercial Bragg mirror is weak at 780nm (25%) and high in infra-red region (nearly 100% at wavelength 1600-1850nm). b) A homemade 9-layer Bragg reflector provides a high reflectivity in visible (75%) and weak in infra-red region (11%).

The pumping spot on the sample is observed thanks to the CCD camera system assembled at side output. Its position can be set with the translational stage of the

microscope. The CCD camera allows a good control of its alignment with respect to the structure. The sample itself is placed on a holder attached to this translational stage.

The size of excitation spot can be estimated with the CCD camera imaging abilities. Figure 2.5 shows an excitation spot on a defect-free honeycomb lattice photonic crystal. The rectangular PC (40x40µm²) is illuminated both by halogen bulb (HAL100). The diameter of excitation spot can be directly estimated from image (Figure 2.5-a/b): typical value of 9µm for objective 63x/0.75 and 13.7µm for objective 40x/0.6 are measured. It can be more precisely measured by analyzing the Gaussian curve fitting for linear optical intensity profile. As indicated in Figure 2.5-c, the profile cross-sections of several excitation spots (Gaussian beam) are plotted as a function of the laser diode current, from 32mA to 69mA (saturation). The spot size of 13.5±0.3µm (objective 40x/0.6) is calculated from width of the Gaussian curves corresponding to I_{max}/e^2. These curves P60 and P69 were not taken into account due to their saturation (flat at top).

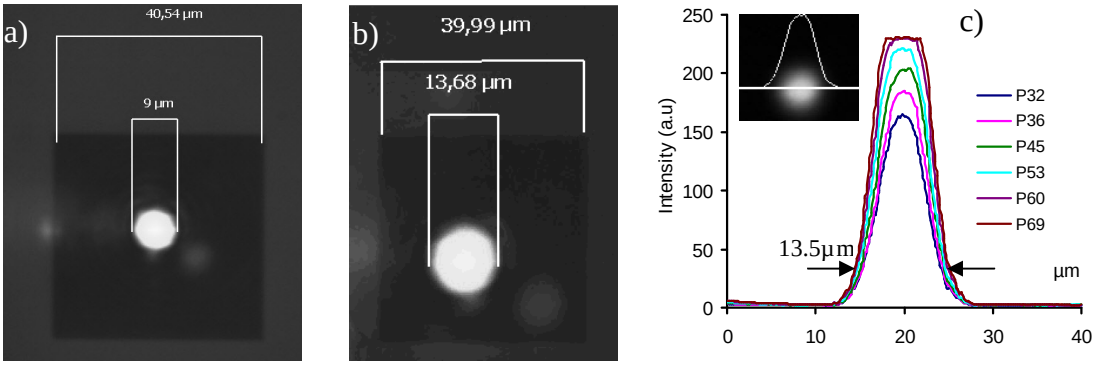

Figure 2.5: Excitation spot on defect-free honeycomb 2D photonic crystal (40x40µm²) recorded by a visible CCD camera. (a): image captured with corrected objective x63/0.75. Excitation spot diameter is measured around 9µm. (b): image captured with objective 40x/0.6, excitation spot diameter is around 13.7µm. (c): excitation profile vs. pumping power (P) of laser diode follows Gaussian shape and is used to estimate the spot size (13.5±0.3 µm, objective 40x/0.6). In this graph, curves P60 and P69 are flat at top due to the saturation and not taken into account of calculation.

b. NSOM scanning system

The heart of system, NSOM head (Figure 2.6, NT-MDT) was placed above the sample on a homemade disk which has its own manual translation stage to position the NSOM tip with respect to nanophotonic structure.

- Shear-force regulation

The distance between the optical near-field probe and the structure surface is kept constant, typically around 5-10 nm by shear-force regulation based on a quartz tuning fork sensor[1,2]. The fiber tip-quartz system vibrates parallel to the surface at the quartz resonance frequency, about 32-36 kHz, with quality factor Q=500-1000. Further piezoeffect is applied: in the presence of mechanical quartz oscillations, the electrical outputs of quartz have voltage response which is used as information signal about amplitude of fiber oscillation. The raster movement of the quartz-fiber tip over surface is controlled by the piezoelectric scanner equipped in NSOM head. Electronics systems simultaneously evaluate the probe position, incorporating data obtained from the feedback system, and control the scanning of the tip and the separation of the tip and sample surface. The information generated as a result of sensing the interaction between the probe and sample is collected and recorded by the computer point-by-point during the raster movement. This enables the measurement of the sample topography. In addition to the optical information (cartography), NSOM can generate topographical image or force data from the sample in the same manner as the atomic force microscope (AFM). These two separate data sets can then be compared to determine the correlation between the physical structures and the optical contrast.

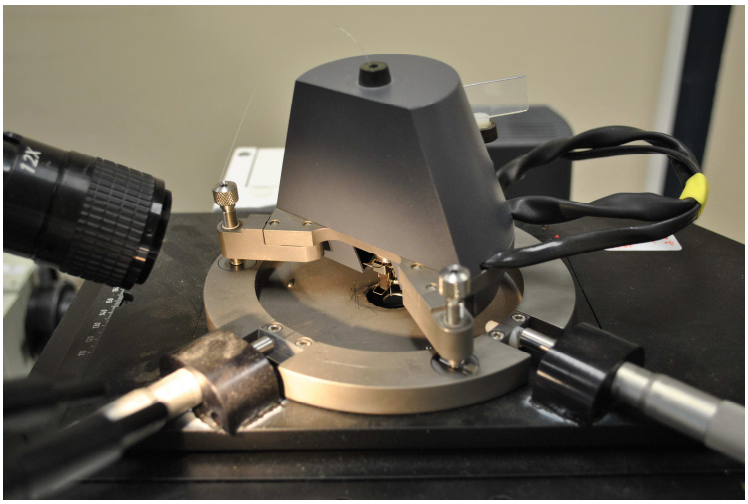

Figure 2.6: NT-MDT NSOM head placed on stand of optical microscope

The calibration of piezo-electronics system can be found in Annex A

- Collection of the optical signal

The optical signal in near-field is collected with an optical probe. These probes can be a tapered bare optical fiber, or a tapered metal-coated optical fiber or another optical probe as described in section 2.1.2. The interaction between the near-field signal and the probe (that has been brought very close to the surface) converts the evanescent fields into propagating fields which are guided into a monomode optical fiber towards the detection system.

c. Optical detection system

The optical signal transmitted by the monomode fiber was directed into a diffraction grating monochromator (Jobin Yvon micro-HR, Figure 2.7) with micro-slits that allows to analyze spectra with spectral resolution up to 0.6nm. A longpass filter with cutoff frequency at 1100 nm is used at the entrance of the monochromator to filter out the excitation laser and ambience light. The monochromator is equipped with an InGaAs thermoelectrically cooled detector. A lock-in detection allows to improve the signal to noise ratio. The modulation frequency is limited by the detector response time. This has an impact on the scanning frequency of the tip and a trade-off has to be done between the detector sensitivity and the scanning speed. 2kHz is a good compromise[2] as it allows a scanning rate of 0.2Hz with a detector sensitivity of 36%.

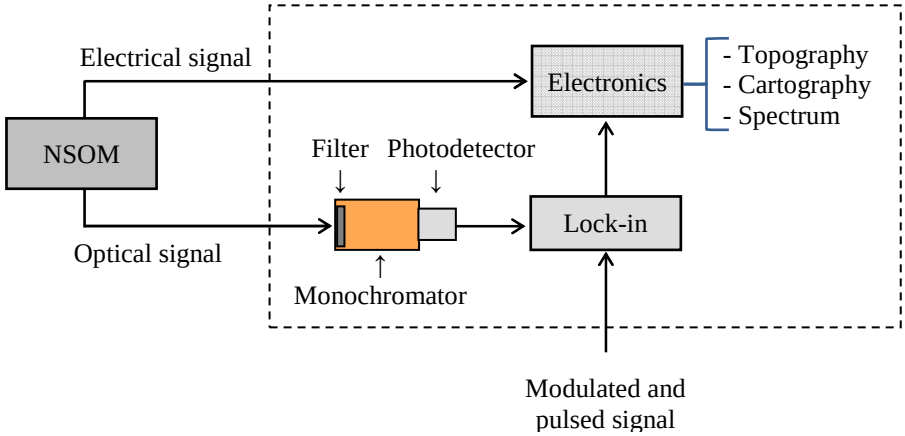

Figure 2.7: Detection system consists of monochromator (filter, optical components and photodetector), lock-in amplifier, electronics devices (computers, oscilloscope), infra-red CCD camera and spectral analyzer can be implemented for future development.

Note that our set up allows also the detection of the far-field signal emitted by the sample. The infra-red light emitted by the structure can be collected from the back side of the sample by the objective that has been used for the excitation. The IR light is then sent back to another microscope output ports equipped with an IR-camera. It is then possible to obtain the image of the radiating light at the surface of the sample.

For calibration procedure of monochromator, see Annex B.

2.1.2. Near-field probes

In near-field optical microscope the spatial resolution of the distributed evanescent field depends at first order on the probe diameter. Therefore the probe has to be small enough, comparable to the size of objects at least, for resolving the nanometric-scale structure of sample. Several properties of such probes are looked forward, for instance for aperture tip, a high brightness, a well-defined circular aperture and a high optical damage threshold[3,4]. To meet these specifications, the fabrication of the probe is a very important. In our experiments, three types of probe have been used: homemade dielectric probe (or silica probe), commercial metallized probe (Al-coating) and bowtie aperture nano-antenna probe (BNA-probe) which has been developed in the framework of the NanoEC program.

a. Silica probes

Generally these kinds of probe are made of optical silica fibers. Some methods have been developed to obtain the good taped probe. One of the most popular approaches is chemical etching (Tuner's method) using hydrofluoric acid HF[5,6]. Our selected fabrication process is quite simple to implement, economic and reproducible. The optical glass fiber selected is F-SMF-28 which supports well telecommunication wavelength at 1550nm. SMF-28 is a single mode fiber with diameter of core/cladding/coating of 9/125/250μm respectively. First, the outer protective polymer layer of a single mode fiber is stripped out, cleaved and dipped into HF (40%) solution at 30^0C during 45 minutes in a Teflon vessel. An organic overlayer (iso-octane) was put on the surface of the solution to protect the fiber mounts from the corrosive HF vapor. Up to eight probes could be fabricated in each batch of fabrication. The mechanism of tapered silica probe formation is due to decreasing meniscus height between hydrofluoric acid and organic over-layer as the fiber diameter is reduced by the etchant[6]. Variation of organic solvent influences the

resulting tip geometry. Although Tuner's method provides higher optical throughput due to larger conical angles (typically 30°), small diameter (around 200nm) it leaves several critical problems due to the sensitivity of the tip shape to environmental impacts such as vibrations, temperature drift during etching process, resulting considerable roughness. This roughness and asymmetry of tapered tip are generally responsible for pinholes in the subsequent aluminum coating and ill-defined optical apertures respectively[7].

In order to improve the probe quality, we attempt to use tube etching method which was proposed elsewhere[8]. According to these reports, instead of stripping out the protective polymer layer of silica fiber before etching as Tuner's method, it is cleaved and flattened. Finally the prepared silica fiber end is dipped into the appropriate solution. Consequently, the whole etching process performed inside a hollow cylinder formed by the fiber's protective polymer coating that withstands degradation by HF.

The solution is mentioned as a mixture of NH_4F, HF and H_2O with strict ratio in volume, here is 5:1:1. For instance, to obtain 35ml of solution, an amount of 25ml NH_4F, 5ml HF 40% (Fluka) and 5ml distillated water is needed and could be used to etch a batch of eight cleaved optical fibers. An organic overlayer iso-octane is used to protect the fiber mounts from the corrosive HF vapor and has no influence on the tip formation process itself. The etching temperature of 30±0.1°C was controlled by a thermostat. The etching process takes place for 15 hours under given conditions. After etching, since chemical salt $(NH_4)_2SiF_6$ is attached to the tip end, it should be rinsed by NaOH solution and then by distillated water for 5 minutes.

With respect to Tuner's method, tips fabricated by tube etching have much larger conical angle (44.30 vs. 28.80) and shorter tip length (120µm vs. 205µm) as shown in Figure 2.8. However, it is disadvantageous since the long duration of fabrication (15hours vs. 45 minutes).

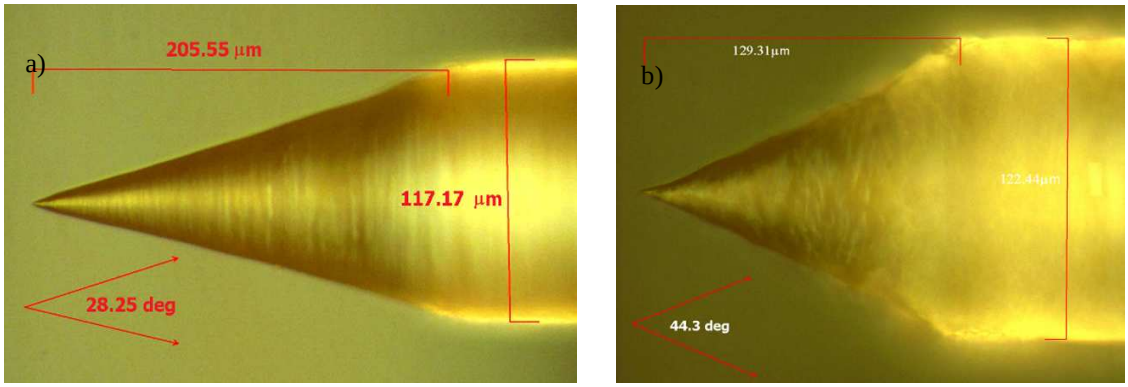

Figure 2.8: Images of near-field tapped probe (by conventional optical microscope) fabricated by chemical etching approaches with two different methods. (a) Tuner's method provides probe with 28° conical angle, 205µm length and 200nm diameter (probe apex). (b) Tube etching method provides probe with 44° conical angle, 130µm length and around 200nm diameter (probe apex).

b. Metal-coated probe

The fabrication of commercial Al-coating circular probe is conducted by Lovalite SAS. The principle of manufacturing process is reported elsewhere[9,10,11,12]. Below describes in brief of practical fabrication process of polymer probe and Al-coating polymer probe for infra-red working condition based on single mode optical fiber.

b.1 Polymer probe fabrication process:

The optical glass fiber selected is also a SMF-28 model. The fiber was first cleaved well and deposited a small drop of photosensitive polymer as indicated in Figure 2.9-a. The laser He-Ne at 532nm was illuminated the drop of polymer and ignite photo-polymerization process through the core of fiber (Figure 2.9-b). The chemical reactions occur during 1second with optical power between 0.2µW to 1µW. Finally, the fiber was rinsed in solvent of methanol or isopropanol to remove the soluble polymer of unexposed area and left the resulting probe (Figure 2.9-c). In order to make the polymer probe more solid, the fiber might be put in the thermo device at 90°C during 12h.

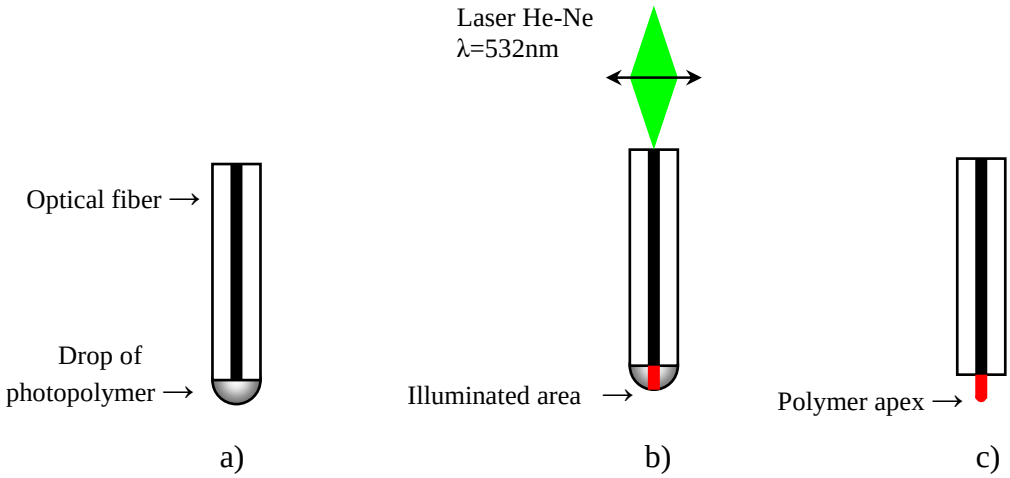

Figure 2.9: Diagram illustrated the manufacturing process of near-field polymer probe by Lovalite. (a) Depositing a drop of liquid photopolymer at the cleaved end of optical fiber. (b) Exposing to laser 532 nm for polymerization process. (c) Resulting probe after rinsing in methanol or an isopropanol solvent.

The obtained polymer probe is of course well aligned at the core and could guide the light to the extremity of fiber. The probe geometry can be adjusted by variation of basic parameters such as the geometry of the deposited drop and the condition of the drop illumination[5]. Typical dimensions of polymer probe obtained with single mode fiber and above-mentioned conditions are 30µm long and 500nm to 1µm of curvature radius. Figure 2.10-a indicates the SEM images of a typical polymer probe.

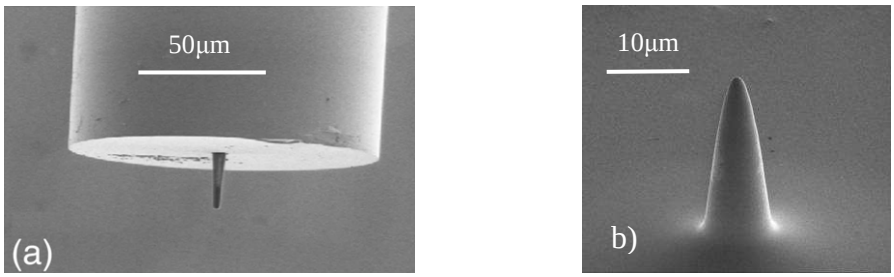

Figure 2.10: SEM images of polymer probe. (a) polymer probe emerges from the core of cleaved monomode optical fiber. (b) Probe metallized by 5nm thickness of Ti and 100nm of Aluminum.

b.2 Al-coating circular polymer probe

The spatial resolution of NSOM optical images is largely governed by the light-transmitting aperture defined at the probe apex by the metallic coating[13]. As the diameter

of an uncoated fiber in the tapered region is reduced beyond the mode-field cutoff of the fiber waveguide, light escapes from the sides of the probe, compromising the characteristics of a well-defined aperture. Thus, a critical parameter in most NSOM probe fabrication procedures is the application of an opaque metal coating to reduce light loss through the tapered region of the fiber, and to confine its emission to the desired aperture. For the visible region of the electromagnetic spectrum, aluminum has the smallest skin depth and thus, in theory, should allow for the minimum effective coating thickness on the probe sides. Moreover, in the infra-red working region Aluminum material has the high conductivity leading to high antenna effect.

In practice, the performance of deposited aluminum coatings is compromised by the tendency of the metal to form grains, and thicker coatings (would be predicted from the theoretical skin depth) are required to prevent light leakage. To compensate for the leakage resulting from granularity, a coating thickness of 100 nanometers with evaporation velocity less than 5nm/s and 10nm/s is usually applied around the taper region of the probe. In case of polymer probe, to improve the gluing of metal on polymer layer and the rigidity of tapered probe under strong illumination, the 5nm-layer of titanium is first deposited. The Al-coating process is conducted in the vacuum chamber of evaporation device (EVA 450) and fiber is rotated to obtain homogeneous thickness. The resulting metal-coating probe (see Figure 2.10-b) fabricated by this procedure obtained transmission coefficient[14] approximate of 10^{-4}-10^{-5}

c. BNA probe

The fabrication of bow-tie nano-aperture (BNA) was the heart of the NanoEc program. Their conception and their development had been performed by Dr. Thierry Grosjean [15] in FEMTO-ST at Besançon, in collaboration with Dusan Nedeljkovic of Lovalite. The BNA can be fabricated at the extremity of a metallized polymer probe as above-described. The operation was performed by FIB (Focused ion beam) method[16]. By selecting the optimal working parameters (current beam equal 9pA and dwelltime equal 100s), the BNA was opened on the polymer metal coating probe as indicated in Figure 2.11. Real dimensions of BNA are in agreement with the designed dimensions: 220nm length, 220nm width, 45nm gap width and 100nm metal thickness.

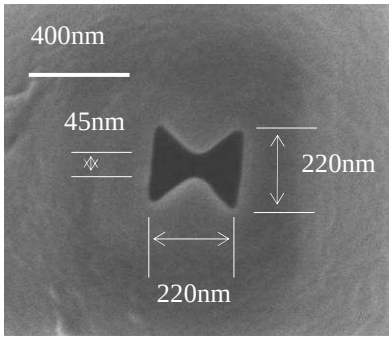

Figure 2.11: Top view SEM image of a bowtie nano-aperture antenna (BNA) on the extremity of metal-coating polymer probe fabricated by FIB.

2.2. Characterization of BNA optical properties.

The far-field measurements of BNA optical properties were performed by Dr. Thierry Grosjean and co-workers at the FEMTO group. The BNA was excited at the resonant wavelength λ=1.55μm in either emission or collection mode to investigate the electric field enhancement and polarization sensitivity properties.

2.2.1. The BNA in emission mode

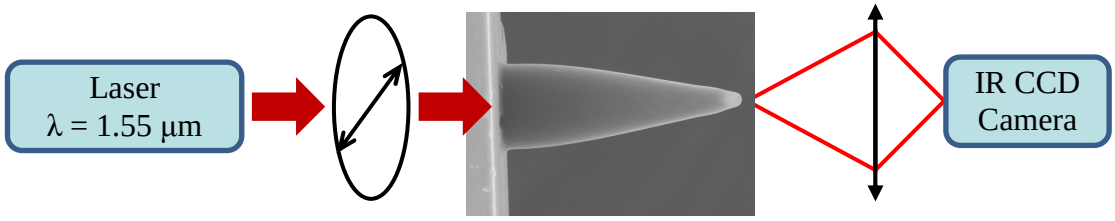

Figure 2.12: Sketch of experimental set-up to observe the transmitted light through BNA in emission mode. A rotating polarizer was employed to select the polarization direction of incident light.

The electric field enhancement at the gap zone and polarization sensitivity of BNA as theoretical prediction in section 1.3 might be qualitatively tested by observing the transmitted light through BNA in emission mode. As shown in the Figure 2.12, BNA-fiber probe was illuminated by a 100μW laser beam at λ=1.55μm polarized in direction either parallel or perpendicular to the BNA gap edge. An IR camera placed after an objective x100/0.9NA was to image the diffracted light on BNA surface. Owing to the strongly limit background excitation fields of BNA, the antenna effect can be unveiled with this imaging

set-up. Figures 2.13-a/b indicate explicitly the differences of far-field intensity emitted from BNA in two orthogonal directions of polarized excitation laser. The bright spot was solely observed (at white arrows) for the excitation light polarized along gap edge, implied that its transmitted light was high. On contrary, the trace of light was seen at the same position if rotation of 90^0. For comparison, these experimental results absolutely agree with the corresponding simulations shown in Figure 2.13-c/d. This demonstrates the expected dipolar antenna effect on these BNAs[17].

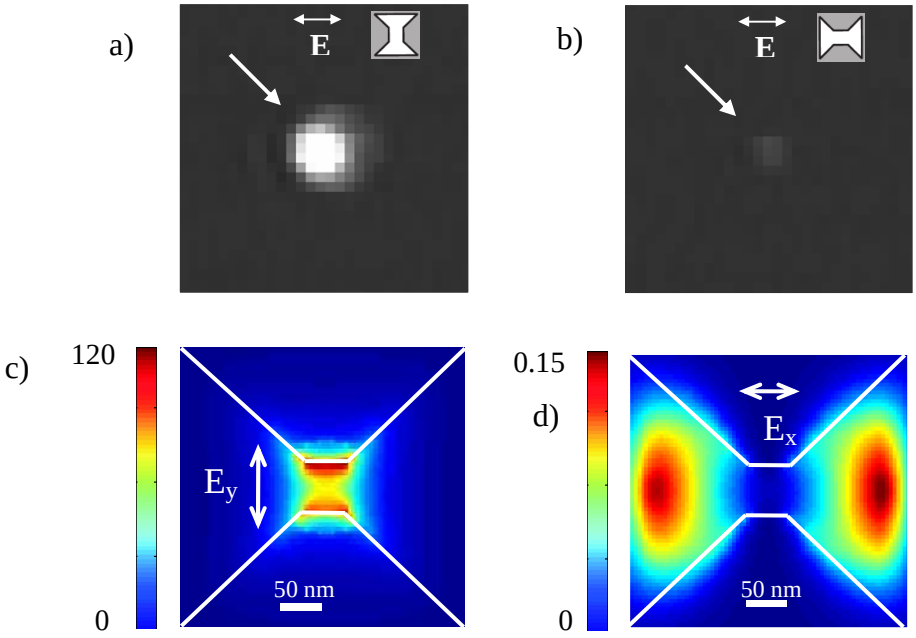

Figure 2.13: a-b) Transmitted light through BNA-probe observing by IR camera with incident light linearly polarized either in parallel (a) and perpendicular (b) direction (see insets). c-d) two corresponding optical images by FDTD-simulation.

2.2.2. The BNA in collection mode

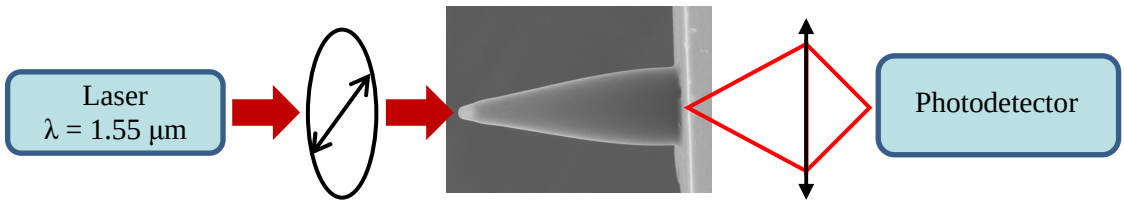

Figure 2.14: Sketch of experimental set-up to mapping the polarization diagram of BNA in collection mode. A rotating polarizer was employed to select the polarization direction of incident light.

This set-up was built to investigate the coupling intensity through BNA as a function of polarization of incident light. This polarization diagram is important to estimate the polarization ratio between E_x^2 and E_y^2-components. Figure 2.14 is present the experimental setup in which BNA works in collection mode and was illuminated by infra-red laser at resonant wavelength 1.55µm. The polarization diagram is constructed by measuring the collected intensity (normalized to the incident light) by aperture antenna while rotating the polarization of incident light. A half-wave plate was used to rotate the linear polarization light 360^0 by step of 10^0. In addition, synchronous detection technique could be used to increase the signal-to-noise of measurement.

Figure 2.15 shows the experimental polarization diagram of the BNA (solid blue line) with respect to fluorescence diagram of a single molecules[17,18] (dashed red line). The agreement between the two curves confirms that the electric dipole moment polarized along the gap edge (horizontal axis in diagram) governs the coupling resonance in the gap of BNA-probe. The polarization ratio (seen as polarization sensitivity) between the two orthogonal components was estimated to be about 1:31 in comparison with the theoretical ratio of 1:37 for plane wave excitation. For a dipole excitation, the theoretical polarization ratio could reach 1:170[17].

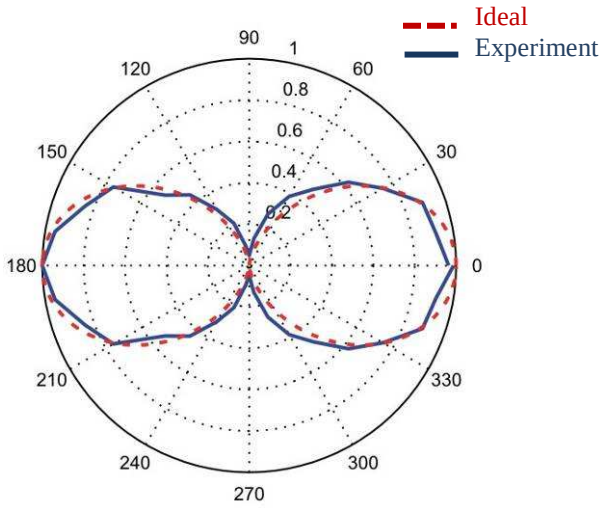

Figure 2.15: Polarization diagram of BNA-tip in collection mode illuminated at resonance wavelength 1.55µm. The dashed red line presents the fluorescence diagram of an ideal nanopolarizer of a single molecule (dipole absorption moment). The blue solid line indicates the experimental optical intensity measured at free end facet of fiber. The collected optical intensity is normalized to the incident light. Experimental polarization

sensitivity (between two orthogonal components) estimated 1:32 with respect to 1:37 in theoretical prediction in case of plane wave excitation.

2.3. Far-field micro-photoluminescence characterization set-up

Far-field characterization yields spectral information of photoluminescence radiating from sample. This far-field set-up enables quick and global analyses of the optical responses of the fabricated structure. It is normally used as a preliminary study prior to NSOM measurements.

To perform these analyses we use a far-field set-up with spectrometer (Figure 2.16). The sample was optically pumped by a pulsed laser diode (805nm, duration of 10ns and duty cycle of 10%) through an IR-corrected Mitutoyo long-working distance objective (x20) at normal incidence. The photoluminescence emitted from the sample was collected by the same objective and directed towards an infra-red spectrometer through optical fiber after passing a 1100nm-long pass filter. A dichroic mirror placed in the optical path enabled to partially reflect the emitted light to an infra-red camera for in-line observation.

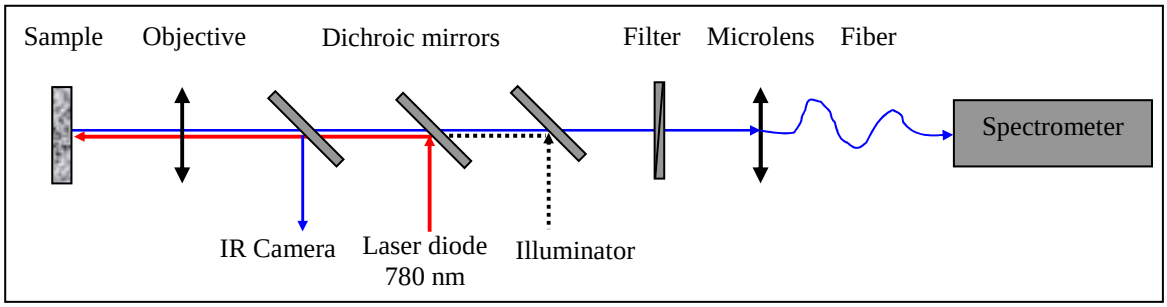

Figure 2.16: Photoluminescence set-up for far-field characterization. Laser diode (red line) at 780nm was pulsed with duration of 10ns and duty cycle equal 10%. An objective was used to excite the quantum well of sample and collect the reflected light (blue line). The radiation light was then directed to spectrometer through fiber for spectral analysis.

2.4. FDTD simulation

The simulation of propagation of light wave in arbitrary geometries can be performed with finite-difference time-domain (FDTD) algorithm. Since the FDTD method is a direct resolution of the Maxwell's curl equations, it therefore includes many effects than other approximation methods.

2.4.1. Principle

All of macroscopic electromagnetism, including the propagation of light in a photonic crystal is governed by macroscopic Maxwell equations[19]. In the mixed dielectric medium composing a region of homogeneous dielectric material, with no free charges or currents, the set of Maxwell's curl equations can be written in cgs units as following:

$$\nabla \cdot \mathrm{H}(\mathrm{r},\mathrm{t}) = 0 \qquad \nabla \times \mathrm{E}(\mathrm{r},\mathrm{t}) + \mu \frac{\partial \mathrm{H}(\mathrm{r},\mathrm{t})}{\partial \mathrm{t}} = 0$$

$$\nabla \cdot \varepsilon(\mathrm{r})\mathrm{E}(\mathrm{r},\mathrm{t}) = 0 \qquad \nabla \times \mathrm{H}(\mathrm{r},\mathrm{t}) - \varepsilon_0 \varepsilon(\mathrm{r}) \frac{\partial \mathrm{E}(\mathrm{r},\mathrm{t})}{\partial \mathrm{t}} = 0$$

where E and H are the macroscopic electric and magnetic fields respectively, ε and μ are relative permittivity and permeability, c is speed of light in vacuum.

Such equations describe a situation in which the temporal change (t) in the E-field is dependent on the spatial variation (r) of the H-field and vice versa. The FDTD method solves the Maxwell's equations by first discretizing the equations via central differences in time (Δt) and space (*Δx*, *Δy* and *Δz*) and then numerically solving these equations by software. The most common method to solve these equations is based on Yee's mesh[20].

In order to implement the FDTD algorithm, both physical and numerical parameters are required.

2.4.1.1 Physical parameters: consist of:

- Material parameters include relative permittivity ε(r,ω) and relative permeability μ(r,ω) as a function of space and frequency. These material properties can be specified by the following formulas:

$$D = \varepsilon_0 E + P$$

$$B = \mu_0 H + M$$

$$P = \varepsilon_0 \left[\chi(\omega) E + \chi^2 E^2 + \chi^3(\omega) \frac{I}{1 + c_{sat} I} |E|^2 E \right]$$

$$M = \varepsilon_0 \left[\chi_m(\omega) H + \chi_m^2 H^2 + \chi_m^3(\omega) \frac{I}{1 + d_{sat} I} |H|^2 H \right]$$

The four terms of equations describe several effects. The first term (ε_0E) presents the linear index of system while second term takes into account the change of

index as function of frequency. The remaining terms describe the non-linear effects of system.

- The electromagnetic field excitation is a dipole emitted around the specific given wavelength at certain spectral profile. The dipole can be oriented in all directions of space giving the polarization of interest. It composes of both spatial and temporal excitation in form $\phi_L(r,t) = \sqrt{P}\, f(r_0) g(r)$ where P is the power of excitation source, $f(r_0)$ is the spatial excitation at the launch plane and g(t) is temporal excitation. The input field is defined in several functions such as a Gaussian function, rectangular step function or multimode function.

2.4.1.2 Numerical parameters

The solution algorithm requires additional input in form of numerical simulation parameters as following:

- A finite computational domain: defines domain limits to be used during the simulation
- The boundary conditions. Several models can be employed; two of the most effective are perfectly matched layer[21] (PML) and periodic boundary conditions[22] (PBC). For the former, both electric and magnetic conductivities are introduced in such a way that the wave impedance remains constant, absorbing the energy without inducing reflections. Meanwhile the latter is employed such that the simulation is equivalent to an infinite structure composed of the basics computational domain repeated endless in all dimensions
- The spatial grid size (Δx, Δy and Δz), temporal grid (Δt) and the length of time for simulation. The spatial grid size must be small enough to resolve the smallest feature of the field to ensure an accuracy simulation. This can be described with respect to the wavelength in materials or geometry of photonic device. Typically, the grid spacing must be able to resolve the wavelength in time, usually less than $\lambda/10$ (in the materials).

  The temporal step size Δt must be satisfied the Courant condition to ensure a stable simulation:

$$c\Delta t < \left(\frac{1}{\Delta x^2} + \frac{1}{\Delta y^2} + \frac{1}{\Delta z^2} \right)^{-1/2}$$

where c is the velocity if light. The software will automatically enforce this condition.

2.4.2. Implementation

The simulation FDTD allows observing the evolution of electromagnetic (EM) field in time at every point of structure and issuing the cartographies (mode pattern) in certain conditions. The spatial and temporal evolution of EM field also reveals the spectral response of structure. To simulation, a dipole with impulse emission in temp is placed on surface, at the center of structure. The temporal development of different components of EM field is measured at different points of structure and by Fourier transform, frequency EM response is obtained. To obtain the spatial distribution of EM mode intensity, FDTD simulation has to be rerun with narrow spectral source where only mode is excited. At this step, quality factor of mode is calculated from the field evolution as function of time. In fact, the quality factor can be extracted from exponential decay of mode in time.

2.5. Fabrication protocols

The two dimensional photonic crystal (2D PC) structures under investigation are composed of an array of air holes fabricated on semiconductor InP slab bonded onto a glass substrate. In order to provide the optical gain material, four InAsP quantum well are embedded in the centre of the InP slab. They act as a source of photoluminescence with an emission spectrum from 1.3µm to 1.65µm. The fabrication processes consist of three main steps: epitaxial growth and layer transfer, lithography and etching.

2.5.1. Epitaxial growth and layer transfer

The basic heterostructure consists of the active membrane, including the quantum wells, grown over an InGaAs etch stop layer, on top of the InP wafer. This stack was grown by molecular beam expitaxy (MBE) at INL. The thickness of active InP slab was chosen to obtain a monomode waveguide at the wavelength of interest[23] (thickness of $\lambda/2n \approx 250$ nm at $\lambda=1500$ nm). The quantum wells InAsP inserted between InP layers by expitaxy.

After the expitaxial growth, a 10nm thick SiO_2 layer is deposited by Plasma Enhanced Chemical Vapour Deposition (PECVD) assisted by Electron Cyclotron Resonance (ECR), this thin layer enables the wafer bonding of the active layers on top of a fused silica host wafer. This step was performed at CEA-LETI. The InP wafer and the etch-stop layer were subsequently removed by wet chemical etching at INL. Finally, a hard mask SiO_2 (90nm thick) is deposited on the top of the active InP slab, to act as a hard mask during etching process.

2.5.2. Electron beam lithography (EBL)

This process enables to pattern nanostructures in an electron sensitive resist[24]. Polymethylmetacrylate (PMMA) was selected as a positive resist, which will therefore become soluble after the electron exposure. The thin film of PMMA is deposited on sample surface by spin coating method and baked in the thermostat at 180° for 90s. With an EBL process, the size and shape of PC holes depend on several key process parameters:

- The electron beam size, which is typically about 10nm, and intensity, around 40pA. The beam focus and astigmatism correction are crucial to obtain a good fidelity in terms of size and shape of PC holes.
- The electron dose (in $\mu C/cm^2$): the size and shape of holes is strongly depends on the dose which is varied in a limited range. If the dose is too weak, it has a fluctuation or no impact on chemical bond of electron resist and thus, patterns are not printed in the PMMA layer. Otherwise, if the dose is too high, more backscattering electrons in the resist make the holes connect each others, and their shape irregular.
- Thickness of hard mask SiO_2 layer where the backscattering phenomenon occurs and the energy of electron beam contribute strongly to the modification of the shape of air holes.

After exposing by electron beam, PMMA resist becomes soluble. The soluble area will be removed by developing in solution NANO MIBK/IPA 1:1. The resulting sample containing structures on PMMA layer is finally post-baked at 100°C for 1mn and ready for the etching step.

2.5.3. Reactive ion etching (RIE)

This step is to transfer the structures on PMMA layer into InP membrane. The RIE technique[25] is designed to give better control of selectivity and anisotropy independently and conducted in the vacuum plasma chamber. The sample is placed in the plasma chamber. The different gas with different conditions is used to create plasma corresponding to purpose of each etching step as listed in table. The details of etching process are shown in Figure 2.17. Table below lists the used gases and working conditions of machine. The SiO_2 layer is first patterned, using the PMMA patterns as a mask, then the InP layer is etched using SiO2 patterns as a hard mask. This two-step process is necessary since the etching selectivity between PMMA and InP is too low.

The advantages of RIE method is its high anisotropy, thanks to sidewall polymerization; selective but less so than plasma etching due higher DC bias and longer mean free path. However some unintentional deposition of the polymerization gas can result in defects if conditions are not optimized.

Table: working conditions for RIE process

Step	Gas	Flow (sccm)	Pressure (mTorr)	P_{RF}(W)	Time (s)
Etching SiO_2	CHF_3	16	15	100	600
Removing PMMA	O_2	20	100	100	120
Etching InP	CH_4	15	30	200	300
	H_2	30			
Removing C	O_2	20	100	100	120
Removing SiO_2	CHF_3	16	15	100	600

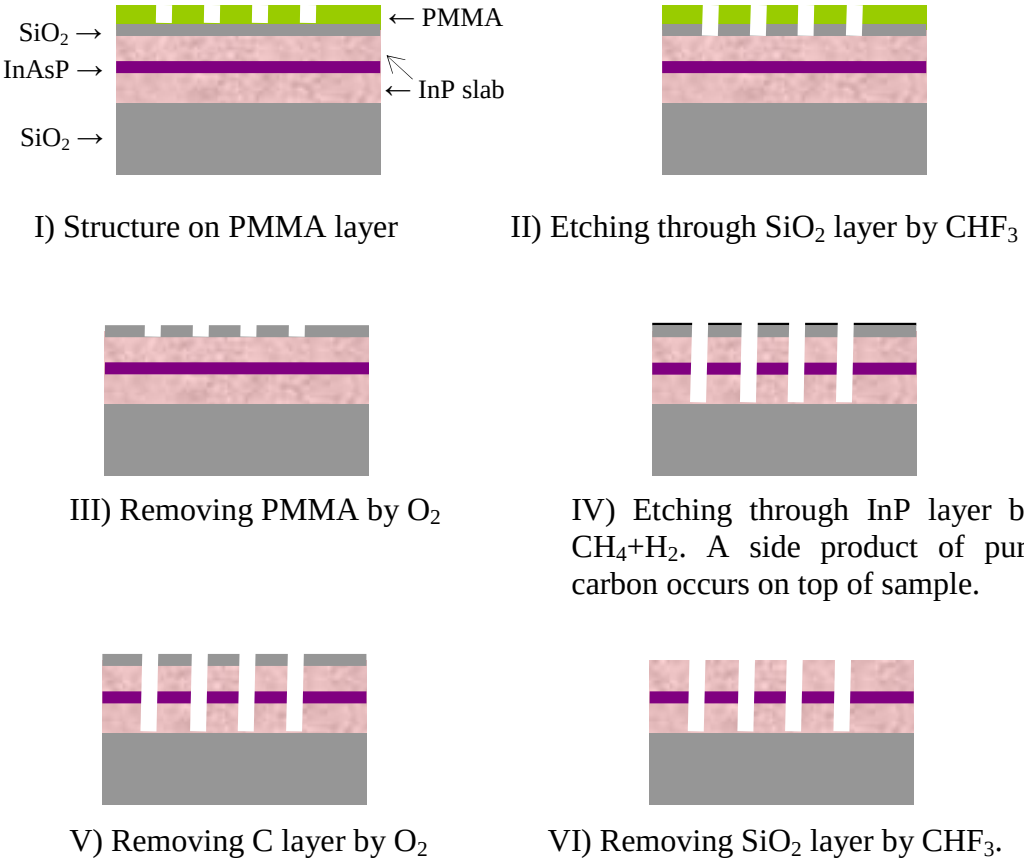

Figure 2.17. Diagram of etching steps to transfer designed structures into InP slab.

Conclusion

We have introduced the main experimental facilities that involved in our research works as well as the FDTD-based numerical simulation principle. First the nanophotonic structures were simulated using FDTD method to obtain the optimal working parameters, then fabricated by EBL and RIE methods. The far-field characterization was first employed to verify the expected optical properties before conducting near-field investigation by NSOM in transmission mode. Several kinds of near-field probes were fabricated for different NSOM purposes such as dielectric, metal-coating or bowtie nano-aperture probes.

References

[1] Nicolas LOUVION, "Microscopie en champ proche optique de structures à base de cristaux photoniques", doctoral dissertation, INL, CNRS UMR 5270 (2005)

[2] Gaëlle LE GAC, "Etude de l'impact d'une pointe SNOM sur les propriétés des modes optiques d'une cavité à base de cristaux photoniques", doctoral dissertation, INL, CNRS UMR 5270 (2009)

[3] Bert Hecht et al, "Scanning near-field optical microscopy with aperture probes: Fundamentals and applications", The Journal of Chemical Physics, Vol. 112, No. 18, pp. 7761–7774 (2000)

[4] J.A. Veerman, A.M. Otter, L. Kuipers, and N.F. van Hulst, "High definition aperture probes for near-field optical microscopy fabricated by focused ion beam milling," Appl. Phys. Lett. 72, 3115 (1998).

[5] D. Turner, US Patent 4,469,554 (1984)

[6] P. Lambelet, A. Sayah, M. Pfeffer, C. Philipona, and F. Marquis-Weible, Appl. Opt. 37, 7289 (1998)

[7] Stockle et al., » High-quality near-field optical probes by tube etching » Appl. Phys. Lett., Vol. 75, No. 2, (1999).

[8] T.Pangaribuan et al., « Reproducible fabrication technique of nanometric tip diameter fiber probe for photon scanning tunneling microscope «, Jpn. J. Appl. Phys.31 (1992).

[9] Renaud Bachelot, Carole Ecoffet, Denis Deloeil, Pascal Royer, and Daniel-Joseph Lougnot, "Integration of Micrometer-Sized Polymer Elements at the End of Optical Fibers by Free-Radical Photopolymerization," Appl. Opt. **40**, 5860-5871 (2001)

[10] Renaud Bachelot, Abdesslame Fares, Radouane Fikri, Dominique Barchiesi, Gilles Lerondel, and Pascal Royer, "Coupling semiconductor lasers into single-mode optical fibers by use of tips grown by photopolymerization," Opt. Lett. **29**, 1971-1973 (2004)

[11] M. Hocine, R. Bachelot, C. Ecoffet, N. Fressengeas, P. Royer and G. Kugel, "End of the fiber polymer tip: manufacturing and modeling", Synthetic Metals, Volume 127, Issues 1-3, 26 March 2002, Pages 313-318.

[12] P. D. Bear, "Microlenses for coupling single-mode fibers to single-mode thin-film waveguides," Appl. Opt. **19**, 2906-2909 (1980).

[13] Bert Hecht et al, "Scanning near-field optical microscopy with aperture probes: Fundamentals and applications", The Journal of Chemical Physics, Vol. 112, No. 18, pp. 7761–7774 (2000)

[14] M. Notomi, "Manipulating light with strongly modulated photonic crystals," Rep. Prog. Phys. 73 (2010) 096501 (57pp)

[15] Grosjean, T.; Ibrahim, I. A.; Suarez, M. A.; Burr, G. W.; Mivelle, M.; Charraut, D. Optics Express 2010, 18, 5809–5824.

[16] Koch, J.; Grun, K.; Ruff, M.; Wernhardt, R.; Wieck, A.D.,"Creation of nanoelectronic devices by focused ion beam implantation", (1999)

[17] M. Mivelle, I. A. Ibrahim, F. Baida, G. W. Burr, D. Nedeljkovic, D. Charraut, J-Y. Rauch, R. Salut, and T. Grosjean, "Bowtie nano-aperture as interface between near-fields and a single-mode fiber," Opt. Express **18**, 15964-15974 (2010)

[18] L. Novotny, M. Beversluis, K. Youngworth, and T. Brown, "Longitudinal field modes probed by single molecules," Phys. Rev. Lett. 86(23), 5251 (2001)

[19] James Clerk Maxwell, "A Dynamical Theory of the Electromagnetic Field", Philosophical Transactions of the Royal Society of London **155**, 459-512 (1865)

[20] *K.S Yee, "Numerical solution of initial boundary value problems in involving Maxwell's equations in isotropic media" IEEE Trans. Antennas propagate., AP-14, 302 (1966)*

[21] *J. Berenger (1994). "A perfectly matched layer for the absorption of electromagnetic waves". Journal of Computational Physics 114 (2): 185–200*

[22] *Schlick T. (2002). Molecular Modeling and Simulation: An Interdisciplinary Guide. Interdisciplinary Applied Mathematics series, vol. 21. Springer: New York, NY, USA. ISBN 0-387-95404-X*

[23] *N. Chauvin, P. Nedel, C. Seassal, B. Ben Bakir, X. Letartre, M. Gendry, A. Fiore, and P. Viktorovitch," Control of the spontaneous emission from a single quantum dash using a slow-light mode in a two-dimensional photonic crystal on a Bragg reflector" Phys. Rev. B 80, 045315 (2009).*

[24] *L. Feldman and J. Mayer. "Fundamentals of Surface and Thin Film Analysis", 54. pp. 130–133. ISBN 0-444-00989-2.(1986)*

[25] *Coburn, J.: Plasma Etching and RIE: Fundamentals and Applications.*

Chapter 3: Theoretical and far-field SBM optical properties

This chapter deals with the far-field optical properties of lowest energy slow Bloch modes of honeycomb 2D photonic crystals. Prior to characterization, FDTD simulations were performed to predict the theoretical behaviors of the modes in terms of spectral characteristic and mode distribution inside the PC. Far-field characterizations that reveal the global spectral properties as well as the polarization characteristic of SBMs are also presented.

3.1. Introduction

As was explained in chapter 1, a honeycomb PC structures, consisting of air holes centered at the vertices of periodically arranged hexagons[1,2] were chosen because of their ability to support slow Bloch modes (SBMs) at the Γ-point of the band Brillouin zone. As shown in Figure 3.1, this type of PC structure does not have a photonic band gap neither in TM nor TE mode. However, near high symmetry points of the first Brillouin zone, they can support modes with both a very low group velocity and a very flat band curvature[3]. In the case of our structure, this occurs at the Γ-point where the k-vector is purely perpendicular to the membrane. This feature is expected to correspond to an enhancement of the local density of optical states (LDOS), which is in theory[4] inversely proportional to the band curvature α (section 1.1). This gives rise to delocalized stationary SBMs. At the Γ-point these modes are above light line and should couple easily with the continuum of radiating free space modes. These properties have lead to a new generation of vertical emitting microlaser[2] in which optical gain is provided by III-V materials. In addition to the vertical emission ability, SBMs have shown to possess the peculiar polarization properties. Furthermore, compared to the triangular or square lattice structures, the air filling factor of a graphite PC is smaller. As a result, in an active structure, a majority of emitters such as quantum dots, would be far from the interfaces created by the PC holes, which would tend to reduce the effect of non-radiative surface recombination[5]. Various application perspectives could be exploited from these optical properties, for instance to design low threshold laser[6], integrated optoelectronic devices or optical tweezers for nanoparticles[7,8,9].

In chapter 1, we showed that one of the important properties of 2D-PC slow Bloch modes is their expansion in the PC. In theory, the mode expansion is determined by the band curvature α (which is intrinsic to the 2D PC design) and the lifetime of the considered mode τ in the structure[4,10]. The lifetime depends on the lateral losses, the out of plane escape of the photons and the modal mismatch which can occur between the SBM and the continuum of the radiated modes. In the case of an active PC, like a microlaser this phenomenon can also be influenced by other mechanisms such as carrier-induced refractive-index change[1]. While 3D FDTD numerical simulation with dipole excitation placed at the center of structure predicts that mode expansion is limited by the 2D PC

boundary, the experimental results show that the lateral confinement of the mode is of the order of the excitation spot size.

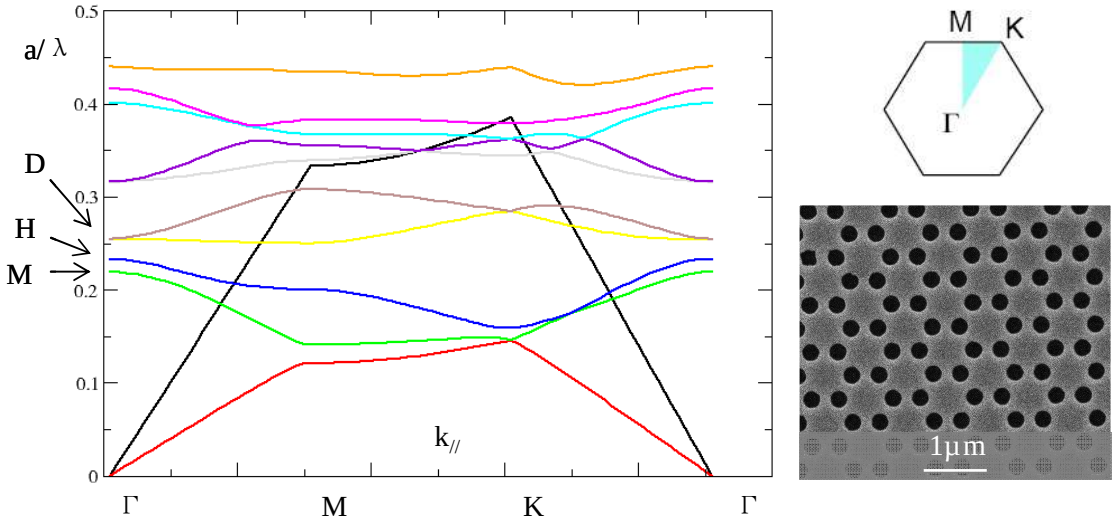

Figure 3.1. Band diagram of a defect-free honeycomb planar photonic crystal calculated using 3D plane wave expansion method by Adel Rahmani. Lattice a= 730nm and air filling factor 20% on 240nm-thick InP slab (n=3.17 at λ=1.55µm). The lowest energy band-edge mode (mode M) could be seen at Γ-point among several higher modes. The upper right image presents high-symmetry points of unit cell in reciprocal space and SEM image of a fabricated honeycomb PC (bottom right).

3.2. Structure design

In our case, active 2D-PCs were designed to support band-edge modes at the Γ-point of the first Brillouin zone[1,2]. The structure consisted of a 240nm-thick monomode slad InP (n=3.17 at λ=1.55µm) bonded on SiO_2 transparent substrate. At the center of the InP slab, four quantum wells of InAsP separated by InP barriers (see Figure 3.2-c) were embedded to provide internal photoluminescence from 1.3µm to 1.65µm. An array of honeycomb-like cylindrical air holes (ε=1) was drilled on InP slab (Figure 3.2-a/b) to provide the periodical dielectric structure with a high contrast of refractive index. The two basic parameters of the honeycomb PC are the lattice parameter a (center-to-center distance of two nearest hexagons) and the hole radius (r). The surface air filling factor was calculated from the following formula:

$$ff = \frac{4\pi}{\sqrt{3}}\left(\frac{r}{a}\right)^2$$

In order to optimize the lattice parameters and study the impact of structure size with respect to mode expansion, several structures with different sizes and different filling factor (depending on the hole radius) have been designed.

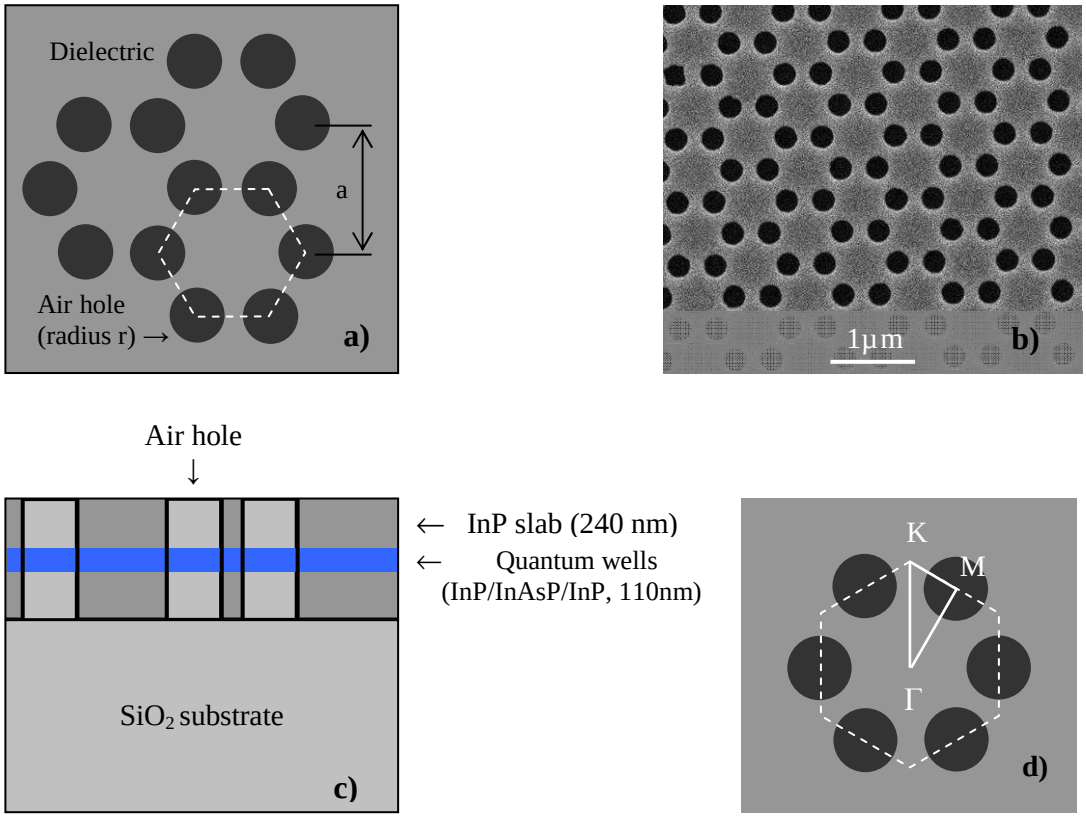

Figure 3.2: Model of defect–free honeycomb 2D PC. a) (Top view). An array of cylinder air holes (white circles, ε=1) centered at the vertex of periodically arranged hexagons on InP slab (grey area, ε=10 at λ=1.55μm). b) (Top view) SEM image of a typical 2D-PC fabricated by E-beam lithography (EBM) and reactive ion etching (RIE) method. Real lattice parameters measured A=730nm, 2r=245nm, then corresponding ff_{air}=0.2 (dose equal 1.6). c) (Side view). Sample includes 240 nm thick InP slab bonded on top of a SiO_2 transparent substrate with four layers of InAsP quantum wells (separated by InP barrier) are embedded at the center of the InP slab. d) The first Brillouin zone with high-symmetry points (Γ-K-M) in the reciprocal space with respect to the real space unit cell.

3.3. Γ-point modes in the honeycomb lattice

Finite-difference time domain (FDTD) method provides in theory the optical properties of the designed PC. Simulation results yield the electromagnetic field distribution in the structures and are used to find the optimal parameters as well as the

optical response of the designed structures. In our case, the FDTD simulation is employed both in 2D (treating the vertical dimension of the PC as infinite) and in 3D (three finite dimensions of PC). Below are presented the simulation results in 2D- and 3D-FDTD.

3.3.1. Monopolar, hexapolar and dipolar modes: 2D calculations

For the sake of computation time, 2D-FDTD was first used to investigate the spectral response of honeycomb crystals. The main consequence is that the resonant wavelengths of the modes can be shifted compared to the real case or the 3D case. However, the 2D intensity pattern found for a mode remains quite similar to the 3D mode intensity pattern that can be found in the middle of the membrane. Conversely, it cannot reveal the real pattern at the surface of the 2D-PC, or its evolution with the z-component.

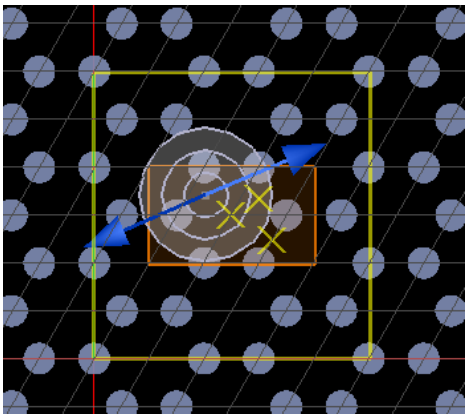

Figure 3.3: 2D-FDTD simulation layout performed for honeycomb PC. The white circles in hexagonal lattice indicate the air holes of PC in InP slab (n=3.17). The arrow shows the orientation of impulsed dipole in TE while the yellow crosses present the position of placing detectors. The structure parameters: lattice size A of 775nm, air hole radius of 130nm. Thus, calculated filling factor and effective index are of 20% and 2.7 respectively.

The simulation was run on FDTD-coded Lumerical software by Dr. Ali Belarouci at INL. For honeycomb PC, the following typical parameters are used: a lattice parameter a=730nm, an air hole radius 2r=245nm, and consequently an air-filling factor of 20%. As shown in Figure 3.3, a pulsed dipole in TE mode, which spectrum covers all possible modes, is placed around the center of PC structure in arbitrary orientation to make sure that it can excite all the possible modes. The arrow in blue indicates the dipole orientation

with respect to the PC structure. Three cross in yellow are the positions of the monitoring detectors.

The optical field was calculated as a function of time in different locations inside the structure. In order to obtain the spectral response of the structure, a Fourier transform of the time-dependent signal was performed.

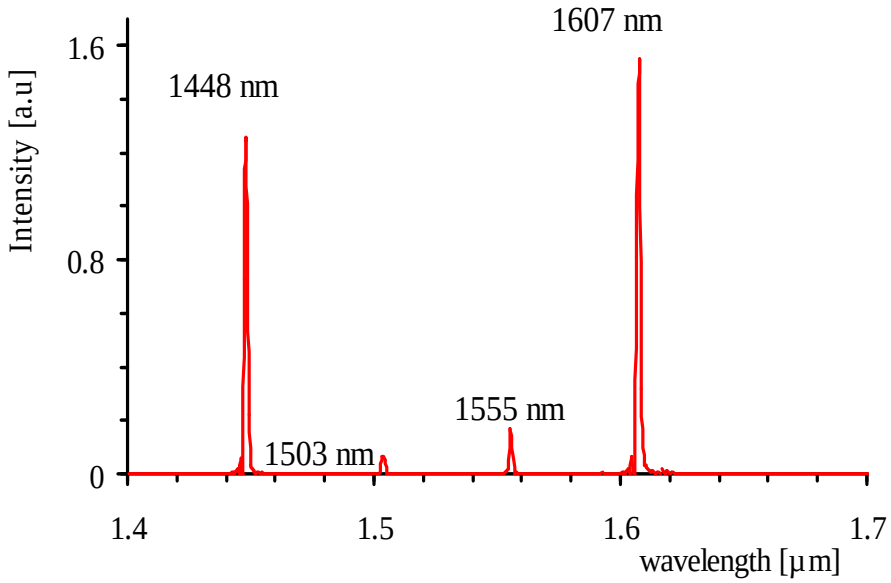

Figure 3.4: Resonant spectral of honeycomb PC (A=730nm and 2r=245nm) computed in 2D-FDTD by a TE dipole excitation.

The frequency spectrum in Figure 3.4 provides various resonant peaks with different quality factors. The longest wavelength is labeled monopolar or mode M at λ=1607 nm. This mode corresponds to the lowest-energy non-degenerated mode at Γ-point shown in dispersion band diagram of Figure 3.1. The second resonant peak at shorter-wavelength in resonant spectrum is named hexapolar or mode H at λ=1555 nm. The difference of resonant wavelength between two modes (Δλ=52nm) confirms the position of non-degenerated mode H at Γ-point as shown in Figure 3.1. The third resonant peak at λ=1448 nm corresponding to the dipolar or mode D. This is a degenerated mode at Γ-point in dispersion band-diagram in Figure 3.1. Below are the details of mode patterns obtained with 2D-FDTD simulation at three above-mentioned resonant peaks.

a. Monopolar mode

It is the fundamental and non-degenerated mode at high symmetric Γ-point of reciprocal space of the honeycomb PC. This slow mode may be predicted to present a high quality factor since laying at the low band curvature and zero in-plane k-vector point. Moreover, due to its symmetry properties, this mode does not couple easily to free-space[3,7]. Basically for this mode, the overlapping integral between the electric components of the field and a plane wave is strictly zero for $k_{//}=0$. Consequently, in theory, this mode should not couple in the vertical direction.

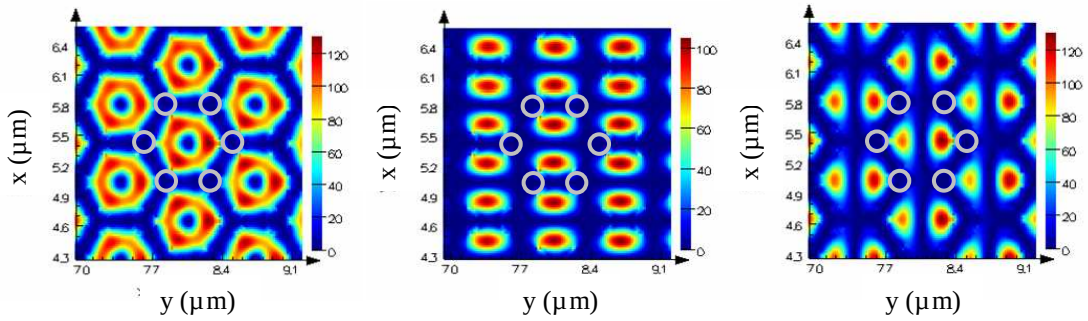

a) Cartography of E^2 b) Cartography of E_y^2 c) Cartography of E_x^2

Figure 3.5: Intensity patterns of mode M at λ=1607 nm. The white circles at the center are present the position of air holes of photonic crystal. a) Total electric field E^2 ($E^2_x + E^2_y$) intensity pattern indicates the doughnut-like shape formed inside the unit cell and no intensity at the center. b) Electric field intensity polarized in y-axis (E_y^2) that is decomposed into two lobes laid symmetrically either side of y-axis. c) Electric field intensity polarized in x-axis (E_x^2) with two separated lobes laid symmetrically either side of x-axis. These results demonstrate the azimuthal polarization of mode M in unit cells.

The 2D-simulation results are shown in Figure 3.5: a honeycomb unit cell (white circles) is presented at the center for reference. We see in Figure 3.5-a that the intensity pattern of the total electric field E^2 ($E^2_x + E^2_y$) of mode M is presented inside each unit cell with a doughnut-like shape (the field forms a ring and has no intensity at its center). The radii of outer and inner ring of doughnut are measured to be about 260nm and 90nm respectively. Figure 3.5-b and c present the partially polarized electric field intensity of mode M along y-axis (E^2_y) and x-axis (E^2_x) on PC surface. In both cases, the doughnuts are split into two separated lobes placed symmetrically either side of considered axes. These results demonstrate the presence of azimuthal polarization of electric field in unit cell of honeycomb PC.

b. Hexapolar mode

This non-degenerated mode is blue-shifted from 52nm with respect to the fundamental mode; it occurs at high symmetric Γ-point of the dispersion diagram. Similar to the fundamental mode, mode H possesses a low band curvature and zero in-plane k-vector in theory[2].

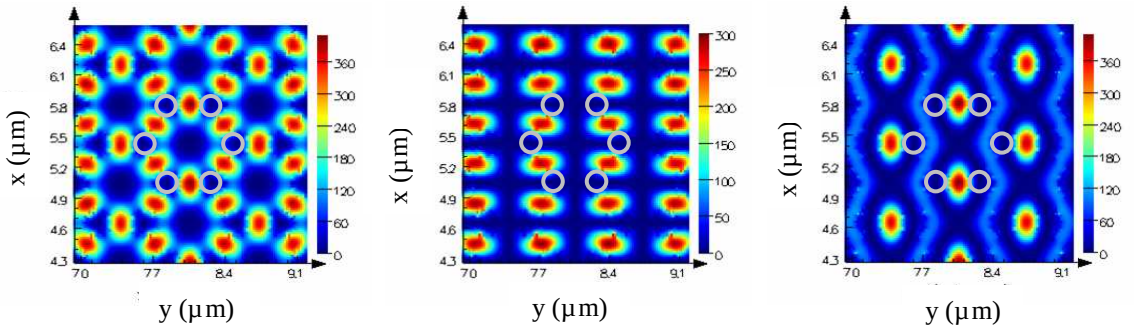

a) Cartography of E^2 b) Cartography of E_y^2 c) Cartography of E_x^2

Figure 3.6: Intensity patterns of mode H at λ=1716.4 nm with the unit cell of PC structure at the center. a) Total electric field E^2 ($E^2_x + E^2_y$) intensity pattern presents the array of bright spots distributed surrounding these air holes of PC and no intensity is found at the center of unit cell. b) Mapping of electric field intensity polarized in y-axis (E_y^2). c) Mapping of electric field intensity polarized in x-axis (E_x^2).

As indicated in Figure 3.6 the intensity patterns of mode H show the modulation of bright spots surrounding the air holes of PC structure. The size of these bright spots is comparable to that of air holes (*2r=245nm*) and no intensity is found at the center of unit cells. Figure 3.6-b/c are shown the intensity maps of polarized electric field along y-and x-axis, E^2_y and E^2_x respectively.

c. Dipolar mode

Unlike two previous modes, this mode is degenerated at the Γ-point of the dispersion diagram. It is blue-shifted of 159 nm with respect to the fundamental mode.

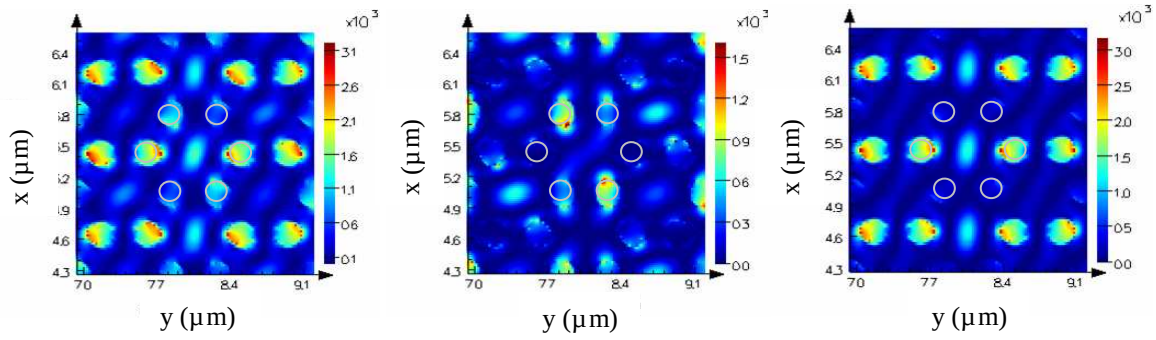

a) Cartography of E^2 b) Cartography of E_y^2 c) Cartography of E_x^2

Figure 3.7 Intensity patterns of mode D at λ=1647.5 nm that inserts the unit cell of PC structure at the center for reference. a) Total electric field E² (E^2_x + E^2_y) intensity pattern presents the modulation of spots distributed in the air holes and at the center of unit cell of PC. b) Mapping of electric field intensity polarized in y-axis (E_y^2). c) Mapping of electric field intensity polarized in x-axis (E_x^2).

As indicated in Figure 3.7 the intensity patterns of mode D present a distribution of light spots in the air holes and at the center of unit cell of PC structure. The mode concentration in air hole (low dielectric material) is the intrinsic property of high frequency Bloch mode in PC[8]. Figure 3.7-b/c shows the intensity maps of polarized electric field along y-and x-axis, E^2_y and E^2_x respectively.

3.3.2. Monopolar mode: 3D computation

Among the various surface addressable band-edge modes located at the Γ-point of diagram (Figure 3.1), we focused particularly on the monopolar mode (mode M), corresponding to the lower energy flat band. This is a non-degenerated mode where the electromagnetic field is well positioned within unit cell, zero in-plane k-vector and strong vertical emission.

In addition to the 2D-FDTD for quick review of the optical response of designed honeycomb structures of PC, 3D-FDTD with perfectly matched layers boundary conditions is used for rigorous prediction of Q-factor, mode intensity and polarization patterns. This simulation work was run by Dr. Adel Rahmani (University of Technology, Sydney). The numerical simulation is performed on a finite 2D PC (20x20 μm^2) with a lattice parameter (A) of 730nm and 245nm hole- diameter (20% of air filling factor). The

membrane consists of a 240nm-thick InP slab on a 1.5µm-thick SiO_2 substrate (Figure 3.8-a). Computational meshes are 30 nm for x, y, and z. The monopolar mode is excited by a dipole placed near the center of the structure. The simulation in Figure 3.8-b presents the total electric intensity of mode M on InP slab surface. It also shows that the mode surface reaches the edges of the PC-structure. The mode intensity is maximum in the centre area of the PC and its global envelop is gaussian. Moreover, in Figure 3.8-c, a closer view into the unit cell indicates that the mode intensity is distributed in each honeycomb lattice unit cell as a "doughnut" with an inner and outer radius of about 90nm and 260 nm, respectively. The electric polarization pattern in Figure 3.8-d shows that the field is azimuthally polarized in each unit cell: the zero of the field intensity in the centre region of each hexagon is due to a phase singularity[11]. Figure 3.8-e/f present the mode intensity mapping for polarized electric field along x (E^2_x) or y (E^2_y).

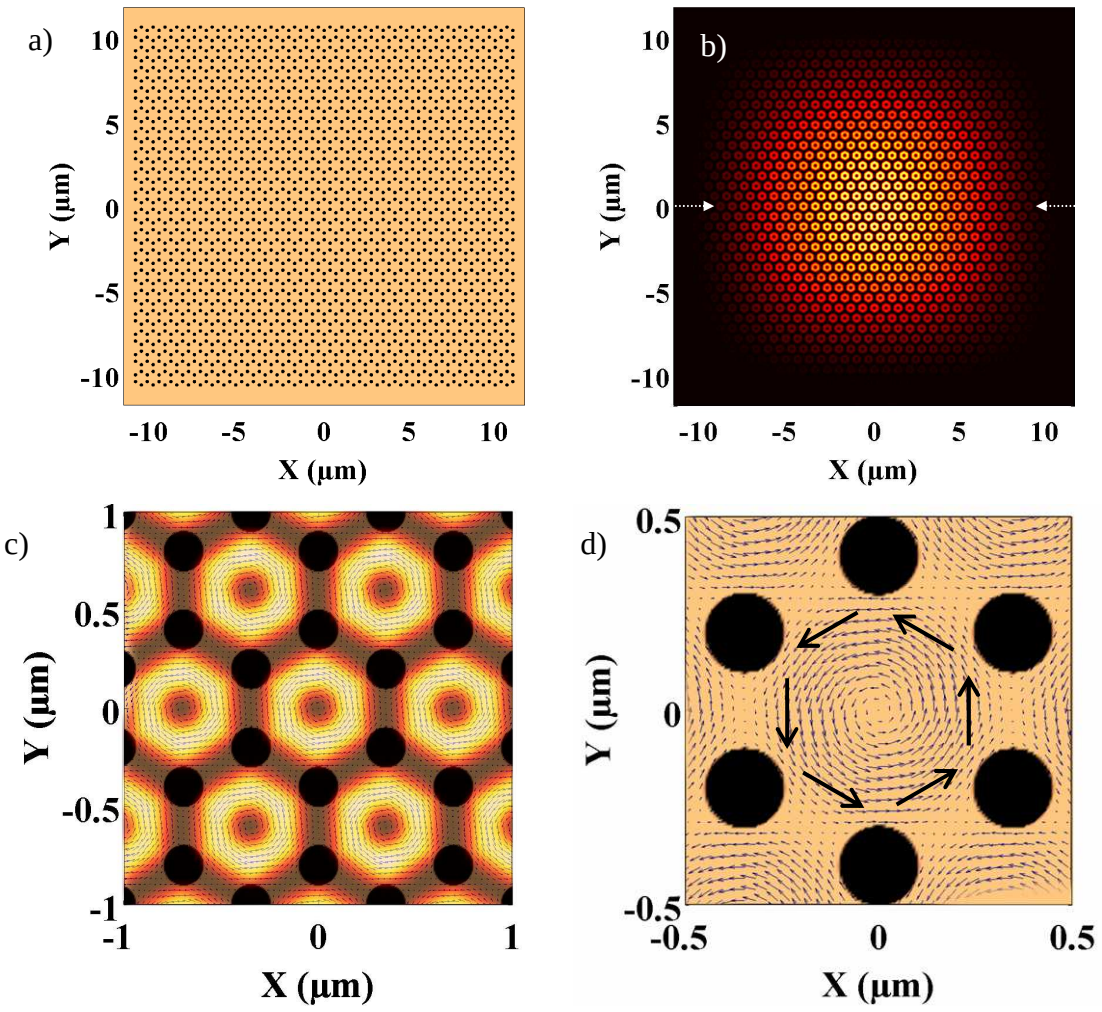

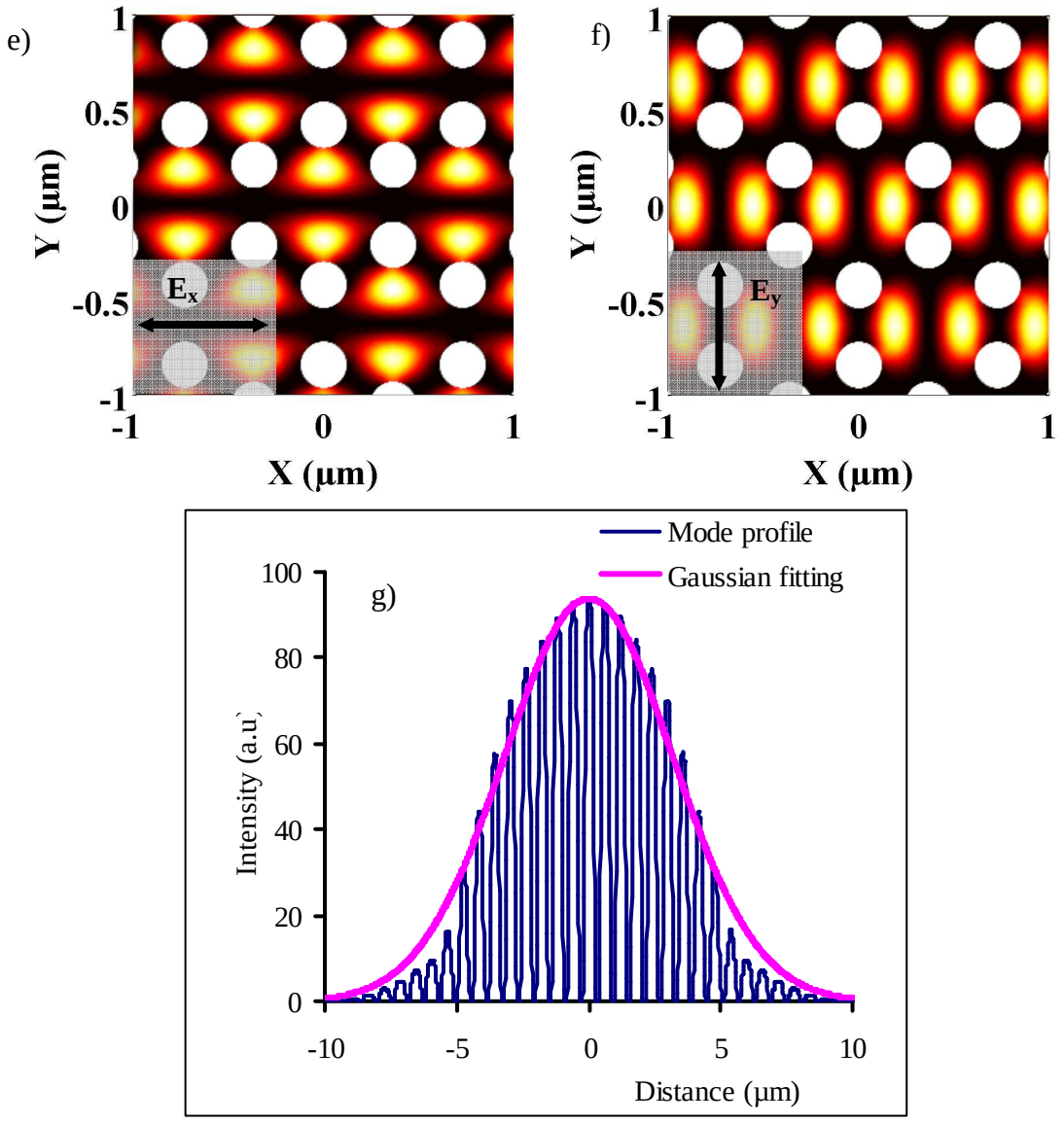

Figure 3.8: Intensity patterns of mode M on InP slab surface by 3D-FDTD. (a) Finite honeycomb 2D PC structure (20x20µm²) with lattice parameter of 730nm and radius of 245nm (20% air filling factor). Two arrows present the cross section for mode profile of (g). (b) Normalized field intensity ($E_x^2 + E_y^2$) at the surface of the PC at 1602 nm. Mode M is excited by a dipole placed near the center of PC structure. The intensity pattern presents the Gaussian-shape expansion limited at the boundary of PC structure. (c) Zoom in the central part of mode pattern in unit cells with air holes in black clearly reveals the mode intensity in doughnut-like shape. (d) Azimuthal polarization map of electric field in unit cell. (e) Normalized field intensity polarized along x (E^2_x) and (f) y direction (E^2_y). (g) The near-field mode profile along the cross section of (a) with Gaussian-fitted envelope.

The evolution of the intensity profile of the monopolar mode at various distances from PC surface to far-field (further wavelength) was also simulated. The total intensity ($E^2_x+E^2_y$) was recorded above surface with distance z which was varied from 0nm (on surface) to 1µm. As indicated in Figure 3.9, the details of doughnut shape in each unit cell are lost in maps at higher z as the mode radiates further from the surface. From distance z=400nm the field intensity at the center of structure vanished. For further distance, maps present a global doughnut shape covering whole structure. Note that in this 3D computation, the computational window prevents to have a larger view of the behaviors of the mode. The doughnut-like shape can then be inferred from the fact that as radiating from near- to far-field the destructive and constructive interferences take place creating the fading of field in the center of the beam.

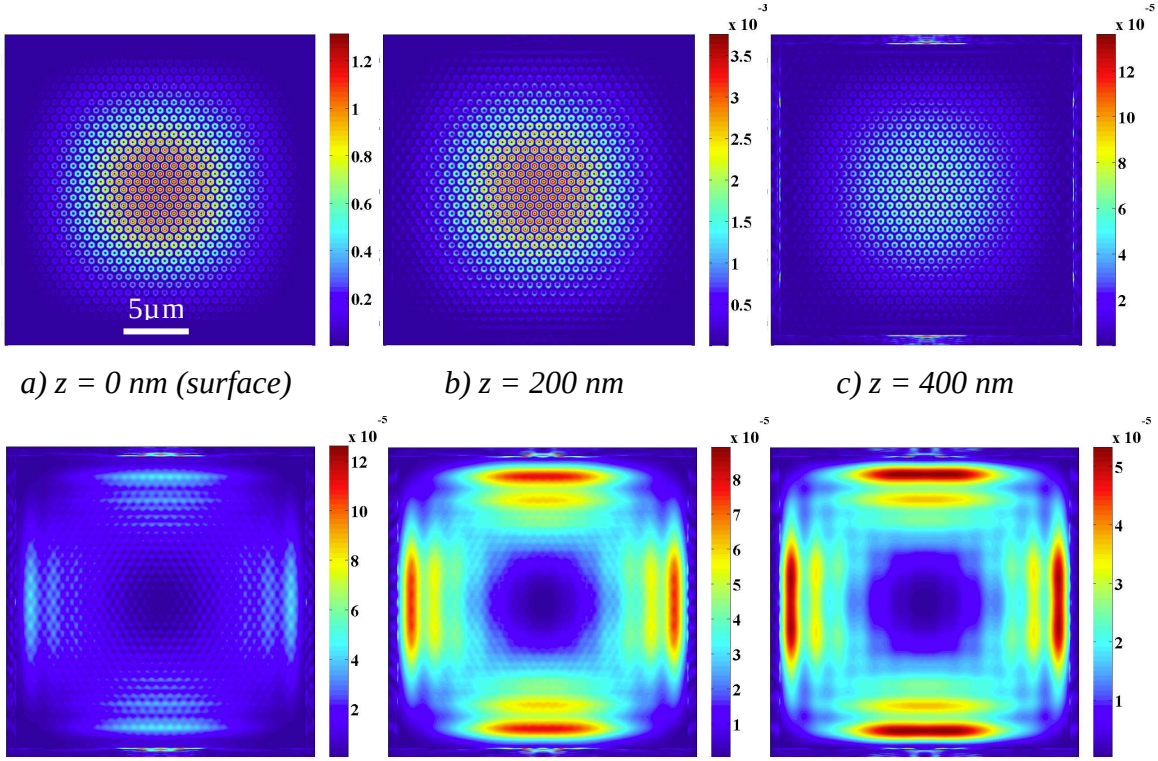

a) z = 0 nm (surface) *b) z = 200 nm* *c) z = 400 nm*

d) z = 600 nm *e) z = 800 nm* *f) z = 1000 nm*

Figure 3.9: Evolution of the intensity profile of the monopolar mode at various distances from PC surface (0 nm) to far-field (1000 nm).

3.4. Fabrication

A finite active honeycomb 2D-PC structure (size of 40x40µm²) is etched to InP slab on SiO_2 substrate. In order to optimize the lattice parameters and study the impact of

structure size with respect to mode expansion, several structure sizes with different filling factor value (by choosing different electron doses during EBL process step) have been fabricated.

The details of micro-fabrication process is referred to section 2.5

3.5. Far-field characterization of slow Bloch modes

Prior to NSOM measurement, the global optical response of the fabricated honeycomb structures are measured at room temperature by micro-photoluminescence. The experimental set-up and conditions can be found in section 2.2.

a. Spectroscopic results

We have fabricated six honeycomb PC structures, named G1 to G6, with different air hole radii. As a result, the filling factor is tuned, and the optical resonances of each structure are shifted. This allows us to determine optimal fabricating parameters and shift the optical resonance toward our desired working region and identify the most adequate structures for near-field purpose.

All experimental conditions are kept the same from G1 to G6. Figure 3.10 shows that the optical resonances of PC significantly shift with respect to their filling factor. The resonant wavelengths decrease with the increasing air filling factor as shown in Figure 3.10-b/c. By comparison to the photonic band-structure at the Γ-point (section 3.1, Figure 3.1) the laser peaks of G2 to G6 are supposed to be the fundamental band-edge mode (or monopolar mode). Note that structure G1 presents two laser peaks with wavelengths separated by 53.8nm (1636.5nm and 1582.7nm). This difference is in the range of two adjacent band-edge modes (monopolar and hexapolar mode) predicted by simulation ($\Delta\lambda$=52nm). The optical images (insets in Figure 3.10-a) taken with IR camera shows the different radiation patterns between mode H (dominant in G1) and mode M (other graphite structures). These could be precisely justified by further NSOM investigations.

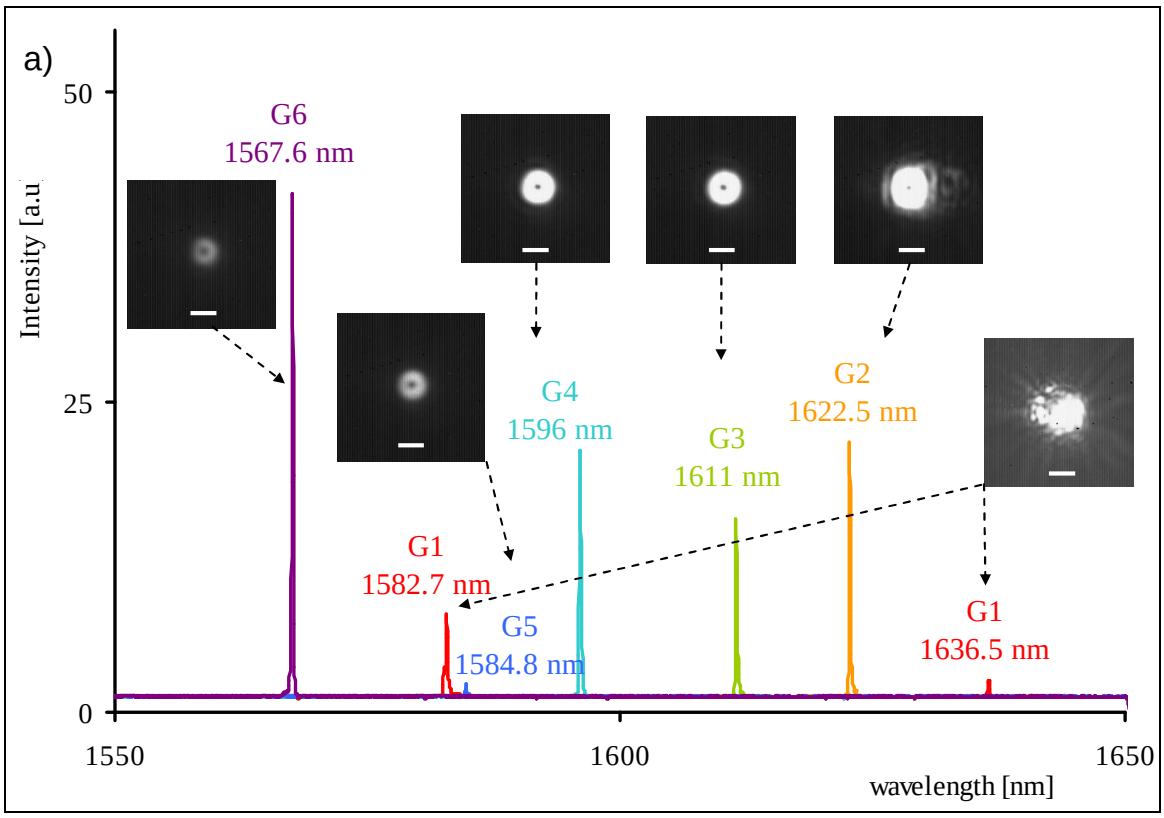

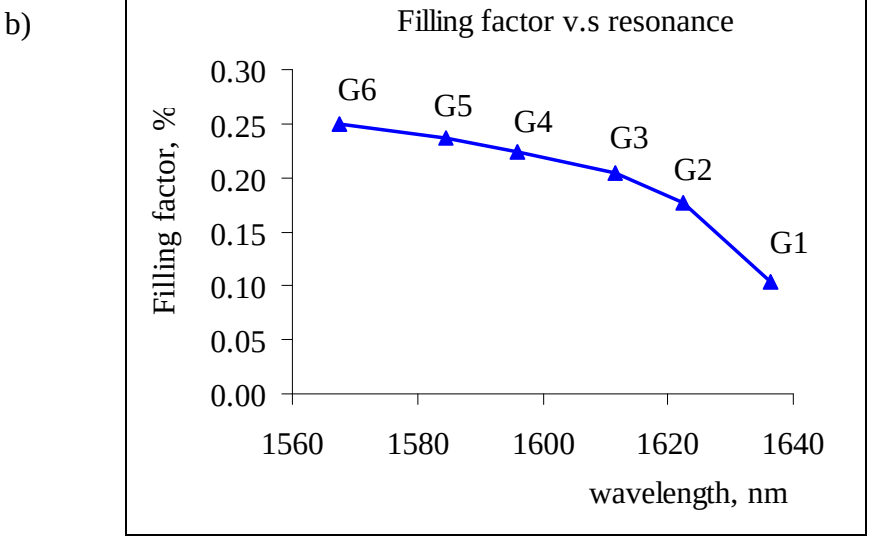

Figure 3.10: a) Far-field spectra of six honeycomb structures (G1 to G6) excited by pulsed 780nm laser diode. From G1 to G6, the doses are increased thus filling factors are increased proportionally. As a result, resonant wavelengths supported by PC are altered inversely. The insets show the images of corresponding radiation modes on the PC surface with scaling bar of 10μm, recorded by an IR camera. b) Graph indicates spectral tuning of monopolar mode with respect to air filling factor.

Table: Air filling factor *vs.* resonant wavelength of structures from G1 to G6 in details. The filling factor was calculated by lattice parameters extracted from SEM images.

	G1	G2	G3	G4	G5	G6
Wavelength (nm)	1635.5(M) 1582.7(H)	1622.5	1611	1596.0	1584.8	1567.6
Filling factor (%)	10.4	17.7	20	22.5	23.7	25

b. Photoluminescence of structure(G3)

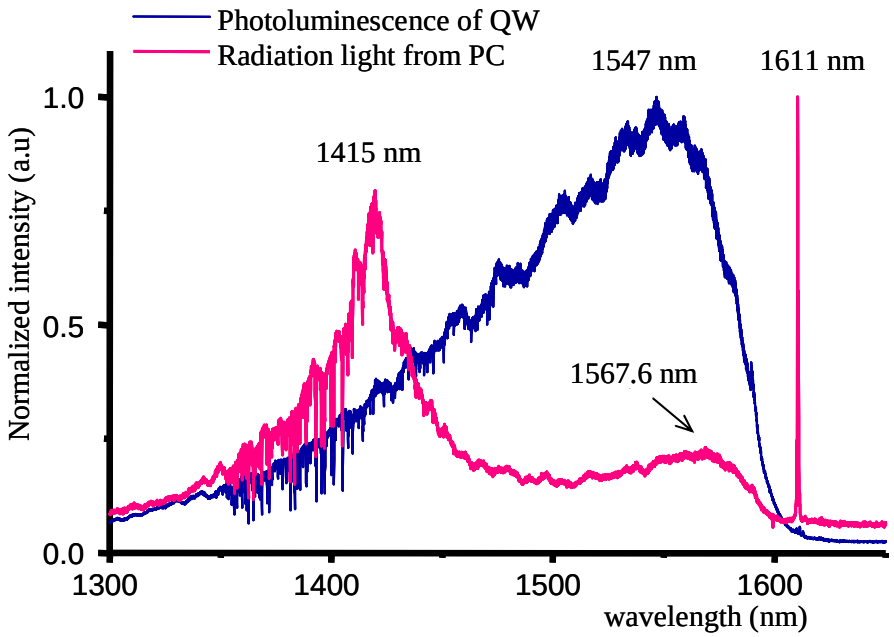

Figure 3.11: Photoluminescence of quantum wells and radiation spectra emitted from G3 InAsP/InP quantum well emits light in range of 1.3µm to 1.65µm. The 2D-PC shows a resonant monopolar mode at 1611nm with high quality factor and other modes at lower Q: hexapolar mode (mode H) at λ= 1567.6 nm and dipolar mode (mode D) at λ=1415nm.

The optical response of active PC and honeycomb structure N°3 are presented in Figure 3.11. Photoluminescence of quantum well InAsP/InP recorded at unpatterned area of sample ranged from 1.3µm to 1.65µm (blue line). On PC structure we detect several resonant modes. Based on the photonic band-diagram indicating the slow light modes associated with the Γ-point, we assume that the fundamental monopolar mode (lowest energy mode M) emerged at λ=1611nm. This mode shows a high quality factor and low lasing threshold. Other modes with lower Q recorded at λ=1567.6 nm and λ=1415nm are

attributed to the hexapolar mode (mode H) and dipolar mode respectively (D). The resonant wavelength associated with mode M in the spectral diagram is in good agreement with the simulation value found for the monopolar mode (1602 nm). To confirm these assumptions, the far-field and near-field investigations must be conducted to characterize the shape and polarization of the radiated beam and the spatial distribution of the mode inside the structure. In this work, we focused on the optical properties of mode M on the G3 structure.

c. IR imaging of slow light modes

- Monopolar mode

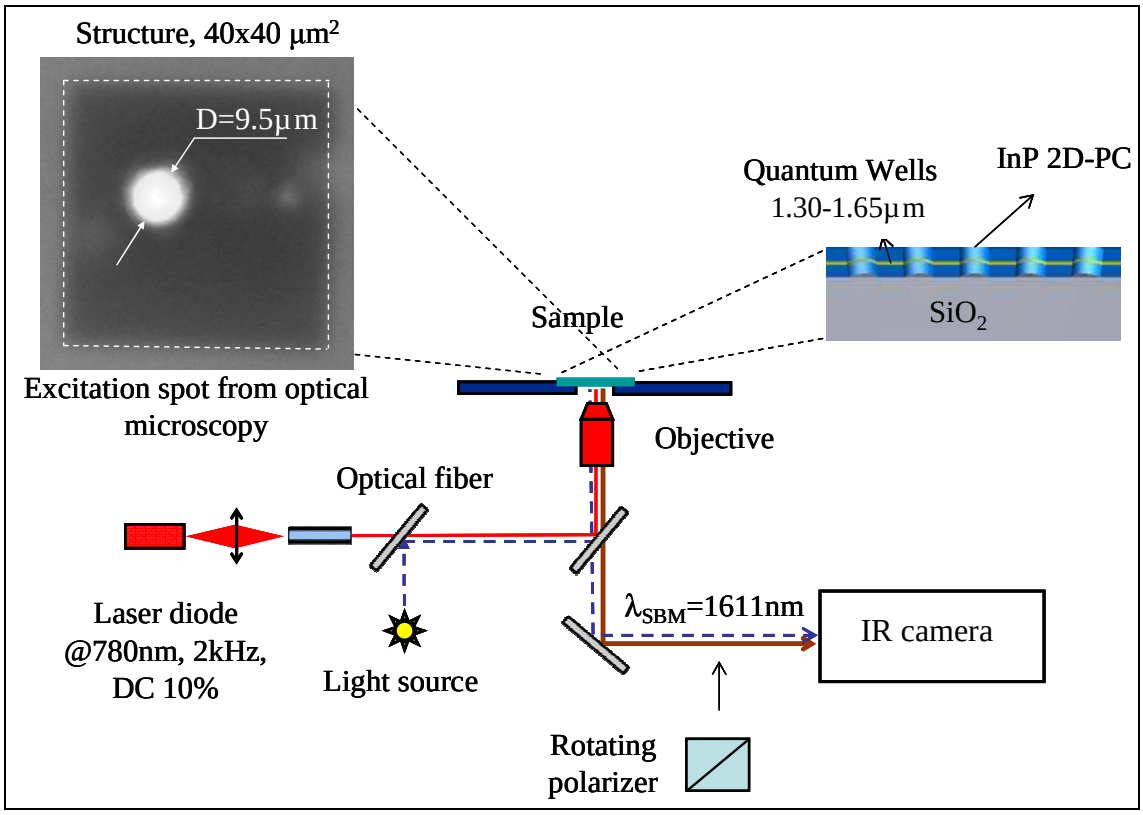

Figure 3.12. Experimental set-up to implementing the far-field analysis of mode M

The experimental set-up for this far-field study was different from photoluminescence measurement described in Figure 2.16, section 2.3. This set-up is built on the stand of an inverted microscope as shown in Figure 3.12. Laser diode modulated at 2kHz and pulsed with duty cycle of 10% was utilized to excite quantum well for photoluminescence through an objective 63x/0.75. The excitation spot size of 9.5µm can be estimated from optical image taken by a visible CCD camera mounted at the output of

microscopy. Photoluminescence of quantum well was observed in the 1.3µm -1.65µm range. The light radiated from the PC is collected by the same objective and directed to an IR InGaAs camera. In order to select the polarized components of light, we use a rotating polarizer placed in front of IR camera. The image was obtained in far-field (as the objective only collected radiating waves) but it does not constitute a radiation pattern as it corresponds to the spatial distribution of the mode intensity at the surface of the structure.

The results are displayed in Figure 3.13. Through IR camera we observed the laser beam vertically radiated from PC structure at λ=1611nm. The first one (Figure 3.13-a) is the image recorded without polarizer: it clearly shows a doughnut-shaped mode. This shape is very different to what simulations predicted for the mode profile (Figure 3.8) at the surface of structure. However, the doughnut shape can be inferred from the fact that these images are recorded in the far-field where processes of destructive and constructive interferences take place and explain the fading of field in the center of the beam[12].

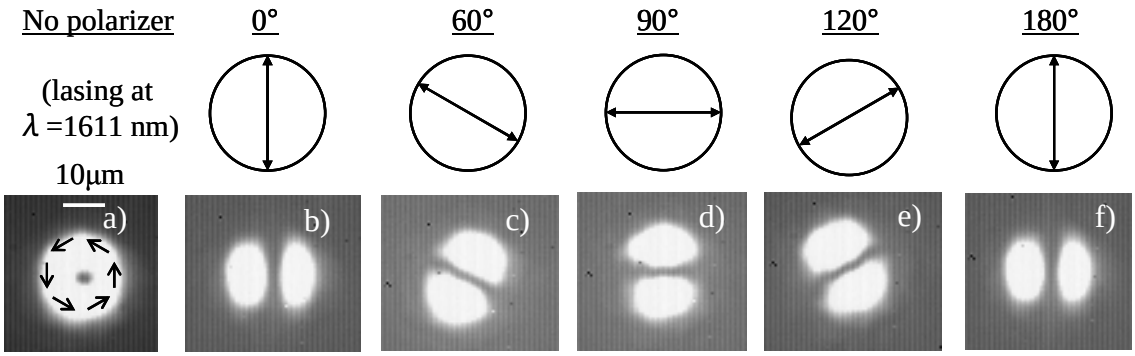

Figure 3.13: Images of the mode at the surface of the PC in the far-field zone (recorded through a microscope objective x63/0.75). a) Image of the mode without polarizer, b)-f) images with a polarizer oriented respectively at 0°, 60°, 90°, 120° and 180°.

The beam patterns recorded with a rotating polarizer are also shown in sequence of images in Figure 3.13 (image b to f). Through the polarizer, the doughnut is transformed into two lobes symmetrically located on either side of the polarizer axis. These results indicate explicitly that the emitted beam is a TEM_{01*} mode with an azimuthal polarization[13,13,14]. This mode can also be expressed as the coherent superposition of two Hermite-Gauss (HG) beams which have two lobes and no radial symmetry[15] (HG_{10} with *x*-polarization and HG_{01} with *y*-polarization). The polarizer effect is to select one of the HG

modes parallel to its orientation. This demonstrates the direct and simple generation of pure azimuthal doughnut laser beam with a 2D-PC honeycomb lattice.

- **Hexapolar mode**

Structure G1 is the only structure that presents a lasing effect for the first excited mode (named hexapolar) of the honeycomb crystal. The lasing wavelength occurs at 1585nm. IR imaging of this mode through the microscope objective shows a very irregular pattern, similar to a speckle pattern, and no clear shape as the monopolar mode. Our hypothesis is that conversely to the monopolar, no constructive interference occurs to shape the emitted beam: for hexapolar mode the emitted light collected by the microscope objective probably comes both from losses and the radiated part of the mode. Indeed, as shown in Figure 3.14, the polarization properties of the light inside a unit cell are very different between monopolar and hexapolar. Figure 3.15 shows a polarization study of the hexapolar mode. Here again no specific polarization behavior appears for this mode.

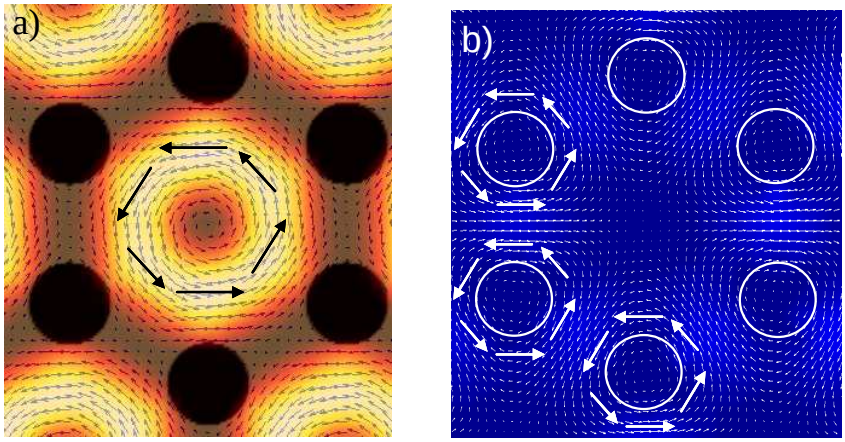

Figure 3.14: Comparison between a) Monopolar polarization inside a unit cell, b) Hexapolar polarization of inside a unit cell.

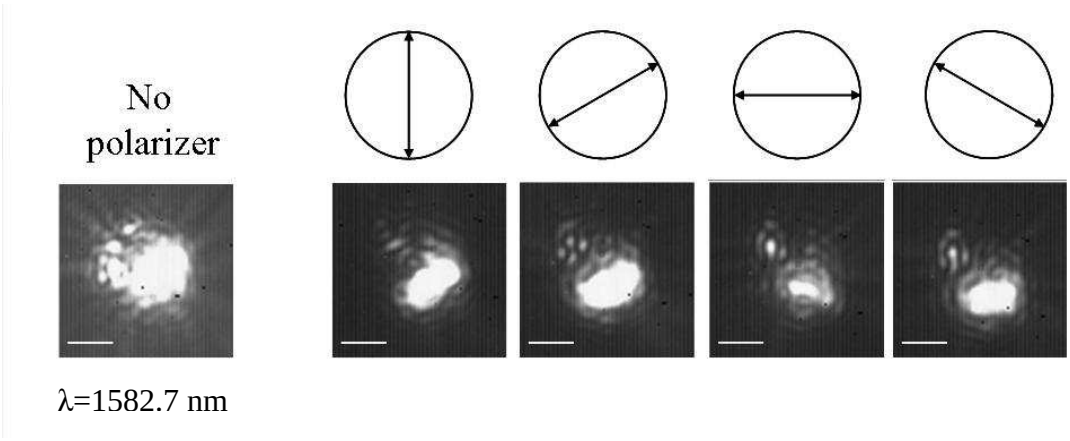

Figure 3.15: Images of the hexapolar mode at the surface of the PC (G1) in the far-field zone (recorded through a microscope objective x63/0.75). a) Image of the mode without polarizer at 1582.7 nm, b)-e) images with a polarizer oriented respectively at 0°, 60°, 90°, 120° and 180°. The scaling bar is 10 µm.

Conclusion

Optical properties of honeycomb 2D-PCs have been theoretically and experimentally investigated. With these kinds of photonic structures, slow Bloch modes at Γ-point can show a very strong lasing effect. For the monopolar mode, far-field characterization confirms the predicted resonant wavelengths. The IR image of the mode shows that it differs completely from the theoretical pattern computed at the surface of the structure. The image obtained by the microscope objective shows a mode with a global doughnut shape that is characteristic of azimuthal polarized laser beams. The global polarization of the beam was found to reflect the polarization of the field in a unit cell of the PC. For the hexapolar mode, the same agreement was found on the spectral position of the mode wavelength. However, conversely to the monopolar mode, the hexapolar mode does not show any peculiar feature in far-field, nor in the shape of the emitted beam, nor in its polarization. Here again, far-field images do not suffice to identify clearly the mode with respect to the simulations. In the next chapter, optical near-field microscopy in applied to reveal the real pattern of these modes at the structure surface.

References

[1] F. Raineri, C. Cojocaru, R. Raj, P. Monnier, A. Levenson, C. Seassal, X. Letartre, and P. Viktorovitch, "Tuning a two-dimensional photonic crystal resonance via optical carrier injection," Opt. Lett. 30, 64-66 (2005)

[2] Ben B. Bakir, Ch, X. Letartre, P. Viktorovitch, M. Zussy, L. Di Cioccio, J. M. Fedeli, "Surface-emitting microlaser combining two-dimensional photonic crystal membrane and vertical Bragg mirror", Applied Physics Letters, Vol. 88, No. 8. (2006)

[3] N. Chauvin, P. Nedel, C. Seassal, B. Ben Bakir, X. Letartre, M. Gendry, A. Fiore, and P. Viktorovitch," Control of the spontaneous emission from a single quantum dash using a slow-light mode in a two-dimensional photonic crystal on a Bragg reflector" Phys. Rev. B **80**, 045315 (2009).

[4] Xavier Letartre, Christelle Monat, Christian Seassal, and Pierre Viktorovitch, "Analytical modeling and an experimental investigation of two-dimensional photonic crystal microlasers: defect state (microcavity) versus band-edge state (distributed feedback) structures," J. Opt. Soc. Am. B **22**, 2581-2595 (2005)

[5] Kiyoshi Asakawa et al, "Photonic crystal and quantum dot technologies for all-optical switch and logic device" New J. Phys. 8 208 (2006)

[6] Ali Belarouci, Taha Benyattou, Xavier Letartre, and Pierre Viktorovitch , "3D light harnessing based on coupling engineering between 1D-2D Photonic Crystal membranes and metallic nano-antenna", Optics Express, Vol. 18, Issue S3, pp. A381-A394 (2010)

[7] K. Sakoda, "Optical Properties of Photonic Crystals," Springer- Verlag, Berlin, Heidelberg (2001).

[8] D. John, Joannopoulos, Steven G. Johnson, Joshua N. Winn, and Robert D. Meade, "Photonic Crystals: molding the flow of the light", Princeton University Press (2008).

[9] M. Notomi, "Manipulating light with strongly modulated photonic crystals," Rep. Prog. Phys. 73 (2010) 096501 (57pp)

[10] J.-M. Gérard and B. Gayral., IEEE Journal of Lightwave Technology, 17, 2089, (1999).

[11] Thanh-Phong Vo, Adel Rahmani, Ali Belarouci, Christian Seassal, Dusan Nedeljkovic, and Ségolène Callard, "Near-field and far-field analysis of an azimuthally polarized slow Bloch mode microlaser," Opt. Express **18**, 26879-26886 (2010)

[12] Sakai, K., Miyai, E., Sakaguchi, T., Ohnishi, D., Okano, T., and Noda, "Lasing band-edge identification for a surface-emitting photonic crystal laser," IEEE J. Sel. Areas Commun., 23, pp. 1335–1340 (2005).

[13] K. Sakai, and S. Noda, "Optical trapping of metal particles in doughnut-shaped beam emitted by photonic-crystal laser," Electron. Lett. 43 (2), 107 (2007).

[14] Eiji Miyai, Kyosuke Sakai, Takayuki Okano, Wataru Kunishi, Dai Ohnishi, and Susumu Noda, "Lasers producing tailored beams", Nature 441, 946 (22 June 2006)

[15] Machavariani, G.; Lumer, Y.; Moshe, I.; Jackel, S.,"Transforming the (0,1)* LG mode with radial polarization to a nearly Gaussian beam by use of a spiral phase element and spatial filter", Proc. SPIE, Vol. 6346, 63461W (2006).

Chapter 4: Optical near-field characterization of SBM

In this chapter we present the experimental results of near-field characterization of honeycomb PC modes. Near-field scanning optical microscopy (NSOM) in transmission mode was employed to record the slow light mode (mode M and H) associated with the Γ-point of the first Brillouin zone using bare dielectric tip, metal-coated tip and nano-antenna-based tip.

4.1. NSOM with conventional tips

Firstly, two kinds of classical near-field tips were considered: homemade dielectric tip fabricated from silica optical fiber and circular aperture tip made of optical fiber-based Al-coated polymer probe.

4.1.1. Dielectric tip

A simple bare silica tip was used in collection mode to probe the mode at the surface of the 2D-PC. The dielectric tip was selected in the first place since it was successfully applied to characterize localized mode in 2D-PC active based microcavity. Moreover, due to its low refractive index with respect to the semiconductor slab, it proves to induce only small perturbation in the electromagnetic environment of the mode.

a. Spectroscopic results

Figure 4.1 shows the photoluminescence spectra of the structure G3 recorded in the far- and near-field at room temperature. The strong and sharp peaks obtained at 1611nm corresponding to resonant laser emission from PC are identical for both far-field (red curve) and near-field (blue curve) measurements. This result confirms that the dielectric tip is indeed non-invasive. FWHM value of the lasing peak (full-with at half-maximum) is essentially limited by the spectral resolution of our spectrophotometer (about 0.6nm).

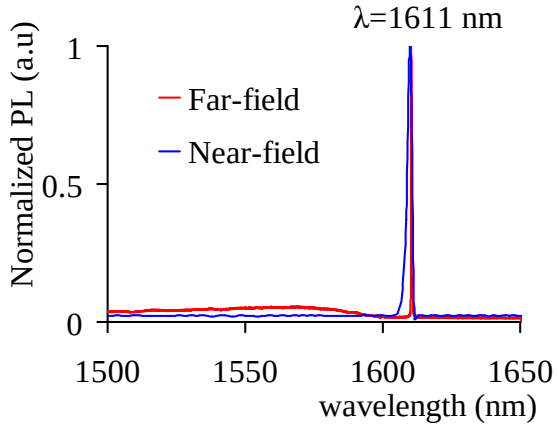

Figure 4.1: Far-field (red curve) and near-field (blue curve) spectra of honeycomb lattice normalized to the maximum intensity. Mode M at λ_{SBM}=1611 nm matching well in two types of measurement proves that dielectric tip does not disturb the electromagnetic field of PC.

The experimental measurement of resonant wavelength is in fair agreement with the computed value of 1602 nm for the monopolar mode. To confirm that we are dealing with the M mode, near-field measurements have been conducted to characterize the spatial distribution of the mode inside the structure. Near-field inspection also allows a deeper understanding of the mode expansion inside the PC.

b. Near-field investigation of mode M

Figure 4.2-c shows an image obtained with a visible CCD camera that displayed the contour of whole PC as well as the position and size of excitation spot (~9.5µm diameter). Figure 4.2-a and 4.2-b present respectively a topographic shear-force image of the structure and the optical image at the wavelength of mode M (1611 nm). Unexpectedly, the near-field image of the mode reveals also a global doughnut shape that has been put in evidence in far-field in the previous section. Unlike the simulation, this image obtained with the bare silica tip shows that the intensity is minimum at the center of the excitation spot where it should be maximum. However, compared to the far-field image (Figure 3.13-a, section 3.5), the near-field image shows additional features: the intensity map exhibits a periodic modulation which fits well the Bloch mode period of the M mode (~730 nm). These sub-wavelength features confirm that the collection of light takes place in the near-field where the evanescent field is more significant. The presence of the global doughnut shape in the near-field image can be explained by the fact that the bare silica tip, besides converting evanescent light at the surface in propagating light, is also able to couple a large amount of radiating light through its flanks. At the Γ-point, mode M emits strongly in the vertical direction to form the doughnut pattern recorded in far-field. Indeed, the propagating light is dominant in the ring of the global doughnut. At the center of the doughnut in Figure 4.2-b where no radiating light is observed due to destructive interference, the optical intensity only comes from the evanescent light. Figure 4.2-d presents the intensity profile crossing the doughnut (line P1 in Figure 4.2-a). By comparing the optical intensity between the ring (maximum value) and the center of doughnut (minimum value), the intensity contrast is calculated about thirty folds. This shows the limits of the bare dielectric tip and confirms that the use aperture tip for strongly radiating structure is necessary.

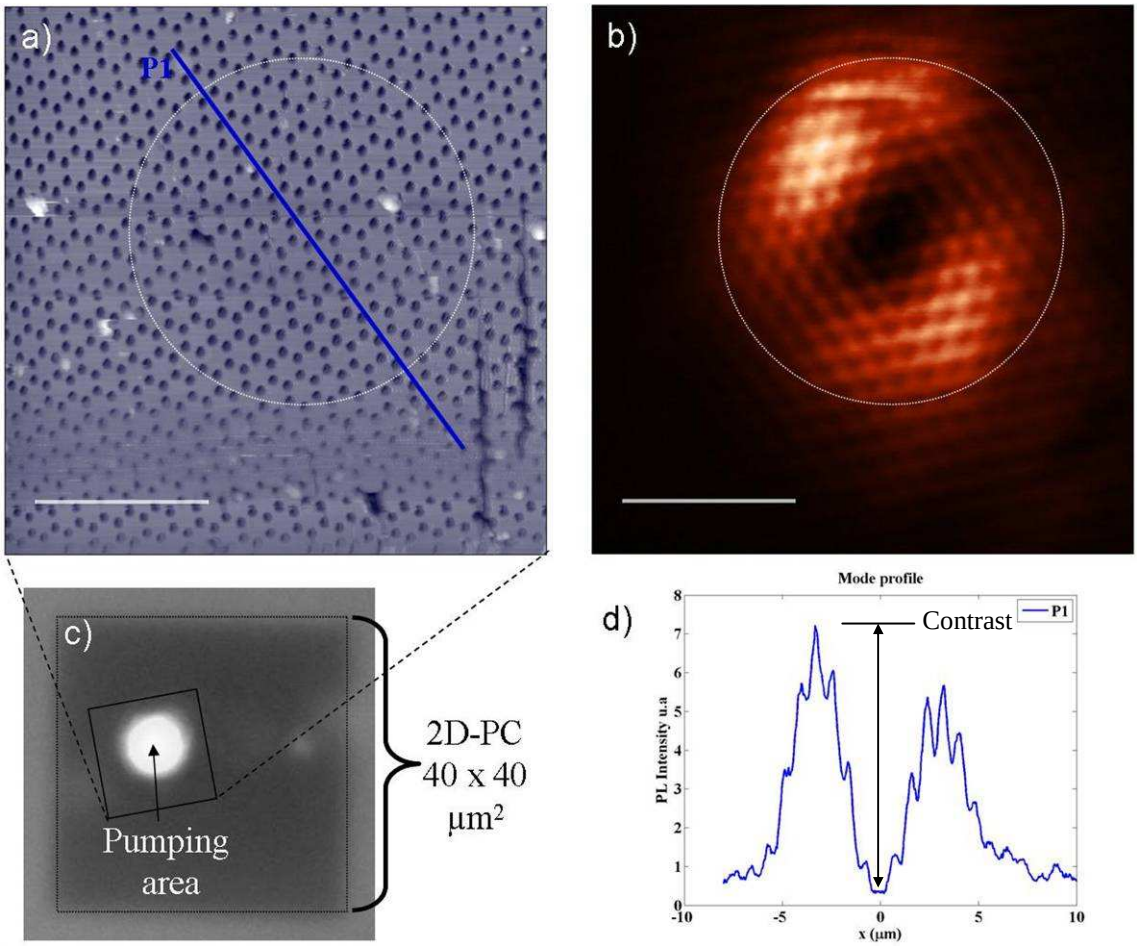

Figure 4.2: a) Topography in shear-force mode b) Near-field distribution of intensity of mode-M recorded with a bare silica tip at 1611 nm, the scaling bar is 5 µm. c) CCD image in the visible range of the excitation spot (780 nm) on the PC structure (size of 40x40µm²), the width of the gaussian beam is about 9.5 µm. d) Mode profile recorded along the line P1 (corresponding to Γ-K direction in the reciprocal space) provides the contrast of mode intensity (thirty times).

In Figure 4.2-b, a dark area crosses the doughnut. We assume that this is probably due to a slight polarization effect caused by the grating element present in the optical chain of our monochromator. Similar patterns of mode M were obtained on other structures (G2, G4).

c. Near-field investigation of mode H and D

NSOM measurements with dielectric tip were also performed to investigate the other Γ-point modes of the honeycomb structure. The results presented here concern the first (hexapolar) and the second (dipolar) excited mode at the Γ-point of the band diagram.

- Hexapolar mode

As for the monopolar mode, for symmetry reason, this mode should not couple in the vertical direction. As escape of the photons are forbidden in the (strictly) vertical direction ($k_{//}=0$), the quality factor of this mode can be sufficiently high to sustain stimulated emission. In the case of structure G1, it was possible to obtain a lasing effect for the hexapolar mode at 1584.4 nm. The spectral analyze in near-field is indicated in Figure 4.3 with a resonant peak at λ=1584.4 nm. Note that for structure G1, the far-field characterization reveals another longer wavelength (*i.e* monopolar mode) at λ=1636.5nm (see section 3.5, Figure 3.10-a) with a weaker emission (however, this mode was not detected in the near-field set-up). The resonant wavelength at 1584.4nm of G1 in near-field was then attributed to the first excited mode, namely the hexapolar mode (mode H).

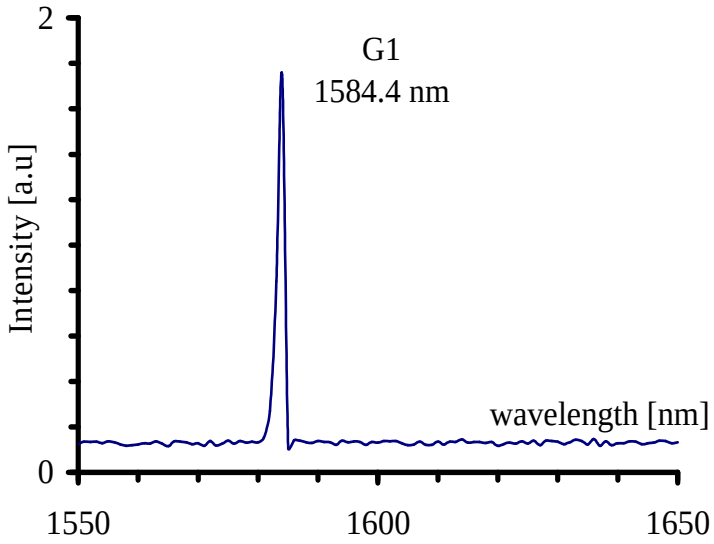

Figure 4.3: Near-field spectra of structure G1 shows resonant peak corresponding to the hexapolar mode on G1

Figure 4.4-a/b show the topographic image and the optical image of the mode measured at λ=1584.4 nm. Firstly, it shows that the image resolution was much better than for the monopolar mode. A resolution of approximately 326 nm (λ/4.5) was achieved which what is usually expected with our bare silica tip functioning in PSTM mode. Here conversely to M mode, the field was strongly purely evanescent with a rather weak radiated component in the vertical direction. The electromagnetic field extended in a large area out of the excitation spot (white circle with diameter of 8.4µm) with an inhomogeneous distribution. Figure 4.5 shows the comparison between the 2D-FDTD

simulation and the measured NSOM image. In spite of the experimental image resolution, the identification of the mode is quite clear and unambiguous.

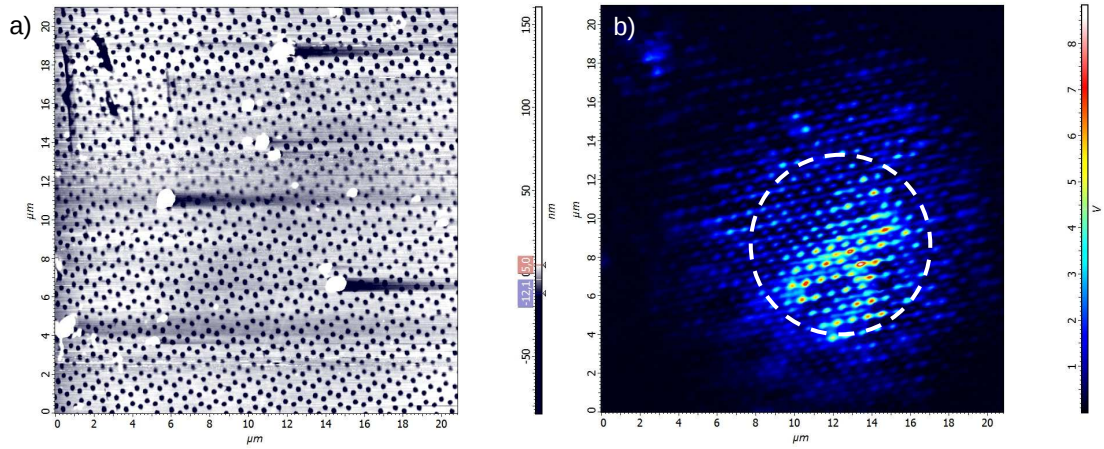

Figure 4.4: a) Shear-force topography of the G1 crystal surface, b) NSOM collected by dielectric tip image of the hexapolar mode . The excitation spot is the dashed line circle, diameter of 8.4μm.

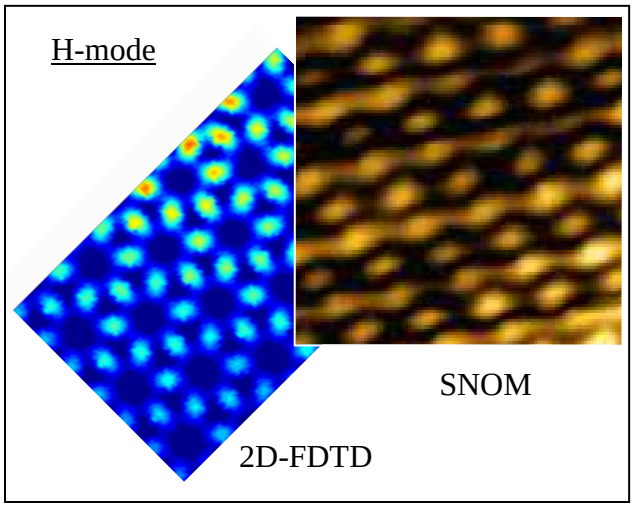

Fig 4.5: (left) 2D-FDTD intensity pattern for the Hexapolar mode and (right) NSOM image of the mode

- Dipolar mode

The dipolar mode is the second excited mode in the Γ-point band-diagram of the honeycomb structure. It is a degenerate mode whose symmetry does not forbid its coupling in the vertical direction. As a result, the quality factor of this mode is lower and experimentally, no lasing effect was achieved with this mode. It was mainly detected with

spontaneous photoluminescence emission. The spectrum of this mode in the near-field is presented in Figure 4.6-a for structure G3 along with the NSOM image measured at 1427nm.

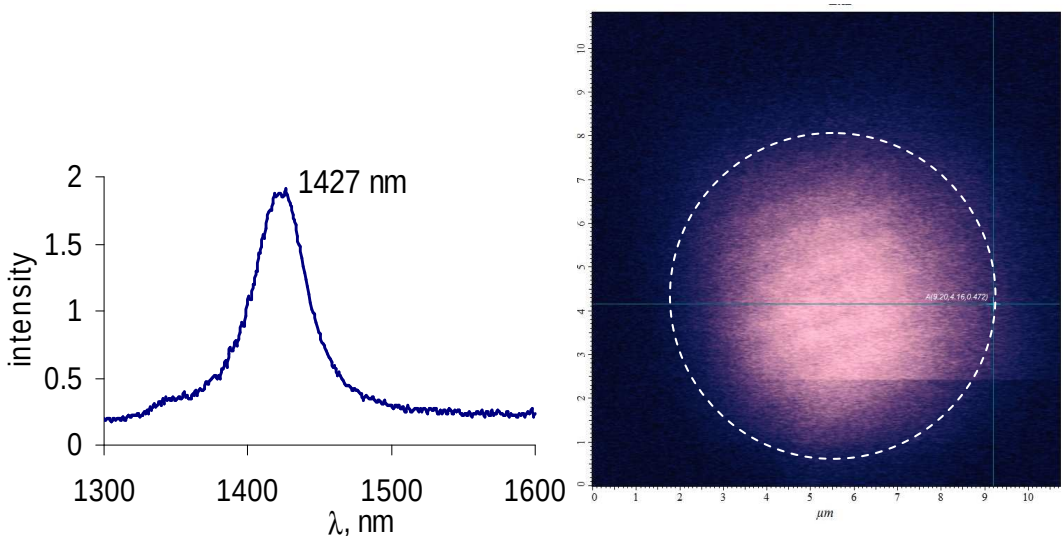

Figure 4.6: a) Near-field spectra of structure G3 shows resonant peak that may correspond to the dipolar mode. b) Corresponding NSOM image at 1427 nm. The position and size of the excitation spot is presented by the white circle.

For this mode, the pattern is homogenous and sub-wavelength features barely visible. As for the monopolar, this image is very different from what was predicted by the simulation. Thus, the identification of such mode as the dipolar mode cannot be as positive as for the two first modes. The optical signal is also very weak and the mode expansion is confined inside the excitation spot.

d. Evolution of mode M from near- to far-field

The evolution of monopolar mode from near to far-field was predicted by the theoretical simulation of section 3.3. The doughnut-like shape was formed as a result of constructive and destructive interference of slow light as propagating into the far-field. The experiments in Figure 4.7-a/b are to verify the simulation results. The intensity patterns were recorded by scanning the dielectric tip at 2µm above the surface. This distance (>λ) was far enough to be considered as far field and to prevent near-field coupling into the silica tip. These scanning far-field patterns were performed on two different honeycomb structures that support monopolar mode. They give the same results

and reveal the doughnut-like shapes (minimum intensity at the center) of slow light in the far-field. Note that the sub-wavelength features that were present in the near-field have disappeared from these images.

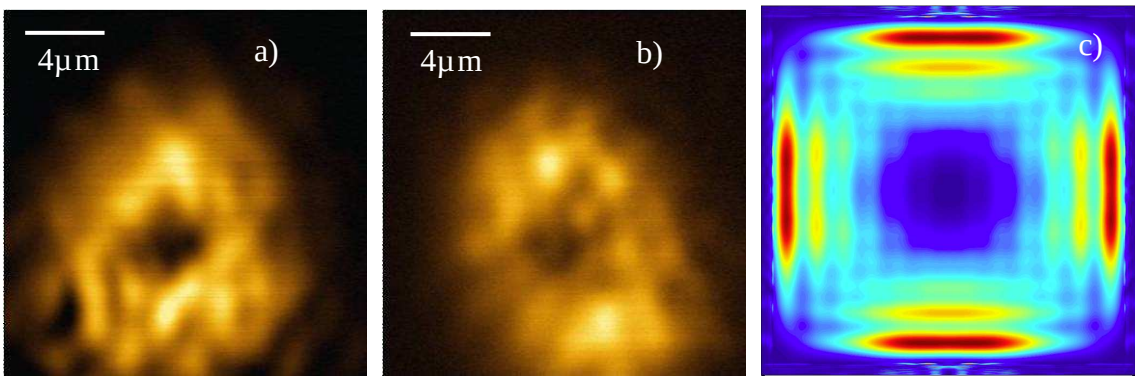

Figure 4.7: The intensity patterns of monopolar mode recorded at distance of 2µm from surface (far-field) by NSOM dielectric tip with various similar honeycomb structures: a) G3 (λ=1611nm) and b) G4 (λ=1595.11nm). These results demonstrate the evolution of radiation monopolar mode from near-to far-field as simulation prediction in c).

In this section, near-field experiments were performed with bare-dielectric fiber tip. The main draw back of this kind of is that it can couple a large amount of radiating field through its bare flanks. For modes emitting in the vertical direction, this tips are not adapted. That is why in the next section, we employ a metal coated polymer tip with an aperture milled at the tip apex in order to minimize the contribution of the vertical radiation into the optical near-field image.

4.1.2. Metal coated tip-based NSOM

With this kind of NSOM tip, the spatial resolution of cartographies is determined by the aperture (see section 2.1.2). However, the aperture cannot be reduced unlimitedly since the optical transmission through the apex will decay exponentially due to cut-off frequency phenomenon. Thus, the resolution of cartographic image and the collected optical intensity is always a trade-off. In this experiment, we use metal coated tips with aperture size of about 100 nm. The fabrication procedure is described in section 2.1.2. The results presented here essentially focused on mode M.

a. Spectroscopic results

In order to confirm that the Al-coated tip is non-invasive and does not perturb the slow mode, we compared the spectra on G3 in the near-field and in far-field. Figure 4.8 shows that they perfectly match. This result was not granted as metal-coated tips have a higher impact on the electromagnetic environment due to the dielectric function of metals. However, as we are dealing with delocalized mode, which present a rather extended area, the impact of the tip may be seen as a small perturbation. This is not the case for localized mode as cavity mode where the mode volume can be in the range order of the tip volume[5].

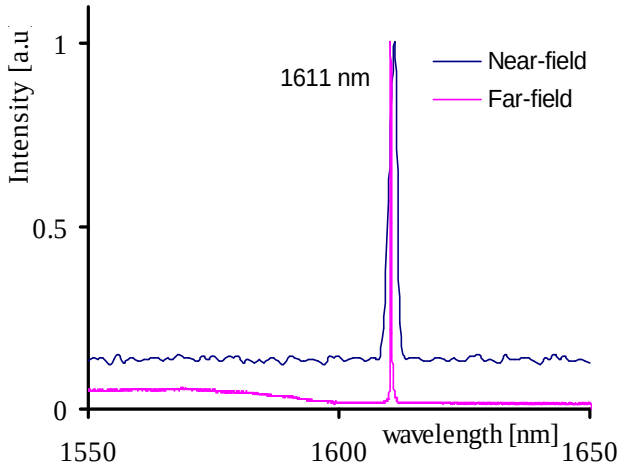

Figure 4.8: The lasing spectra measured in far-field (pink curve) and near-field (blue curve) by metal coating NSOM tip. Two identical resonant peaks confirm the non-invasive metal-coating tip to the near-field distribution on surface of PC

b. Monopolar mode characterization with Al-coated tips

Topographic and near-field images recorded with two different tips are shown in Figure 4.9. In the Figure 4.9-a/b where tip N°1 was used, the global doughnut still appears. However, new features are also visible in the centre, exactly where the radiating field vanishes: in each unit cell of the PC, small doughnuts are now visible. In the Figure 4.9-c/d with tip N°2, the global doughnut has almost disappeared to the benefit of a triangular array of small doughnuts which is a clear signature of the monopolar mode as predicted by simulation. Indeed, by quantitative measurement, the new contrast of optical intensity between the ring of the large doughnut and its centre is reduced approximately to thirteen fold for tip N°1 and fivefold for tip N°2. The difference between two intensity mappings of Figure 4.9-b/d are probably due to different aperture sizes of the metal coated tips. We

assumed that the aperture of tip N°1 is larger than tip N°2 because the amount of signal collected is higher: it also explained why the spatial resolution of optical image with tip N°2 is better (~265 nm or λ/6). It also confirms that unlike the bare silica tip, the metal coating tip succeeds to reveal the fine structure of the SBM.

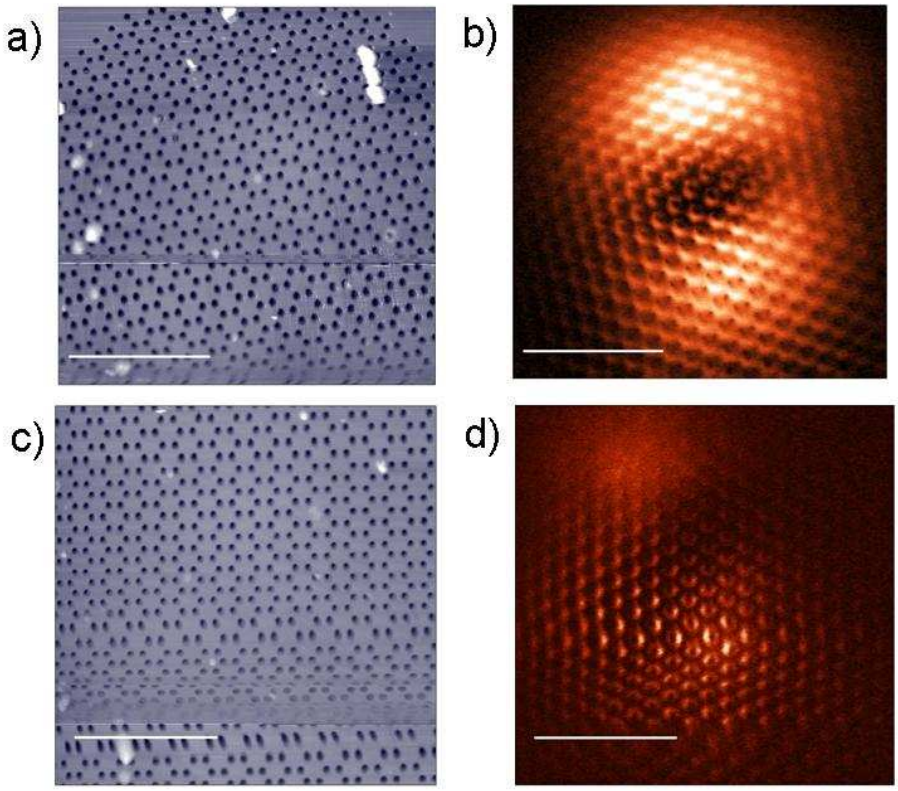

Figure 4.9: a) Topography in shear-force mode with metallized tip N°1. b) Near-field distribution of intensity of mode-M recorded with tip N°1 at 1611 nm, the scaling bar is 5 µm. c) Topography with tip N°2. d) Near-field distribution of intensity of mode M recorded with tip N°2 at 1611 nm. The scaling bar is 5 µm.

Figure 4.10 shows the zoom-in at the center area of Figure 4.9-d. The array of small doughnuts is indeed present in each unit cell of the honeycomb lattice. The dimensions of these doughnuts are 310 nm for the outer radius and 70 nm for the inner radius which is comparable with the theoretical prediction in Figure 3.8 of section 3.3.

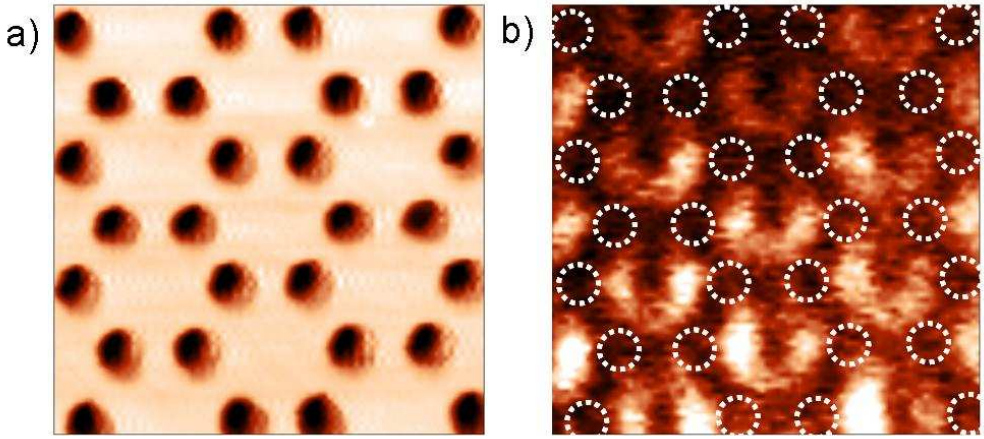

Figure 4.10: Detail of the M-mode at the center area of Figure 4.9-d. a) Topographic image b) Optical near-field image at 1611 nm (2.5µm x 2.5µm), circles indicate holes positions of the 2D-PC.

From near-field images, mode expansion inside the PC can also be inferred. Figure 4.11-a presents the mode expansion recorded under the same excitation conditions as Figure 4.9. Though the tip is still collecting an amount of radiating light which accounts for the slight non-uniformity of the mode, it clearly shows that the mode reaches a maximum at the centre and decreases monotically, in agreement with the predicted, theoretical mode profile (Figure 3.8-g of section 3.3.2).

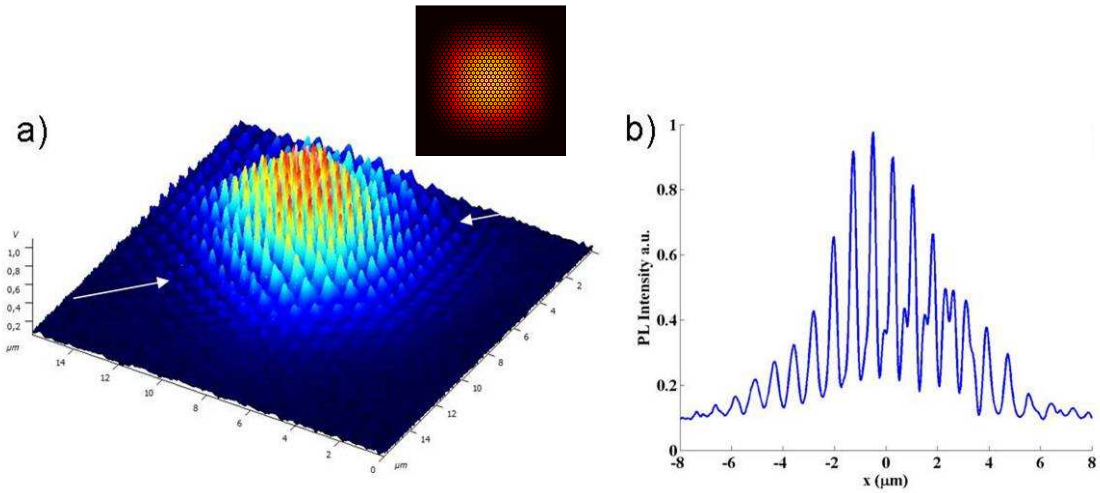

Figure 4.11: a) Near-field intensity distribution of mode-M collected with tip N°2 at 1611 nm and (inset) simulation of mode pattern. b) Mode section recorded along the white arrow direction of a).

Cross section recorded along the symmetry axe of the honeycomb lattice as shown in Figure 4.11-b yields an estimation of the size of the mode at the surface of the PC: considering the decay of the mode at $1/e^2$, the width of the mode is $(12.8 \pm 1)\mu m$ which is of the same order of magnitude as the excitation spot. Taking this as the diameter of the beam waist, a divergence of 2° is expected for this beam. The correlation between the excitation spot size and the mode surface tends to confirm the modification of refractive-index induced by the pump. The SBM mode confinement is attributed to the optical well created by the step-index existing between the pumped area and the unpumped area[1]. Experiments with variable pumping area to study the relationship between the pump size and the mode size are described in the section 4.3

Other measurements could also be conducted to investigate the mode distribution of the hexapolar and dipolar modes. However, for the hexapolar mode, we don't expect to have more information than what the dielectric is able to yield. For the dipolar mode, the optical signal emitted in spontaneous emission may be not sufficient to obtain a clear image.

Conclusion

We successfully investigated the near-field distribution of slow Bloch monopolar mode at Γ-point on perfect honeycomb structure by NSOM in collection mode. The array of doughnut patterns repeated by unit cell is obtained. This result enables the unambiguous identification of the monopolar mode with the 3D-FDTD simulations. In addition, the simple and direct generation of pure azimuthally doughnut laser beam with a 2D-PC honeycomb lattice is demonstrated. This opens up the way to other perspectives for the development of such micro-lasers, as the total field symmetry of azimuthally polarized mode makes it suitable for applications as optical trapping[2] or high numerical aperture focusing. The importance of the tip selection for studying III-V photonic crystal structures is also demonstrated. With vertical emitting structures bare silica tip is not adequate for near-field mode inspection. Conversely, metal coating tip is able to reveal the near-field patterns of the optical modes. However, the collected intensity is much weaker due to the nano-size of aperture. The ideal tip should be designed to optimize the coupling between the mode and the tip. Functionalized tips with nano-antenna could meet this requirement[3]. Besides, as nano-antenna response is polarization dependent, it should yield local information on the polarization of the mode at the surface.

4.2. Surface mode with BNA-tip

In this part we present the NSOM results obtained with BNA-tip acting as nano-collector and polarizer to investigate the full optical properties of slow Bloch mode on defect-free honeycomb planar photonic crystal. The full optical images of electromagnetic field distribution of slow modes in both polarization components are revealed in the first time. These results allow to validate the BNA-probe concepts using in optical near-field characterization of nanophotonic structures.

4.2.1. Introduction

The near-field experiments are performed with the NSOM set-up that has been described in section 4.1. The BNA-tip working in collection mode is used to map the slow Bloch mode intensity patterns at the PC surface. In NSOM shear-force mode, the constant distance of about 5-10nm between BNA and 2D PC surface is regulated by piezoelectrics with feedback loop. In our measurements, the orientation of BNA tip is fixed with respect to the scanning direction. To record the different polarization components (E^2_x, E^2_y), the sample must be rotated while other experimental conditions are kept unchanged.

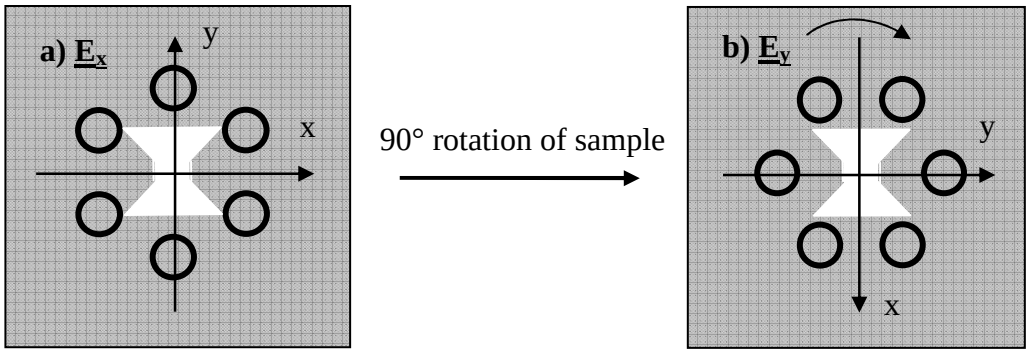

Figure 4.12: Definition of x and y-axis attached to unit cell of PC determines the in-plane components of electric fields E_x and E_y. The optical axis of BNA orients horizontally with respect to this page and was kept unchanged during experiment as convention. The configuration a) was used to map the E^2_x intensity component (the optical axis of BNA is parallel to the x-axis). b) For E^2y component, the sample must be rotated so that the BNA axis is parallel to the y-axis.

By convention, the x-axis and the y-axis will be defined with respect to the honeycomb lattice unit cell. Figure 4.12 presents the definition of coordinate x-y axes attached to the hexagon configuration of PC.. In Figure 4.12-a, the BNA axis is parallel to the x-axis and this is used to map the intensity of E_x component. In Figure 4.12-b, the sample is rotated of 90° so that BNA axis is now parallel to the y-axis of the sample and this is used to map the intensity of E_y-component.

Scanning of the BNA-tip in the near-field allows to measure the topography and cartography simultaneously. They provide information of PC structure, optical resonances, distribution of mode on surface, the polarization status of electric field and the expansion of mode over structure. We will mainly focus on the monopolar mode of structure G3.

4.2.2. Spectroscopic results

The interaction of near-field tip to Bloch mode of PC has been investigated recently since it may lead to several new effects, such as optical loss inducing, mode quenching, non-linear effect, quality factor modification, spectral tuning for micro-laser[4,5] or photon funneling... However, the contribution of these effects to the near-field modes is still unknown and under investigation. These leave problems to record the real optical response of PC, to truly probe the Bloch mode pattern or accurate interpretation of NSOM optical images. Especially, if the NSOM experimental results are aimed at study of the mode distribution on PC structure, as in our case, the optical impact of NSOM tip must be taken into account.

Figure 4.13 shows spectra of the slow Bloch laser mode (M) recorded by photoluminescence set-up in far-field (red curve) and by NSOM set-up with BNA-tip[(*)] in near-field (blue curve). In both configurations the experimental conditions, such as the PC structure, excitation laser diode (power and pulsed condition) are kept unchanged for comparison. The BNA-tip of NSOM operates in shear-force mode (located 10nm from surface) to ensure the immersion of tip in near-field zone. As a result, we find in the

[*] The lasing peaks are obtained in both cases of E_x- and E_y-polarization as in Figure 4.13 with BNA-probe working in collection mode. The resonant wavelengths are identical for both E_x and E_y-components.

spectra that, the lasing wavelength was not altered without and with the present of BNA-tip, corresponding to the case of far-field and near-field measurement as indicated in Figure 4.13-a. This indication is re-proved by far-field radiation image taken by IR camera in Figure 4.13-b. No change occurs as brings the BNA-tip to the doughnut vice versus. Again, this is a very good indication that the tip does not perturb the near-field slow Bloch mode. Conversely to cavity mode, large stationary modes as well as slow band-edge modes are more robust to small perturbation as a BNA-tip.

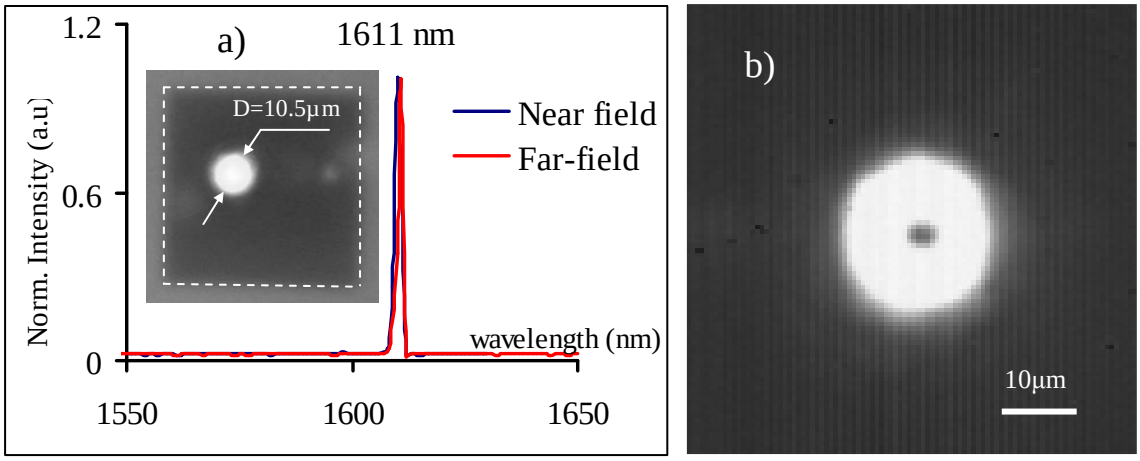

Figure 4.13: a) Near- and far-field spectra of lasing mode. The inset presents the excitation spot. b) The far-field radiation surface pattern of mode M in doughnut shape (taken by IR camera) is unchanged in presence of BNA-tip.

4.2.3. Polarization investigation

As above-mentioned, the intensity mode patterns depend on the orientation of BNA-axis versus the structure. The partial polarization of field (E^2_x or E^2_y) has been recorded by BNA-tip according to NSOM configurations shown in Figure 3. The following sections will address these results in details.

a. E^2x intensity pattern

In order to map the E^2_x-component of slow Bloch mode M on PC structure, the BNA and structure orientation have to fulfill the configuration of Figure 4.12-a (BNA axis is parallel to the x-axis of structure). The 40x40µm² honeycomb structure is illuminated through an objective x40/0.6NA by a 780nm-pulsed pumping laser. The excitation light

forms a spot on sample with diameter of 10.5µm. The details of NSOM set-up and operating conditions were described in section 2.1.

Figure 4.14 presents the NSOM topographic and optical images of the E^2_x-component intensity of the monopolar lasing mode at λ=1611 nm. Figure 4.14-a shows the shear-force image with scanning area of 15x15µm² in which the air holes in honeycomb structures are clearly visible (black circles). This demonstrates the ability of BNA-tip to yield correct topography despite its dimension and confirms the near-field working mode of NSOM. The inset at left corner of this image indicates the direction of BNA axis with respect to a unit cell of PC structure. The 10.5µm-pumping laser spot is shown as a dashed blue circle. A small defect imprinting on PC structure (blue arrow) is used as a marker to identify the rotation of sample. The other white spots are "dust" particles and do not impact on the distribution of mode in the optical image.

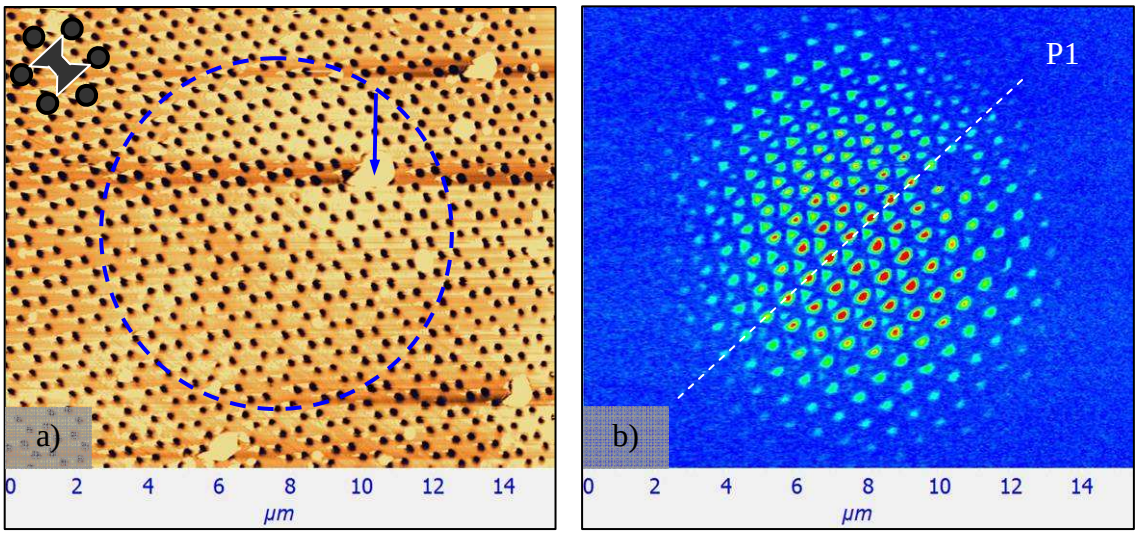

Figure 4.14: NSOM images of honeycomb 2D PC. a) A shear-force topography with honeycomb structures confirms the near-field mapping of NSOM. A PC defect at blue arrow (indicated also in cartographic image) plays as a marker for sample orientation when rotating. The dashed blue circle presents the excitation spot position with diameter of 10.5µm. b) E^2_x-component of fundamental mode M obtained with BNA-tip at λ=1611nm with marker. The dashed line P1 presents the cross section of mode profile.

We observe the modulation of mode (bright spots) with periodicity of 730nm in optical image of Figure 4.14-b. This value is of the same order as the fabricated lattice parameter of PC and strictly confirms the ability of BNA-tip to couple the evanescent field

on surface. The dashed line P1 in this figure presents the mode profile in order to reveal the periodicity of spots and the expansion shape as shown in Figure 4.15. The mode seems to be confined in a "cavity" created by excitation spot in which the highest intensity falls at its center. The fitting curve (in pink line) with Gaussian function is in a good agreement with the simulation prediction as shown in Figure 3.8-g of section 3.3.2. The mode expansion will be discussed more detailed in section 4.3.

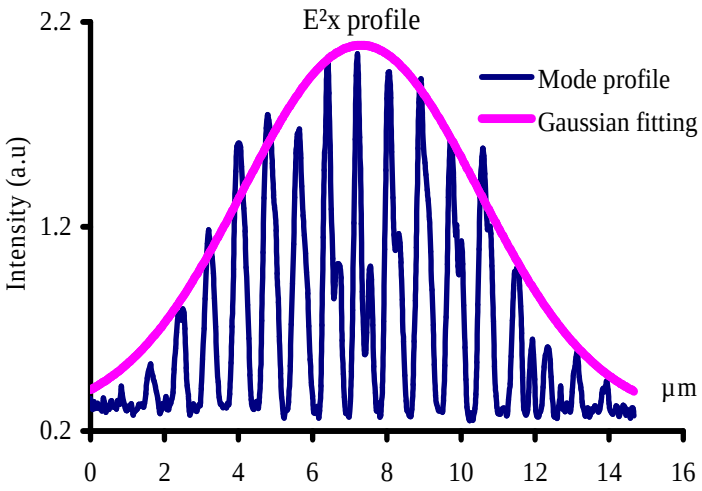

Figure 4.15: E_x intensity profile of mode M along cross section P1 in Figure 4.14-b. The maximum intensity is in the center of profile. The Gaussian envelop fitted to the mode profile confirms the Gaussian expansion of mode as simulation prediction.

In order to identify the mode distribution with respect to the photonic crystal structure, the overlap of topographic and optical image is performed. Figure 4.16-a presents a zoom into a unit cell of an experimental intensity pattern; the PC structure, deduced from the topography is in black. As a result, we found that the field distributes inside each unit cell and is decomposed into two lobes separated by the BNA-axis direction (horizontal) Figure 4.16-b. shows the 3D-FDTD simulation obtained for E^2_x The results obtained by BNA-tip agree very nicely with the simulation prediction of E^2_x field pattern.

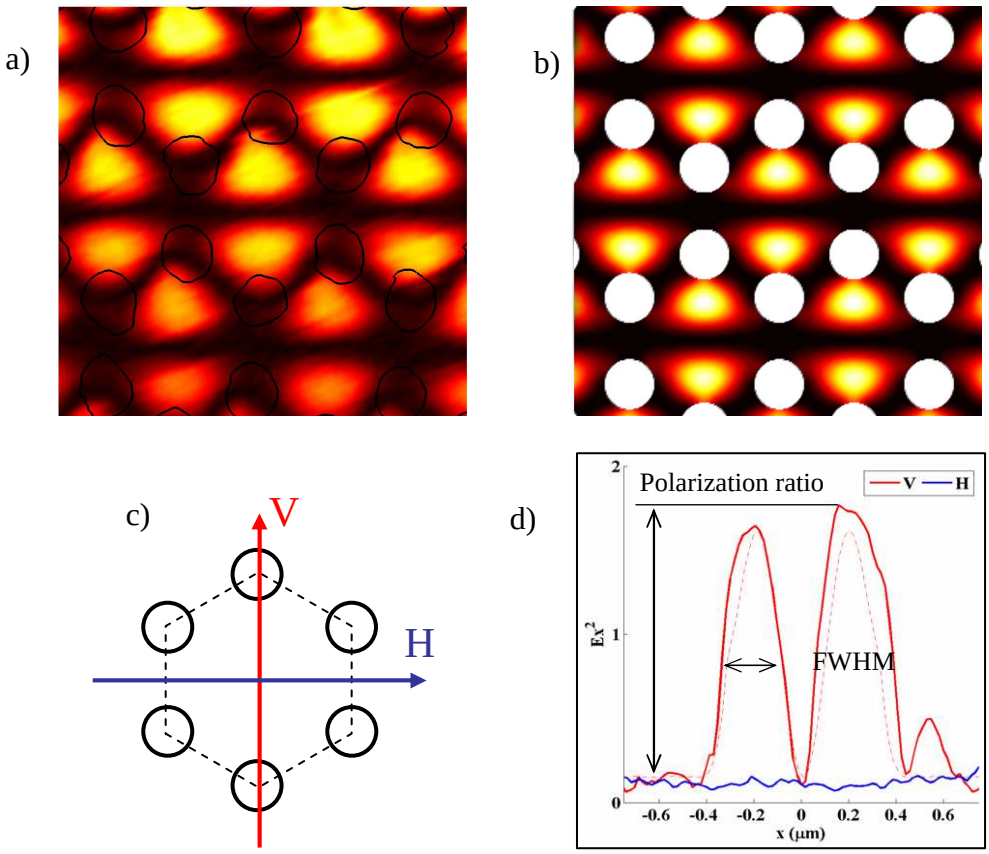

Figure 4.16: Zoom of near-field intensity pattern and its profile. (a) Experimental intensity pattern obtained by BNA-tip. Black circles are present the air holes of PC structure which are obtained by matching with topographies. (b) Image shows numerical simulation result of E²x-component pattern at several unit cells. The white circles present the air holes of PC structure. c) Sketch defines the cross section directions. Vertical direction (V, red) is parallel to y-axis while Horizontal one (H, blue) is orthogonal and parallel to x-axis. (d) Intensity profiles along V- (blue), H-direction (red) of figure a) with respect to simulation profile of figure b).

b. Polarization ratio in E^2_x-pattern

The mode profiles along the horizontal and vertical sections of unit cell of E^2_x are plotted in Figure 4.16-d along with the theoretical profiles. The red curve in vertical direction shows two strong peaks where E_x-component is dominant. On contrary, E_x-component is almost zero in the horizontal direction (blue curve). In the horizontal direction, only the Ey-component is present. The experimental blue profile simply shows that no Ey-component was coupled into the fiber through the BNA tip. Actually, the polarization ratio is difficult to evaluate as the remnant intensity polarization is of the

order of the background noise. A minimum value is estimated to be 1:150 (of the order of the signal to noise ratio). By comparison, the signal to noise ratio obtained with a circular aperture tip is in the order of 10. It evidences the fact that the BNA tips indeed play the role of a nano-polarizer. FWHM (full width at half maximum) value estimated from Figure 4.16-d can provide information about the lobe size. This is also much greater than the theoretical value of 1:37 presented in section 2.2. However, this last value was calculated in the case of a plane wave illumination and should be corrected in the case of dipole excitation for instance.

This result demonstrates the fact that BNA can couple efficiently the field parallel to its optical axis. It also proves that NSOM cartography in Figure 4.16-a) contains only the E^2_x-component. This property is due to the polarization sensitivity provided by the feedgap of BNA. In theory, BNA resonates only with the electric field polarizing along its optical axis while filters out the orthogonal components[3, 6]. We also see that the experimental width of the lobes (260 nm) is very close to the theoretical value (250 nm). It means that the field modulation is greater or of the range of the tip resolution. It may indicate that the tip resolution is underestimated and that we could obtain the real tip resolution with smaller field modulation.

c. E^2y intensity pattern

The E^2_y-component of slow Bloch mode M on honeycomb PC structure is recorded with PC structure rotation of 90^0 (configuration of Figure 4.12-b) in comparison with the case of E^2_x-component as shown in section 4.2.3. As a result, the BNA optical axis is parallel to the x-axis of structure. The experimental conditions (the same location and scanning area on a given structure, objective, pumping power, pulsed condition of laser, excitation spot size and BNA-tip in collection mode) are kept unchanged with respect to the case of E^2_x mapping in order to compare the obtained results between the intensity of E_x- and E_y-components.

Figure 4.17 presents the NSOM topographic and cartographic images of E^2_y-component intensity of lasing mode at λ=1611 nm. Figure 4.17-a shows the shear-force image with 15x15µm² scanning area in which the air holes (black circles) in honeycomb structures are clearly visible. This image proves the ability of BNA-tip to reveal the correct topography with high spatial resolution and also justify the near-field working

mode of NSOM set-up. The inset at left corner of this image indicates the direction of BNA axis with respect to a unit cell of PC structure which is rotated 90^0. A small defect at the blue arrow on topography is used to verify the rotation of sample.

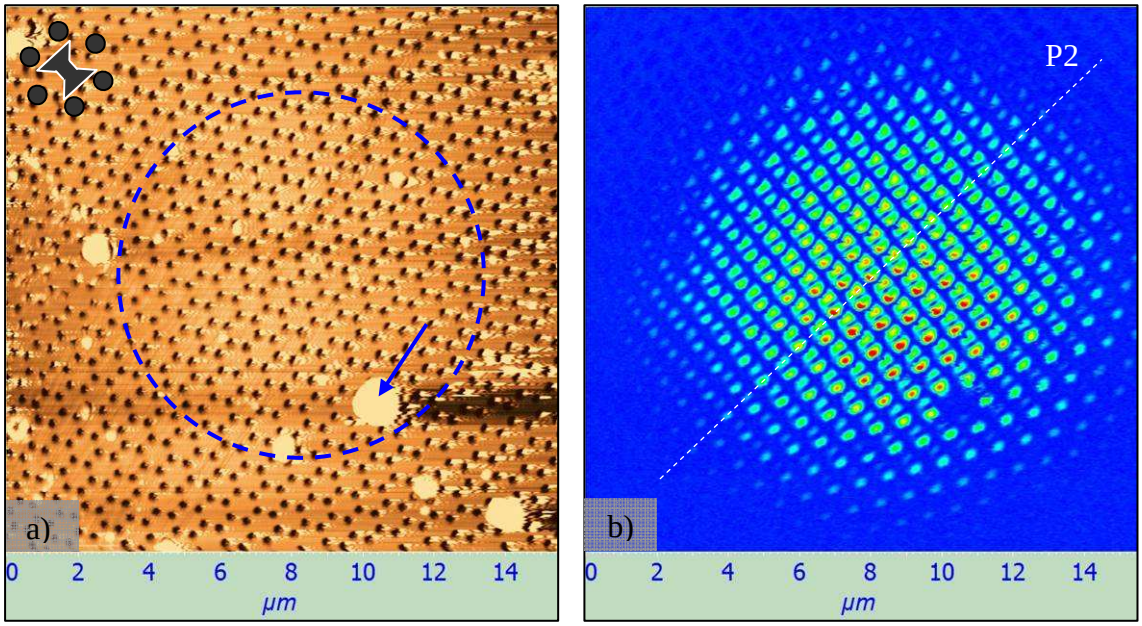

Figure 4.17: NSOM images of honeycomb 2D PC. a) shear-force topography with honeycomb structures confirms the near-field mapping of NSOM. A PC defect at the blue arrow (indicated also in cartographic image) now rotates 90^0 with respect to the case of E_x-component. The dashed blue circle presents the excitation spot position with diameter of 10.5µm. b) E^2_y-component cartography of the fundamental mode M obtained with BNA-tip at λ=1611nm. The dashed line P2 presents the cross section of mode profile.

Similar to the case of E^2_x-component mapping, we observe the modulation of slow Bloch mode (bright spots) with periodicity of 730nm in optical image of Figure 4.17-b. This period is the same order of the fabricated lattice parameter of PC and thus confirms the ability of BNA-tip to couple the evanescent field on PC surface. In order to reveal the periodicity and the expansion shape of mode on surface, the profile along the dashed line P2 is shown in Figure 4.18. At the center of profile, the mode intensity gets highest and decays as a Gaussian function to the edge of excitation spot. The Gaussian envelop (pink curve) demonstrates the simulation prediction. However, unlike the simulation, the PC structure size is not responsible for mode confinement but the excitation spot is[1]. Further discussions of mode expansion can be found in section 4.3.

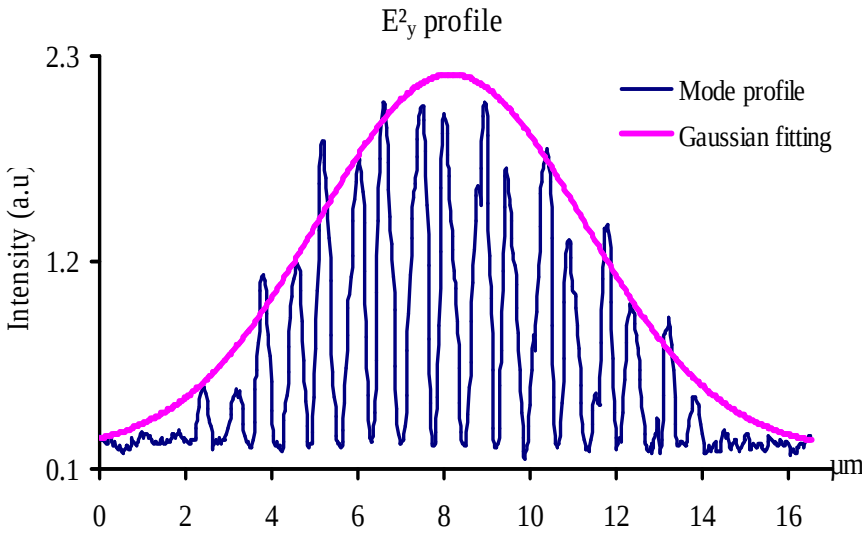

Figure 4.18: E^2_y-profile of mode M along cross section P2 of Figure 4.17-b. The maximum intensity is in the center of profile. The Gaussian envelop fitted to the profile confirms the Gaussian expansion of mode as simulation prediction.

Figure 4.19-a presents the zoom into unit cells of an experimental intensity pattern with presence of PC structure in black circles. This pattern allows to identify the mode distribution with respect to honeycomb structure done by the overlap of topographic and optical image. As for E^2_x, we find that E^2_y-component distributes only inside each honeycomb unit cell. The pure doughnut-like shape of total field intensity ($E^2_x+E^2_y$) in unit cells is now decomposed into two lobes separated by BNA-axis in vertical direction. These results obtained by BNA-tip perfectly agree with the simulation prediction of E^2_y field pattern as shown in Figure 4.19-b.

a) b)

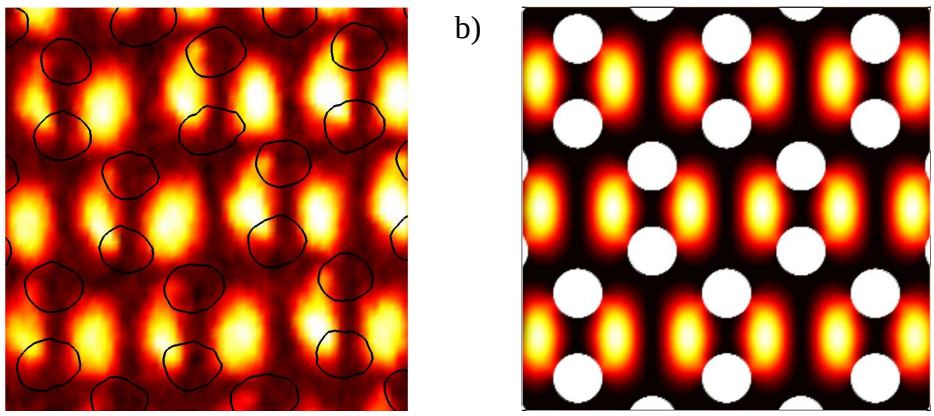

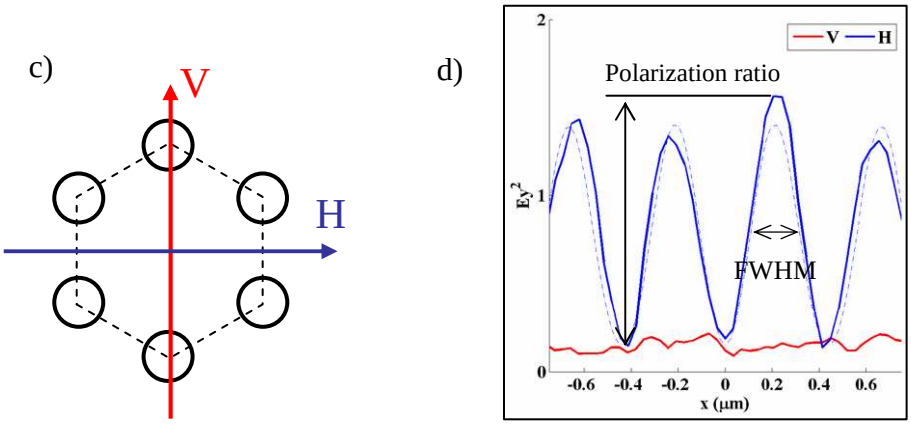

Figure 4.19: Zoom of near-field intensity pattern and profile. (a) Experimental intensity pattern obtained by BNA-tip. Black circles present the air holes of PC structure which are obtained by matching with topographies. (b) Image shows numerical simulation result at several unit cells for E^2_y-component. The white circles present the air holes of PC structure. c) Sketch defines the cross section directions. Vertical direction (V, red) is parallel to y-axis while Horizontal one (H, blue) is orthogonal and parallel to x-axis. (d) Intensity profiles along V- (blue), H-direction (red) of figure a) with respect to simulation profile of figure b).

d. Polarization ratio in E^2_y-pattern

Mode profiles shown in Figure 4.19-d along vertical and horizontal directions (sketched in Figure 4.19-c) for each component in a unit cell could provide the information about polarization ratio between two orthogonal components. The blue curve in horizontal direction with four periodic peaks present the field intensity where E^2_y-component is dominant. On contrary, the red one in vertical direction E^2_x-component is dominant (as shown previously in Figure 4.16-d). The red profile only show background noise which confirms that no E_x component was coupled into the BNA tip. We see that the experimental lobe size is quite identical to simulation result (dashed blue line). The results obtained for E^2_y-component is very similar to those showed previously for the E^2_x-component. The same polarization ratio was reached.

In summary, experimental measurements of E^2_x and E^2_y-component demonstrate explicitly the fact that BNA is able to provide a specific sensitivity to the vectorial electromagnetic field along its optical axis. In this sense, BNA-tip acts as an efficient

nanopolarizer for probing the optical field in the neighborhood of the structures used in nano-photonics with unprecedented spatial resolution and field enhancement.

4.2.4. Electric field coupling enhancement

Field enhancement and confinement are the natural phenomenon in antenna theory. They occur because an antenna concentrates electromagnetic energy into a tight space of feedgap thereby generating a zone of high energy density. As simulation, the enhancement of electric field is attributed to the oscillating electric dipole as charges accumulates inside the feedgap of BNA[3,7]. These optical properties are responsible for increasing the spatial resolution of optical images and near-field coupling efficiency. The experimental coupling efficiency is a direct factor that reflects the field-enhanced ability of BNA and is able to estimate as following method.

Estimation of coupling enhancement (Φ)

We supposed that the intensity indicated in NSOM cartography (I_{carto}) is governed by a function of several parameters:

$$I_{carto} \sim I_{LD} \times F_{tip} \times F_{slit} \times F_M \qquad (1)$$

Where I_{LD}: optical intensity measured at the output of laser diode. This value is typical kept constant (around 3.8mW) by applied the same electrical intensity (57mA) in pulse generator.

F_{tip}: coupling coefficient of tip (ability to couple the evanescent field) being calculated by ratio of in-coupling and out-coupling intensity of tip

F_{slit}: the transmission function of slit versus slit opening on monochromator. This will be determined experimentally at 70µm and 40µm of slit opening.

F_M: multiple factor of monochromator (equal 1 or 10).

If we did experiment at the same conditions in both cases (experimental configuration, objective, conditions of laser diode and resonant wavelength), the coupling efficiency (Φ) of BNA-tip may be calculated as the ratio of coupling coefficient between BNA-tip (BNA) and metal coating tip (Metal). From equation (1) we deduce Φ value by comparing both sides of equation in cases of BNA and Metal.

$$\Phi_{coupling} = \frac{F_{tip}^{BNA}}{F_{tip}^{Metal}} = \frac{I_{Carto}^{BNA}}{I_{Carto}^{Metal}} \times \frac{I_{LD}^{Metal}}{I_{LD}^{BNA}} \times \frac{F_{Slit}^{Metal}}{F_{Slit}^{BNA}} \times \frac{F_{M}^{Metal}}{F_{M}^{BNA}} \quad (2)$$

The optical intensity in NSOM cartographies I_{Carto} was measured at the same position on photonic crystal in two cases. Since applied voltage of laser diode was kept constant, the ratio of I_{LD} in equation 2 is equal unity. The table below provides the values of involved parameters.

	I_{carto} (V)	I_{LD}	F_{Slit}	F_M
BNA-tip	2.4	57mA/3.6mW	0.155 (at 40µm)	1
Metal tip	1.2	57mA/3.6mW	1.0 (at 70µm)	10

Replaced into (2): $\Phi_{coupling}$ = (2.4/1.2) x (1.0/0.155) x (10/1) = 130 ± 5%

The error of 5% is attributed to F_{slit} experimental measurement.

Even if the calculated value of the coupling efficiency is not absolute, it is possible to give a relation between a NA-tip versus a metal-coating tip: we found a relative value of two orders of magnitude. The simulation provides a value of 350, which is of the same order as experimental result.

4.2.5. Electric field confinement- Spatial resolution

The field confinement inside the gap zone is responsible for the spatial resolution of NSOM optical images. However, it also alters the resonant spectrum of nano-antenna (increase of gap size leads to blue-shift) as the restoring force between the polarized charges varies with the gap size[4]. The gap size is limited by the spatial resolution of fabrication devices. Recently, a 30nm-gap size bowtie nanoantenna was fabricated and used to pattern nanostructures on polymer resist with FWHM of 30nm[8].

The BNA-tip used in our experiment have gap sizes of 45nm in order to resonate at the wavelength of 1.55µm. In order to estimate the spatial resolution of these NSOM cartographies, Fast Fourier Transform (FFT) of E^2x and E^2y optical images are performed to estimate he spatial cut off frequency of the optical image. The Figure 4.21-b/d shows the FFT images of E^2_x and E^2_y cartographies with two corresponding center cross section profiles (Figure 4.21-e/f). The FFT spatial frequency profiles of mode in reciprocal space

at the lowest peaks present the detectable limitation between two spots on optical images. In order to enhance the low intensity peaks, the background light at center of FFT image was removed. The inversed values of the lowest peaks provide the spatial resolutions of cartographies in real space. As a result, the feature of 135 nm (~ λ/12) and 120 nm (~ λ/13) are obtained for E^2_x for E^2_y images respectively. It is clear that in case of BNA-tip, the spatial resolution of optical image is a convolution between the aperture dimension of BNA (45nm) and optical distance of these separated nano-objects. As indicated in Figure 4.20, the spatial resolution values are corresponding to the closest distances between two lobes in the unit cell of E^2_x and E^2_y-components which are found approximately 135nm and 120nm respectively. The different distances explain the different values of spatial resolution for E^2_x and E^2_y-optical images obtained with the same BNA-tip. This also demonstrates the ability of BNA-tip to reveal all the smallest optical spots in cartographies.

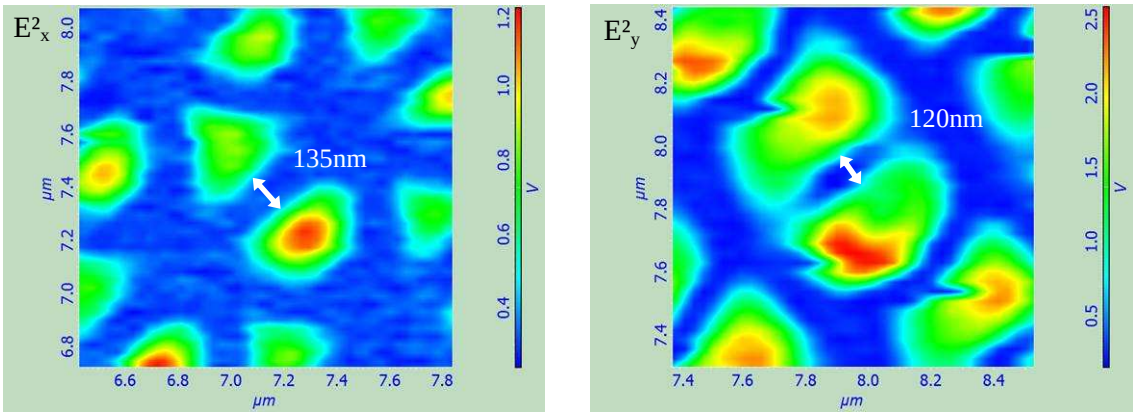

Figure 4.20: Zoom of cartographies to show the modes E^2_x and E^2_y in unit cell. The spatial resolution corresponds to the distance between two closest lopes.

The spatial resolution achieved on cartographies is in good agreement with theoretical ability of BNA-tip to resolve the objects placed in distance. As we said previously, since the closest distance between two objects in unit cell is limited to 120nm ~ λ/13 as simulation, the real spatial resolution of BNA-tip might be higher than the value of λ/13.

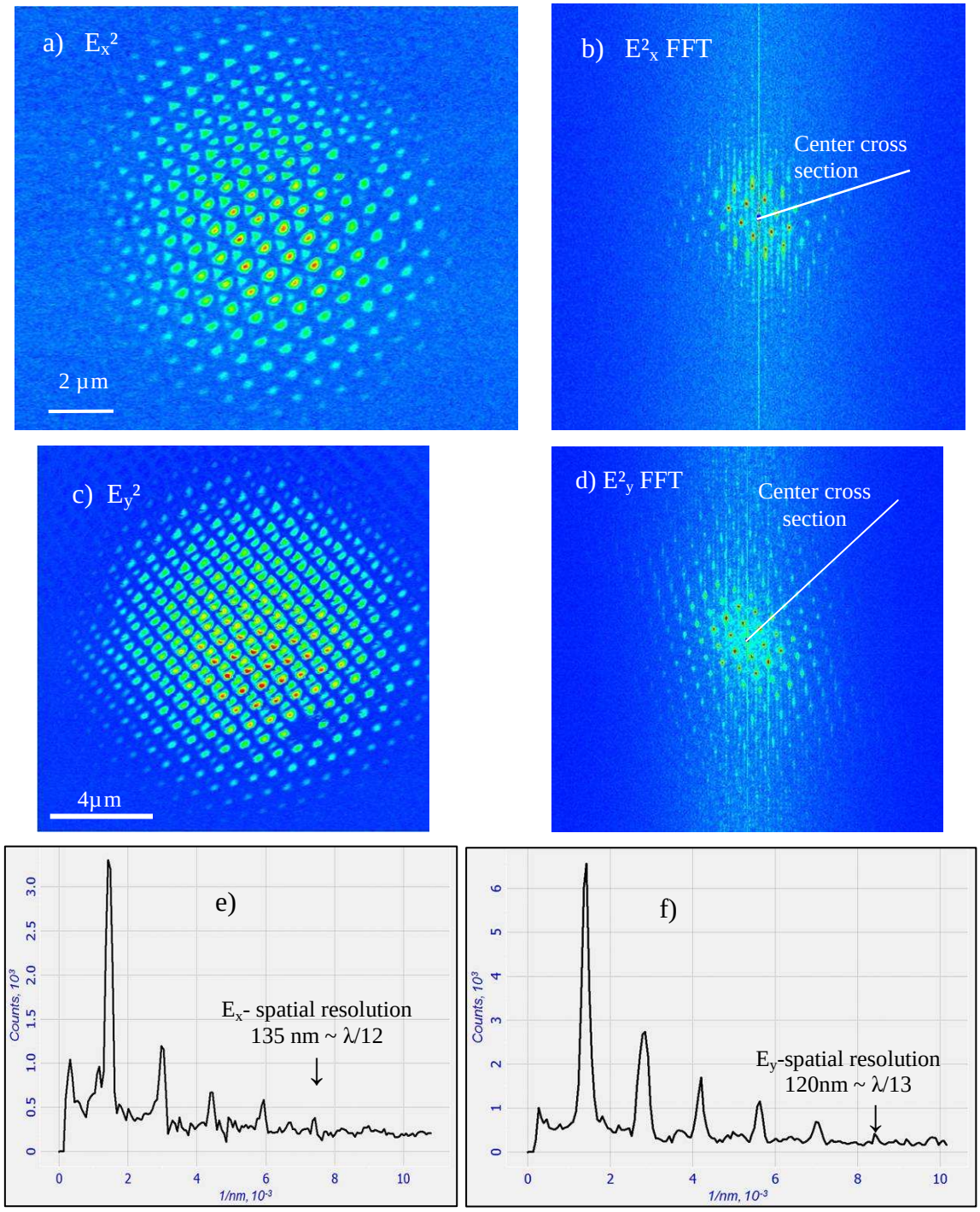

Figure 4.21: a/c) E^2_x and E^2_y cartographies of mode M at λ=1611 nm, mapping with BNA-based NSOM. b/d) Fast Fourier Transform (FFT) of E^2_x and E^2_y cartographies, with the cross sections through the center. The strong background light at the center of FFT images is removed to emerge the low intensity peaks. e/f) The spatial frequency profile of E^2_x and E^2_y mode in b) and d) in reciprocal space shows the detection limit at 7.4 (nm^{-1}) for E^2_x and 8.3 (nm^{-1}) for E^2_y. The inversed values provide the spatial resolutions, which are 135 nm (~ λ/12) for E^2_x and 120 nm (~ λ/13) for E^2_y in real space.

Conclusion

We have characterized the optical properties of slow Bloch modes on defect-free honeycomb PC using NSOM based on BNA-probe. This tip acts as nano-collector and nano-polarizer thanks to their abilities for field confinement and enhancement at gap zone. The NSOM optical images were successful to reveal the details of electric field components (intensity and polarization) distributed in each unit cell of PC with the least spatial resolution of $\lambda/13$. The enhancement of electric field by BNA-tip was also recorded in comparison with the metal-coating probe, and is of two orders of magnitude. The excellent agreement between the simulation and experimental results has strongly demonstrated the validity of using BNA-probe for further investigations on nanophotonic structures.

4.3. Surface mode expansion

4.3.1. Introduction

As presented in section 4.2, there is a discrepancy between simulation and experiment results about the slow light mode expansion on PC. The simulation predicts that in perfect PC slow light mode could expand to the PC boundaries. However, in our case we are dealing with active structures, where the pump light matter interaction can play a major role on the light confinement. Several effects can be involved: index changes (induce by to carrier-injection or thermal effect) or gain guiding (confinement by the gain). Our experimental results demonstrated that the confinement of slow light always takes place around the excitation spot. Some experiments have been conducted to determine the mechanism responsible for the light confinement.

4.3.2. Measurement of excitation spot size (S_E)

The excitation spot size is an important parameter as it determines the excited area of structures as well as the optical density of pumping light. In order to change the excitation spot size (S_E) one could use the objectives with different magnifications. In fact our experiments were mainly performed using two objectives (x63/NA0.75 and x40/NA0.6) that have very good transmission in infra-red region.

The transparent sample was pumped by a modulated laser diode (λ=780nm) and a corrected objective was used to focus pumping light on structure, from its backside. The reflected light was collected by the same objective and directed to visible CCD camera for in-line observation of the sample. In this way, the excitation spot size can be measured with the optical images provided by this camera. Figure 4.22 presents the intensity profiles of the excitation spot on sample with the two objectives: 40x (Figure 4.22-a) and 63x (Figure 4.22-b). Pumping profile curves can be well-fitted with a Gaussian function (indicated in pink solid lines). By convention, the spot size corresponds to the width of the Gaussian curve (taken at I_{max}/e^2) (see Annex C). As a result, we obtained the values of L_{40X}=9.8µm (spot width with objective 40x) and L_{63X}=6.4µm±0.2 (with objective 63x). The error of 0.2µm in L_{63X} is caused by the mismatch in fitting between the real profiles and Gaussian functions.

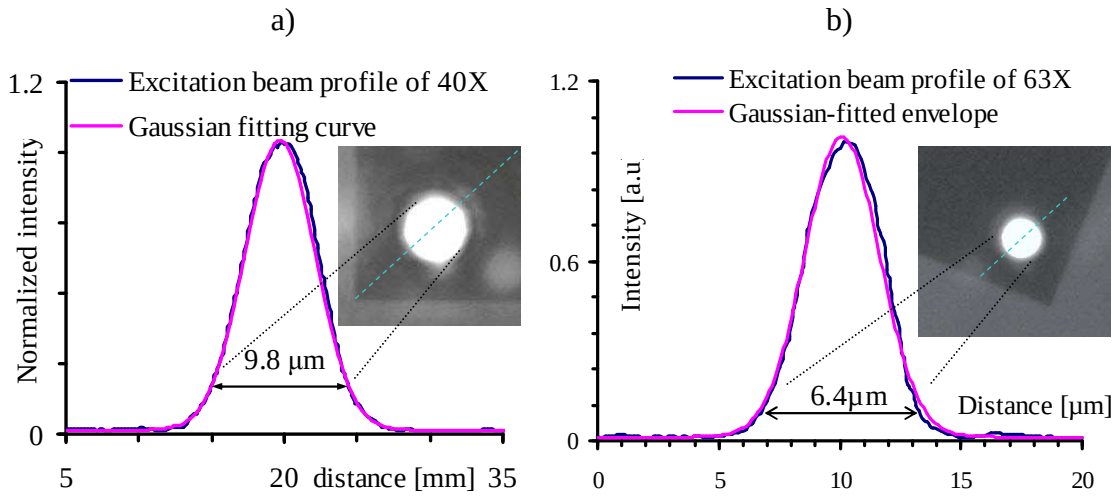

Figure 4.22. Excitation spot size (S_E) on estimated from optical images captured by CCD camera. Spot size is estimated at the width of Gaussian-fitted envelope (amplitude of 1/e²). a) Spot size with 40X objective of 9.8µm. b) Spot size with 63X objective of 6.4µm. The insets in two figures show optical images taken by visible camera.

4.3.3. Surface mode (L_M) v.s Pumping power (P_{LD})

First, we investigated the impact of pumping power on the confinement of light. In order to minimize the unwanted contributions of other factors to our NSOM optical patterns, the experimental conditions were kept unchanged between two measurements (using objective X40, x-direction-oriented BNA-tip and the same mapping location). The pumping power of laser (at λ=780nm) was controlled precisely by impulse generator and monitored by indicator. There are two levels of laser power were used: P_{LD}=44µA (close to the lasing threshold) and 100µA (maximum supplied current of device).

Figure 4.23-a/b show the NSOM optical images mapped with BNA-probe for E_x^2-component. The surface expansion in several directions was measured as the diameter of circle limited by the visible bright spots in optical images. With pumping power of 44µA, the mean value of expansion is 17.68 ±1.46 (µm). This value for P_{LD}=100 µA is 12.9±1.46 (µm). The error of 1.46µm is equivalent to the error of taking the bright spots at the boundary or twice of lattice A (0.73µm) of honeycomb.

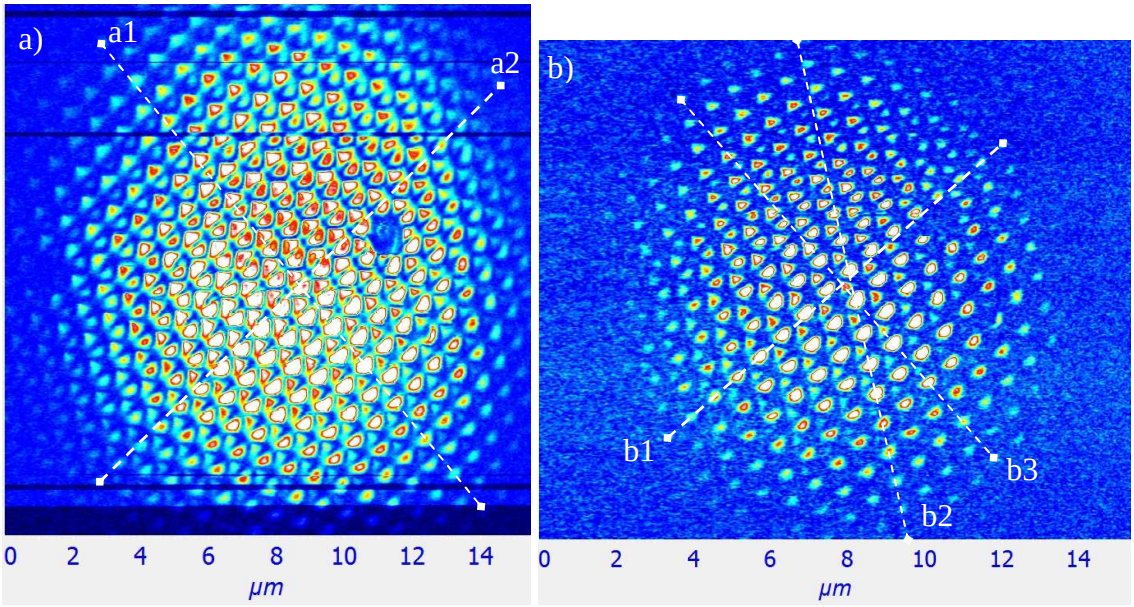

a1=17.84µm a2=17.51µm Conditions: objective X40 (S_E = 9.8µm), E^2x-components P_{LD}=44µA	b1=12.41µm b2=12.68µm b3=13.28µm Conditions: objective X40 (S_E = 9.8µm), E^2x-components P_{LD}=100µA

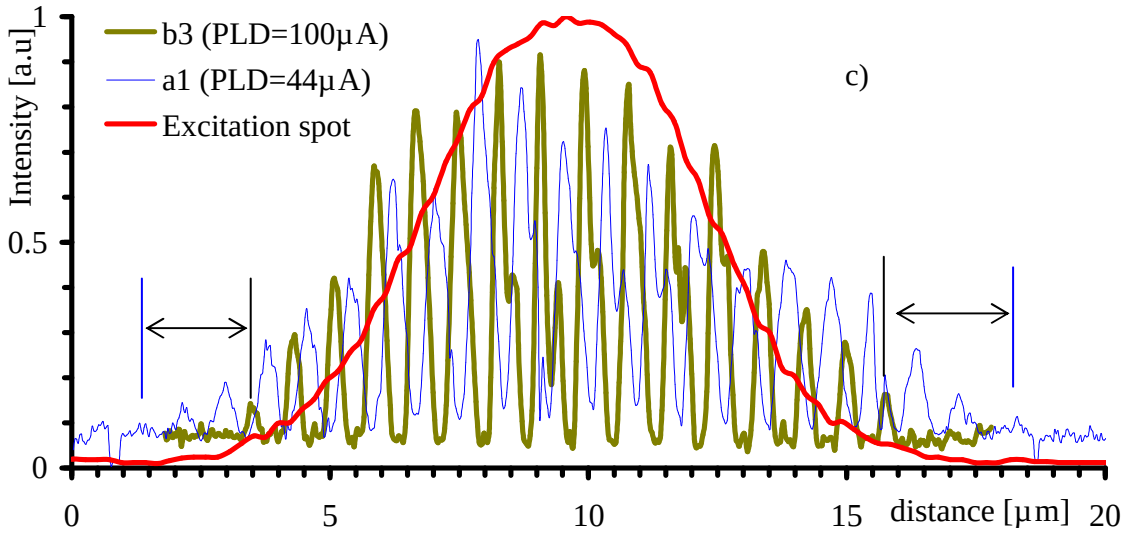

Figure 4.23: a-b) E^2_y NSOM optical patterns obtained with BNA-tip. The expansion length of mode was determined by measuring the longest distance between visible bright spots (along the cross section profile a1, a2 (Figure a) and b1, b2, b3 (Figure b)) and taking the mean value.c) Overlapping of profile cross section along a1 and b3 on optical images and excitation profile (red curve). The arrows show the expansion length (µm).

These results tend to show that the mode is more confined with a higher pumping power. However, the explanation is still unclear. If the confinement was due to an index induced change, the pumped area should see its global index decreasing because, as the band curvature is negative for this mode at the Γ-point, the index variation should also be negative[9]. In our case, we observe a red-shift of the lasing wavelength with the increasing power (see Figure 4.24), which means that thermal effects are dominant and that the index of the pumped zone increases. A confinement by the gain would explain a larger mode area with a higher pumping power. We observe an opposite behavior.

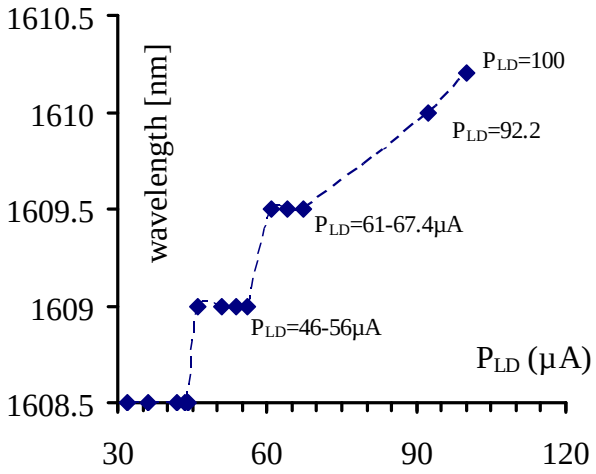

Figure 4.24. Lasing peaks red-shift with increasing pumping power.

4.3.4. Surface mode (S_M) *v.s* Excitation spot size (S_E)

In this experiment, we investigated the impact of the excitation spot size (by changing the objectives) on the surface mode expansion. The mode patterns were mapped using BNA-probe the as shown in Figure 4.25. From these images, the total expansion of the mode can be easily estimated. The mode expands in the structure with a hexagonal symmetry and we can easily define the mode boundaries. Despite the different excitation conditions, we found a similar mode width of 15µm for both cases. For the small excitation spot (x63), the mode radius is 4µm greater that the excitation spot (radius of 3.2µm). For the big excitation spot (x40), the mode radius is only 2.4 µm greater that the excitation spot. However, the lasing wavelengths are a little different which probably means that the power received by the structure is not strictly the same and compensate the

spreading of the pump by the objective. Note that in each case there is no obvious evidence for surface mode dependent along Γ-M and Γ-K.

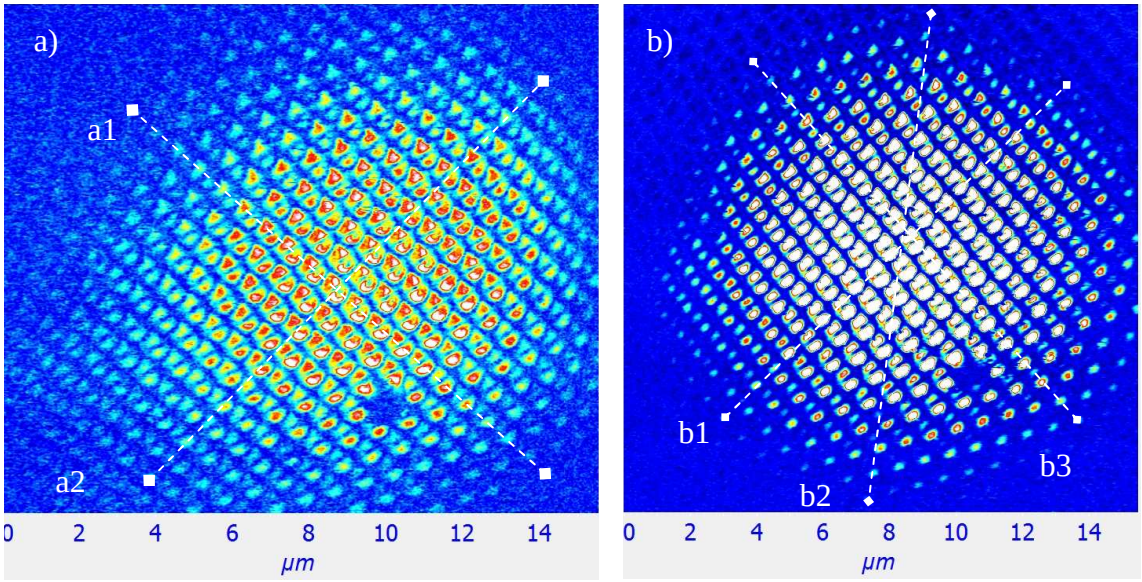

a1=14.36µm a2=14.64µm Conditions: E^2_y-components S_E = 6.4µm (objective X63) λ=1609.6 nm	b1=14.34µm b2=15.34µm b3=15.26µm Conditions: E^2_y-components, S_E = 9.8µm (objective X40) λ=1610 nm

Figure 4.25: a/b) NSOM E^2_y mapping- of slow modes on 2D-PC using BNA-probe. The pumping spot sizes were changed by using 2 objectives: X63 (S_E = 6.4µm) and X40 (S_E = 9.8µm). The pumping power was unchanged between two measurements.

Conclusion

We experimentally demonstrated the strong impact of the laser pumping intensity on the confinement of slow light mode. Though mechanisms that govern this phenomenon could be complicated and unclear, we have discussed and proposed our explanations. We also investigated the dependence of surface mode on spot size of pumping laser (S_E) and along Γ-M and Γ-K direction of band-diagram. Further investigations are in progress to clarify the surface mode dependence with the excitation spot.

References

[1] *F. Raineri, C. Cojocaru, R. Raj, P. Monnier, A. Levenson, C. Seassal, X. Letartre, and P. Viktorovitch, "Tuning a two-dimensional photonic crystal resonance via optical carrier injection," Opt. Lett. 30, 64-66 (2005)*

[2] *K. Sakai, and S. Noda, "Optical trapping of metal particles in doughnut-shaped beam emitted by photonic-crystal laser," Electron. Lett. 43 (2), 107 (2007).*

[3] *M. Mivelle, I. A. Ibrahim, F. Baida, G. W. Burr, D. Nedeljkovic, D. Charraut, J-Y. Rauch, R. Salut, and T. Grosjean, "Bowtie nano-aperture as interface between near-fields and a single-mode fiber," Opt. Express 18, 15964-15974 (2010)*

[4] *A. F. Koenderink, R. Wüest, B. C. Buchler, S. Richter, P. Strasser, M. Kafesaki, A. Rogach, R. B. Wehrspohn, C. M. Soukoulis, D. Erni, F. Robin, H. Jackel, and V. Sandoghdar, "Near-field optics and control of photonic crystals," Photon. Nanostrut. 3(2-3), 63–74 (2005)*

[5] *G. Le Gac, A. Rahmani, C. Seassal, E. Picard, E. Hadji, and S. Callard, "Tuning of an active photonic crystal cavity by an hybrid silica/silicon near-field probe," Opt. Express **17**, 21672-21679 (2009)*

[6] *Guo, H. et al.,"Optical resonances of bowtie slot antennas and their geometry and material dependence,", Opt. Express 16, 7756–7766 (2008)*

[7] *I. A. Ibrahim, M. Mivelle, T. Grosjean, J.-T. Allegre, G. W. Burr, and F. I. Baida, "Bowtie-shaped nanoaperture: a modal study," Opt. Lett. **35**, 2448-2450 (2010)*

[8] *A. Sundaramurthy, P. J. Schuck, N. R. Conley, D. P. Fromm, G. S. Kino, and W. E. Moerner, "Toward nanometer-scale optical photolithography: utilizing the near-field of bowtie optical nanoantennas." Nano Lett. 6, 355-360 (2006).*

[9] *F. Bordas, doctoral dissertation, INL, CNRS UMR 5270*

Chapter 5: Disordered Photonic Crystal

In this chapter we investigate the optical properties of novel disordered photonic crystal. Two separated concepts of disordering the PC are introduced, fabricated and characterized by photoluminescence and NSOM.

5.1. Anderson localization (AL) and disordered PC

Wave localization in random media has been theoretically predicted by P. W. Anderson in 1958.[1] In this report he stated the possibility of localization of wave function of a quantum particle in a random potential around the region where the particle was initially placed. The theory of this localization might be applicable to all sorts of quantum mechanical as well as classical wave phenomena such as electronic wave, acoustic waves, matter waves, and light waves.[2,3,4,5]

Most experimental attempts to achieve this Anderson localization (AL) of light were performed in fully random media[6,7] (*e.g.* aggregates of fine grains), but experienced the difficulty of achieving high scattering cross-section along with a low absorption loss. The problem of random media is that no control can be exerted over the frequency or the spatial extension of the localized mode. A promising proposal to control over these parameters is to use photonic crystals. Peter Lodahl[8] has recently proposed to control the multiple scattering of light by inducing small amount of disorder in periodic photonic crystal. In a perfect 2DPC, stationary modes are the Slow Bloch modes present at the high symmetry point of the band-diagram. The idea is to use a structure presenting a photonic band gap and to consider the effect of disorder on a band-edge Slow Bloch mode. Breaking the structure symmetry produces multiple scattering of light which can interfere and lead to Anderson-localized modes. These modes are supposed to appear at random positions into the crystal in a frequency range close to the initial wavelength of the band-edge SBM. However, the physics of transition from order to disorder is so far not quite clear, especially in 2D systems where localization depends on the sample size and the optical losses. Some concepts generally used in random media as the localization length can be used in the case of randomized photonic crystal. In random media, the localization length L_{loc} is defined as the exponential decay length of the confined modes after averaging over many realizations of disorder. To observe localization in a 2D system, the structure dimension has to exceed L_{loc}. Secondly, the optical loss length should also be larger than the localization length. This implies that the increase of the in-plane scattering, which tends to reduce L_{loc}, has to be small enough to keep the in-plane losses reasonably small. However, other concepts are more difficult to transpose from random media to randomized PC. For instance, the scattering length l_s and the k-vector do not cover the

same physical processes. The scattering length is usually the average length between two scattering events, which can be easily related to the density of scattering elements and the scattering cross section into the random media. In 2D-PC, the scattering length is not so easy to define. It corresponds to the length-scale at which the mode is scattered by structural imperfection of the lattice, namely the disorder. Concerning the k-vector which is usually $2\pi/\lambda$, it can be replaced by the wave-vector of the coherent slow Bloch mode. This has allowed John[9] to reinterpret the classical Ioffe-Regel criterion that states the strong localization is possible in three dimensional random media if the condition $k\, l_s<1$ is met for periodic dielectric media with k, the wave vector of the SBM and l_s, the scattering length of the mode. The use of Slow Bloch modes which are present at the edge of Brillouin zone is particularly interesting because the wave vector of a band-edge mode tends toward 0 and allows these criterions to be fulfilled as indicated in the band-diagram of Figure 5.1.

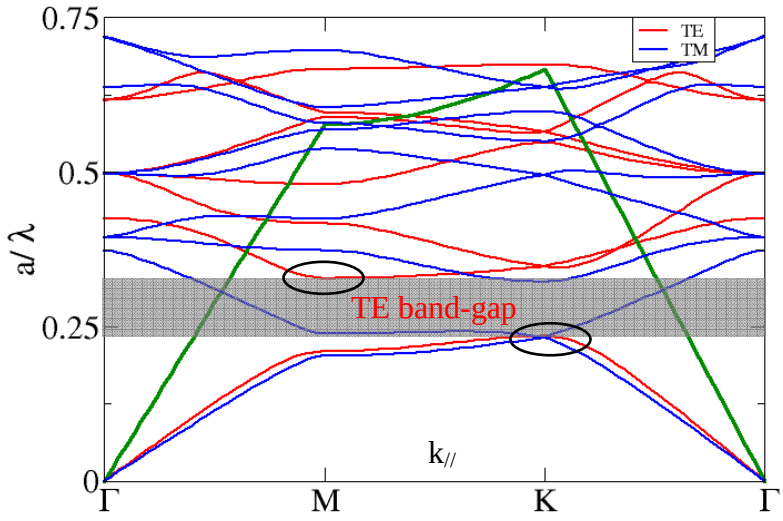

Figure 5.1. Photonic band diagram of an ordered triangular photonic crystal (structured by the array of air holes in active InP membrane, a=460nm and r=0.3a). Band-diagram presents the TE band-gap and band-edge modes at M- and K-points (black circles).

In this work, the objective was to conceive new designs of disordered structure based on active triangular photonic crystal and to show the experimental evidence of light localization by disorder. To reach this goal, we have applied near-field scanning microscopy to active randomized photonic crystals. We studied two types of structures: in the first structures, conceived by Seiji Takeda and Romain Peretti during their postdocs with Pierre Viktorovich at INL, the disorder was induced by randomly displacing each

hole of the crystal (fluctuation of the hole position, section 5.2). The second type of structures has been studied in the framework of collaboration with the National University of Seoul and the international associate laboratory with Korea. The structures have been fabricated by Jeongkug Lee and HeonSu Jeon. In these 2D-PCs, the positions of air holes were fixed but their sizes were randomized with a certain amount of disorder (modification of hole size, section 5.3).

5.2. Fluctuation of the hole position

5.2.1. 2D-DPC design

The disordered structures are based on an ordered triangular PC (OPC) with given lattice parameters (radius of air hole: *r=185nm*, lattice constant: *a=530nm*). The DPCs are made by randomly displacing every air holes of the ordered structure with the same displacement distance δ (nm) but with a different displacement angle θ_m (θ_m value could vary from *0* to *360*°) as indicated in Figure 5.2. The resulting DPCs have the same filling factor but its photonic band-gap is shifted with respect to the OPC. δ value is set between *0* and *a/2-r* (δ*=0* means no displacement or ordered PC). δ is the most important parameter and is used to specify such DPC. It will be used to identify the transition from Bloch mode in OPC to Anderson localized mode in DPC. For strong disorder (when δ is close to *a/2-r*) the photonic band-gap may disappear and optical losses increase. As a result lasing effect may be prohibited since only spontaneous emission is present.

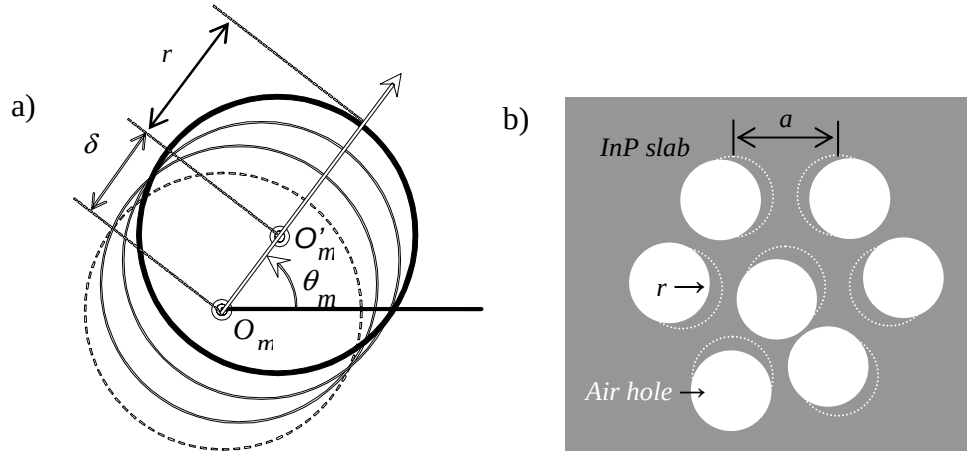

Figure 5.2: a) Schematic diagram of the 2D triangular disordered PC (DPC) by randomly displacing the air holes of the normal PC (OPC) to any direction with the constant distance δ (nm). The angle θ_m to the horizontal axis measures the direction of displacement. The dashed circle (center O_m) represents the ordered positions of air hole in OPC while the solid one (center O'_m) indicates the disordered positions. b) The DPC structure (white circles) drilled in InP slab where the dashed circles indicates the ordered structure.

In this experiment, several DPC structures have been designed with different values of δ (0nm, 10nm, 20nm and 40nm): they are named as DPC-δ (*e.g* DPC-10 means DPC with δ=10nm).

5.2.2. Fabrication

The 2D-PCs were fabricated on InP slab including four layers of quantum well and bonded onto glass substrate as the structures shown in section 5.2.1. The refractive index periodicity of PC was created by drilling a triangular array of air holes (n_{air}=1) into InP slab (n_{InP}=3.17 at λ=1.55nm) using nanofabrication processes (EBL and RIE). The PC structure size was extended to 36µm×42µm (80×80 rows). Several ordered and disordered structures are made with different doses (electron beam intensity in EBL process) in order to obtain the closest structures to the designed parameters. Figure 5.3-a/b/c show several SEM images of the fabricated structures corresponding to cases of a) *δ=0* (ordered), b) *δ=10 nm* (disordered) and c) *δ=40 nm* (disordered). The disorder is difficult to observe with a visual control with fluctuation of 10nm in Figure 5.3-b but is confirmed by the corresponding FFT of the SEM images as indicated in Figure 5.3-e/f). The lattice parameters measured on such SEM images gave the value of r=158nm and a=530nm. These real values will be used to compute the mode patterns as indicated in the next section 5.2.3.

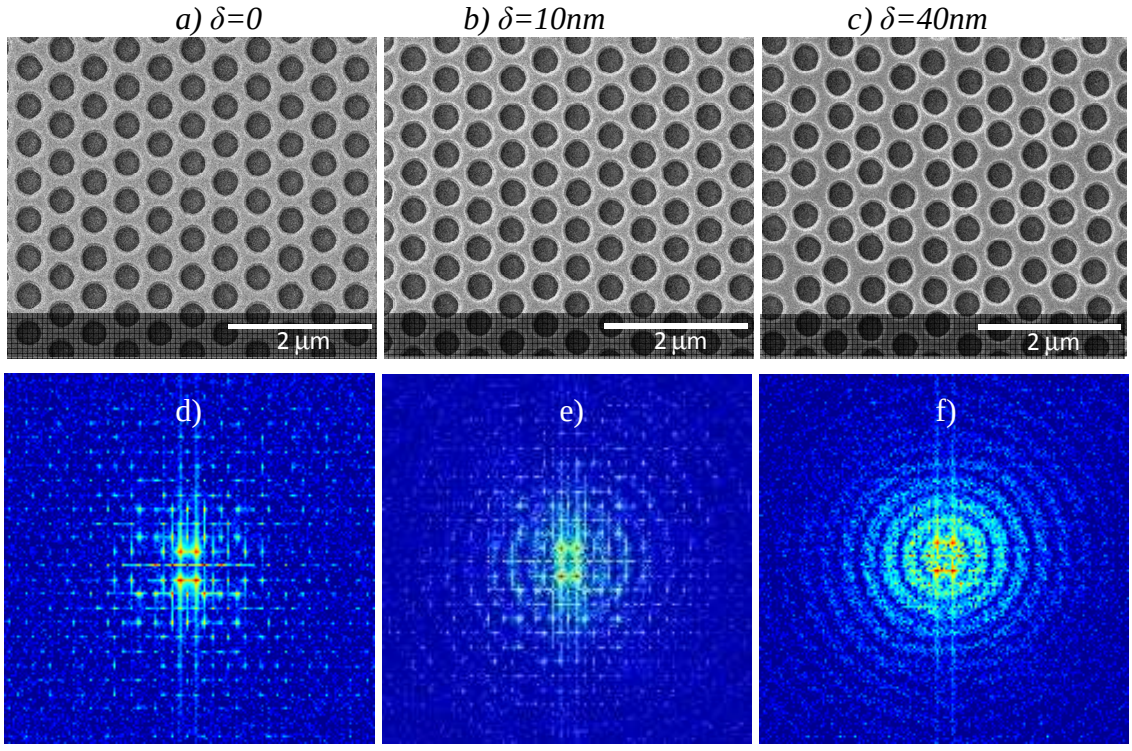

Figure 5.3: a-b-c) SEM images of triangular PC structures in cases of δ=0 (ordered), δ=10 nm (DPC-10) and δ=40 nm (DPC-40) respectively. d-e-f) Fast Fourier Transforms (FFT) of corresponding SEM images in a-b-c) reveal clearly the periodicity of OPC structure (δ=0), less periodicity with δ=10nm and no periodicity if δ increase to 40nm.

The Fourier transforms of the SEM images reveal the information of disorder on structure. The periodicity of OPC (*δ=0*) is explicitly shown in Figure 5.3-d with periodic bright spots. We observe the fluctuation of periodic spots in DPC-10 because some noise appears into the FFT image (Figure 5.3-e). The periodicity of the structure disappears completely (Figure 5.3-f) with δ=40nm.

5.2.3. Simulation

The 2D-FDTD simulation was performed for both ordered and disordered triangular PCs in order to understand the disorder effect on the distribution of the electromagnetic field and identify the transition from Bloch mode to Anderson localization mode. The real lattice parameters (r=185 nm and a=530 nm) extracted from SEM images were used to construct the photonic mode patterns without gain.

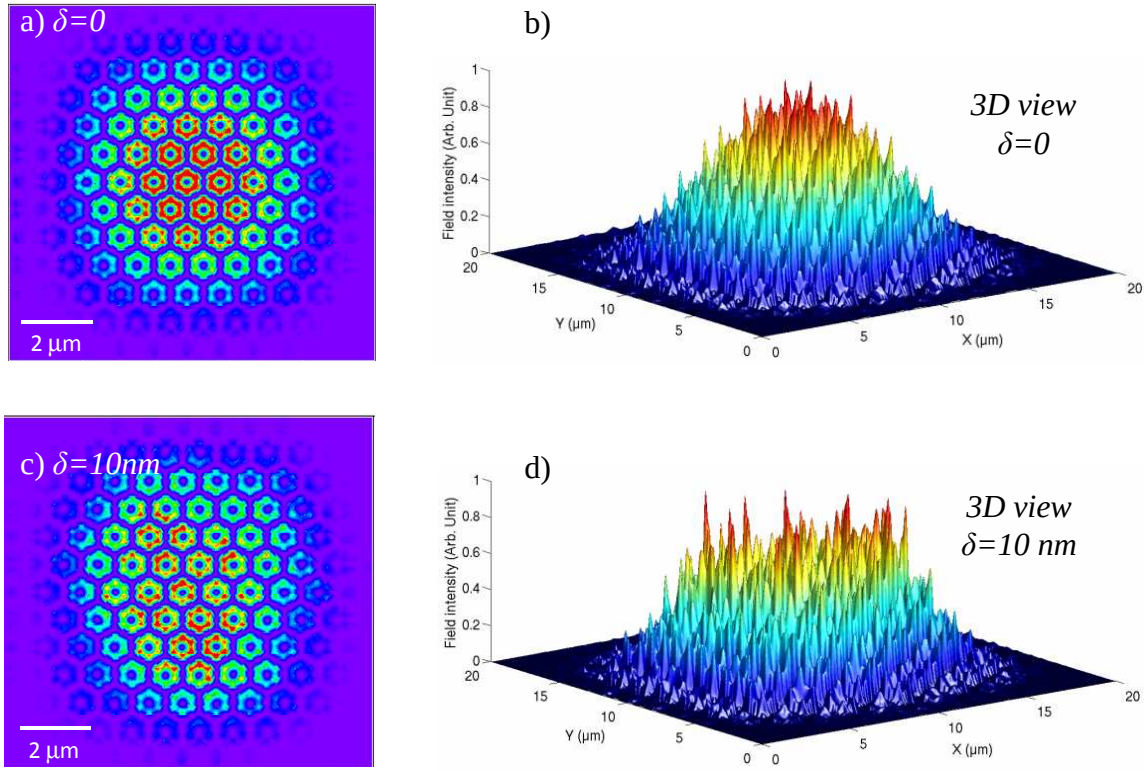

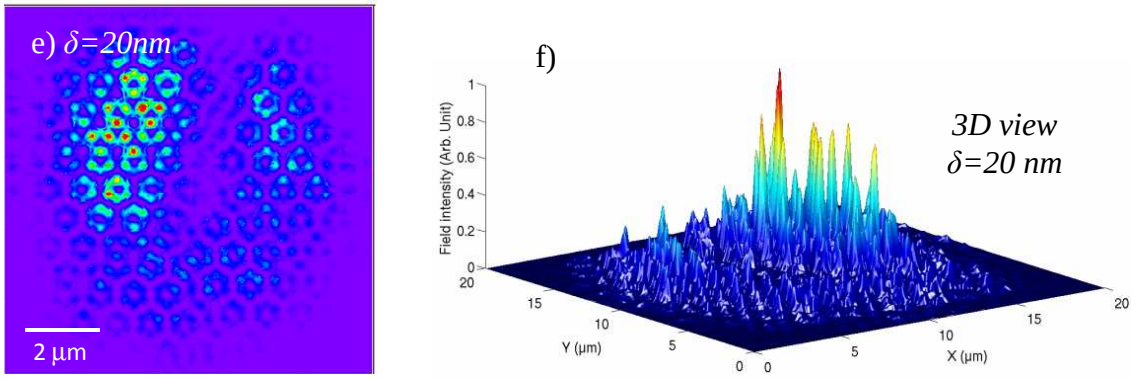

Figure 5.4: 2D-FDTD computes the mode patterns of triangular PC with lattice parameters extracted from SEM images of fabricated PC for three cases of OPC (δ=0nm) δ=10nm (DPC-10) and δ=20nm (DPC-20). a/b) The optical images of K-mode OPC reveal the modulation at unit cells and Gaussian-like shape of mode envelop (highest intensity at the center). c/d) The optical response of DPC-10 reveals the slight distortion in field distribution the but the Gaussian-shape of envelope still remain. e/f) The transition from slow Bloch mode to Anderson localization mode could be explicitly observed in optical pattern of DPC-20.

The band-edge mode at K-point was excited by a TE-polarized pulse. In order to avoid excitation of several modes, the excitation pulse is modulated by a temporally Gaussian envelop. The simulation patterns are shown in two and three dimensions in Figure 5.4. With OPC (*δ=0*, Figure 5.4-a/b), the electromagnetic field is distributed quite uniformly and reach the highest intensity at the center of structure. The modulation of the delocalized slow Bloch mode is clearly observed. When a slight randomness of δ=10nm is added into the PC (DPC-10 structure (Figure 5.4-c/d)), the slow mode distribution is perturbed but remains quite delocalized. However, if we introduce more randomness (δ=20nm) into the PC (DP-20 structure Figure 5.4-e/f), the distribution is distorted with no field intensity focused at the center. The slow Bloch mode is now Anderson localized at some specific locations which seems to indicate a localization of light by disorder.

5.2.4. Experimental results

a. Spectroscopic analysis.

Far-field measurements in Figure 5.5 were conducted by Dr. Romain Peretti with the photoluminescence set-up and pulse condition of laser diode described in section 2.3.

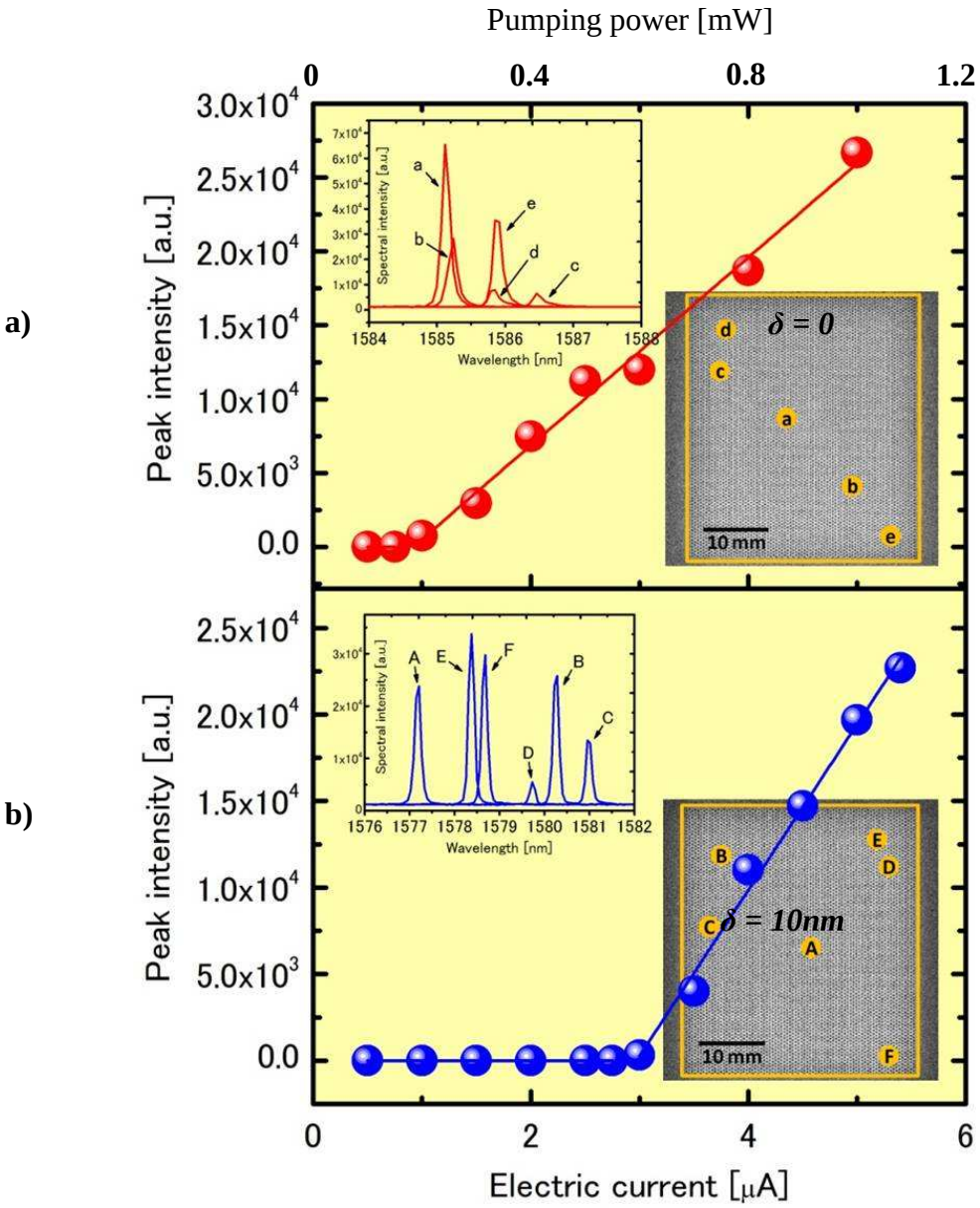

Figure 5.5 Lasing properties obtained by far-field measurements. Emission peak intensity is plotted as a function of pumping power (pulsed laser diode at λ=805 nm) for DPCs with (a) δ=0 nm and (b) δ=10 nm. Clear lasing threshold behaviors are observed. The inset spectra show the lasing peaks at different excitation spots on the RPCs and spectrally analyzed by a spectrophotometer equipped with a cooled InGaAs photodiode array. The excitation spots which correspond to each spectrum are indicated by yellow circles in the inset of the SEM images, where the yellow squares indicate the boundaries of OPCs. The plots of peak intensities in a and b are obtained at the excitation spots b and A in SEM inset images, respectively

The inset at the upper left corner of Figure 5.5-a shows the far-field lasing spectra at several excitation positions (a-b-c-d-e-f) on the OPC (SEM image at lower right corner). As a result, we observe the homogeneous resonant wavelengths of band-edge modes at λ=1585.5 nm with a slight fluctuation (Δλ=1.5nm). This fluctuation could be understood as the unavoidable local imperfection of nanofabrication process. The lasing effect and low lasing threshold of slow Bloch mode was confirmed in Figure 5.5-a by changing the pumping power at the same position b and plotting versus the intensity of resonant peaks.

Similarly, Figure 5.5-b presents the optical properties of DPC-10. The lasing threshold is observed for the sharp lasing peak by plotting the pumping power versus resonant peaks at the position A in SEM inset image (at lower right corner). Compared to structures with δ = 0 nm shift value in Figure 5.5-a, this threshold value is three folds higher reflecting the more optical losses (thus lower Q). The lasing spectra graph (inset at upper left corner) recorded at several excitation positions (A-B-C-D-E-F) on DPC-10 indicates the blue-shift and the spectral distribution of resonant peaks is now extended over bandwidth of $\Delta\lambda \sim 4$ nm. The wider distribution of lasing peaks proves that photonic band-edge mode was perturbed by the introduced structural randomness.

b. Blue-shift explanation

Blue-shift phenomenon of valence band-edge mode in DPC could be explained as depicted in Figure 5.6. In DPC, the band-gaps are modified from one to another position. Let consider the band-edges mode at valence band (below band-gap position) which represents as small circle either in green, blue or red. If we have a band-edge photon with frequency ω_A at position A (green arrow), it will be "absorbed" or rather transmitted at position B because the band-edge of B is higher. But this photon will be reflected if encountering the band-gap zone of position C which presents a lower band-edge and so on... However, if we excite a band-edge photon at the highest band-gap of position B (frequency ω_B, blue arrow), this photon will be always backscattered since it encounters the band-gaps everywhere. Similarly, if we create a band-edge photon at the lowest band-gap at position C, it will be transmitted then lost in other regions because it does not face any band-gap to get scattered. Generally, we see that the photons at the higher frequencies will have more possibility to survive in DPC. On contrary, the lowest ones will be absorbed completely. This phenomenon causes the blue-shift of band-edge mode in DPC.

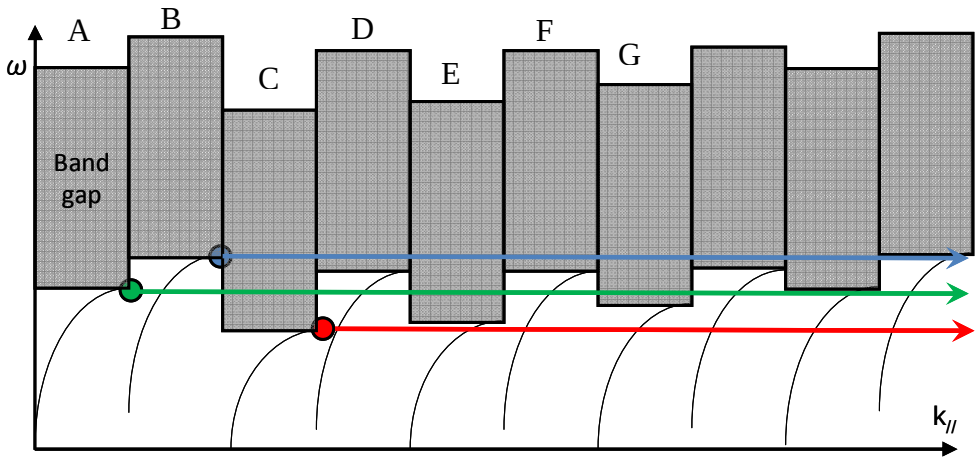

Figure 5.6: Sketch illustrates photon behavior in the altered valance band-edges at several locations of DPC that causes the blue-shift.

Analogously, we could predict that conduction band-edge modes of disordered PCs might provide the red-shift since the lower frequency photons are likely to encounter the band-gap and get backscattered. Indeed, this hypothesis will be demonstrated in next section 5.3.3 with another type of disordered PC.

c. NSOM measurements

This near-field method is used to map the electromagnetic field distribution in DPC. The detail of NSOM set-up and operating conditions are described in section 2.1. We use a pumping laser at λ=780nm with an excitation spot size around 9.5µm. The near-field light is collected by a dielectric tip placed 5-10nm above the structures surface by shear-force regulation. As the K-point mode of the valence band is a slow Bloch mode under the light line, the light at the surface of the PC is mostly evanescent and the bare dielectric tip is adapted.

c.1 Ordered PC

Figure 5.7 presents the NSOM topographic and cartographic images of an OPC. The red circle indicates the pumping area of about 9.5µm. The shear-force topography (12.5x12.5µm²) of Figure 5.7-a shows the periodic triangular structure but also a small topographic defect. The intensity pattern recorded at λ=1562nm in Figure 5.7-b presents periodic bright spots revealing the slow-bloch mode collected by the near-field tip. We also observed that the distribution of the band-edge mode is quasi-homogeneous except at certain position. The expansion of the band-edge mode over in the PC structure can be

also viewed clearly in Figure 5.7-c by applying a high-pass filter (cut-off frequency of $2/\lambda_{SMB}$ for the mode spatial frequencies) to the intensity cartography of Figure 5.7-b. However, some "localized" intensity or brighter spots are visible in the optical image. They happen to occur at the position of the defect as shown in red arrow. They also may be caused by unavoidable structural fluctuations. Figure 5.7-d shows a cross section profile of the mode fitted by a Gaussian envelope. This profile is in agreement with the simulation prediction of the OPC mode distribution profile showed in section 5.2.3.

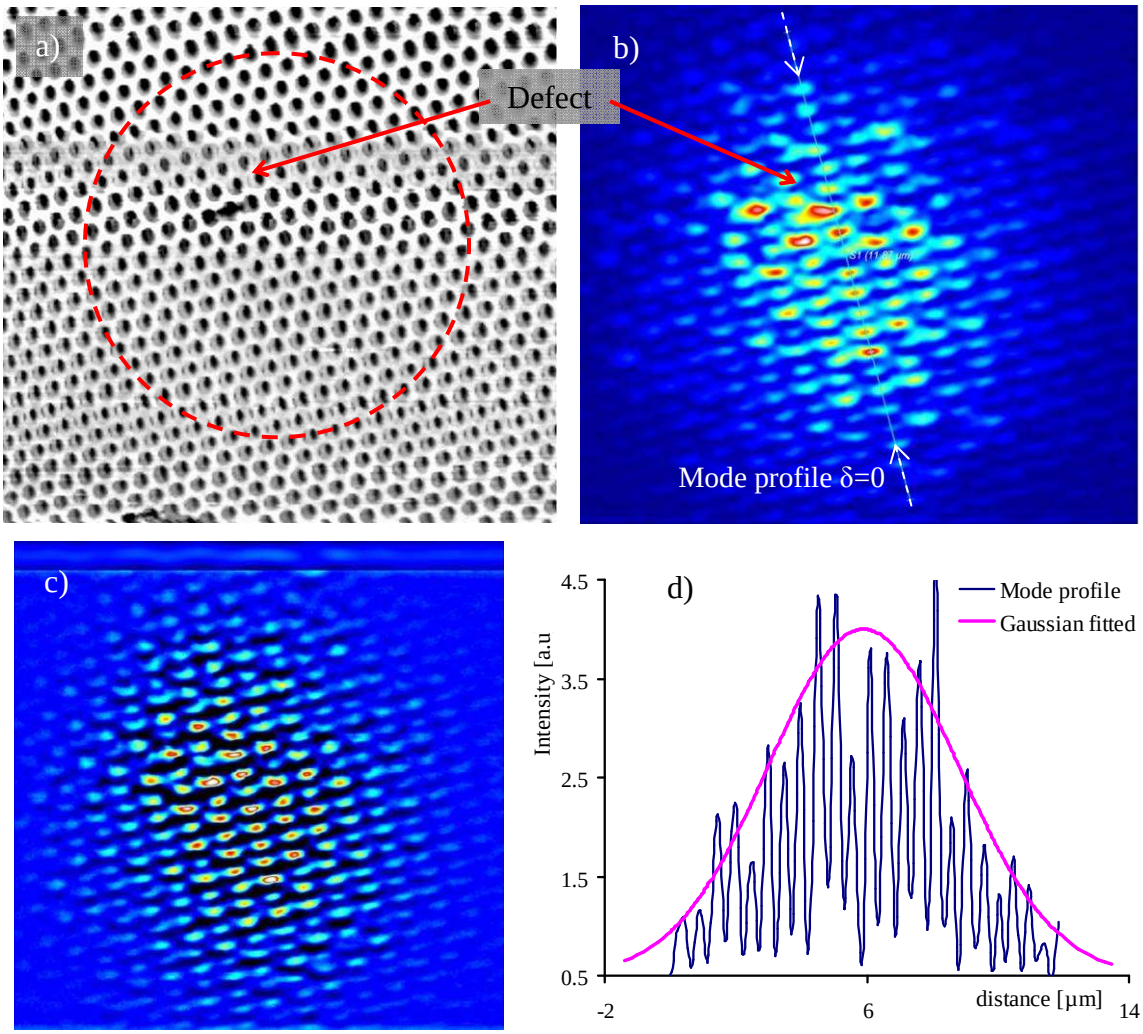

Figure 5.7: NSOM results of an OPC. a) Topography (12.5x12.5µm²) shows the periodic triangular structure of OPC and a small defect (red arrow). The red circle with diameter of 9.5µm indicates excitation spot position. b) Intensity pattern of mode with Gaussian envelope is mapped at λ=1583nm. The localized spots are attributed to the defect on structure (red arrow). c) High-pass filter with cut-off wavelength at $\lambda_{SMB}/2$ is applied on optical pattern of b) to reveal more clearly the periodicity and distribution properties. d)

Mode profile along Γ-M direction shows the Gaussian distribution (pink line) of band-edge mode in OPC.

c.2 Disordered PC (δ =10nm)

The mode distribution of DPC-10 was investigated by the same NSOM setup. Figure 5.8-a shows the shear-force topography of a disordered triangular structures in scanning area of 7x7µm². In Figure 5.8-b, the corresponding optical image of the lasing mode at λ=1555nm reveals localized spots at certain locations of the DPC instead of the periodic mode distribution obtained with OPC. The overlap between NSOM topography (Figure 5.8-a) and intensity cartography (Figure 5.8-b) confirms that the localized modes are generated by the disorder in the structure rather than the defects. However, with randomness of 10 nm, the modulation properties of band-edge modes of OPC still remains in DPC-10 as shown in Figure 5.8-c using high-pass filter (~ $\lambda_{mode}/2$). This result indicates a preserved band-gap of PC and illustrates the interplay of order-and-disorder. Considering the mode profile across the localized spots in DPC-10 in Figure 5.8-d (back solid line), we find that the tails of these localized modes decay exponentially with localization length around 3.7µm-4.5µm. In comparison with the profile intensity of OPC (red solid line) which follows the Gaussian distribution, the exponential decay of mode can presume the presence of Anderson localization (AL) due to the disorder in structure. Note that in Figure 5.8-d the vertical axis in logarithmic scale.

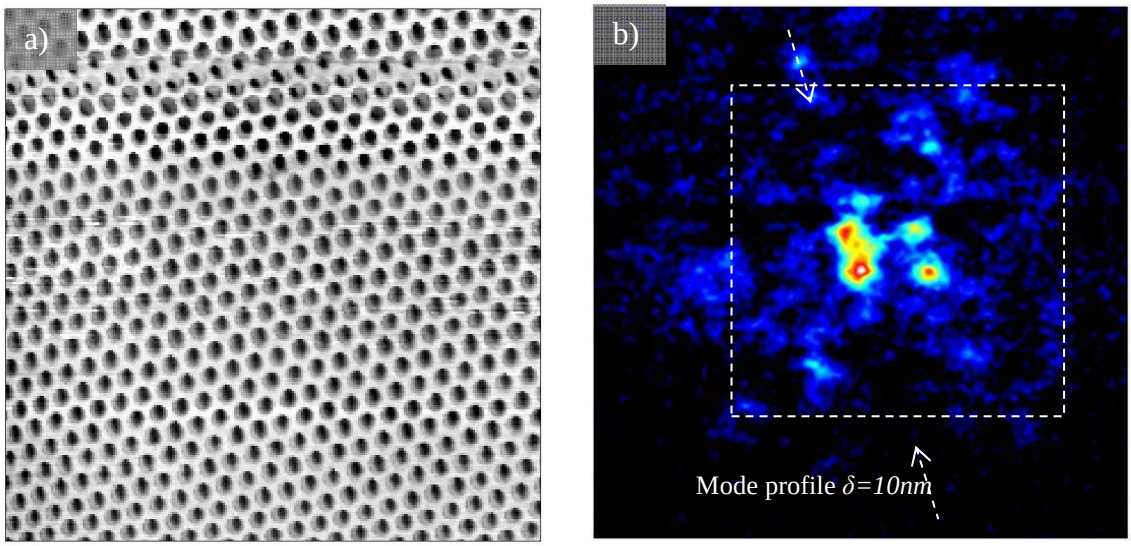

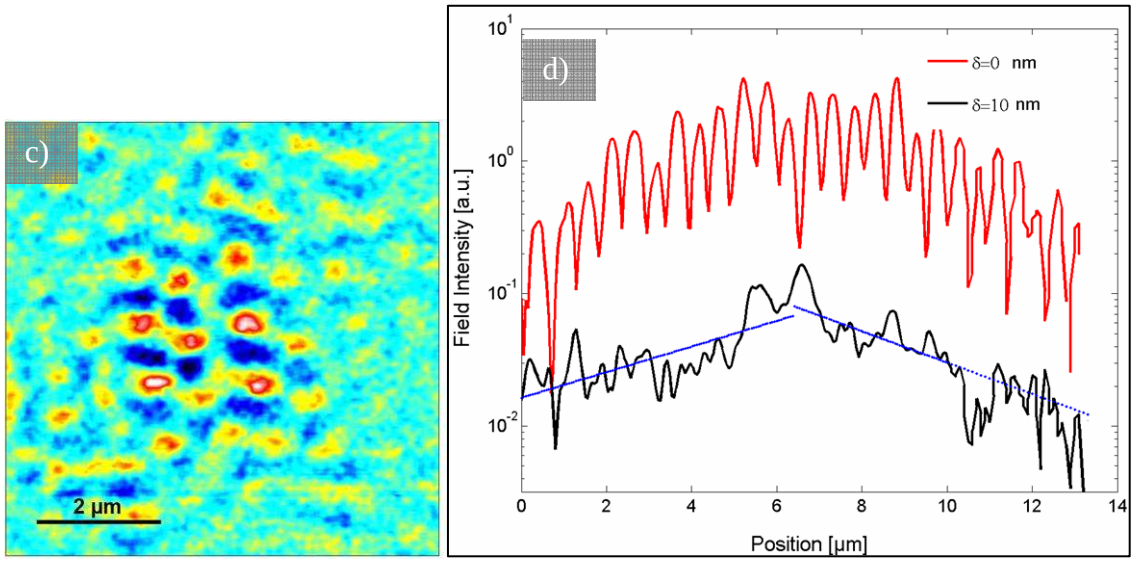

Figure 5.8: NSOM results of a DPC-10. a) Topography (7x7µm²) shows the triangular structure of DPC-10 without defect. b) Intensity pattern is mapped at λ=1583nm reveals the AL at certain locations of disordered structure. c) High-pass filter with cut-off frequency at $\lambda_{laser}/2$ is applied on optical pattern to reveal the remains of periodic properties of ordered PC. d) Mode profiles along Γ-M direction of DPC-10 (black solid line) show an exponential decay at the tails presuming AL in DPC-10.

c.3 Disordered PC (δ = 20nm)

Slight disorder in PC could generate AL mode with extremely high Q and small modal volume. However, too much disorder in DPC reduces Q and volume V quickly[10], and may prevent lasing to occur. As illustrated in Figure 5.9, two main sources of losses are attributed to disorder: first disorder increases lateral losses by narrowing of the band-gap (the red arrow points toward the right). Second, disorder also induces vertical losses by increasing the optical coupling of the SBM to the radiation continuum (the red arrow points toward the left). Both effects reduce the SBM lifetime below the time necessary to observe the lasing effect.

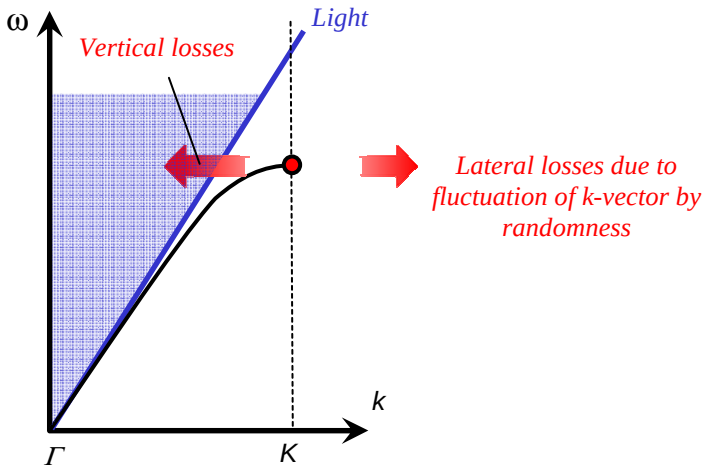

Figure 5.9: Diagram illustrates the losses (two red arrows) on strongly DPC (δ>20nm) that cause disappearance of lasing effect of band-edge mode.

More specifically, the alteration of Q/V ratio in DPC can be explained using the fluctuation of band-gap in DPC as following:

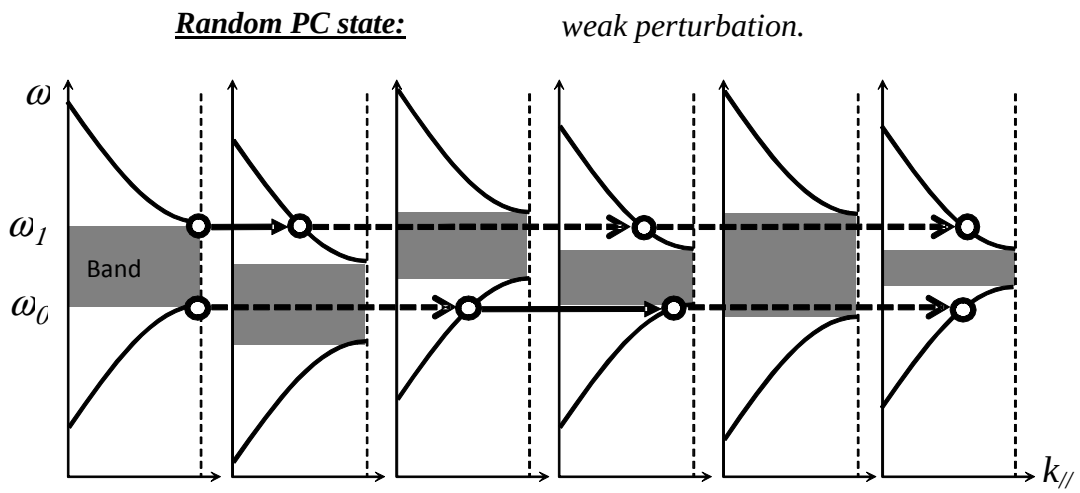

Figure 5.10: a) Weak perturbation of PC structure leads to the increase of Q factor and decrease of modal volume V.

Figure 5.10-a illustrates the alternation of band-gap from region to region in DPC. With weakly disordered PC, band-gap slightly fluctuates from its original position. Thus, the band-edge photons might be strongly backscattered since they have possibility to encounter the band-gap in the adjacent regions and then Anderson localization occurs with blue-shift. As a result, it provides the increase of Q factor and decrease of modal volume.

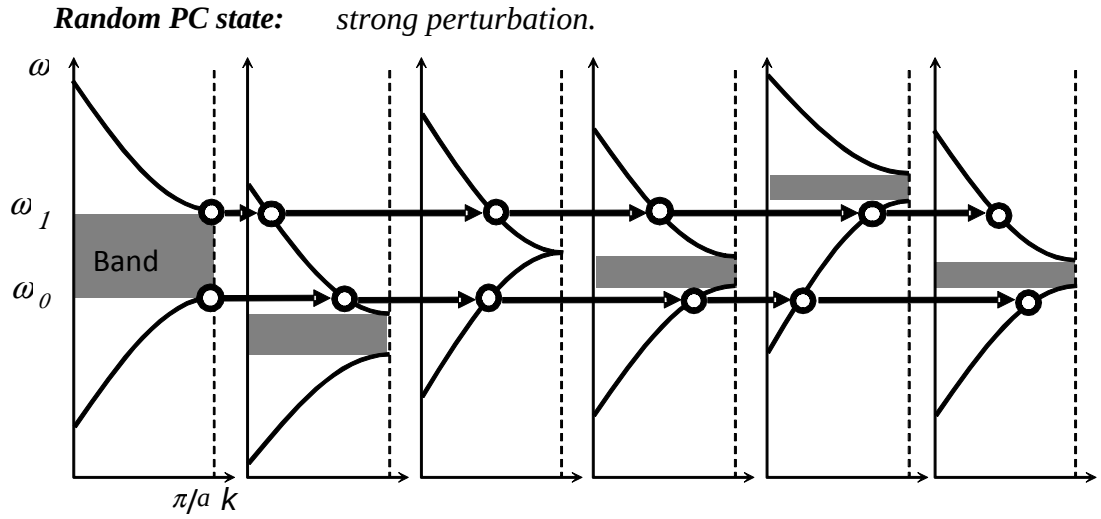

Figure 5.10: b) Strong perturbation of PC structure (δ > 20nm in theory), on contrary leads to the decrease of Q-factor and increase of modal volume V.

However, with strongly disordered PC, band-gaps can fluctuate completely out of valence and conduction bands of adjacent regions or even collapsed at certain locations in structure as shown in Figure 5.10-b. As a result, photons can not be localized in structure since they have been transmitted and lost. This fact makes Anderson localization loosened and disappeared and leads to the decrease of Q-factor.

In order to confirm these assumptions, we performed NSOM characterizations on DPCs with high displacement δ=20 nm. For such structures, we observed only spontaneous emission spectra and no lasing modes or threshold behavior as shown in optical image of Figure 5.11-c.

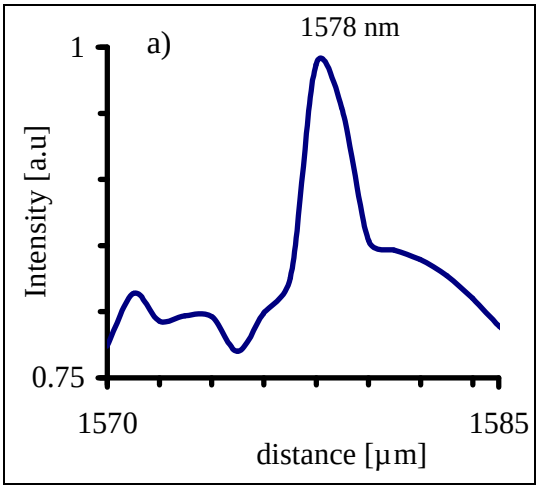

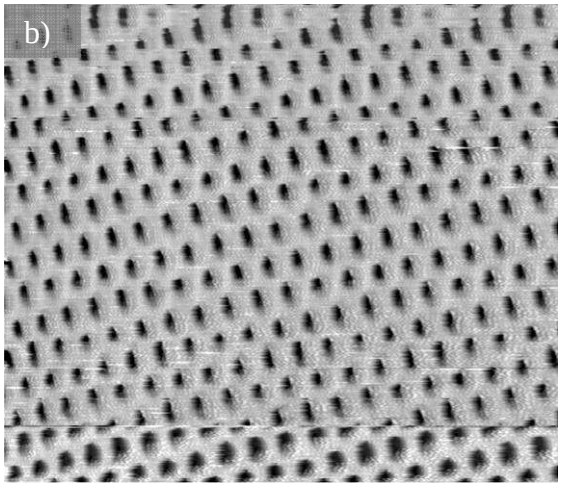

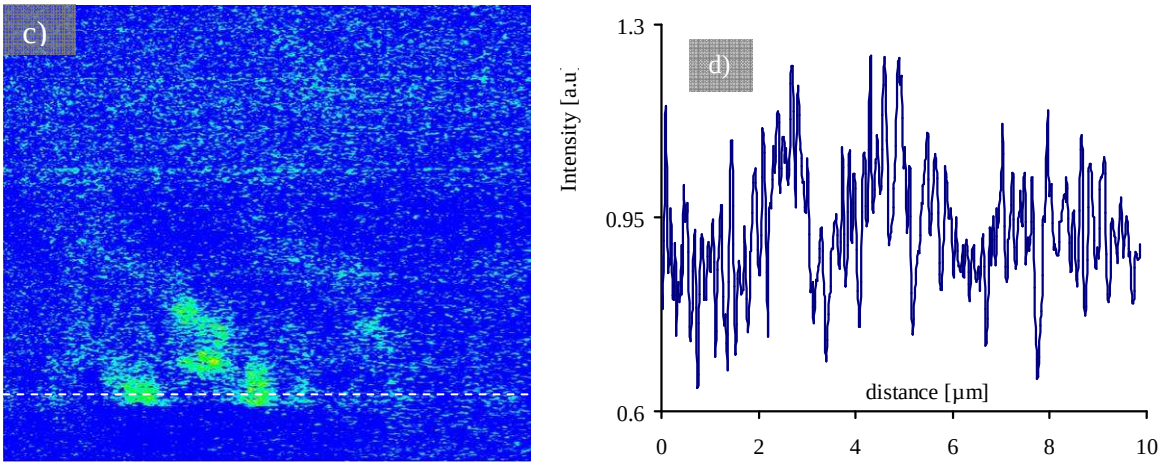

Figure 5.11: NSOM results with dielectric tip of DPC-20. a) Near-field spectrum with resonant peak at λ=1578nm. b) Topography (8x8µm²). c) Corresponding optical NSOM image at resonant wavelength shows the "localized" mode with low Q-factor. d) The profile of mode in c) presents the high background noise and very low Q-factor for localized mode in DPC-20.

Conclusion

In this section, we showed by NSOM characterization that a random displacement value of 10 nm of the holes of a OPC makes extended Slow Bloch Mode into Anderson localized mode. Those results are consistent with theoretical predictions of FDTD simulations. Our results also show for the first time AL modes spatially resolved within a disordered photonic band-gap structure.

5.3. Modification of the hole size.

Recently, µNOEL group of Heonsu Jeon in Seoul National University proposed the photonic crystals counterparts of the well-known mixed semiconductors[11]: these new crystals are called Mixed Photonic Crystals (MPC) or Disordered Photonic Crystal (DPC). As semiconductor alloys consist in two or more randomly mixed semiconductors, the mixed phonic crystal is obtained by mixing together two or more photonic crystals with different parameters. As in solid state physics, this approach also allows to perform photonic band-gap engineering[12,13]. In that case, it is important to be able to determine the spectral position of the band-gap. This position can be easily inferred by using band-edge laser: the lasing frequencies give immediately the band-gap edge position. That is why, as for the previous disordered crystals, the basic structure used to fabricate MPC is photonic crystal band-edge laser. The disordered PCs are prepared by structurally differentiating photonic atoms (holes) and arranging them into a two-dimensional 2D-PC[14].

5.3.1. 2D MPC design

Unlike the position fluctuation method discussed in section 5.2 where air holes were dislocated by a constant displacement δ, these MPCs were generated by a modification of the air hole size compared to the normal PCs (shrunk or extended) with a given composition ratio between the number of small (S) and large (L) holes (Figure 5.12). MPC with the composition x is noted $S_{1-x}L_x$ ($0 \leq x \leq 1$) in which $x=0$ or $x=1$ means that MPC is homogeneous and contains small or large holes respectively. We also define the radius difference between the largest and the smallest holes as $\Delta r = r_L - r_S$. The number of type of photonic atoms in MPC must also be considered (a type of photonic atoms refers to holes that have the same radius). Thus, the MPC can be specified by its composition ratio x, the number of atom types and the radius difference Δr.

In this experiment, MPCs were designed to present the same composition ratio x $(x=0.5)$ but different number of atoms (4 or 40 atoms) and different value of Δr. The disorder of PC structures was introduced by mixing randomly the different photonic atoms as illustrated in Figure 5.12.

Simulations are in progress to compute the optical properties of such MPCs.

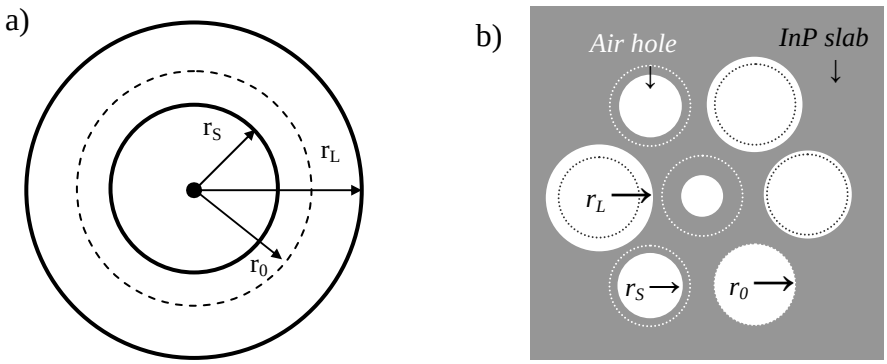

Figure 5.12: a) Schematic diagram of the 2D triangular mixed PC (MPC) by random modification of the air holes radius corresponding ordered PC. r_0, r_S, r_L being the original (order), small and large radius of air holes respectively. b) The MPC structure (white circles) drilled in InP slab where the dashed circles indicates the ordered structure.

5.3.2. Fabrication

As introduced in section 5.2, these MPCs were fabricated by SEM and RIE on an active membrane of InP embedded QWs at the center. Four types of crystals had been fabricated:

- Ordered PC (OPC) with triangular lattice (*a=470nm, r = 0.3a*), PC size of 40x40μm.
- Weakly disordered PC (WDPC): presents the same lattice period as OPC, a small variation of the air hole sizes ($\Delta r = r_4 - r_1$ = 0.03a) and is mixed of four types of holes $r_1 < r_2 < r_3 < r_4$ (atoms), or forty types of holes.
- Strongly disordered PC (SDPC): presents the same lattice period as OPC, a large variation of the air hole sizes ($\Delta r = r_4 - r_1$ = 0.09a) and is mixed of four or forty photonic atoms.
- Very strongly disordered PC (VSDPC): presents the same lattice period as OPC, a very large variation in air hole sizes ($\Delta r = r_4 - r_1$ = 0.15a) and is mixed of four or forty photonic atoms.

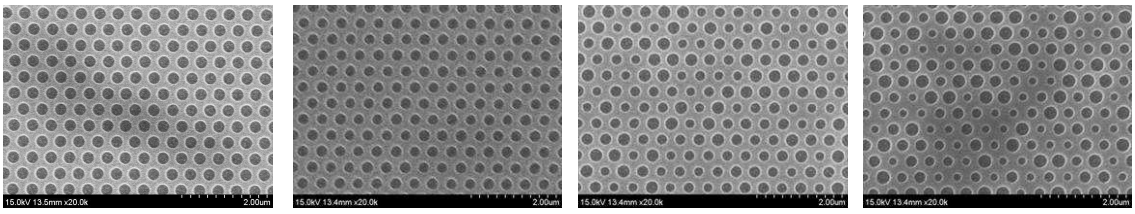

Normal PC
r = 0.3*a*, *a=470nm*

Weakly disordered PC
$r_L - r_S$ = 0.03*a*

Strongly disordered PC
$r_L - r_S$ = 0.09*a*

Very strongly disordered PC
$r_L - r_S$ = 0.15*a*

Figure 5.13: SEM images of four types of DPCs on InP membrane.

5.3.3. Experimental results

5.3.3.1. Spectroscopic analyses.

Far-field optical measurements were performed at Seoul National University to characterize the optical properties of all the fabricated MPCs. Figure 5.14-a presents the spectra of four types of PCs (ordered PC, weakly disordered PC, strongly disordered PC and very strongly disordered PC) which have the same numbers of atoms (40), configurations (n°3) and doses (n°3). Ordered PC has two resonant lasing peaks (blue curve) corresponding to two band-edge modes at K-point (λ= 1628.6 nm) and M-point (λ=1515.4 nm). In case of disordered PCs, resonant lasing peaks are also observed at K-point with blue-shift (all structures) and at M-point with red-shift (weakly DPC) depending on the degree of disorder (*Δr/a* ratio) as indicated in Figure 5.14-b. The blue-shift or red-shift of the band-edge modes are probably due to the fluctuations of the MPC band-gap as was explained in section 5.2.4-b.

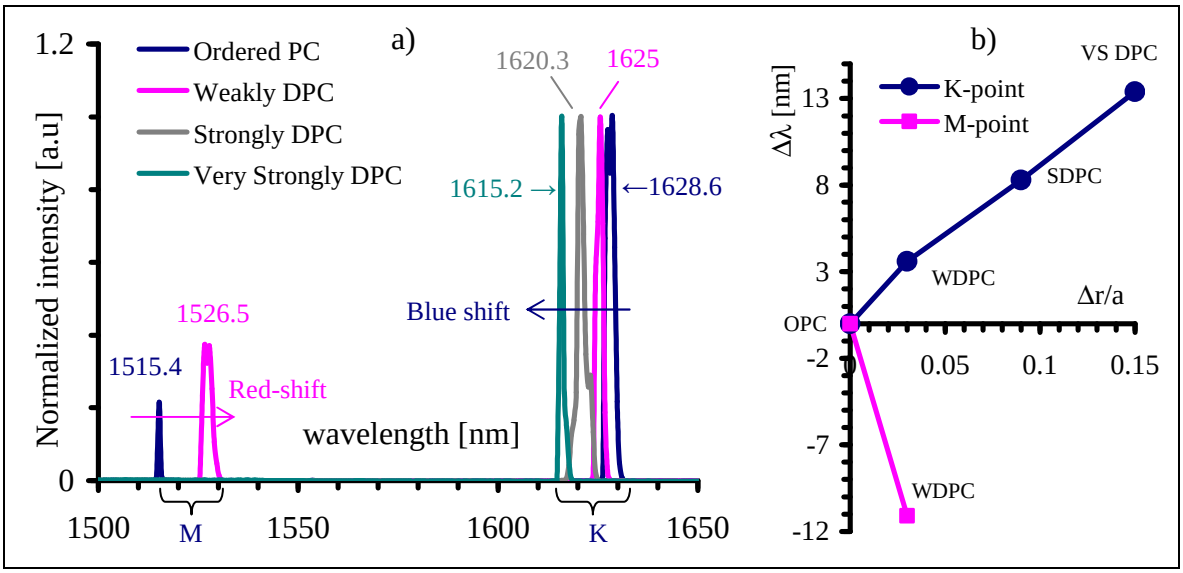

Figure 5.14: a) Far-field measurements of four kinds of DPCs with the same experimental conditions on the same configurations (40 atoms, configuration 3, dose 3). b) The blue-shift and red-shift of wavelength versus Δr/a ratio (disorder degrees).

Note that a lasing effect is obtained even in the case of very strongly disordered structures. Furthermore, the resonant peaks depend more on the disorder degree (weak, strong, very strong) than on the disorder configuration (linked to the random) as shown in Figure 5.15. This Figure shows spectra concerning another very-strongly-DPCs containing 40 types of atoms but fabricated using a different dose (dose 5) compared to the VSDPC

of Figure 5.14 (dose 3). The spectra correspond to three different configurations of disorder while keeping the other parameters unchanged and present all the lasing peak of the K-point band-edge mode for each structure. The Figure shows that they all lased around 1579 nm with a fluctuation of the lasing wavelength of approximately 2nm. By comparison, the ordered PC corresponding to dose 5 presents a lasing peak at 1595 nm. The shift induced by disorder is, as in the previous case of Figure 5.14, much more important (16 nm) than the value of 2 nm induced by the random configurations. Such result explicitly demonstrates that the lasing effect of MPC depends weakly of the configuration but is rather a collective effect of randomly mixed photonic atoms[4].

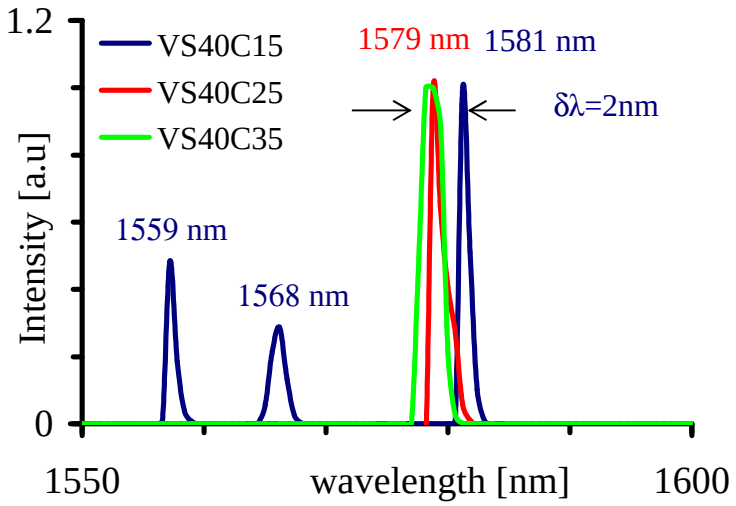

Figure 5.15: The resonant lasing peaks shift less than 2nm between different configurations of the same type of MPCs (40 atoms, configuration 1-2-3, dose 5).

Note that for structure VS40C15, several peaks are present: the longest wavelength (at 1581 nm) which is also present in the other two structures; and two other modes at 1568 nm and 1559 nm which are not detected in the other structures. The presence of other modes is probably due to disorder in the PC structures which makes the band-gap fluctuated, and then improves the scattered light in DPCs. To better understand what those modes represent, MPCs have also been investigated by NSOM measurements using dielectric tip. As these K-point modes are basically under the light line, the kind of tip is well-adapted.

5.3.3.2. NSOM measurements

a. Ordered PC (OPC)-dose n°3

In the near-field set up, the K-point band-edge lasing mode was excited and detected at λ=1627nm (Figure 5.16-a) which corresponds nicely to the far-field measurement presented in figure 5.14. However, the other band-edge mode at M-point was not detectable, probably because the near-field set-up failed to achieve the threshold condition for obtaining the laser effect. The NSOM dielectric probe reveals the intensity pattern of the K-point mode at 1627 nm. The intensity distributions are presented in Figure 5.16-b (2D view) and Figure 5.16-c (3D view). The mode profile in Figure 5.16-d along cross section P shows the Bloch mode modulations distributed by a Gaussian envelop where the highest intensity concentrates near the central area. At some locations the intensity is slightly fluctuated due to unavoidable imperfection in fabrication of PC.

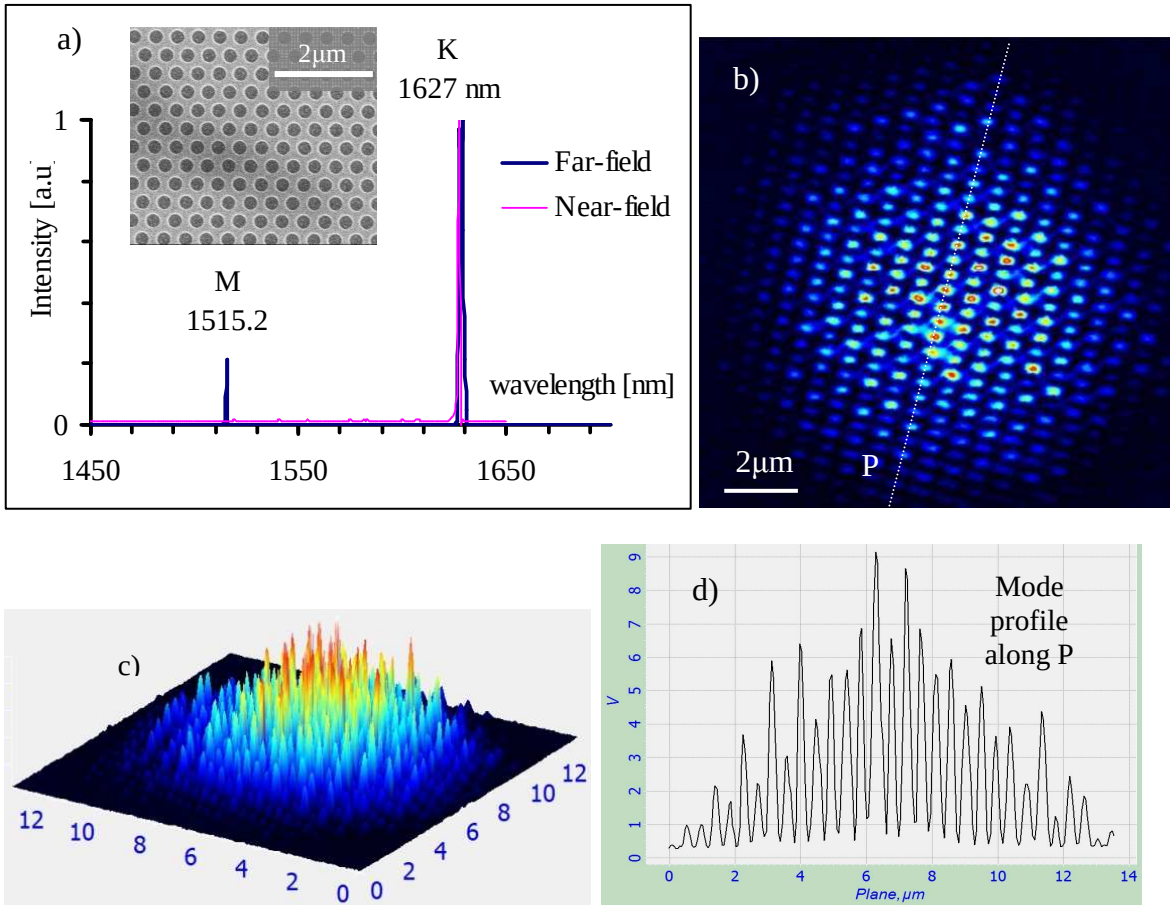

Figure 5.16: a) far-field spectral measurement of OPC (blue curve) provides two band-edge modes at K-point (1628.6nm) and M-point (1515.2nm). However in near-field measurement only mode at K-point is visible. b) near-field intensity pattern of OPC at λ=1627nm by NSOM indicates the Gaussian distribution of mode reflecting the excitation spot. c) 3D view of optical pattern in b). d) Intensity profile along cross section P in b) demonstrates the Gaussian distribution of mode.

b. Weakly Disordered PC (WDPC)-dose n°3

NSOM images were performed on WDPC contained 4 levels of atoms. Far-field characterization performed at Seoul National University predicted a resonant wavelength of 1622 nm (for the 40-type atoms the resonant wavelength is 1625 nm).

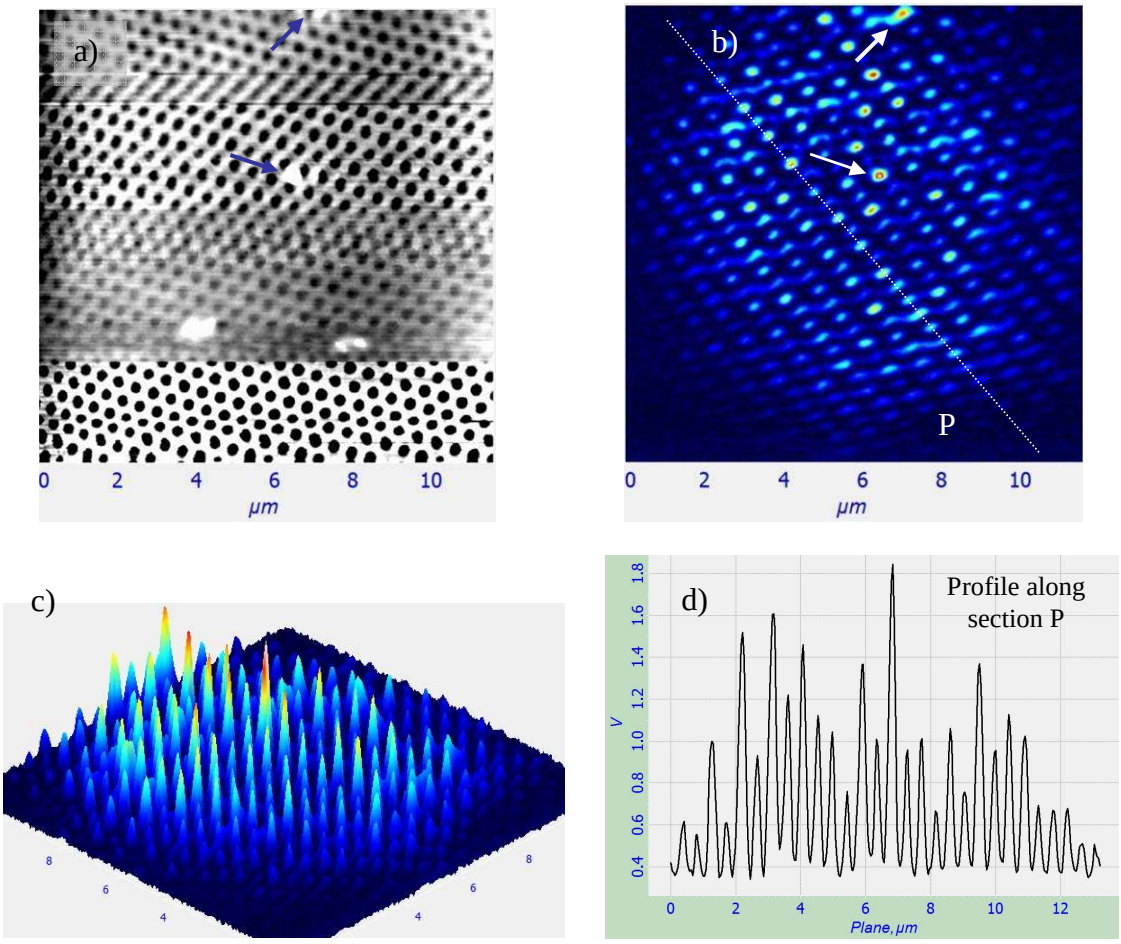

Figure 5.17: NSOM images of a weakly DPC at λ=1628nm show the spread of intensity over structure in comparison with the OPC. The arrows indicate defects on surface. a) NSOM topography. b) NSOM cartography with two localized modes at the positions of defects. c) 3D view of mode distribution of b). d) Mode profile along cross section P in b) demonstrates the beak of Gaussian distribution intensity in WDPC.

Figure 5.17-a/b/c yield the intensity distribution of the lasing band-edge mode which is slightly different with respect to the OPC (Figure 5.16-b/c). Light intensity is still spread over the structure but partially localized in some areas. For instance, the global envelop of the mode is not gaussian but is still extended across the structure as shown in mode profile of Figure 5.17-d. However, the localized spots (the white arrows in Figure 5.17-b) may be

due to defects in PC structures (corresponding blue arrows in Figure 5.17-a). Moreover, the wavelength of the MPC laser is 1628nm very close to the OPC one's and shifted compared to far-field measurements. This discrepancy in the resonant wavelengths is still unclear and has to be confirmed by other measurements.

c. Very Strongly-DPC (VS-DPC)

As shown in the spectral analysis, the far-field measurements performed on the forty-atom VS-DPC (configuration 1, dose 5) reveals lasing emissions at several resonant wavelengths with large blue-shift (~16 nm) with respect to OPC. The near-field spectral measurement showed in Figure 5.18 reveals actually that the resonant wavelengths also strongly depend on positions. This can be explained by the band-gap fluctuation model. Figure 5.18 shows local spectra obtained with the dielectric NSOM tip at three different positions on VS-DPC (see inset) using the same illumination. Note that the far-field spectra was measured by illuminating the whole structure with an optical fiber which enables to excite all allowed modes (four lasing peaks in this case).

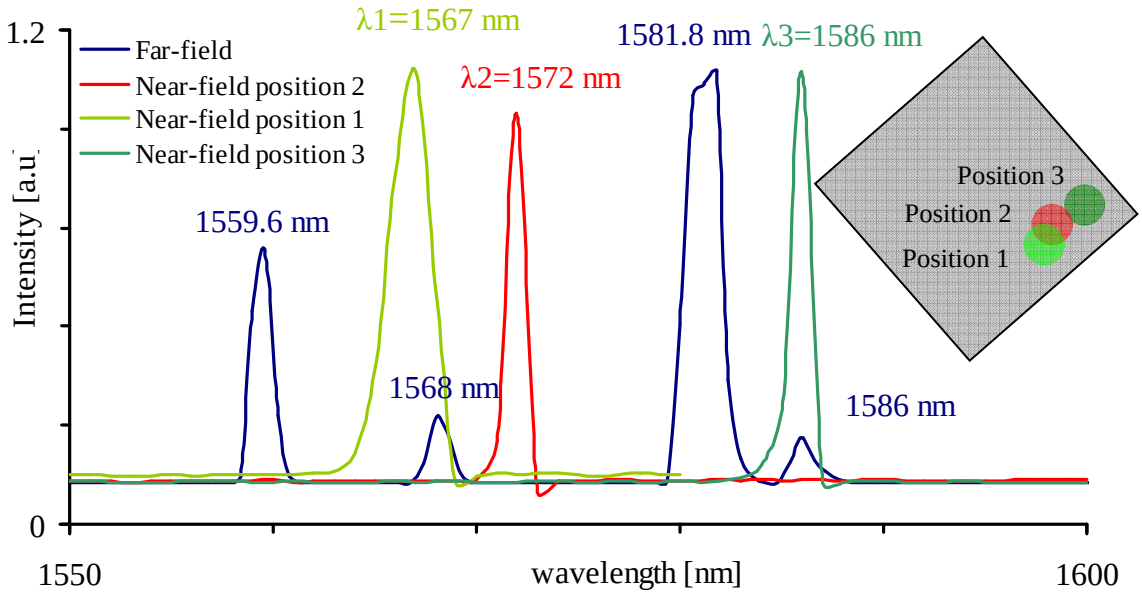

Figure 5.18: Far- and near-field spectrum of VS-DPC with 40 atoms. Far-field spectrum (blue curve) reveals four lasing peaks. Near-field measurements at several positions in this structure (inset) provide the corresponding resonant wavelengths.

Near-field spectra recorded at the position 1 and 3 reveals two lasing modes at λ_1=1567nm and λ_3=1586nm respectively which were identical to the lasing peaks obtained

by far-field measurement. However, at position 2, near-field measurement reveals the new peak which was not detected with far-field set-up. This may be due to the fact that the local excitation in near-field enables to provide higher optical density (because of small pumping area) to excite these modes which have high lasing threshold. Moreover, this mode is under the light line, theoretically does not have much vertical emission, thus difficult to detect in far-field using low numerical aperture objective.

Figure 5.19 shows the NSOM images recorded at the 3 positions. The dashed arrows pointed from optical images to topographies indicate the corresponding positions of localized modes in structure. The comparison between cartographies and topographies also proves that no defect contributes to these localized modes and which confirms the role of disorder in the process of localization.

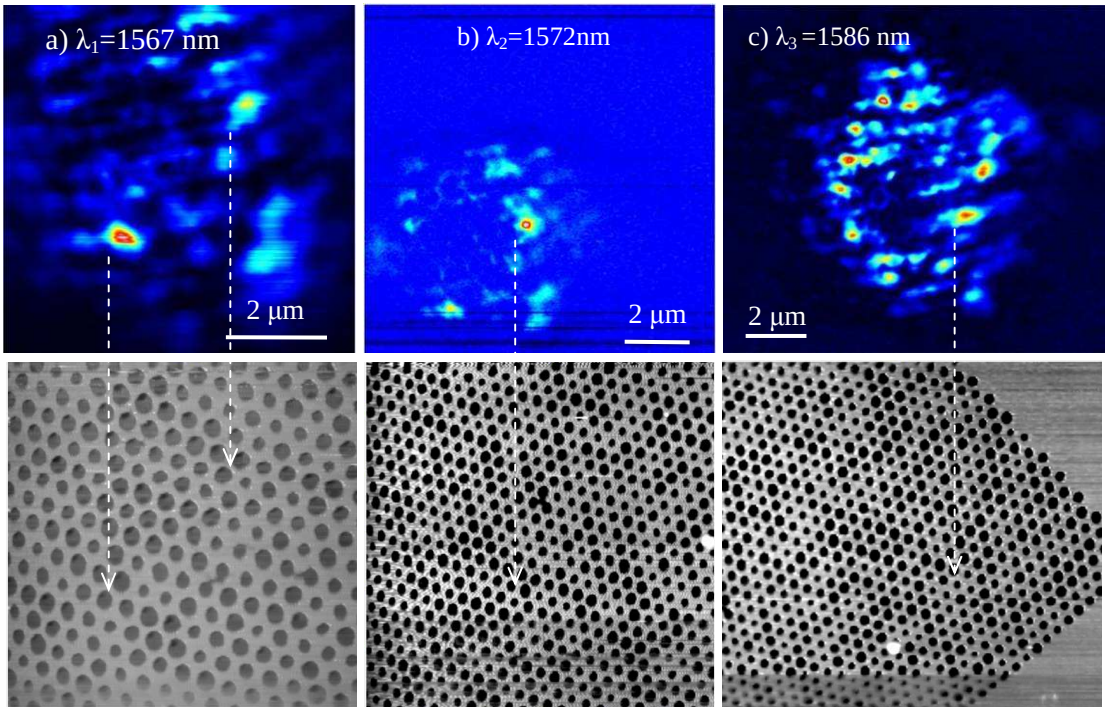

Figure 5.19: NSOM optical images at the resonant wavelength corresponding to positions 1 (a)-2(b)-3(c) in Figure 5.18. The localized modes are clearly visible at some locations in cartographies and verified not due to the defects by matching with the topographies (below).

Note that the mode at 1586 nm spread into the structure. It may confirm that this mode is linked to the former slow-Bloch mode of the ordered crystal which has been partly localized by the disorder. The other two modes have their wavelengths in what

should be the remaining band-gap. They are strongly localized in some tiny areas of the crystal and can only be detected when the tip is above the mode.

Conclusion

We have reported the first time ever the direct observation of phase transition from slow light mode to localized mode due to the disorder of structure with a sub-wavelength resolution. The random lasing wavelengths of these localized modes vary on different locations of structure. Our experimental results concerning the systematic shift of MPC spectra as composition ratio change and configuration-independent were also coherent with studies by μNOEL group.[14]

References

[1] *Anderson, P. W. "Absence of diffusion in certain random lattices". Phys. Rev.* ***109****, 1492-1505 (1958).*

[2] *Zhong, J.; Stocks, G.M. Localization/Quasi-delocalization transitions and quasi-mobility-edges in shell-doped nanowires. Nano lett. 2006, 6, 128-132.*

[3] *Sundqvist, P.; Garcia-Vidal, F. J.; Flores, F; Moreno-Moreno, M; Gómez-Navarro, C.; Bunch, J. S.; Gómez-Herrero, J. Voltage and length-dependent phase diagram of the electronic transport in carbon nanotubes. Nano lett. 2007, 7, 2568-257.*

[4] *Weaver, R. L. Wave Anderson localization of ultrasound. Motion 1990, 12, 129-142.*

[5] *Roati, G., D'Errico, C., et al. Anderson localization of a non-interacting Bose-Einstein condensate. Nature* ***453****, 895-898 (2008).*

[6] *Wiersma, D. S.; Bartolini, P.; Lagendijk, A. ; Righini. R. Localization of light in a disordered medium. Nature* ***1997****, 390, 671-673.Cao, H. et al.; "Spatial Confinement of Laser Light in Active Random Media," Physical Review Letters, vol. 84, No. 24, pp. 5584-5587, Jun. 12, 2000.*

[7] *Cao, H. et al.; "Spatial Confinement of Laser Light in Active Random Media," Physical Review Letters, vol. 84, No. 24, pp. 5584-5587, Jun. 12, 2000.*

[8] *P. T. Kristensen, P. Lodahl and J. Mørk, "Light propagation in finite-sized photonic crystals: Multiple scattering using an electric field integral equation", Journal of the Optical Society of America B,* ***27****, 228-237 (2010)*

[9] *John, S. "Strong localization of photons in certain disordered dielectric super lattices". Phys. Rev. Lett.* ***58****, 2486-2489 (1987).*

[10] *Topolancik, J., & Vollmer, "F. Random high-Q cavities in disordered photonic crystal waveguides". Appl. Phys. Lett. 91, 201102-1-3 (2007)*

[11] *F. Capasso, "Band-gap engineering - from physics and materials to new semiconductor-devices," Science 235(4785), 172–176 (1987)*

[12] *H. J. Kim, Y. G. Roh, and H. Jeon, "Photonic bandgap engineering in mixed colloidal photonic crystals," Jpn. J. Appl. Phys. 44(40), L1259–L1262 (2005)*

[13] *H. J. Kim, D. U. Kim, Y. G. Roh, J. Yu, H. Jeon, and Q. H. Park, "Photonic crystal alloys: a new twist in controlling photonic band structure properties," Opt. Express 16(9), 6579–6585 (2008)*

[14] *Sunghwan Kim, Sungjoon Yoon, Hyojun Seok, Jeongkug Lee, and Heonsu Jeon, "Band-edge lasers based on randomly mixed photonic crystals," Opt. Express 18, 7685-7692 (2010)*

Conclusion

In this thesis, we have characterized the near-field and far-field optical properties of honeycomb 2D PC from theoretical simulation to experimental measurements. Calculated photonic band-diagram presented the three first slow Bloch modes at high symmetric Γ-point labeled as monopolar mode (mode M, lowest energy), hexapolar mode (mode H) and dipolar mode (mode D). The numerical simulations of optical intensity patterns were performed in finite honeycomb 2D PC both in 2D and 3D-FDTD. Mode M always presented high quality factors at very low band curvature, leading to low threshold vertical emission laser. As simulation, mode M indicated the electric field distribution in doughnut shape with azimuthal polarization in each unit cell. The mode expansion was only limited by the structure size of PC and obtained the Gaussian shape reflecting the excitation profile of TE dipole. The partial field components E^2_x and E^2_y of mode M in PC structures indicated the decomposing of doughnuts into two lobes laid on either side of the polarization axis.

Honeycomb 2DPC was designed to support the telecommunication wavelength (resonated at λ=1.55μm), with lattice parameters A=730nm and an air hole diameter of 245nm. Several structures were fabricated in InP slab-bonded glass substrate with four layers of quatum well InAsP at the center of waveguide, using EBL and RIE microfabrication processes.

The far-field measurements by photoluminescence set-up were employed on PC structures for spectra analyses. We observed strong lasing from different PC structures in which resonant spectra suffered blue-shifts with increasing of air filling factors. The monopolar mode was dominant in most structures with resonant wavelengths around 1.55μm. We also observed the doughnut-shape on IR camera due to the constructive and destructive interferences as mode M radiated from near- to far-field. Further characterizations of the polarization of the emitted beam demonstrated the azimuthal polarization state of this light.

NSOM measurements were performed for near-field investigation of field distribution and polarization of slow Bloch modes. No perturbation of near-field probe to local field was recorded during experiments indicated by the identical resonant wavelength

between far-field and near-field measurements. First, conventional probes, including dielectric tapered fiber and circular aperture Al-coating probes were employed. For dielectric we recorded the limited spatial resolution ($\lambda/4.5$) in optical pattern that is lower than the required value to reveal the doughnut in each unit cell of honeycomb structure as simulation. This was explained as the unexpected coupling of propagating light to the flank of dielectric probe, so optical pattern contained a lot of low spatial frequency components and reduced the spatial resolution. The circular aperture probe, however, can filter out effectively the propagating light; therefore successfully reveal the doughnut in unit cell as simulation prediction.

Using BNA-probe the NSOM measurements gave insight about slow Bloch modes thanks to high spatial resolution ($\lambda/13$) and coupling enhancement. These results included the azimuthal polarization in unit cell, intensity patterns of E_x and E_y-components, mode confinements. The further investigations indicated that the real mode expansion is in the range of excitation spot size and may be governed by mechanisms involving carrier-induced refractive-index change.

Finally, we performed for the first time the direct observation of random lasing from AL modes in DPC hetero-structures. The localized lasing modes induced by a certain degree of structural randomness were observed using NSOM with sub-wavelength resolution. This work provides the first guide for designing random photonic band gap structures that exhibit AL, such as 2D-DPC. This approach is applicable to the fabrication of advanced devices such as micro-laser and single photon sources. Due to high photon confinement efficiency and structural robustness toward omnipresent fabrication imperfections, DPCs might be ideal to realize novel photonic devices and provide an innovative tool for fundamental studies.

The further studies based on NSOM set-up with various NSOM probes could be:

1) Investigating the dependence of structure size on the surface expansion of slow light mode using BNA-probe.
2) Measuring the transmission spectra of BNA-prove to identify their resonant peaks.
3) In some later experiments, we observe the perturbation of near-field modes with presence of near-field probes as well as the shift of resonant spectra. However, we

are not able confirm and understand entirely this phenomenon except the observation in IR camera. Thus, the perturbation of near-field probes, including conventional probes and antenna probes to the near-field modes in PC should be studied further.

4) The 3D-FDTD simulations of Anderson's localization on DPC are in progress. These numerical results are very important to understand the mechanism behind the localized electromagnetic fields in DPC and generation of Anderson's localization

5) The perspective of using disordered photonic crystals to realize micro-lasers should be investigated further.

6) Investigation of coupling of EM field to the bow-tie antenna placing closely on PC surface to realize the photon funneling effect are in progress.

Annex A

Calibration of piezo-electric system of NSOM

Before using the NSOM head or after long time operation, one has to calibrate its piezo-electronics system. Two reference samples are used: sample TGX01 for x-y axis and TGZ02 for z axis. The calibration process is as follow:

a. Scanning sample with present system for topography.

b. Then, using proper software to measure the dimensions of reference structures along x-y-z. Taking mean value.

c. Calculation of multiple factor A= (mean value of x)/(reference value of x). The same for B(y) and C(z).

d. Correcting the value Xr, Yr and Zr in the file of SMENA.par (in folder SMENA NSOM): (Old Xr)/A=(new Xr). The same for Yr and Zr.

The table below lists all of calibration parameters using for present piezo-electric system:

	Reference value	Measured value	Mea./Ref.	Old value	New value
x(µm)	3.0	3.02	A=1.01	Xr= 0.0767	Xr=0.07594
y(µm)	3.0	3.24	B= 1.08	Yr=0.0764	Yr=0.07074
z(nm)	101.8	116.0	C= 1.1395	Zr=0.66	Zr=0.5792

Annex B

Calibration of monochromator

For calibration of monochromator we used two reference laser diodes (1.3µm and 1.55µm) and spectrum analyzer. To get rid of any ambient influence, a longpass filter at 1100nm cut off frequency was used. The process is described following:

a. Making spectrum of given 1.3µm laser diode (peak at 1298.5nm) by spectrum analyzer. Setting device at the highest resolution (around 0.02nm) so that we can obtain the best spectral graph.

b. Then making spectrum of the above laser by monochromator with optimum slit opening (12µm in this case) to obtain the best spectral resolution and sufficient intensity.

c. Comparing the shift of two peaks between the reference spectral graph (step a) and the measured one (step b).

d. Repeating the above steps (a to c) with 1.55mm reference laser diode (peak at 1535.8nm) and the same conditions.

e. Final we obtained the mean value of -5.484nm (the old is -2.876) for calibration process.

In addition, we found that position of optical fiber as being injected into monochromator also impacts on spectra: the further the tip end to reflecting mirror, the more the red-shift occurs and the maximum value obtained about 0.33nm. On contrary, rotation of fiber around the fiber input does not impact on its spectra.

Annex C

Gaussian function

A Gaussian function (named after Carl Friedrich Gauss) is a function of the form:

$$I(x) = I_{off} + I_0 \exp\left[-\frac{8(x - x_0)^2}{L^2}\right] \quad (*)$$

where: I_{off}, I_0 being the offset value and the height of the curve's peak value.

x, x_0 being the independent variables and position of the centre of the peak respectively;

L being the width of the bell, or the size of Gaussian curve in our case. This value is defined at I_0/e^2, e is the Euler constant (~ 2.71828).

Figure below illustrates the Gaussian curves as a function of variable x. Since the intensity profile of excitation spot and the slow Bloch modes on surface of sample follows the Gaussian distribution, this function could used to calculate the excitation spot size, mode expansion... which are defined as a value of L

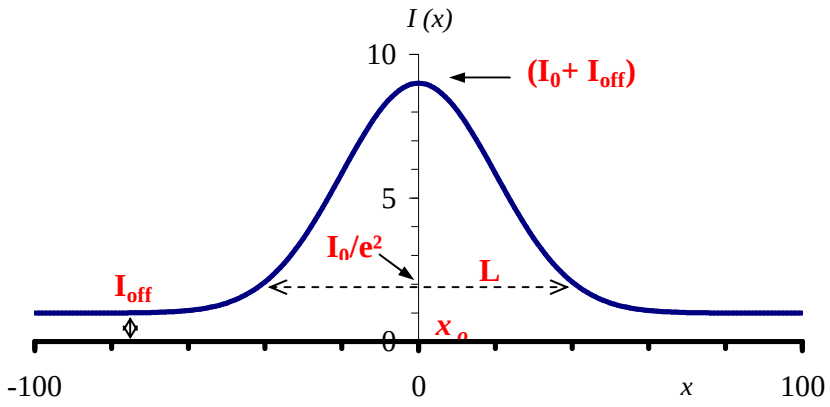

Illustration of Gaussian curve as a function of variable x.

Optical near-field characterization of slow-Bloch mode based photonic crystal devices

2D-Photonic crystal (PC) structures have enabled the fabrication of a wide variety of nanophotonic components. In perfect PCs, the exploitation of the enhanced local density of states at critical points of the band diagram has attracted considerable attention. Near these points, where the group velocity vanished, low curvature flat bands give rise to delocalized and stationary optical slow Bloch modes (or slow light modes). Properties of slow light make them good candidates to enhance Purcell or various non-linear effects or to design low-threshold lasers. Among these modes, slow Bloch modes (SBMs) emitting in the vertical direction, i.e. located at the Γ-point of the Brillouin zone are particularly interesting for integrating 2D PC architectures with free space optics. In particular, some SBMs proved to be suitable for achieving strong vertical emission with peculiar polarization properties. Other promising applications concern disorder: by introducing a controlled randomness into the PC structure, it is possible to induce a transition from slow Bloch mode (in ordered PC) to Anderson's localization (in disordered PC) as a function of disorder degree.

In this PhD dissertation, Slow Bloch modes have been studied and characterized by the means of Near-field Scanning Optical microscopy (NSOM). We particularly focused on Slow Bloch laser mode at Γ-point of a honeycomb 2DPC. This NSOM technique enables to visualize the evanescent component of the mode with a spatial resolution below the diffraction limit. In this work, we showed that the far-field and the near-field image of the mode at the 2D-PC surface are different and that near-field results yield a better insight in the real mode structure inside the PC slab in agreement with theoretical prediction. The importance of the probe selection (bare silica, metallized tip and bow-tie aperture nanoantenna) for studying III-V photonic crystal structures was also demonstrated. Besides intensity measurement of the electromagnetic field, the polarization of the electric field has been measured at the nanoscale for the first time by using a bow-tie nano-antenna probe. These results enable the unambiguous identification of the modes with the 3D-FDTD simulations.

In this work is also reported the first observation of two-dimensional localization of light in two types of 2D random photonic crystal lasers, where Slow Bloch Mode (SBM) is scattered by artificial structural randomness in triangular PCs. The structural randomness is introduced whether by nanometer displacements in the positions of lattice elements (air holes), whether by variation of the hole diameters. The direct near-field imaging of the lasing mode by use of NSOM for the first time, allowed us to observe the transition of the extended planar SBM to be Anderson localized.

Les structures à cristaux photoniques bidimentionnels ont permis la fabrication d'une large variété de composants nanophotoniques. En particulier, dans les PC parfaits, la densité locale d'états optiques se trouve exacerbée au niveau des points de symétrie du diagramme de bande. Près de ces points, où la vitesse de groupe tend vers zéro, la faible courbure de bande courbure de bande donne lieu à des modes stationnaires, dits de lumière "lente" (ou modes de Bloch lents). Les propriétés de la lumière lente en font de bons candidats pour améliorer l'effet Purcell, pour produire des effets non-linéaires ou pour concevoir des lasers à faible seuil. Parmi ces modes, les modes de Bloch lent émettant dans la direction verticale, c'est à dire situé au niveau du point Γ de la zone de Brillouin, sont particulièrement intéressants pour intégrer des architectures 2D avec de l'optique en espace libre. En particulier, certains de ces modes ont permis la réalisation d'émission laser dans la 3e direction avec des propriétés de polarisation particulières. D'autres applications prometteuses concernent le désordre : en introduisant un désordre aléatoire mais contrôlé dans la structure photonique, il est possible d'induire une transition entre le mode de Bloch lent de la structure ordonnée vers un mode localisé par le désordre, de type localisation d'Anderson dans une structure faiblement désordonnée.

Dans cette thèse, les modes de Bloch lents ont été étudiés et caractérisés en Microscopie optique en champ proche. Nous nous sommes concentrés sur les modes en Gamma de la structure graphite. Le SNOM a permis de visualiser la composante évanescente du mode avec une résolution spatiale inférieure à la limite de diffraction. Dans ce travail, nous avons montré que le champ lointain et de l'image en champ proche du mode à la surface du cristal photonique sont différentes et que seules les mesures en champ proche permettent de rendre compte du mode réel à l'intérieur de la membrane de cristal photonique, en accord avec prédiction théorique. L'importance du choix de la sonde (silice, pointe métallisée, Nano-antenne) pour l'étude des structures à cristaux photoniques a également été démontrée. Outre la mesure d'intensité du champ électromagnétique, la polarisation du champ électrique a été mesurée à l'échelle nanométrique pour la première fois par l'aide d'une antenne à ouverture papillon. Ces résultats permettent d'identifier sans équivoque des modes avec les simulations 3D-FDTD.

Dans ce travail est également rapporté la première observation de la localisation de la lumière dans deux types de lasers aléatoires à base de cristaux photoniques bidimensionnels. Le caractère aléatoire est introduit soit en déplaçant les positions des motifs du cristal (trous d'air), soit en faisant varier de façon aléatoire le diamètre des trous. Pour la première fois nous avons observé directement par SNOM la localisation de la lumière dans le cristal désordonné. Cela nous a permis d'observer la transition de morphologie du mode de Bloch lent entre le cristal ordonné et le cristal désordonné.